Quantifying Natural CO_2 Emissions from Mofettes at the Starzach Site in Southwest Germany with a Low-Cost Sensor Network

Dissertation

der Mathematisch-Naturwissenschaftlichen Fakultät

der Eberhard Karls Universität Tübingen

zur Erlangung des Grades eines

Doktors der Naturwissenschaften

(Dr. rer. nat.)

vorgelegt von

Yann Georg Büchau

aus Hamburg

Tübingen

2025

Gedruckt mit Genehmigung der Mathematisch-Naturwissenschaftlichen Fakultät der Eberhard Karls Universität Tübingen.

Tag der mündlichen Qualifikation:	03.02.2026
Dekan:	Prof. Dr. Thilo Stehle
1. Berichterstatter:	Prof. Dr. Jens Bange
2. Berichterstatter:	Prof. Dr. Peter Dietrich

License

Abstract

The natural carbon dioxide (CO_2) degassings at the Starzach site near the Black Forest in southwestern Germany are recovering from a century of industrial exploitation. CO_2 of presumably non-volcanic magmatic origin is released into the atmosphere via a cluster of mofettes of different sizes or diffusively through the soil, in patterns following a geological fault line running from southwest to northeast. Since the end of the industrial mining period in 1995, no comprehensive estimation of the total degassing rate at the site is available. This work presents three independent quantification approaches for the core Starzach mofette area ($20\,\mathrm{m} \times 20\,\mathrm{m}$) with a focus on cost-effectiveness, each addressing a specific spatial scale: Degassing quantification of the most active mofette via volumetric flow rate measurement ($465\,\mathrm{kg\,d^{-1}} \pm 16\,\%$, roughly extrapolated to other mofettes in the core Starzach mofette area: $\sim 1500\,\mathrm{kg\,d^{-1}}$), near-surface flux-gradient method validated by eddy covariance (EC) measurements (max. $25\,\mathrm{mg\,m^{-2}\,s^{-1}}$, areal extrapolation: $\sim 900\,\mathrm{kg\,d^{-1}}$), and a custom divergence-theorem based method deriving CO_2 transport vectors from cross-correlations between atmospheric point measurements across the site ($3266\,\mathrm{kg\,d^{-1}} \pm 42\,\%$), which is considered the most representative of the three due to its spatial coverage. Based on this, it is suggested that including other visible mofettes and abandoned boreholes within around 100 m distance brings the total CO_2 emission of the Starzach site to an order of magnitude of roughly $10\,\mathrm{t\,d^{-1}}$. All techniques utilized low-cost equipment, with CO_2 sensors priced well below 100 € per piece, and were embedded in a wireless sensor network that enabled real-time remote monitoring. Low-cost equipment proved to be sufficiently accurate for emission quantification at the Starzach site. The difference between the results of the three employed methods demonstrates the importance of a hierarchical measurement approach covering different spatial scales as suggested by Sauer et al. (2013) because cross-validation becomes possible.

Zusammenfassung

Nach einer langen industriellen Förderperiode im letzten Jahrhundert nehmen die natürlichen Kohlenstoffdioxid (CO_2)-Emissionen an den Starzacher „Kohlensäurequellen“ nahe des Schwarzwaldes im Südwesten Deutschlands wieder zu. Das Gas gilt als nichtvulkanisch-magmatischen Ursprungs und tritt in Starzach durch Mofetten oder diffus durch den Boden entlang einer linienförmigen, südwestlich-nordöstlich verlaufenden, geologischen Störung an die Oberfläche. Seit dem Ende der industriellen Förderung in 1995 gibt es dort keine umfassende Messung oder Abschätzung der gesamten CO_2-Ausstoßrate. Diese Arbeit stellt drei unabhängige, kostengünstige Quantifizierungsansätze für das Starzacher Kernmofettengebiet ($20\,\mathrm{m} \times 20\,\mathrm{m}$) vor, die jeweils unterschiedliche Raumskalen abdecken: direkte Ausstoßmessung der aktivsten Mofette durch Volumenflussmessung ($465\,\mathrm{kg\,d^{-1}} \pm 16\,\%$, geschätzte Hochrechnung auf die Mofetten im Kerngebiet: $\sim 1500\,\mathrm{kg\,d^{-1}}$), bodennaher Gradientenansatz validiert mit Eddy-Kovarianzmessungen (max. $25\,\mathrm{mg\,m^{-2}\,s^{-1}}$, auf Kerngebiet extrapoliert: $\sim 900\,\mathrm{kg\,d^{-1}}$) und eine neuartige Methode, bei der CO_2-Transportvektoren aus Kreuzkorrelationen zwischen atmosphärischen Konzentrationsmessungen abgeleitet und mithilfe des Gaußschen Integralsatzes kumuliert werden ($3266\,\mathrm{kg\,d^{-1}} \pm 42\,\%$). Aufgrund der größeren räumlichen Abdeckung wird die letzte Methode als die repräsentativste der drei angesehen. Basierend darauf wird der CO_2-Ausstoß zusammen mit anderen sichtbaren Mofetten und den übrigen ehemaligen Förderbrunnen im Abstand von etwa 100 m auf rund $10\,\mathrm{t\,d^{-1}}$ geschätzt. Für alle drei Methoden wurden kostengünstige Sensoren (unter 100 € pro Stück) verwendet und in ein kabelloses Netzwerk integriert, was Echtzeitüberwachung ermöglicht. Es konnte gezeigt werden, dass die Präzision kostengünstiger Sensorik für die CO_2-Quantifizierung in Starzach ausreichend ist. Die Unterschiede zwischen den Ergebnissen der drei Methoden zeigt die Wichtigkeit eines hierarchischen Messansatzes und der Abdeckung mehrerer räumlicher Skalen, wie von Sauer u. a. (2013) motiviert, damit Kreuzvalidierungen möglich werden.

Acknowledgements

This work was funded by the German Research Foundation (DFG), grant number BA 1988/19-1. The Alfred-Teufel foundation covered the costs of most of the equipment and components used in the development of the necessary measurement systems. Special thanks to Max-Richard Freiherr von Rassler, who kindly granted access to the site on his property.

I would like to thank my supervisors Jens Bange and Carsten Leven for their considerate and supportive guidance throughout this dissertation and the overarching projects. Thanks to my coworkers in the Environmental Physics working group, especially to Martin Schön, Kjell zum Berge, Andreas Platis, and Ines Schäfer for being excellent and reliable colleagues, who provided advice and practical help when needed. I also thank all contributing students whose theses I co-supervised, as well as all student assistants, especially Björn Riebandt, for many hours of exciting lab work and the always interestingly challenging field implementation. It was a joy working with all of you. Particularly motivating was to see how the available free and open source operating systems and software packages enable a wide range of experimentation in research. I am furthermore grateful for the support of my friends and family, my dear wife Silke, my brothers Marc and Ben, my inspiring daughter Hannah, and my soon-to-be-born second child.

Contents

Glossary **8**

Symbols **9**

1 List of Publications **10**

1.1 First-Author Publications 10

1.2 First-Author Conference Contributions Related to this Dissertation 11

1.3 Data Publications Related to this Dissertation 11

2 Introduction **12**

2.1 The Starzach site 14

2.2 Objectives / Research Questions 17

3 Quantifying CO_2 Emissions at the Starzach Site **18**

3.1 Dynamics of Atmospheric CO_2 Concentration at the Starzach Site 18

3.2 Degassing of an Individual Mofette 22

3.3 Eddy Covariance / Flux-Gradient Method: Vertical Turbulent Flux 28

3.4 Deriving Areal CO_2 Emissions with a Sensor Network 37

4 Conclusion **42**

5 Outlook **44**

6 References **46**

7 Appendix **58**

A Büchau et al. (2022): Atmospheric CO_2 dynamics in Starzach 59

B Büchau et al. (2024a): CO_2 Exhaust of a Single Starzach Mofette 75

C Büchau et al. (2024b): PARMESAN Meteorological Analysis Software 95

D Büchau and Bange (2025): Starzach CO_2 Emission Quantification with Sensor Network 104

Glossary

ADE Advection-Diffusion Equation

CCS Carbon Capture and Sequestration

CH_4 methane

CO_2 carbon dioxide

DFG German Research Foundation

EC eddy covariance

GHG greenhouse gas

H_2O water vapour

I^2C Inter-Integrated Circuit

IRGASON Integrated CO_2/H_2O Open-Path Gas Analyzer and 3D Sonic Anemometer

MITRAS Microscale Transport and Stream Model

FOSS Free and Open Source Software

MOST Monin-Obukhov Similarity Theory

N_2O nitrous oxide

NDIR Non-Dispersive Infrared

PARMESAN Python Atmospheric Research Package for Meteorological and Timeseries Analysis

WPL Webb, Pearman, and Leuning

Symbols

Symbol	Description	Value/Units	Pages
g	acceleration in Earth's gravity	$\sim 9.8\,\mathrm{m\,s^{-2}}$	29
ρ_{air}	air density	$\mathrm{kg\,m^{-3}}$	28
ρ_{CO2}	CO_2 mass concentration	$\mathrm{kg\,m^{-3}}$	9, 28, 38
$\rho_{\mathrm{CO2}}\,(t, \vec{p})$	CO_2 mass concentration in time and space	$\mathrm{kg\,m^{-3}}$	38
K_{CO2}	vertical exchange coefficient for CO_2	$\mathrm{m^2\,s^{-1}}$	28–30, 34–36
K_{H2O}	vertical exchange coefficient for H_2O	$\mathrm{m^2\,s^{-1}}$	34–36
$\dot{V}$	volumetric flow rate	$\mathrm{m^3\,s^{-1}}$	22, 24–26
F_{CO2}	upwards CO_2 mass flux	$\mathrm{kg\,m^{-2}\,s^{-1}}$	28, 29, 34–36
F_{H2O}	upwards H_2O mass flux	$\mathrm{kg\,m^{-2}\,s^{-1}}$	34
$\vec{F}_{\mathrm{CO2}}\,(t, \vec{p})$	CO_2 transport vector in time and space	$\mathrm{kg\,m^{-2}\,s^{-1}}$	38, 39
u^*	friction velocity	$\mathrm{m\,s^{-1}}$	29–31, 33, 36
R^*	universal gas constant	$\sim 8.3145\,\mathrm{J\,mol^{-1}\,K^{-1}}$	22
RH	relative humidity	%	23, 24
L_{v}	latent heat of vaporization	$\sim 2500\,\mathrm{kJ\,kg^{-1}}$	34
$\vec{p}$	vector pointing to location in space	m	9, 38, 39
$\dot{m}_{\mathrm{CO2}}$	mass emission rate of CO_2	$\mathrm{kg\,s^{-1}}$	22, 38–41, 45
r_{CO2}	molar mixing ratio of CO_2 in dry air	mol/mol	28
M_{air}	molar mass of dry air	$\sim 0.029\,\mathrm{kg\,mol^{-1}}$	22, 28
M_{CO2}	molar mass of CO_2	$\sim 0.044\,\mathrm{kg\,mol^{-1}}$	22, 28
X_{CO2}	molar fraction of carbon dioxide (CO_2) in air	$\mathrm{mol\,mol^{-1}}$	22–24
ϕ	Monin-Obukhov stability function	dimensionless	29, 30, 36
$\mathrm{L_{MO}}$	Obukhov length	m	29
p	atmospheric pressure	Pa	22, 23
$\mathrm{Ri_b}$	bulk Richardson number	dimensionless	31, 32
$\vec{u}_{\mathrm{CO2}}\,(t, \vec{p})$	CO_2 movement speed vector in time and space	$\mathrm{m\,s^{-1}}$	38
S	surface area	$\mathrm{m^2}$	38, 39
T	temperature	K	22–24
θ_{v}	virtual potential temperature	K	29
t	time	s	9, 38, 39
V	volume	$\mathrm{m^3}$	39
κ	von Kármán constant	~ 0.4	29, 30
w	upwards vertical wind speed	$\mathrm{m\,s^{-1}}$	28, 29
z	height above ground	m	28–31

1 List of Publications

1.1 First-Author Publications

This cumulative dissertation is based on the following four peer-reviewed articles, of which the full texts are available in Appendix A, Appendix B, Appendix C, and Appendix D:

[1] Büchau, Y. G. and Bange, J. 'Quantification of Natural CO2 Emissions from Mofettes Using a Low-Cost Sensor Network at the Starzach Site in South-West Germany'. In: *PLOS Climate* 4.11 (25th Nov. 2025), e0000741. ISSN: 2767-3200. DOI: 10.1371/journal.pclm.0000741.

[2] Büchau, Y. G., Leven, C. and Bange, J. 'A Portable Low-Cost Device to Quantify Advective Gas Fluxes from Mofettes into the Lower Atmosphere: First Application to Starzach Mofettes (Germany)'. In: *Environmental Monitoring and Assessment* 196 (11th Jan. 2024), 138. ISSN: 1573-2959. DOI: 10.1007/s10661-023-12114-8.

[3] Büchau, Y. G., Mashni, H., Bramati, M., Savvakis, V., Schäfer, I., Jung, S., Miranda-Garcia, G., Hardt, D. and Bange, J. 'PARMESAN: Meteorological Timeseries and Turbulence Analysis Backed by Symbolic Mathematics'. In: *Journal of Open Source Software* 9.94 (9th Feb. 2024), 6127. DOI: 10.21105/joss.06127.

[4] Büchau, Y. G., van Kesteren, B., Platis, A. and Bange, J. 'An Autarkic Wireless Sensor Network to Monitor Atmospheric CO2 Concentrations'. In: *Meteorologische Zeitschrift* 31.4 (13th Oct. 2022), 331–345. DOI: 10.1127/metz/2022/1125.

1.2 First-Author Conference Contributions Related to this Dissertation

[1] Büchau, Y., Platis, A., van Kesteren, B. and Bange, J. *Ein Autarkes, Kabelloses Sensornetzwerk Zur Überwachung Natürlicher CO2-Emissionen*. DACH2022-236. Leipzig, Deutschland: DACH Meteorologie Tagung 21.-25. Mar 2022, Copernicus Meetings, 25th Mar. 2022. DOI: 10.5194/dach2022-236.

[2] Büchau, Y. and Bange, J. *Überwachung natürlicher CO2 Emissionen unter Verwendung eines Netzwerks aus kostengünstigen Sensoren*. Garmisch-Partenkirchen, Germany: DACH Meteorologie Tagung 18.-22. Mar 2019, Copernicus Meetings, 19th Mar. 2019. URL: https://meetingorganizer.copernicus.org/DACH2019/DACH2019-77-1.pdf (visited on: 08.09.2025).

[3] Büchau, Y., Leven-Pfister, C. and Bange, J. *A Dense Sensor Network to Monitor Natural CO2 Emissions*. poster presentation. Copenhagen, Denmark: EMS Annual Meeting 2019, Copernicus Meetings, 10th Sept. 2019. URL: https://meetingorganizer.copernicus.org/EMS2019/EMS2019-77-1.pdf (visited on: 08.09.2025).

[4] Büchau, Y., Putze, U. and Bange, J. *Environmental Influences on a Network of Low-Cost CO2 Sensors*. presentation. Budapest, Hungary: EMS Annual Meeting 2018, Copernicus Meetings, 5th Sept. 2018. URL: https://meetingorganizer.copernicus.org/EMS2018/EMS2018-497.pdf (visited on: 08.09.2025).

1.3 Data Publications Related to this Dissertation

[1] Büchau, Y. *CO2 Time Series Data of Eleven Sensor Stations in Summer 2022 at the Starzach Site in South-Western Germany*. dataset. Zenodo, 4th Sept. 2025. DOI: 10.5281/zenodo.17055782.

[2] Büchau, Y. and Bange, J. *Dynamics of CO2 Concentration and Meteorological Parameters at the Starzach Mofette Site in 2020 Observed with Sensirion SCD30 Sensor and Gill MaxiMet GMX541 Compact Weather Station*. dataset bundled publication. PANGAEA, 2023. DOI: 10.1594/PANGAEA.963917.

[3] Büchau, Y., Dörner, L. and Bange, J. *Short-Term Comprehensive CO2 Degassing Dataset from a Mofette at the Starzach Site in Winter 2022 Obtained with a Custom Flow Meter, Including Atmospheric Variables*. dataset bundled publication. PANGAEA, 2023. DOI: 10.1594/PANGAEA.963786.

2 Introduction

Over two hundred years ago, Fourier (1824) first outlined the warming effect that the Earth's atmosphere exerts on Earth's surface: Incoming solar short-wave radiation heats up the surface, which emits part of the received energy back outwards in the form of long-wave radiation. This energy is partly absorbed and subsequently radiated back by the atmosphere, effectively keeping the surface temperature more elevated than it would be without an atmosphere – a process later compared to 'the glass of a green-house' by Ekholm (1901). Arrhenius (1896) identified atmospheric CO_2 as the driver of a global temperature increase should its release through industrial coal combustion continue. In the last century, subsequent quantification of the increasing atmospheric CO_2 concentration was initiated (Keeling, 1960; Callendar, 1958) and awareness of its anthropogenic origin rose (Broecker, 1975; Sawyer, 1972). By now, there is a clear consensus among climate scientists that human activities are the reason for recent global warming (Cook et al., 2016). In 2015, the Paris Agreement (UNFCCC, 2015) was negotiated by the majority of world countries to work towards a reduction of anthropogenic greenhouse gas (GHG) emissions and its consequences. Still, GHG concentrations continue to rise, and with them the atmospheric temperature (Calvin et al., 2023). Recently, global average temperature first exceeded the pre-industrial levels by 1.5 K, a threshold the Paris agreement had sought to mitigate (Cannon, 2025). In terms of contribution to the greenhouse effect, the currently most important anthropogenic GHG is CO_2 due to its high atmospheric concentration (415 ppm = 0.0415 vol% global average in 2021, Calvin et al., 2023), thereafter following the more effective GHGs methane (CH_4) and nitrous oxide (N_2O), which are however less prevalent in the atmosphere (Mar et al., 2022; Etminan et al., 2016; Wallace and Hobbs, 2006).

Anthropogenic CO_2 emissions (from fossil fuel combustion, cement production, and land-use change: $36.4 \pm 1.8\,\mathrm{Gt\,a^{-1}}$, Friedlingstein et al., 2023) are by a large margin the driving source of atmospheric CO_2. Natural geological origins such as subaerial volcanoes, volcanic lakes, mid-ocean ridges, tectonic, hydrothermal or inactive volcanic areas, are estimated at only 1–2 % of anthropogenic CO_2 emissions ($\sim$600 $\mathrm{Mt\,a^{-1}}$, Orcutt et al., 2019; Burton et al., 2013; Mörner and Etiope, 2002). But the Earth mantle serves as a consistent source of non-anthropogenic CO_2: Magmatic fluids in the upper crust (10–15 km depth) often reach vapor-saturation and contain a significant amount of dissolved CO_2 (Lowenstern, 2001). Crystallization then causes CO_2 exsolution (Dasgupta, 2013), allowing the gas to ascend further to the surface through pathways such as geological faults, and to eventually enter the atmosphere through volcanoes (Carapezza et al., 2009), via mofettes (Lübben and Leven, 2018; Rogie et al., 2000), geysers (Glennon and Pfaff, 2005), or similar features. While reduction of anthropogenic CO_2 emissions is a matter of policy and technology use (Liu et al., 2025; Dabla-Norris et al., 2023; Acemoglu et al., 2016; Rosenfeld et al., 2000), natural sources of CO_2

in contrast constitute a mostly invariant, yet rather uncertain baseline that is still not conclusively understood and needs further quantification (Wong et al., 2019; Burton et al., 2013). To fully assess the global GHG budget, it is thus important to investigate both anthropogenic and non-anthropogenic CO_2 sources.

The last decades have seen the development of a variety of technologies and methods to quantify CO_2 emissions into the atmosphere, ranging from large-scale satellite-based inference over ground-based remote sensing approaches to in-situ techniques for precise local measurements. An overview is given in the introductions of Büchau et al. (2024a, Appendix B, page 77) and Büchau and Bange (2025, Appendix D, page 105) and summarized here. A collection of local approaches with very narrow spatial extents is typically used for *bottom-up* estimates, where emission rates from individual known point sources are summed, approximated or extrapolated to deduct a total areal emission rate. As this requires exact knowledge of the location, mechanism and prominence of all sources, bottom-up estimates can underestimate significantly ('factors two or more', Nisbet and Weiss, 2010), in certain cases even producing a sign inversion (CO_2 flux from land-use change in the Brazilian Amazon anomalously considered a sink via bottom-up approaches, Tejada et al., 2023). While bottom-up approaches are mostly concerned with individual sources, *top-down* methods attempt to derive source information from measurements of the sources' impacts, i.e. in most cases the local increase of atmospheric CO_2 concentration (Upton et al., 2024). However, depending on the spatial scale of interest, the boundary between bottom-up and top-down approaches may be fluid, as will become evident from this work.

Satellites can provide global CO_2 concentration data in the atmosphere on the kilometer scale (Pan et al., 2021) but lack resolution to study point sources in detail, for which ground-based measurements are necessary as a complement (Streets et al., 2013). In volcanic settings, remote sensing methods based on absorption spectroscopy are often used to quantify atmospheric gas concentrations up to a few kilometers distance (Feitz et al., 2018; Williams-Jones et al., 2008; Horton et al., 2006; Galle et al., 2003). These techniques need a known spectrum as reference such as a direct line of sight to the sun, the moon, or lava to assess the absorption of the trace gas of interest in the optical path (Platt et al., 2018; Stremme et al., 2012). This renders it difficult to apply at non-volcanic locations, around heavy vegetation, or in valleys, where in-situ measurements are more suitable.

In meteorological studies, the eddy covariance (EC) method is one of the most valued in-situ measurement techniques to quantify the vertical transport of trace gases (Mauder et al., 2021; Eugster and Merbold, 2015). Fast ($\geq$10 Hz) measurements of gas concentration and wind speed are correlated for a direct measurement of the vertical flux caused by turbulent eddies. The flux-gradient approach can be used to approximate this turbulent flux from slower measurements of the vertical concentration gradient (Zhao et al., 2019; Xiao et al., 2014). However, the EC

method requires several assumptions in its common application, most notably spatially homogeneous terrain and emissions, a negligible average vertical wind speed, as well as neglecting any advective transport (Mauder et al., 2021). Furthermore, footprint analysis can become nontrivial (Leclerc, 2014). Eddy covariance results are hence more difficult to interpret in complex terrain such as mountainous areas, or in areas with highly scattered and heterogeneous emission hotspots.

Point measurements of atmospheric gas concentrations distributed in a region of interest can be used in a variety of ways to derive areal emissions, for example employing inverse Lagrangian transport modelling (Pisso et al., 2019; Lin et al., 2003; Draxler and Hess, 1998), numerical solutions of the Advection-Diffusion Equation (Schaper et al., 2024), its simplified analytical solutions (Gaussian puff or plume model, Krause et al., 2023; Stockie, 2011), and divergence theorem-based methods (Ryoo et al., 2019; Karion et al., 2013), in descending order of complexity. A common application for the latter simpler methods is methane leakage detection in natural gas infrastructure (Bell et al., 2023). All abovementioned methods typically require knowledge of the wind vector either from measurements or model output and the assumption that the gas of interest is indeed transported with it, which is not necessarily the case for dense gases and in complex terrain.

The most direct assessments of gas emissions are provided by measurements at the source such as soil degassing measurements with accumulation chambers (Carapezza et al., 2009; Lewicki et al., 2009), the dynamic concentration method (Camarda et al., 2019; Gurrieri and Valenza, 1988), or in general by deploying sensors and probing facilities into the ground via Direct Push Technology (Sauer et al., 2013; Leven et al., 2011). For strong advective fluxes from the subsurface into the atmosphere, such as from vents or mofettes, measurements of the volumetric flow rate have proven effective (Lübben and Leven, 2022; Rogie et al., 2000).

This diverse arsenal of techniques underscores the challenges involved in measuring gas emissions. Sauer et al. (2013) suggest utilizing a combination of the above methods in a 'hierarchical monitoring approach' to investigate emissions at a given location and balance their respective strengths and weaknesses. In this work, this methodical fusion is applied for quantifying the natural CO_2 degassing from mofettes at the Starzach site in Germany, which is introduced in the following.

2.1 The Starzach site

The Starzach site is situated at the foot of a northern slope in the upper Neckar valley, east of the Black Forest in southwestern Germany (Figure 1). It is one of the few sites in and around Germany where natural (i.e. not-anthropogenic) CO_2 of geological origin is emitted from the Earth. Other prominent sites are located in the Volcanic Eifel in western Germany, such as the Andernach geyser, a cold-water geyser with the globally highest water fountain during an eruption (40–60 m, Glennon and Pfaff, 2005). During its restoration in 2001 it was measured to emit $\sim$350 kg of CO_2 per eruption, which would naturally repeat with a period of 1.5–2 h, but has to be regulated due to operational

Figure 1: *Overview of the Starzach site in southwestern Germany, highlighting the spatial distribution of its CO_2 degassing activity, the deployed measurement equipment, and relevant emission quantification studies with estimated CO_2 emission rates given in kg d^{-1}. Figure adapted from Büchau et al. (2022, Appendix A, page 61, kindly provided by the publisher under a CC-BY-4.0 license), with the following changes: Annotations of the aerial imagery on the right-hand side (drone photogrammetry from 2019 by Martin Schön) were updated, and the maps on the left-hand side were replaced with current views from OpenStreetMap.org ('Tracestrack Topo' layer, 16.10.2025). Map data © OpenStreetMap contributors (OpenStreetMap.org/copyright), SRTM, GEBCO, SONNY's LiDAR DTM, NASADEM, ESA WorldCover; Maps © Tracestrack, licensed under CC-BY-4.0.*

requirements, so this value can't be directly extrapolated to yearly emissions (Krauthausen, 2025; Myers et al., 2020). Another notable CO_2 degassing location in the Volcanic Eifel is the *Laacher See* volcanic lake, estimated to emit about 14 t km^{-2} d^{-1} (Goepel et al., 2015), which extrapolated to its surface area (3.31 km^2, Gal et al., 2011) would amount to roughly 17 kt a^{-1}. In the Western Eger Rift in the Czech Republic, just outside the eastern German border, two mofette fields were measured to have a soil CO_2 flux of 30 t d^{-1} and 23 t d^{-1}, and a degassing from mofettes of 3 t d^{-1} and 0.6 t d^{-1} respectively (Kämpf et al., 2019). It is noticeable that in the published scientific literature, comprehensive investigations of the total annual emissions of such CO_2-emitting sites are sparse.

The same is the case for the Starzach site. Lübben and Leven (2018) summarize the site's geological setting and history. They link the CO_2 degassings to a geological fault zone in the major tectonic Swabian-Franconian direction, which is evident from the arrangement of degassing hotspots (yellow dots) along a southwesterly/northeasterly line in Figure 1. In the 1900s, industrial extraction of the emitted CO_2 took place, with extraction rates of individual wells of 1000–4000 t a^{-1} recorded in the 1980s, but outputs gradually stagnated until mining was terminated entirely in 1995. The site has been recovering since then, with slowly redeveloping CO_2 exhaust in the form of

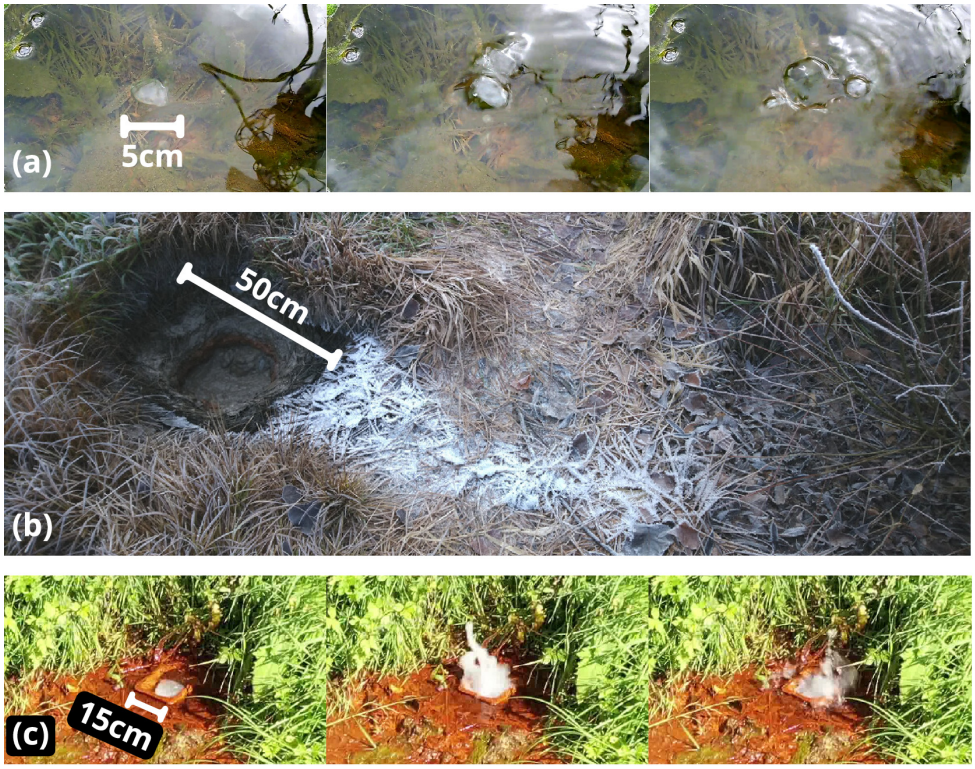

Figure 2: *Examples of CO_2 degassing at the Starzach site. Figure reproduced from Büchau et al. (2022, Appendix A, page 62, kindly provided by the publisher under a CC-BY-4.0 license).* **(a)** *diffuse degassing, small ascending gas bubbles (during spring 2020 flooding),* **(b)** *mofette with largest diameter, examined in 2015 by Lübben and Leven (2022),* **(c)** *picture by Martin Schön in 2019, groundwater monitor well, turned into the site's most active mofette shortly after its deployment in 2014.*

mofettes and diffuse degassing through the soil (Figure 2). The emitted gas is a mixture of mostly CO_2 (over 98 %), nitrogen (about 1 %), and trace amounts of helium, argon and methane. In 2015, Lübben and Leven (2022) measured the sites's most active mofette at the time (Figure 2b) to emit $\sim$75 kg d^{-1}. Since then, there were no further quantification attempts at the Starzach site, except for those presented in this work in the following. Lübben and Leven (2018) also suggest the Starzach site as a natural analogue and methodical testbed for a leaky Carbon Capture and Sequestration (CCS) reservoir. CCS is an often proposed (Štefanica et al., 2016; Szulczewski et al., 2012), actively tested (Bui et al., 2018), though controversial (Lefstad and Rivadeneira, 2025; Braun, 2017; Krüger, 2017; Stephens, 2015), global warming mitigation technique, where CO_2 from human activities is captured, and subsequently compressed into subsurface geological formations instead of releasing it into the atmosphere. As there are only few operational CCS sites worldwide (Bui et al., 2018), studying natural analogues such as the Starzach site is a practical opportunity to test several observational methods as suggested by Sauer et al. (2013).

2.2 Objectives / Research Questions

The objective of this dissertation is to quantify the natural CO_2 emissions at the Starzach site, with a focus on cost-effectiveness, real-time monitoring capability, scalability, and transferability to similar gas-emitting sites. The following research questions are addressed:

RQ 1: What are the dynamics of atmospheric CO_2 concentration at the Starzach site?

RQ 2: What is the CO_2 release rate of the visibly most active mofette at the Starzach site?

RQ 3: What regularities in the degassing of an individual mofette are observable?

RQ 4: At what rate does the core Starzach mofette area ($20\,\mathrm{m} \times 20\,\mathrm{m}$) emit CO_2 in total?

RQ 5: To what degree are low-cost sensors and approaches capable of this quantification?

These research questions are answered throughout the following text, and a summary is given in the Conclusion in section 4.

3 Quantifying CO_2 Emissions at the Starzach Site

The investigation of the above research questions necessitates multiple approaches. The following sections describe the respective methods and present and discuss their results. Subsection 3.1 introduces measurements of atmospheric CO_2 concentrations and meteorological parameters at the Starzach site. In subsection 3.2, the degassing of the site's most active mofette is examined with a custom-built funnel system. Subsection 3.3 relates vertical gradients of CO_2 concentration close to a mofette to vertical turbulent fluxes measured with the EC method (flux-gradient approach). Finally, a network of CO_2 sensors is used to estimate the average total CO_2 emission rate at the Starzach site, from cross-correlations between time series and Gauss's divergence theorem, in subsection 3.4. The meteorological calculations for these investigations were performed with the Python Atmospheric Research Package for Meteorological and Timeseries Analysis (PARMESAN) described in Büchau et al. (2024b, Appendix C).

3.1 Dynamics of Atmospheric CO_2 Concentration at the Starzach Site

The indispensable foundation of in-situ gas emission quantification schemes is a reliable measurement of atmospheric gas concentrations. Under the premise of keeping costs low for later scalability, four small, embedded, and commercially available Non-Dispersive Infrared (NDIR) CO_2 sensors with unit prices well below 100 € were selected for evaluation: SenseAir LP8, theben CO_2 module, Cubic CM1106, and Sensirion SCD30 (Table 2). These sensors only require a low-voltage power supply ($\leq$5 V). Most have an Inter-Integrated Circuit (I^2C) interface, rendering them easily connectable to microcontrollers with the Free and Open Source Software (FOSS) Arduino framework, which is increasingly used for field studies due to its suitability for prototyping (Kim et al., 2020). With only a few centimeters in size, the selected CO_2 sensors are very compact, as their typical application is indoor air quality monitoring in places such as offices or ventilation systems. Consequently, they target CO_2 concentrations commonly found at workplaces (600–4000 ppm, Franco and Leccese, 2020), and have an upper detection limit of at most the concentration humans typically exhale (4–5 vol%, Tsoukias et al., 1998). At the time of sensor selection, the market offer for comparable CO_2 sensors designed specifically for outdoor use and with a large measurement range was very limited.

Field conditions present much larger extremes in temperature and relative humidity than indoors. To determine which sensor is best suited for continuous CO_2 measurements at the Starzach site, the four sensor candidates were first tested under laboratory conditions in a calibration chamber to assess their CO_2 measurement behaviour under a variety of temperature and relative humidity combinations (Büchau et al., 2022). The results (Figure 3) show that data of all four sensor models mostly lies within a margin of error of $\pm$100 ppm $\pm$10 % in their respective output ranges. However, three of the four sensor models have properties that render application at the Starzach

site problematic: Despite its excellent overall precision, the SenseAir sensor has a pronounced cross-sensitivity to humidity, which is a common problem of NDIR CO_2 sensors (Feng et al., 2024; Martin et al., 2017; Kondo et al., 2014; Mayrwöger et al., 2010). This is in line with results of Müller et al. (2020), who used the same sensor model. While the Cubic sensor is equally precise as the SenseAir sensor, its limited output range prevents its use in the direct vicinity of mofettes. In contrast, the theben sensor covers the widest range of CO_2 concentrations, but its response becomes non-linear above 10 000 ppm (1 vol%). Finally, in contrast, the Sensirion SCD30 sensor has a very linear output, a decent measurement range up to 40 000 ppm (4 vol%) and a built-in temperature and relative humidity sensor, making it the best out of the four sensor options for CO_2 measurements at the Starzach site. Subsequent field comparisons against an EC station directly above a mofette at the Starzach site confirm the Sensirion sensor's suitability under outdoor conditions (Büchau et al., 2022, Appendix A, page 70).

Continuous measurements with a Sensirion SCD30 sensor at 50 cm height above ground, close to a dry mofette, together with meteorological parameters from a Gill MaxiMet GMX541 compact weather station in 2 m height at the site selected due to its ease of use and comprehensive set of measurements, reveal a pronounced diurnal cycle of the atmospheric CO_2 concentration (Figure 4, Büchau et al., 2022): At nighttime, CO_2 levels are highly elevated and reach concentrations up to the sensor's upper limit of 4 vol%, a value two orders of magnitude above global average concentration (415 ppm in 2021, Calvin et al., 2023). The low nightly wind speeds ($\sim$0.2 m s^{-1}, blue dashed line in Figure 4) favor ground-level accumulation of the emitted CO_2, which is roughly 50 % denser than air at standard conditions (Foken et al., 2021) and therefore negatively buoyant. This CO_2 trapping is enhanced by atmospheric stability, which increases at night due to radiative cooling of the surface and inhibits

Table 2: *Tabular comparison of four low-cost NDIR CO_2 sensors evaluated for application at the Starzach site, reproduced from Büchau et al. (2022, Appendix A, page 65, kindly provided by the publisher under a CC-BY-4.0 license)*

	Sensirion SCD30	**SenseAir** LP8	**CUBIC** CM1106	**theben** CO2 Module
	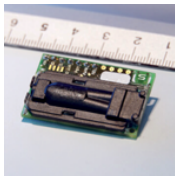	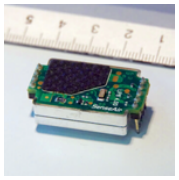	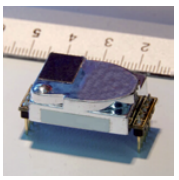	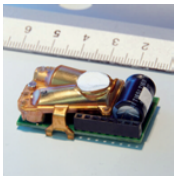
unit price at the time of writing		well below 100 €		
target CO_2 range [ppm]	400–10 000	0–10 000	0–2 000	0–5 000
output CO_2 range [ppm]	0–40 000	0–10 000	0–2 000	0–N.A.
accuracy (acc. to manufacturer)	±30 ppm ± 3 %, ±2.5 ppm/K	±50 ppm ± 3 %	±50 ppm ± 5 %	±50 ppm ± 3 %*
average power consumption	≈ 60 mW	≈ 1 mW	≈ 200 mW	≈ 30 mW
shortest output interval [s]	2 s	16 s	1 s	15 s
behaviour outside target CO_2 range	linear	–	–	non-linear
behaviour outside output CO_2 range	constant	constant	constant	non-linear
humidity cross-sensitivity	negligible	strong	negligible	negligible
temperature sensor	SHT31	onboard	onboard	onboard
humidity sensor	SHT31	–	–	–

* increases to up to ±100 ppm ± 5 % * for CO_2 concentrations above 2 000 ppm

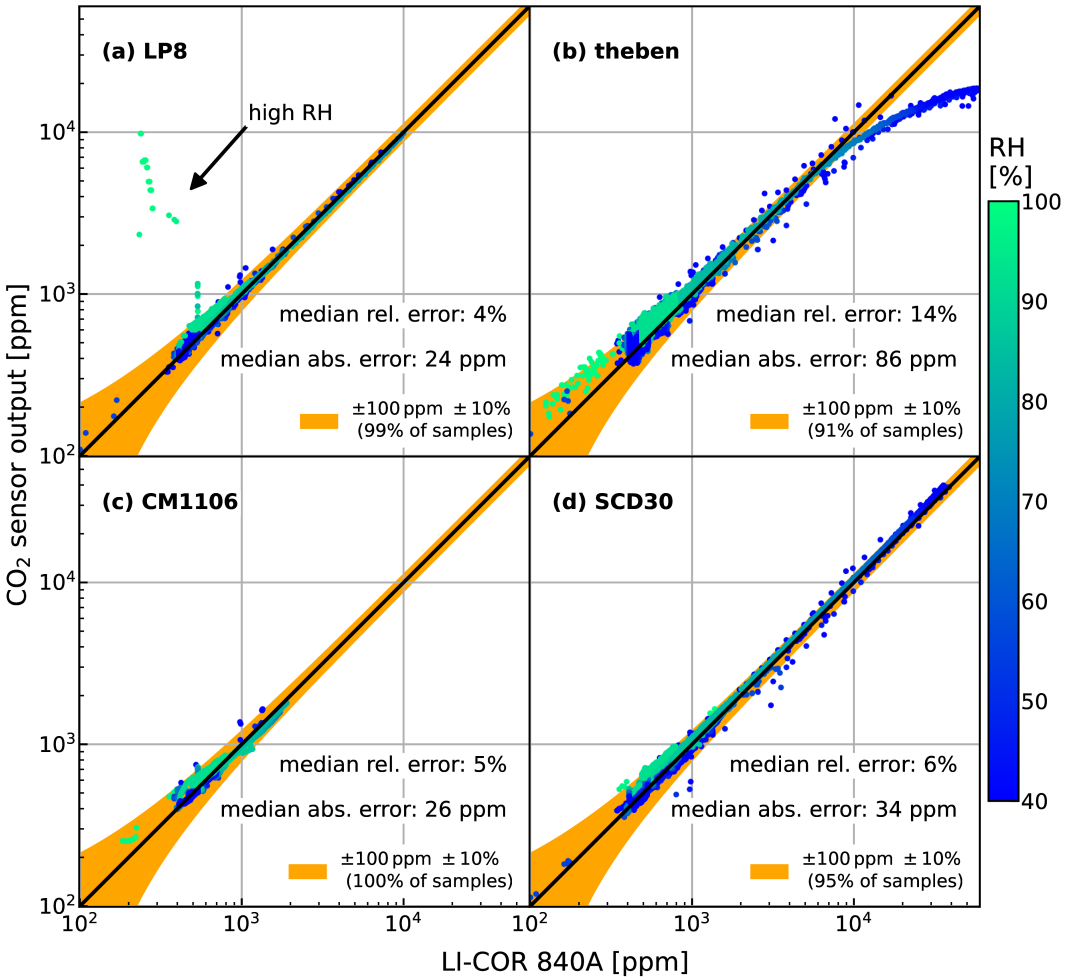

Figure 3: *Calibration of four low-cost CO_2 sensors (Table 2) in an EdgeTech RH Cal calibration chamber with LI-COR 840A closed-path infrared gas analyser as reference. Different combinations of temperature and relative humidity were produced by the calibration chamber while CO_2 from a pressurised gas bottle was periodically injected into the measurement chamber. Figure reproduced from Büchau et al. (2022, Appendix A, page 66, kindly provided by the publisher under a CC-BY-4.0 license). An additional figure with temperature coloration is available in Appendix A, page 67.*

vertical mixing. When wind-induced mixing redevelops at sunrise, the accumulated CO_2 is dispersed again. This near-surface accumulation of CO_2 is one answer to Research Question 1. The vertical turbulent transport of CO_2 is quantified in detail in subsection 3.3.

Another notable observation in Figure 4 is the presence of a distinct diurnal cycle of the wind direction, which is especially prominent in summer (top plot). The Starzach site is located at the foot of the northern slope of the upper Neckar valley, which runs in west-east direction with a slightly meandering shape. Insolation causes warming, and thus abatic upwinds, at the respective irradiated slopes in the north of the valley, pulling with it the air from inside the valley. Conversely, cooling air forms catabatic winds flowing down the valley slopes at night. Both results in a predominantly northwards wind direction at the Starzach site, with a superimposed daily oscillation caused by the meandering shape of the valley (Büchau et al., 2022).

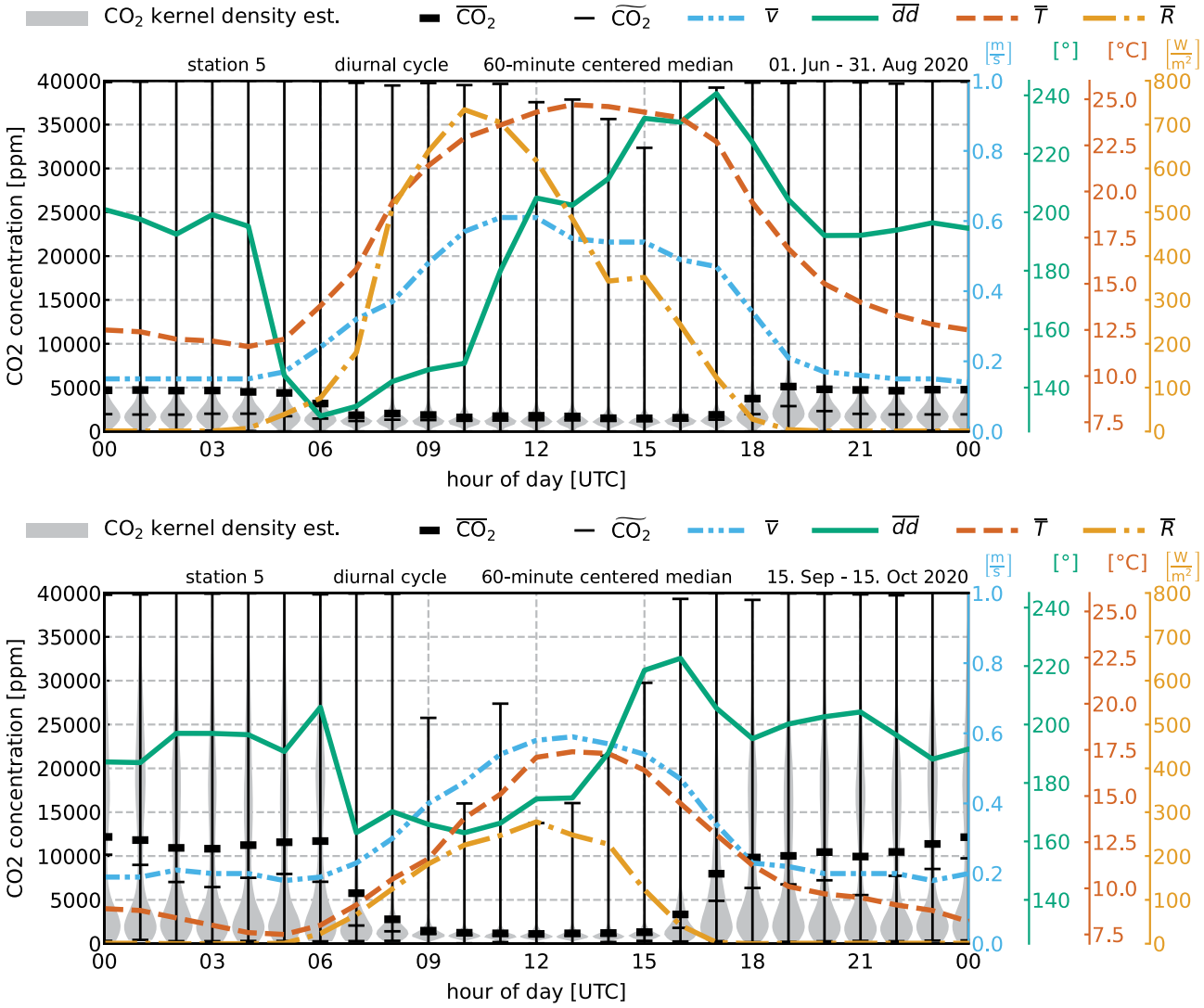

Figure 4: *Diurnal cycle of CO_2 concentration and meteorological parameters at the Starzach site in summer and autumn 2020. CO_2 measurements ($\overline{CO_2}$: mean, $\widetilde{CO_2}$: median) originate from a Sensirion SCD30 sensor 50 cm above ground, close to a dry mofette (Appendix A, page 70). The meteorological quantities ($\overline{v}$: wind speed, $\overline{dd}$: wind direction, $\overline{T}$: temperature, $\overline{R}$: global solar irradiance) were measured with a Gill MaxiMet GMX541 compact weather station in 2 m height (Appendix A, page 65). Figure reproduced from Büchau et al. (2022, Appendix A, page 71, kindly provided by the publisher under a CC-BY-4.0 license).*

3.2 Degassing of an Individual Mofette

With an understanding of the average atmospheric CO_2 concentration dynamics at the Starzach site from the previous section, a closer investigation of its sources, the mofettes, will help answer Research Question 2 and 3, and if the observed diurnal CO_2 pattern in Figure 4 is really only an atmospheric phenomenon. There are several mofettes of different sizes and activity at the site (Figure 1). For only one of those, the most active at the time (Figure 2b), there exists a degassing estimate from 2015 by Lübben and Leven (2022), who determined a CO_2 emission rate of 53–99 $\mathrm{kg\,d^{-1}}$ with a funnel system. However, as Lübben and Leven (2018) mention, the site is recovering from a century of industrial mining, having depleted the natural CO_2 exhaust almost entirely, but which is now redeveloping. This prior estimate is thus probably outdated and needs to be remade. Channeling the vented gas through a measurement funnel for quantification is a reasonable approach, and has already been applied in similar settings (non-volcanic CO_2 emissions in Italy, Rogie et al., 2000), but care needs to be taken which sensors are selected. Typically, an anemometer for air, such as a hot-wire anemometer, is used to measure flow speed in the funnel, which is then multiplied with its cross-section to calculate the flow rate $\dot{V}$ [$\mathrm{m^3\,s^{-1}}$]. This flow rate can be combined with measurements of pressure p [Pa], temperature T [K], and CO_2 mole fraction X_{CO2} [$\mathrm{mol\,mol^{-1}}$] in the funnel to determine the mass flow rate $\dot{m}_{\mathrm{CO2}}$ [$\mathrm{kg\,s^{-1}}$] (Büchau et al., 2024a, Appendix B, page 80):

$$\dot{m}_{\mathrm{CO2}} = X_{\mathrm{CO2}} \cdot \dot{V} \cdot \frac{p \cdot M_{\mathrm{CO2}}}{R^* \cdot T} \tag{1}$$

M_{CO2} [$\sim$0.044 $\mathrm{kg\,mol^{-1}}$, Foken et al., 2021] is the molar mass of CO_2, and R^* [$\sim$8.3145 $\mathrm{J\,mol^{-1}\,K^{-1}}$, Foken et al., 2021] the universal gas constant. A maximum error estimation of this equation reveals that the respective maximum expected relative errors (in percent) of its input variables sum up to the maximum expected error of $\dot{m}_{\mathrm{CO2}}$ (Büchau et al., 2024a, Appendix B, page 83). This is important to determine how precise $\dot{m}_{\mathrm{CO2}}$ can be measured, a reflection neither Lübben and Leven (2022) nor Rogie et al. (2000) have detailed. When quantifying CO_2 gas flow, the problem with most common air anemometers, with the notable exception of expensive ultrasonic anemometers, is that they are medium-dependent. The output of thermal anemometers, such as hot-wire anemometers, depends on the medium's density. The same is true for Pitot-tubes and propeller anemometers (Foken et al., 2021; Pindado et al., 2012). As the molar mass M_{CO2} of CO_2 is approximately 50 % higher than that of dry air M_{air} [$\sim$0.029 $\mathrm{kg\,mol^{-1}}$, Foken et al., 2021], gaseous CO_2 is denser than air as well, which can introduce an non-negligible error when measuring CO_2 flow speed while keeping the assumption of measuring in air. Luckily, there exists a widely used type of anemometer that is largely density independent: the cup anemometer. Here, the density-dependent drag forces, acting on the opposite cups, cancel out under stationary flow (Büchau et al., 2024a, Appendix B, page 81), rendering it practically independent of the passing medium's density. For this reason, a miniature cup anemometer was chosen to quantify the CO_2 exhaust from a Starzach mofette.

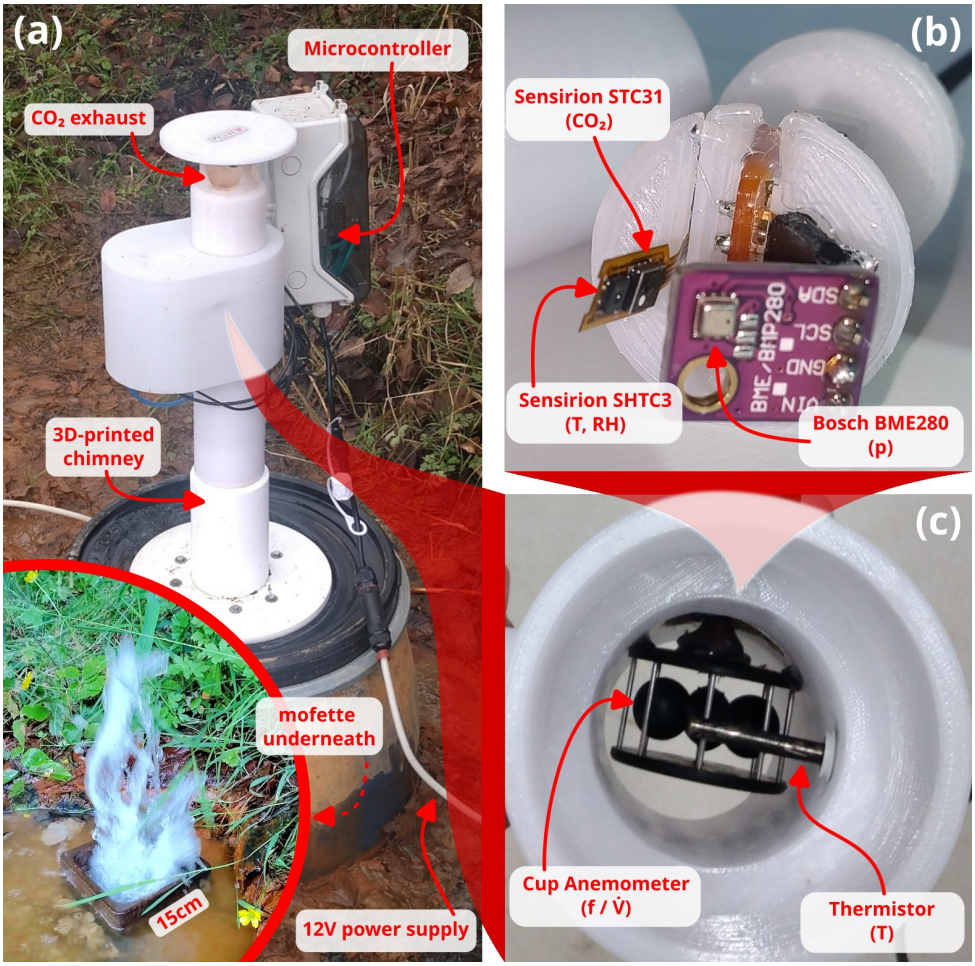

Figure 5: *Gas flow funnel system mounted over the groundwater monitoring well (Figure 1, installed in 2014, which turned into a mofette shortly after deployment) at the Starzach site in 2022. Figure reproduced from (Büchau et al., 2024a, Appendix B, page 80, licensed under CC-BY-4.0).*

Another critical quantity in Equation 1 is the gas content X_{CO2}. CO_2 is commonly quantified with NDIR technology, but as mentioned in the previous subsection 3.1, the market availability of such CO_2 sensors, designed for up to 100 % concentration, and withstanding extreme humidities under outdoor conditions is very limited – even more so in the low-cost segment. The alternative Sensirion STC31 CO_2 sensor was selected for this purpose. Its measurement principle is based on heat conductivity of the surrounding gas, which is an indirect method, and thus requires certain information such as atmospheric pressure p, temperature T and relative humidity RH [%] to be communicated digitally to the sensor for it to complete its measurement. To provide these measurements, a Bosch BME280 sensor and a temperature-sensitive resistor (thermistor) was used. These sensors were connected to a microcontroller for data recording and wireless transmission, and mounted inside a 3D-printed segmented, modular chimney that can be mounted on a halved barrel with removable lid to be placed over a mofette (Figure 5).

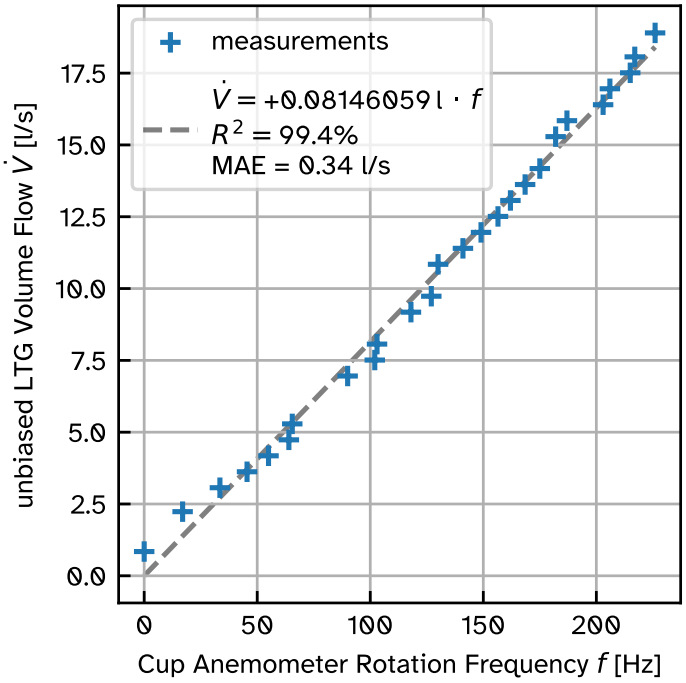

Figure 6: *Calibration of cup anemometer rotation frequency in the funnel (Figure 5c) to volumetric flow rate measured with an LTG 227VM-05 flow meter, with linear fit (gray dashed line). Figure reproduced from (Büchau et al., 2024a, Appendix B, page 84, licensed under CC-BY-4.0).*

All sensors were subsequently calibrated or validated individually (Büchau et al., 2024a). The cup anemometer's rotational frequency was directly calibrated to the flow rate $\dot{V}$ of a reference flow meter to an accuracy of $0.34\,\mathrm{L\,s^{-1}}$ (Figure 6). The other sensors were validated in a calibration chamber, where several combinations of T, RH, and X_{CO2} were generated, with a LI-COR 840A closed-path gas analyser as reference. It could be verified that the Sensirion STC31 is accurate to a precision of ± 1 vol% ± 3 % (Büchau et al., 2024a, Appendix B, page 86), and the thermistor to ± 0.1 K (Büchau et al., 2024a, Appendix B, page 87).

With the sensors calibrated, this funnel setup was deployed at the Starzach site in February 2022 (Figure 5), and mounted over the site's most active mofette – by that time the groundwater monitoring well introduced in 2014 (Figure 2c, Büchau et al., 2024a), which apparently presents an easy path for uprising gas to the surface. As an independent reference measurement of $\dot{V}$, plastic bags were attached to the funnel and filled sequentially with degassed CO_2. The bags' volumes were estimated geometrically from measurements of their length and diameter, and each filling was timed with a stopwatch (Büchau et al., 2024a, Appendix B, page 84). This process is depicted in detail for a reiterated setup based on differential pressure measurements one year later in Herrmann (2023, their Figure 12, page 20). The corresponding time series of $\dot{V}$ (Figure 7) reveals that the flow rates determined via bag fillings (white boxes) are well in line with the flow rate measured with the cup anemometer. The measured flow rate from the groundwater monitoring well mofette spreads between 1–6 $\mathrm{L\,s^{-1}}$ with an average close to $3\,\mathrm{L\,s^{-1}}$, and a variance of $1.27\,\mathrm{L^2\,s^{-2}}$, of which 50 %

can be attributed to a periodic eruption cycle repeating every 3–5 s (according to the main peak in Figure 7, yellow-marked region). This periodicity can be explained with a pressure equilibrium that is oscillating in height inside the well pipe (Büchau et al., 2024a): The water column inside the pipe exerts a certain pressure at the bottom, where its wall is perforated and groundwater can seep in. The uprising CO_2 accumulates at this depth, until its pressure is high enough to overcome the water pressure threshold, enabling the gas to be released to the surface, taking some water with it in an eruption. Afterwards, groundwater fills the well again, and the cycle repeats. This short-term periodicity on the scale of a few seconds is one answer to Research Question 3.

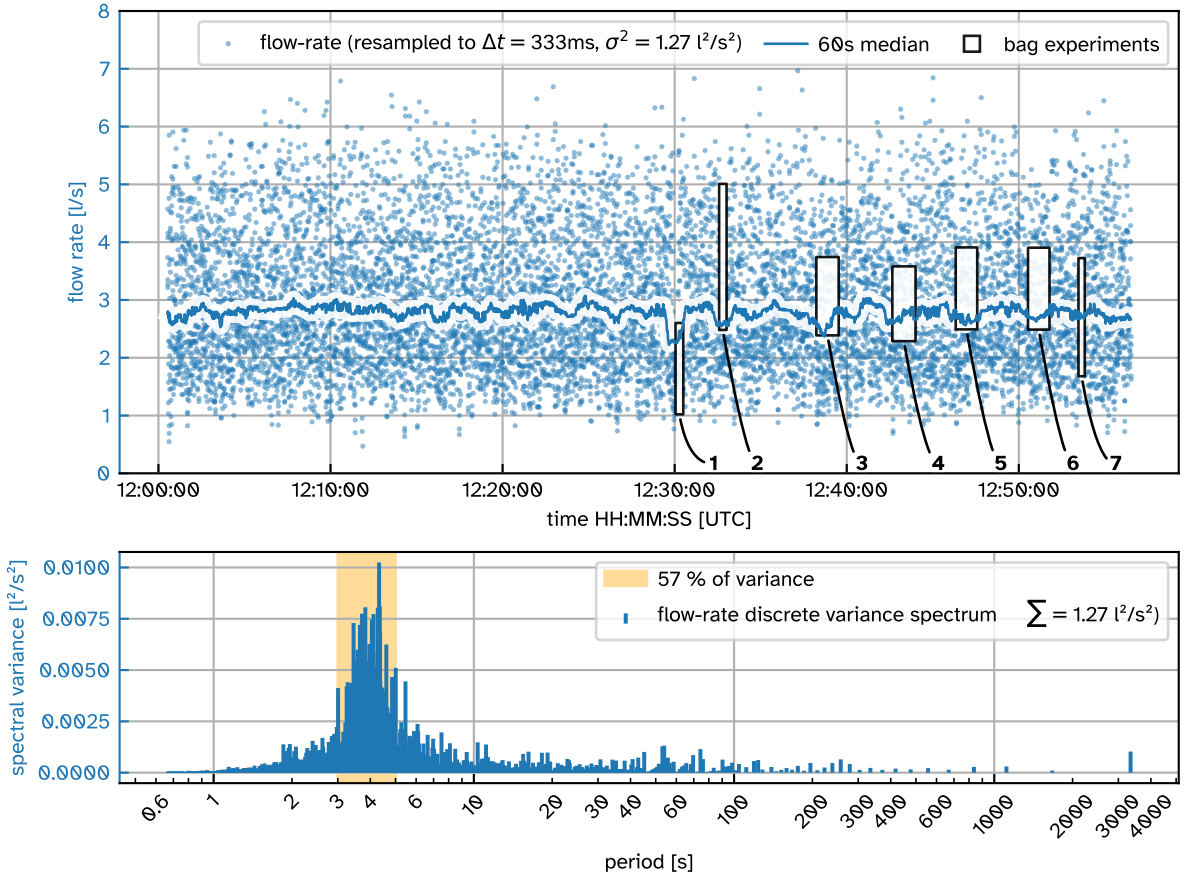

Figure 7: *One hour on the 03.02.2025 (Büchau et al., 2023) of flow rate $\dot{V}$ data measured by the setup shown in Figure 5 over the groundwater monitoring well mofette in at the Starzach site. The seven white boxes in the top plot depict the flow rate determined by filling plastic bags of estimated volume with CO_2 exhausted through the funnel (Büchau et al., 2024a, Appendix B, page 84). The bottom plot is a discrete spectrum of the top time series. Figure reproduced from (Büchau et al., 2024a, Appendix B, page 85, licensed under CC-BY-4.0).*

One week of data was recorded in February 2022 with the setup shown in Figure 5, and is presented in Figure 8 together with meteorological parameters from a Gill MaxiMet GMX541 compact weather station in 2 m height at the site. There are several interesting features in these recordings that help understand mofette degassing at the Starzach site. Most strikingly, there are two events (marked in gray), where the flow rate abruptly increases by nearly 25 % within minutes, then only slowly decays back to the baseline of $3\,\mathrm{L\,s^{-1}}$ over the next day. Such behaviour was already observed by Lübben and Leven (2022) on another mofette, but deemed a measurement anomaly, an assumption that can hereby be disproved. Instead, these sudden flow rate increases are likely similar to cold-water geyser mechanics (Büchau et al., 2024a): Rising CO_2 continuously enters and dissolves in a water-filled subsurface cavity until saturation. When no more CO_2 can be dissolved, bubbles of gas start rising, which displace water and as such reduce pressure, starting a positive exsolution feedback, ending in an eruption (Han et al., 2013; Glennon and Pfaff, 2005). It can be argued that the observed flow rate events at the Starzach site are a weaker and slower version of this process (Büchau et al., 2024a). The low-intensity seismic events recorded in the area seem to have no influence on their occurrence (second plot in Figure 8), which is expected for the above theory. Excluding these events, the CO_2 mass flow baseline averages to $465\,\mathrm{kg\,d^{-1}}$ ±16 % (Büchau et al., 2024a, Appendix B, page 89), which answers Research Question 2. This value is an order of magnitude higher than the previous measurement of 53–99 $\mathrm{kg\,d^{-1}}$ in 2015 by Lübben and Leven (2022), indicating that the degassing activity has dramatically increased over the seven years in between the measurements of Lübben and Leven (2022) and Büchau et al. (2024a). Extrapolating this measurement to the core Starzach mofette area ($20\,\mathrm{m} \times 20\,\mathrm{m}$, Figure 1), based on the amount and activity of the visible mofettes, a rough estimate of $\sim$1500 $\mathrm{kg\,d^{-1}}$ of total CO_2 emissions (Research Question 4) can be made (Büchau and Bange, 2025). Otherwise, none of the meteorological parameters – most notably atmospheric pressure, which is known to have an effect on comparable gas emissions through 'atmospheric pumping' (Forde et al., 2019; Nilson et al., 1991; Rinehart, 1972) – appear to influence the degassing of the examined mofette. So for Research Question 3 it can be concluded that there is a short-term eruption cycle every 4 s (Figure 7, yellow region), a slower cycle probably on a scale of several days, but no diurnal cycle or influence from atmospheric parameters (Figure 8). A slightly elevated eruption frequency (every 3 s) and roughly 20 % higher $\dot{V}$ was observed by student Herrmann (2023) one year later in summer 2023, suggesting a possible seasonal periodicity based on groundwater level.

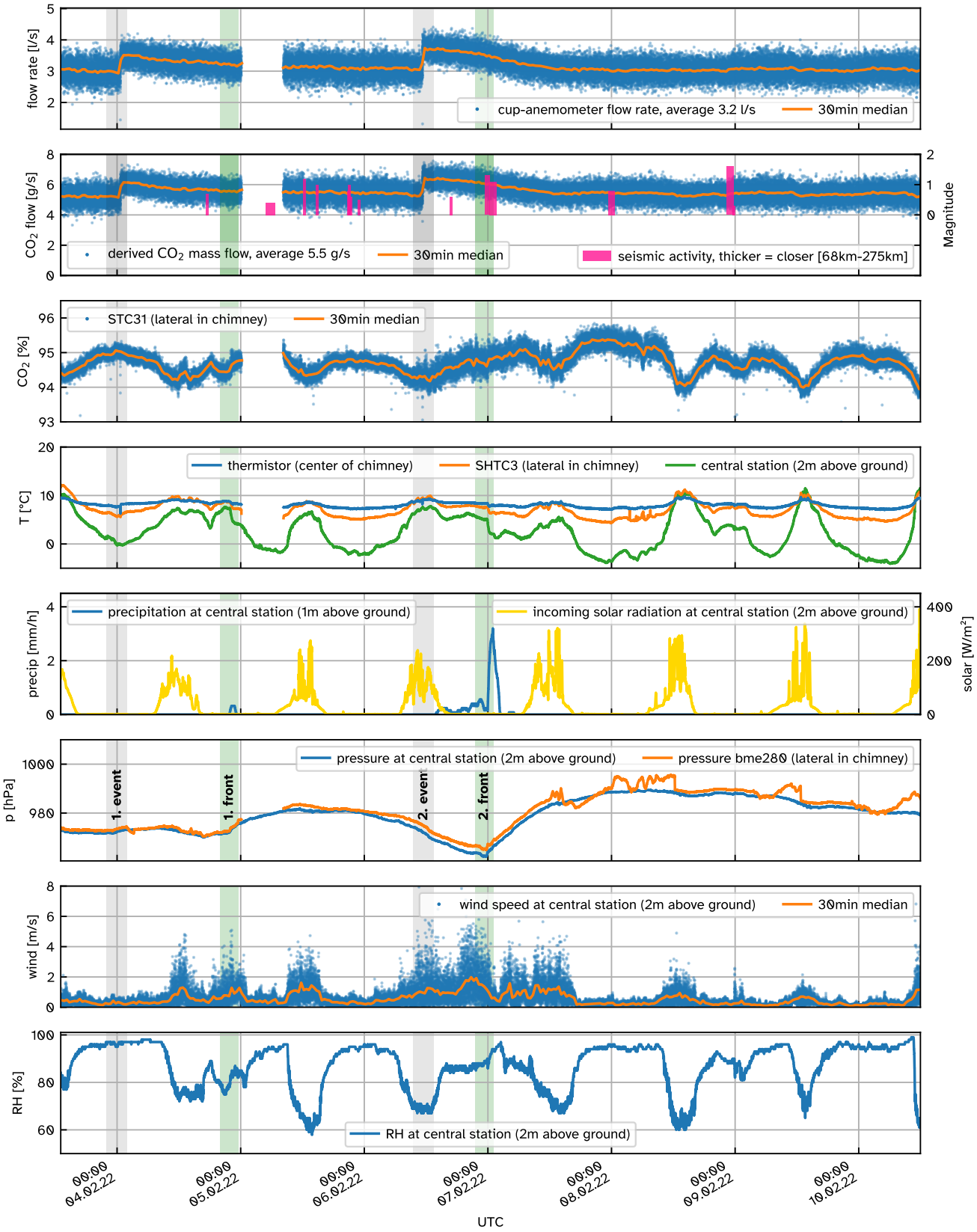

Figure 8: *One week of CO_2 exhaust measurements of the groundwater monitoring well mofette at the Starzach site in February 2022, with the setup shown in Figure 5, together with meteorological parameters of a Gill MaxiMet GMX541 compact weather station. Seismic activity data in the second plot was taken from erdbeben.led-bw.de. Figure reproduced from (Büchau et al., 2024a, Appendix B, page 88, licensed under CC-BY-4.0).*

3.3 Eddy Covariance / Flux-Gradient Method: Vertical Turbulent Flux

The following subsection 3.3 has not appeared in any publication yet and is separate from the works listed in section 1. From the measured accumulation of CO_2 at night in Figure 4, the question arises whether measurements of the vertical CO_2 concentration gradient with low-cost sensors can be used to estimate the CO_2 emissions at the Starzach site. A technique that relates a vertical concentration gradient to the resulting vertical turbulent transport is the flux-gradient approach, a first-order turbulence closure and formulation of Fick's first law of diffusion, but for diffusion by turbulent eddies (Wichura and Foken, 2021; Leclerc and Foken, 2014; Monson and Baldocchi, 2014; Pope, 2000; Stull, 1988). Intuitively, one might express it as

$$F_{\mathrm{CO2}} = -K_{\mathrm{CO2}} \frac{\Delta \rho_{\mathrm{CO2}}}{\Delta z} \ , \tag{2}$$

where a CO_2 mass concentration ρ_{CO2} [kg m^{-3}] difference in height z [m] (above minus below) results in a vertical turbulent mass flux F_{CO2} [kg m^{-2} s^{-1}], controlled by an exchange coefficient (or 'eddy diffusivity') K_{CO2} [m^2 s^{-1}]. This form is flawed, however, because vertical movements in the atmosphere cause density changes, which propagate to trace gas concentrations such as ρ_{CO2}, skewing the estimated gradients. Fluxes calculated based on volume concentrations such as Equation 2 can either be corrected with the common Webb, Pearman, and Leuning (WPL) correction or by working with dry molar mixing ratios instead (Mauder et al., 2021; Webb et al., 1980), because of their invariance to temperature or pressure changes (Gu et al., 2012). For Equation 2, this results in the slightly more elaborate expression (Zhao et al., 2019; Xiao et al., 2014)

$$F_{\mathrm{CO2}} = -K_{\mathrm{CO2}} \underbrace{\frac{M_{\mathrm{CO2}}}{M_{\mathrm{air}}} \rho_{\mathrm{air}} \frac{\Delta r_{\mathrm{CO2}}}{\Delta z}}_{\text{corrected density gradient}} \tag{3}$$

where M_{CO2} and M_{air} are the molar masses of CO_2 and dry air respectively, ρ_{air} [kg m^{-3}] the density of dry air, and r_{CO2} [mol/mol] the dry molar mixing ratio of CO_2, which is the mole ratio of CO_2 to dry air, i.e. all other parts in the gas mixture, excluding the fluctuating gases CO_2 and water vapour (H_2O). This parametrisation of the vertical turbulent gas flux in Equation 3 can be used if only slow averages of gas concentration measurements at different heights are available, which is suitable for the low-cost approach option discussed in this work. If instead fast measurements of upwards wind speed w [m s^{-1}] (e.g. from an ultrasonic anemometer) and dry molar gas mixing ratios (e.g. from a fast infrared gas analyser) are available, the vertical turbulent flux can be calculated directly with the widely used eddy covariance method (Mauder et al., 2021):

$$F_{\mathrm{CO2}} = \rho_{\mathrm{air}} \overline{r_{\mathrm{CO2}}' w'} \tag{4}$$

Prime notation (e.g. w') means deviation from the average, so $\overline{r_{\mathrm{CO2}}' w'}$ is the covariance between r_{CO2} and w, a quantification of how short bursts in upwards wind speed coincide

with temporary increases in trace gas presence, i.e. its net upward transport. Optical gas analysers, like the Campbell Scientific Integrated CO_2/H_2O Open-Path Gas Analyzer and 3D Sonic Anemometer (IRGASON) deployed at the Starzach site, rely on Bouguer-Lambert-Beer's law to derive trace gas concentrations (in units of atoms, molecules or mass per unit volume) from the absorption of light in their measurement volume (Heard et al., 2021; Burba et al., 2012). As for Equation 2, volumetric gas concentrations are influenced by density fluctuations during vertical movements or mixing with other gases, so the instrument's concentration measurements first need to be converted to dry molar mixing ratios for Equation 4 (Heard et al., 2021), which can be done with PARMESAN (Büchau et al., 2024b). If fast EC measurements are available, the exchange coefficient K_{CO2} can be determined by an offset-less linear regression of F_{CO2} from Equation 4 against the corrected density gradient in Equation 3. This exchange coefficient K_{CO2} is the crucial variable in Equation 3 to estimate vertical turbulent gas transport from gradients. It is not a constant, but can be expected to depend on atmospheric mixing and stability parameters. In absence of fast EC measurements, K_{CO2} needs to be parametrised. The most common parametrisation of K_{CO2} is the 'aerodynamic model' (Zhao et al., 2019; Xiao et al., 2014; Cellier and Brunet, 1992; Stull, 1988):

$$K_{\mathrm{CO2}} = \frac{\kappa \; u^* \; z}{\phi} \tag{5}$$

with $\kappa \approx 0.4$ being the von Kármán constant (Stull, 1988), u^* [$\mathrm{m\,s^{-1}}$] the friction velocity, z the geometric mean of upper and lower measurement heights, and ϕ [dimensionless] the Monin-Obukhov stability function, an empirical, positive function that equals one under neutral conditions and increases with atmospheric stability. Over the last decades, several suggestions for parametrisations of ϕ have been made (Lee et al., 2021; Lee and Buban, 2020; Grachev et al., 2008; Foken, 2006; Businger et al., 1971; Dyer and Hicks, 1970; Businger et al., 1967), however the initial proposals for the stable and unstable cases summarised by Dyer (1974) are still used today in flux-gradient studies (Zhao et al., 2019; Xiao et al., 2014):

$$\phi = \begin{cases} \frac{1}{\sqrt{1-16\,(z/\mathrm{L_{MO}})}} & \text{for } \frac{z}{\mathrm{L_{MO}}} < 0 \text{ (unstable conditions)} \\ 1 & \text{for } \frac{z}{\mathrm{L_{MO}}} = 0 \text{ (neutral conditions)} \\ 1 + 5\frac{z}{\mathrm{L_{MO}}} & \text{for } \frac{z}{\mathrm{L_{MO}}} > 0 \text{ (stable conditions)} \end{cases} \tag{6}$$

This expression in Equation 6 dominantly depends on the Obukhov length $\mathrm{L_{MO}}$ [m] (Stull, 1988):

$$\mathrm{L_{MO}} = -\frac{u^{*3} \cdot \theta_{\mathrm{v}}}{\overline{\theta_{\mathrm{v}}' w'} \cdot g \cdot \kappa} \tag{7}$$

where θ_{v} [K] is the virtual potential temperature, w the upwards vertical wind speed, and g [$\sim$9.8 $\mathrm{m\,s^{-2}}$, Stull, 1988] the acceleration in Earth's gravity. At this point, a significant problem becomes apparent: The kinematic heat flux $\overline{\theta_{\mathrm{v}}' w'}$ necessitates fast EC measurements – the very requirement one seeks to eliminate with the flux-gradient method in Equation 3. A solution to this

conflict can be approached iteratively (Busch et al., 1976; Delsol et al., 1971), non-iteratively (Louis, 1979), or by only examining neutrally stratified conditions ($\phi_{\text{neutral}} = 1$, Equation 6), which simplifies Equation 5 to

$$K_{\text{CO2}} = \kappa \, u^* \, z \tag{8}$$

Considering that the degassing of an individual mofette does not feature any diurnal pattern, and is instead rather constant over time (subsection 3.2, first two plots in Figure 8), filtering for only neutral conditions is not expected to introduce a significant selection bias. The above flux-gradient and eddy covariance Equations can be formulated analogously for H_2O, which is commonly measured in EC setups.

Application at the Starzach site

To determine how well the eddy covariance and flux-gradient method can be applied to quantify the CO_2 emissions at the Starzach site, a small-scale gradient measurement setup was newly deployed in summer 2023 close to a mofette, with four Sensirion SCD30 sensors each above (at 100 cm height) and below (20 cm) a Campbell Scientific IRGASON EC station (60 cm) as shown in Figure 9. Operating an EC station this close to the ground and its vegetation is rather unconventional. Typically, eddy covariance is performed in the constant flux (or 'inertial') sublayer, where turbulent

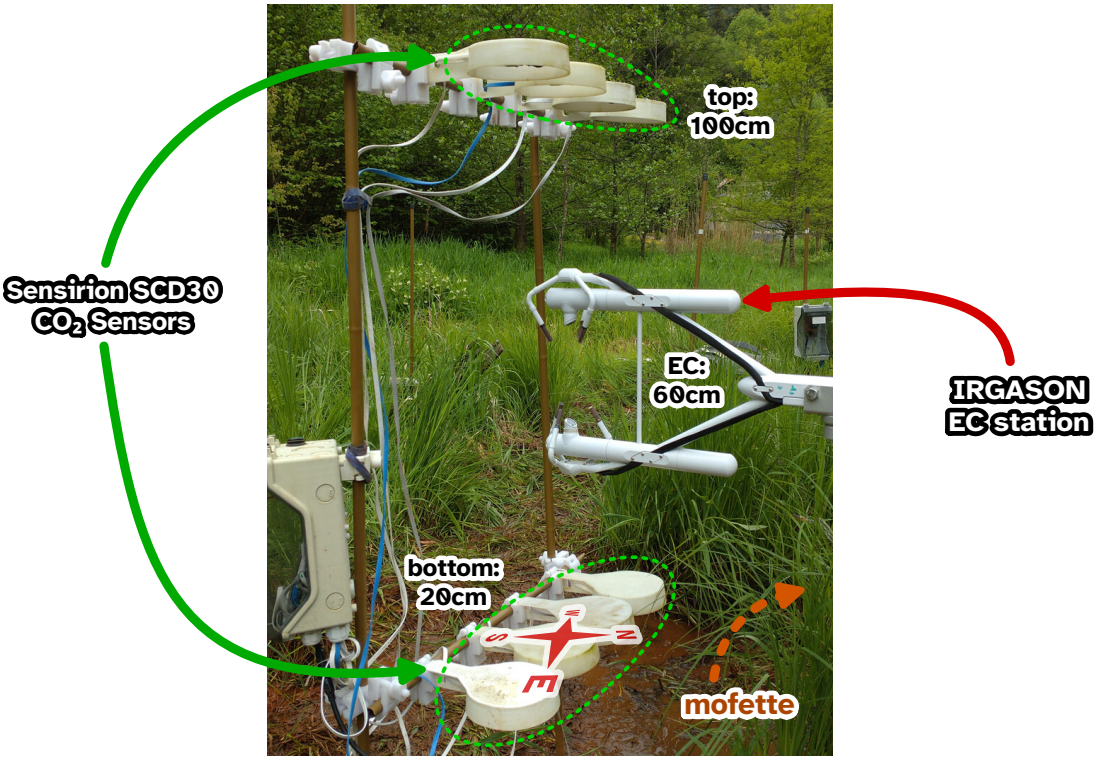

Figure 9: *Flux-gradient setup close to the ground, next to the Starzach site's mofette with the largest diameter (30 cm, Figure 2b, examined in 2015 by Lübben and Leven, 2022). Four Sensirion SCD30 low-cost CO_2 sensors each are mounted 40 cm above and below a Campbell Scientific IRGASON eddy covariance station at 60 cm height. Measurements of this setup are shown in Figure 10 and Figure 11.*

fluxes are approximately constant with height and not influenced by individual roughness elements anymore (Grimmond and Ward, 2021; Stull, 1988). This requires measurement heights that are significantly higher than any obstacles or trees in the area. Being located at the foot of a valley slope and surrounded by high trees (Figure 1), this requirement cannot be easily fulfilled at the Starzach site. It is also a common problem that CO_2 fluxes from emission sources such as mofettes might be too low for detection via EC as they become indistinguishable from background fluxes (Sauer et al., 2013), especially at elevated measurement heights. In addition, the need for careful footprint analysis arises with increased measurement height. Footprint analysis determines which parts of the surface contribute to what degree to the measured fluxes. These footprint estimation routines are often nontrivial (Kljun et al., 2015; Leclerc, 2014; Vesala et al., 2008; Kormann and Meixner, 2001). With these above considerations, it was decided to measure close to the surface, next to a CO_2 source, a mofette. For this setup, some footprint estimations are explicitly not applicable, for example because friction velocity u^* and measurement height z are too low (Kljun et al., 2004), but a simple estimation according to Hsieh et al. (2000) yields a horizontal footprint peak distance around 2 m, so a footprint area of roughly 2 m^2. Sixteen days of measurements in July/August 2023 of gas mixing ratios, the respective gradients, mixing and stability parameters, eddy covariance fluxes, and derived and parametrised exchange coefficients for CO_2 and H_2O are shown in Figure 10 and Figure 11.

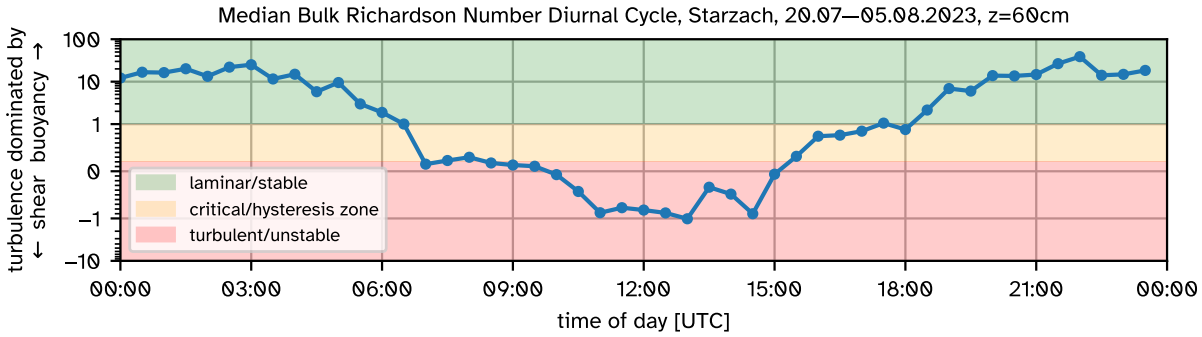

Figure 10: *Median diurnal cycle of bulk Richardson number* $\mathrm{Ri_b}$ *[dimensionless] calculated according to Stull (1988) for the time period of Figure 11 in 2023 at the setup shown in Figure 9. The temperature difference was taken from the upper and lower Sensirion SCD30 sensors. The horizontal wind speed difference was scaled to their height difference from wind speed measurements of the IRGASON eddy covariance station in the center and the Gill Maximet GMX541 compact weather station in two meters height still located on site as depicted in Büchau et al. (2022, Appendix A, page 65, and Figure 1).*

Eddy Covariance. All quantities in Figure 10 and Figure 11 show a pronounced diurnal pattern. At night (18:00–06:00 UTC), shear-driven turbulence generation is inhibited by atmospheric stability ($\mathrm{Ri_b} \gg 1$, Figure 10), while around noon (11:00–13:00 UTC), the stratification is unstable ($\mathrm{Ri_b} \approx -1$, Figure 10). In general, atmospheric mixing is very reduced this low above the ground, with an average u^* below 0.1 m s^{-1}, a maximum of 0.3 m s^{-1}, and a wind speed maximum of only 1 m s^{-1} in the entire measurement period (Figure 11). Water vapour mixing ratio is highest at

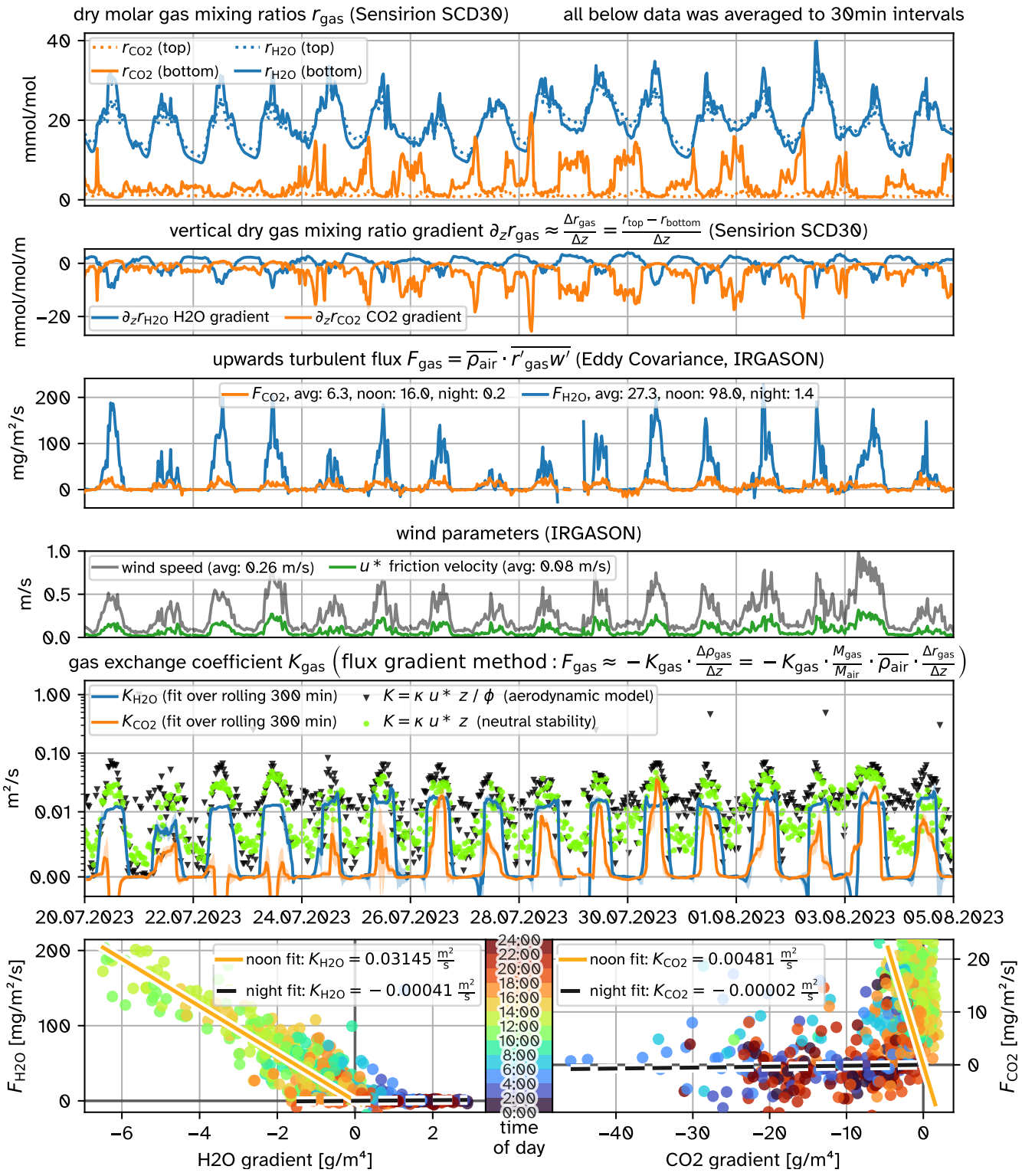

Figure 11: *Sixteen days of 30 min-averaged data recorded with the flux-gradient setup next to a mofette shown in Figure 9. From the time series of CO_2 and H_2O mass concentration (top row) measured with the slow Sensirion SCD30 low-cost sensors arranged above (100 cm) and below (20 cm) the IRGASON eddy covariance station (60 cm), the vertical gradients are derived (second row). Eddy covariance fluxes (third row) and mixing parameters (fourth row) are calculated from the IRGASON EC station. The slope of an offset-less linear fit of flux over gradient (bottom row) constitutes the solid lines in the fifth row, in comparison to the common aerodynamic model parametrisation derived from mixing and stability parameters (Equation 5 and Equation 8, Zhao et al., 2019; Xiao et al., 2014). The time ranges for noon (11:00–13:00) and night (18:00–06:00) are based on the Richardson number $\mathrm{Ri_b}$ in Figure 10.*

noon and lowest at night (Figure 11), controlled by insolation-driven evaporation from vegetation and the wet soil (clayey, 25–35 % volumetric water content, groundwater depth ∼70 cm, Wüsteney, 2023) at daytime, and the wet mofettes, which emit CO_2 gas through a water column (subsection 3.2). The bottom Sensirion SCD30 sensors in 20 cm height are close to these sources and therefore register higher H_2O mixing ratios than the upper sensors at daytime, visible in the negative gradient. The lower temperatures at night lead to a reduced saturation water vapour pressure, and thus an overall lower amount of H_2O molecules in the gas phase. Without solar irradiance driving evaporation, this saturation limit of H_2O explains its nightly gradient inversion (now positive), as the surface temperature drops faster through radiative cooling than the temperature of the above air layers, allowing those to hold more water vapour. The vertical turbulent H_2O flux is positive (upwards) at daytime as expected, but stays negligible at night, despite this gradient inversion, as the friction velocity u^*, a proxy for atmospheric mixing, approaches zero. With a peak magnitude between 100–200 $\mathrm{mg\,m^{-2}\,s^{-1}}$, the measured near-surface EC fluxes of H_2O at the Starzach site are comparable to literature values from studies over grassland, forests, agricultural fields, and lakes (Table 3).

The corresponding measurements for CO_2, however, show contrasting results (Research Question 1). Similar to previous measurements (Figure 4), CO_2 mixing ratios are only moderately elevated at daytime, but highly increased at night, especially close to the surface, and can reach similar magnitudes as for H_2O (∼2 %), which is very uncommon at sites without such CO_2 sources (c.f. studies in Table 3). One important observation is the pronounced nightly gradient of CO_2: While the CO_2 variability 20 cm above the surface (solid orange line in the first plot of Figure 11) is high and exhibiting significant peaks, its mixing ratio in 100 cm height (dashed orange line in the first plot of Figure 11) only reaches a maximum of around 0.3 %, emphasizing the accumulation of the denser CO_2 near the surface, especially at night. Carbon dioxide is an inert gas under typical atmospheric conditions, and its saturation vapour pressure is an order of magnitude higher (≈60 bar, Meyers and Van Dusen, 1933) than atmospheric pressure (≈1 bar), so there are no saturation effects for CO_2 as reasoned for H_2O above. In summary, the CO_2 gradient is anticorrelated (−50 %) to the H_2O gradient and has larger peaks, but is practically always negative, i.e. there is less CO_2 in the above air than down at the surface, where the gas is emitted from mofettes. There are some days where the CO_2 gradient is very slightly positive at noon, though. A possible explanation for this could be a footprint effect, where top and bottom sensors retrieve carbon dioxide from two different sources due to the site's heterogeneity, or in part also a numerical artifact, because the Sensirion SCD30 sensor's effective measurement uncertainty (±100 ppm ±10 %, Figure 3) is not much smaller than the involved mixing ratio differences. The turbulent flux of CO_2 often parallels the water vapour flux in progression, with a maximum at noon and some negative values in the morning and evening transitions or

Table 3: *Literature values of peak upwards and downwards CO_2 and H_2O fluxes and exchange coefficients K_{CO2} and K_{H2O} [$m^2\,s^{-1}$], from eddy covariance field studies. The numbers were either taken from the respective article texts or estimated from the available graphics, converted to the target unit, and rounded to sensible precision. If necessary, water vapour flux F_{H2O} [$kg\,m^{-2}\,s^{-1}$] was approximated by dividing latent heat flux (if available) by the latent heat of water vaporization L_{v} [$\sim$2500 $kJ\,kg^{-1}$, Stull, 1988]. Studies that employed a flux-gradient approach in addition to the eddy covariance method are marked with* **(FG)**.

	CO_2			**H_2O**	
	$F_{\mathrm{CO2}}\uparrow$	$F_{\mathrm{CO2}}\downarrow$	K_{CO2}	$F_{\mathrm{H2O}}\uparrow$	K_{H2O}
study location, time and setting	$\mathrm{mg\,m^{-2}\,s^{-1}}$	$\mathrm{mg\,m^{-2}\,s^{-1}}$	$\mathrm{m^2\,s^{-1}}$	$\mathrm{mg\,m^{-2}\,s^{-1}}$	$\mathrm{m^2\,s^{-1}}$
Dyer and Maher (1965): over **grassland**, Kerang and Hay, Australia, spring and autumn 1964	-	-	-	20–100	-
Alfieri et al. (2009): over **semiarid grassland** in Colorado, USA, spring to autumn 2004 **(FG)**	0.2	0.2	-	60	-
Kulmala et al. (2008): over boreal pine **forest floor** in Hyytiälä, Finland, summer 2005	0.22	0.044	-	18–36	-
Schrier-Uijl et al. (2010): over dairy **farm area** in Oukoop, Netherlands, 2006	-	0.1–0.4	-	-	-
Patel et al. (2011): semiarid subtropical **agricultural site**, UttarPradesh, India, 2009	0.15	0.25–1.15	-	-	-
Van Kesteren et al. (2013): over **wheat field** in Merken, Germany, summer 2009	0.4	1.5	-	160	-
Meredith et al. (2014): over **forest canopy** in Massachusetts, USA, summer 2011 **(FG)**	0.2	1	-	130	-
Shao et al. (2015): over **Western Lake Erie**, USA, 2011–2013	0.2–0.4	0.2–0.4	-	10-60	-
Chor et al. (2017): over **Amazon forest**, Brazil, summer 2013 **(FG)**	0.5	0.5–1	-	150	-
Xiao et al. (2014): over **Lake Taihu**, China, 2012–2014 **(FG)**	0.2	0.1	-	100	-
Esters et al. (2021): over ice-covered/ice-free **Lake Erken**, Sweden, 2015–2018	0.07–0.13	0.04	-	-	-
Zhao et al. (2019): over small **fish ponds** in subtropical climate in China, spring and autumn 2016 **(FG)**	0.01–0.1	-	0.1–0.2	26	-
Czubaszek and Wysocka-Czubaszek (2023): over **wheat**, **maize**, **oilseed rape** in Białystok, Poland, spring–summer 2016	0.2	1–2	-	-	-
Van Ramshorst et al. (2024): over **grassland** and **agroforestry** in Mariensee, Germany, 2020–2021	0.9	0.9	-	120–160	-
Hounshell et al. (2023): over small **freshwater reservoir**, Falling Creek Reservoir, Virginia, USA, 2022–2021	0.9–1.8	0.5–0.9	-	-	-
This dissertation, 60 cm over **mofette field**, Starzach, Germany, summer 2023 (Figure 11)	**25**	**5–10**	0.005–0.03	100–200	0.008–0.02

at night. Expectedly, compared to the broad selection of eddy covariance studies in Table 3, which cover a wide range of different ecosystems and environments, the upwards CO_2 fluxes in Starzach ($\sim$25 mg m^{-2} s^{-1}) are two orders of magnitude larger. The upwards CO_2 fluxes in Table 3 typically originate from nighttime plant respiration or emissions from water bodies, and downwards fluxes from photosynthesis. Based on this, for the Starzach site it can be concluded that these processes contribute far less to the measured near-surface turbulent CO_2 fluxes than the degassing from mofettes.

Extrapolating F_{CO2} over the core Starzach mofette area to estimate the total CO_2 emissions at the Starzach site (Research Question 4) is not really possible due to the small footprint area of $\sim$2 m^2 as estimated above. However, a plausibility check can be performed. It was concluded in subsection 3.2 with a funnel system that the direct degassing of an individual mofette does not vary significantly over diurnal times scales (Figure 8). This implies that the observed diurnal pattern of F_{CO2} in Figure 11 is a phenomenon of atmospheric mixing. Consequently, it is reasonable to choose the average measured peak value of F_{CO2} ($\sim$25 mg m^{-2} s^{-1}, third plot of Figure 11, daytime F_{CO2} maximum) for further total areal estimation. The examined mofette from subsection 3.2 emits 5.5 g s^{-1} of CO_2 gas (Figure 8). To reach this rate, the peak F_{CO2} value would need to be assumed over an unrealistically large area of 15 m $\times$ 15 m, indicating that F_{CO2} is underestimating or neglecting a large part of gas transport, because in reality there are many more mofettes in such an area around the EC station. Underestimation is expected for the EC method, because it cannot quantify the accumulation of CO_2 below its measurement height (60 m) in this setup ('storage term', Mauder et al., 2021), a process that is evidently very important at the Starzach site. Furthermore, Equation 4 explicitly neglects advective transport (Mauder et al., 2021), vertically, but most importantly, horizontally. This horizontal transport of CO_2 is quantified in detail in Büchau and Bange (2025), which is discussed in subsection 3.4 below. Büchau and Bange (2025) calculate an emission rate of 3266 kg d^{-1} (38 g s^{-1}) for the core Starzach mofette area (20 m $\times$ 20 m). Extrapolating F_{CO2} from the EC measurements in Figure 11 over this area yields only 864 kg d^{-1} (10 g s^{-1}), reinforcing the supposition of underestimation.

Exchange Coefficients. Figure 11 also shows the exchange coefficients K_{CO2} and K_{H2O}, fitted from Equation 3 and Equation 4, and parametrised including atmospheric stability (Equation 5) and for assumed neutral conditions (Equation 8). The fitted K_{H2O} shows a consistent pattern over the measurement period, with a plateau of 0.01–0.02 m^2 s^{-1} around noon, a few negative anomalies in the morning and evening transitions, and diminishing to zero at night. This is expected, as mixing is inhibited at night (Figure 10), preventing a turbulent flux, regardless of any present gradient. For CO_2, however, the fitted K_{CO2} is much more variable at daytime, but also reduces to zero at night. The noon peak is mostly similar in magnitude to K_{H2O}, although often smaller, but is shorter, and does not feature a plateau. Furthermore, during three days, this peak is actually negative,

which originates from the anomalous positive daytime CO_2 gradient discussed above. This difference in variability of the fitted exchange coefficients K_{H2O} and K_{CO2} could be an indication of their respective sources' heterogeneity: While the dominant daytime water vapour sources (vegetation, wet soil, standing water) are distributed rather homogeneously around the EC setup (Figure 9), mofettes of different sizes are scattered in the vicinity, making measured fluxes and gradients highly dependent on wind direction and individual eddies transporting the CO_2. Documenting turbulent exchange coefficients K_{CO2} or K_{H2O} measured with the eddy covariance and flux-gradient method is uncommon in the scientific literature, as can be concluded from Table 3, where only a single study (Zhao et al., 2019) reports $K_{\mathrm{CO2}} \approx 0.1\text{–}0.2\,\mathrm{m^2\,s^{-1}}$, though not fitted, but parametrised via Equation 5 and other approaches. This reference is an order of magnitude larger than the exchange coefficients determined here. According to Equation 5, the exchange coefficient K_{CO2} can be expected to scale proportionally with the geometric mean of the gradient measurement heights, which was five times higher in the setup of Zhao et al. (2019), bridging the gap between their K_{CO2} estimate and the values in Figure 11.

So while the fitted, 'real' exchange coefficients K_{CO2} and K_{H2O} in Figure 11 appear reasonable, their parametrisations based on Equation 5 and Equation 8 deviate significantly from them. At daytime, parametrisations overestimate up to one order of magnitude (note the logarithmic scale above $0.01\,\mathrm{m^2\,s^{-1}}$ in Figure 11), and at night they practically never diminish to zero. The latter is especially problematic when estimating F_{CO2} only from mixing ratio differences at different heights with Equation 3, as the nightly CO_2 gradients are very pronounced (Figure 11), resulting in an extreme overestimation of F_{CO2} with the flux-gradient approach. Interestingly, the simpler neutral parametrisation (Equation 8) is often less biased than the parametrisation including atmospheric stability (Equation 5), which arguably uses more physical information. Developing a system-specific, custom stability function ϕ and fitting it as part of Equation 5, instead of fitting the exchange coefficients as a whole, could improve this, but will probably still not be able to capture the unexpected behaviour in the first days of Figure 11. As reasoned in the above description of the system in Figure 9, this setup is rather unconventional due to its proximity to the surface. It is known that in the roughness sublayer, Monin-Obukhov Similarity Theory (MOST), on which the flux-gradient method is ultimately based, fails (Chor et al., 2017; Stull, 1988), when wind speeds become calm and u^* is low, as is the case here. Considering this, the agreement of fitted and parametrised K_{CO2} and K_{H2O} is acceptable under certain circumstances such as neutral stability, though the exact conditions would need further site-specific investigation to be reliable with a widespread network of low-cost CO_2 gradient measurements (Research Question 5). While the neutral stability condition prevents the flux-gradient method from being applied at night at the Starzach site, its suitability under neutral conditions might complement other independent CO_2 quantification methods that fail at daytime.

3.4 Deriving Areal CO_2 Emissions with a Sensor Network

Both previously described methods for answering Research Question 4, the total CO_2 emission rate at the core Starzach mofette area (subsection 3.2: $\sim$1500 kg d^{-1}, subsection 3.3: $\sim$900 kg d^{-1}), were each ultimately based on averages of one single point measurement. But a location with a spatial heterogeneity such as the Starzach site necessitates areal measurement coverage. Therefore, a low-cost sensor network was deployed at the Starzach site (Büchau et al., 2022), and data of eleven Sensirion SCD30 CO_2 sensors scattered across the site in 30 cm height in summer 2022 (Figure 12) is available (Büchau, 2025). From the pronounced vertical CO_2 gradient in Figure 11 it is evident that such a low measurement height is necessary, as it comprises the most significant CO_2 dynamics, and measuring above 1 m height is not advisable.

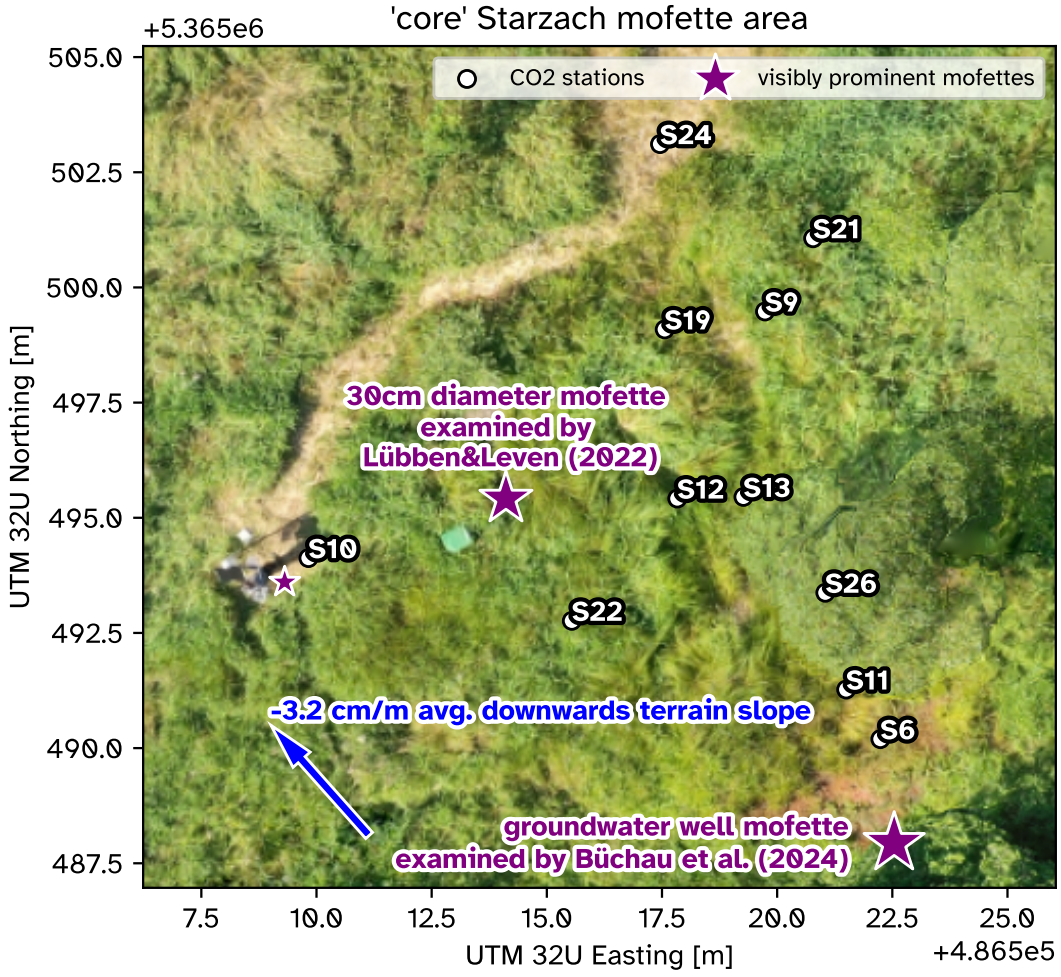

Figure 12: *Eleven CO_2 sensor stations (white dots) scattered across the core Starzach mofette area in summer 2022. This figure shows the region within the red dashed rectangle in Figure 1 in detail. Purple stars indicate the most active mofettes at the time. The mofette near the center is depicted in Figure 2b, the groundwater well mofette near the lower right-hand corner is shown in Figure 2c. The background picture was taken in 2019 by Martin Schön. Figure reproduced from Büchau and Bange (2025, Appendix D, page 108, licensed under CC-BY-4.0)*

There exist several top-down methods to derive trace gas emissions from point measurement time series, most notably transport modelling with Eularian atmospheric models (Badeke et al., 2021; Maronga et al., 2020; Zängl et al., 2015), inverse Lagrangian transport modelling (Pisso et al., 2019; Lin et al., 2003; Draxler and Hess, 1998), numerical solutions of the Advection-Diffusion Equation (ADE) (Schaper et al., 2024), its analytical solutions such as the Gaussian puff or plume model (Krause et al., 2023; Stockie, 2011), and 'mass balance' approaches based on Gauss's divergence theorem (Ryoo et al., 2019; Karion et al., 2013). Eularian and Lagrangian modelling approaches require significant computational resources and preparation. Solving the ADE numerically is possible if there is a manageable amount of peaks (i.e. local maxima) in the time series. The same is true when applying its analytical solutions. In both cases dispersion coefficients, contaminant release times and magnitudes, potentially also their locations, and a velocity field need to be fitted iteratively, depending on the available information and dimensionality. At the Starzach site, the nightly transport of CO_2 can be assumed to be horizontal, as no vertical mixing takes place (Figure 11), so it can be reduced to a two-dimensional problem. Each of the eleven Starzach CO_2 sensor time series features around 1000 peaks per day (Figure 13, and Appendix D, page 109, Büchau and Bange, 2025), and while the locations of the most active mofettes are evident, there exist several smaller, dry mofettes, in addition to invisible 'diffuse' degassing at the site (Büchau et al., 2022, Figure 1 and Figure 2a). Furthermore, typical meteorological wind vector measurements in 2 m height seem to be mostly decoupled from the CO_2 movements at the surface (Büchau and Bange, 2025). This renders ADE-based approaches challenging for the entirety of the Starzach site, however they can be viable in limited subregions for certain exemplary situations with less degrees of freedom.

The unrepresentativeness of wind measurements from the Gill MaxiMet GMX541 compact weather station at the site (Büchau et al., 2022) for CO_2 movements at lower heights requires estimating the CO_2 movement speed vector $\vec{u}_{\mathrm{CO2}}\,(t, \vec{p})$ $[\mathrm{m\,s^{-1}}]$ at a given time t [s], and location $\vec{p}$ [m] via other means. One approach is to exploit the similarity between neighbouring stations' time series: A high cross-correlation between time series of two stations indicates that the same volume of gas has passed through both. Dividing the distance vector between those stations by the corresponding time shift of that correlation maximum (Figure 13) then yields $\vec{u}_{\mathrm{CO2}}\,(t, \vec{p})$. The product of movement speed $\vec{u}_{\mathrm{CO2}}\,(t, \vec{p})$ and CO_2 concentration $\rho_{\mathrm{CO2}}\,(t, \vec{p})$ $[\mathrm{kg\,m^{-3}}]$ then describes the CO_2 transport $\vec{F}_{\mathrm{CO2}}\,(t, \vec{p})$ $[\mathrm{kg\,m^{-2}\,s^{-1}}]$:

$$\vec{F}_{\mathrm{CO2}}\,(t, \vec{p}) = \vec{u}_{\mathrm{CO2}}\,(t, \vec{p}) \cdot \rho_{\mathrm{CO2}}\,(t, \vec{p}) \tag{9}$$

Carefully-weighted averaging (Büchau and Bange, 2025, Appendix D, page 111) facilitates inter- and extrapolation of $\vec{F}_{\mathrm{CO2}}\,(t, \vec{p})$ onto the entire Starzach core mofette area (Figure 14). There are now two ways to integrate $\vec{F}_{\mathrm{CO2}}\,(t, \vec{p})$ over a region of interest to determine the total mass emission rate $\dot{m}_{\mathrm{CO2}}$ within: integration of the flux along a boundary surface S $[\mathrm{m^2}]$ or of its divergence in

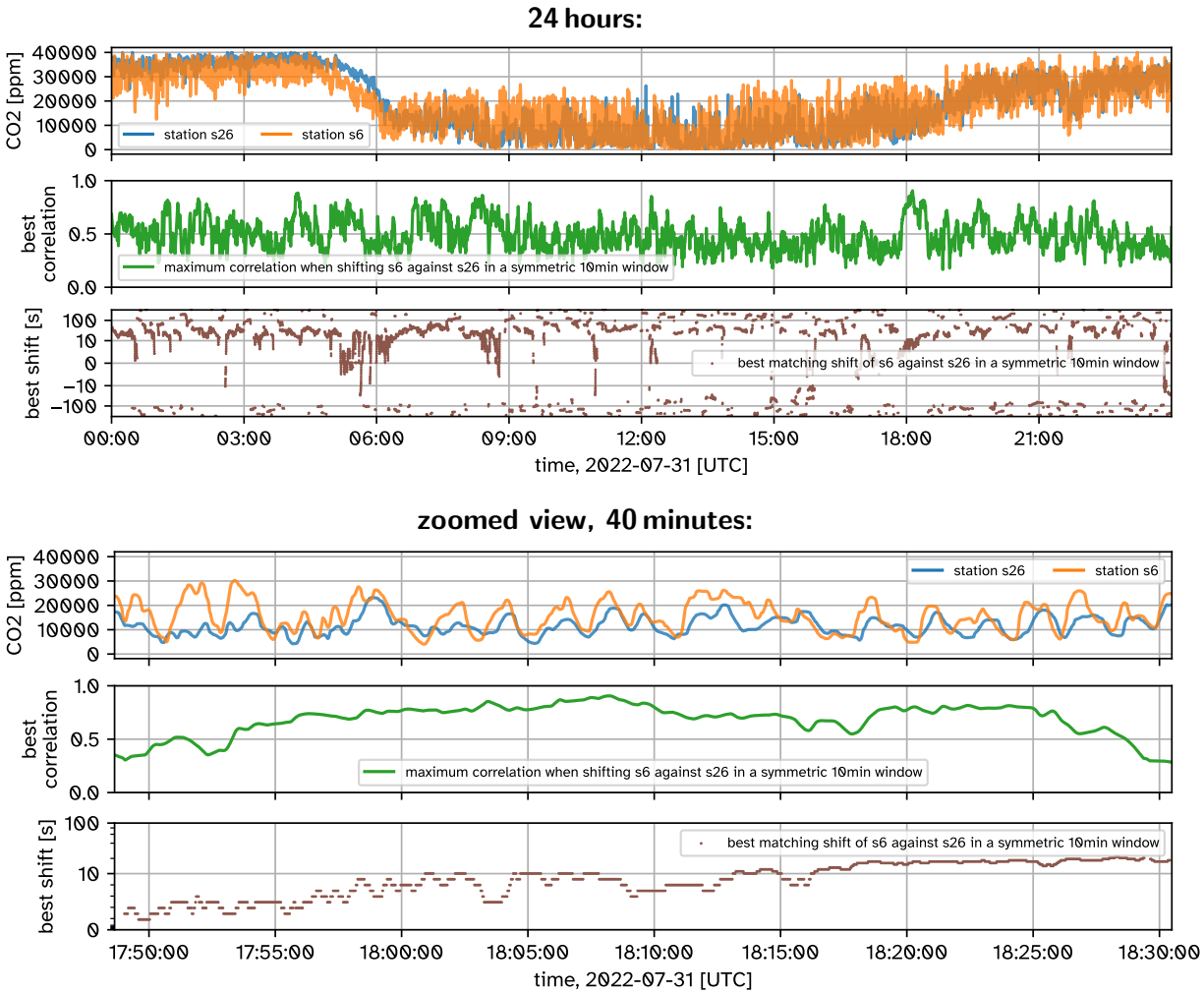

Figure 13: *CO_2 time series of station 6 and 26 (Figure 12) at the Starzach site in summer 2022 (top subplots), their maximum cross-correlation in a 10 min rolling window (center subplots), and the corresponding time shift (bottom subplots). A positive time shift indicates that the CO_2 time series of station 6 needs to be moved forward in time to match that of station 26. Figures reproduced from Büchau and Bange (2025, Appendix D, page 110, licensed under CC-BY-4.0)*

the enclosed volume V [m^3], both of which are linked via Gauss's divergence theorem (Büchau and Bange, 2025; Simmonds, 1994):

$$\underbrace{\dot{m}_{CO2}}_{\text{emission rate}} = \underbrace{\int_S \vec{F}_{CO2}(t,\vec{p})\, dS}_{\text{mass flow through boundary}} = \underbrace{\int_V \nabla \cdot \vec{F}_{CO2}(t,\vec{p})\, dV}_{\text{mass emergence within boundary}} \tag{10}$$

For the core Starzach mofette area, the latter integration of the CO_2 transport's divergence over a volume is preferred, as the data quality at the outer boundary is low due to the extrapolation. Weights can be applied during this volumetric integration to ensure that extrapolated points have less influence on the result, as depicted in Figure 14 by the fading opacity of the black $\vec{F}_{CO2}(t,\vec{p})$ arrows. Based on the insights from subsection 3.3 and Figure 11 in particular, the integration volume V is chosen as the lower 1 m of the atmosphere in the core Starzach mofette area (20 m × 20 m), and only nightly data is used, where vertical fluxes can be neglected. The above process is explained in detail in Büchau and Bange (2025, Appendix D, page 109).

For validation of this cross-correlation and divergence-theorem-based method, it was applied to the subregion downstream of the groundwater well mofette (white rectangle in Figure 14), of which the emission rate is known from subsection 3.2 ($5.5\,\mathrm{g\,s^{-1}}$, Figure 8), in addition to fitting a series of Gaussian puffs (Büchau and Bange, 2025, Appendix D, page 116, $4.8\,\mathrm{g\,s^{-1}}$). These three independent estimates could be shown in Büchau and Bange (2025, Appendix D, page 116) and the blue line in Figure 15 ($517\,\mathrm{kg\,d^{-1}} \approx 6\,\mathrm{g\,s^{-1}}$) to be well in agreement.

Applied to the core Starzach mofette area, Equation 10 gives a total CO_2 release rate of $3266\,\mathrm{kg\,d^{-1}}$ ±42 %, averaged over late summer 2022 (orange line in Figure 15), another estimate for Research Question 4. As only eleven sensor stations were available, the spread of this result is rather high, but can be expected to decrease with a better spatial coverage of the site. Compared to the previous estimates of $\dot{m}_{CO2}$ made above (subsection 3.2: $\sim$1500 $\mathrm{kg\,d^{-1}}$, subsection 3.3: $\sim$900 $\mathrm{kg\,d^{-1}}$), this result is also much higher, doubled and tripled, respectively. Even

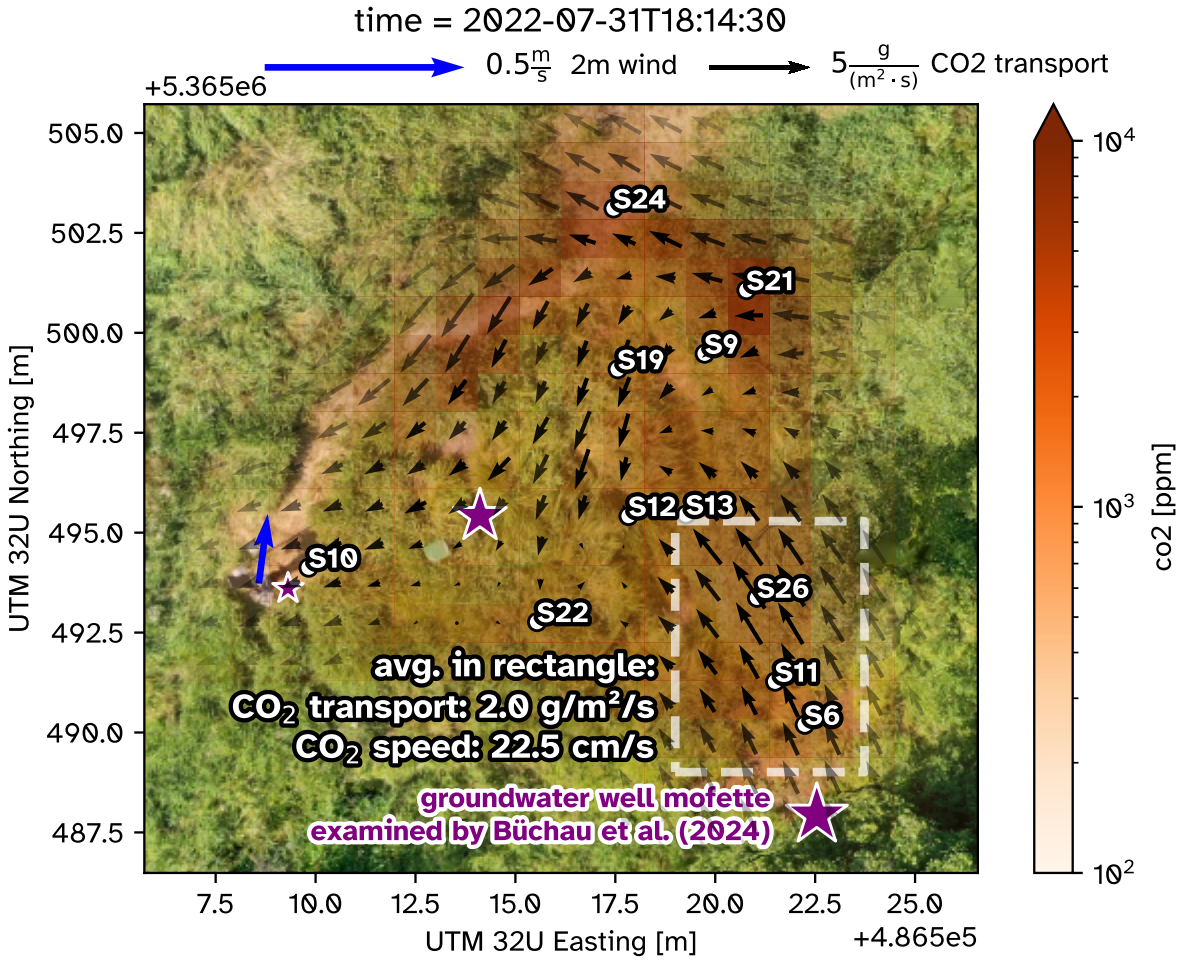

Figure 14: *Eleven CO_2 sensor stations (white dots) scattered across the core Starzach mofette area in summer 2022. Purple stars indicate the most active mofettes at the time. The mofette near the center (between s10 and s12) was examined by (Lübben and Leven, 2022) in 2015. The black arrows depict the advective transport of CO_2 derived from cross-correlations between the stations' CO_2 time series. The background picture was taken in 2019 by Martin Schön. Figure reproduced from Büchau and Bange (2025, Appendix D, page 114, licensed under CC-BY-4.0)*

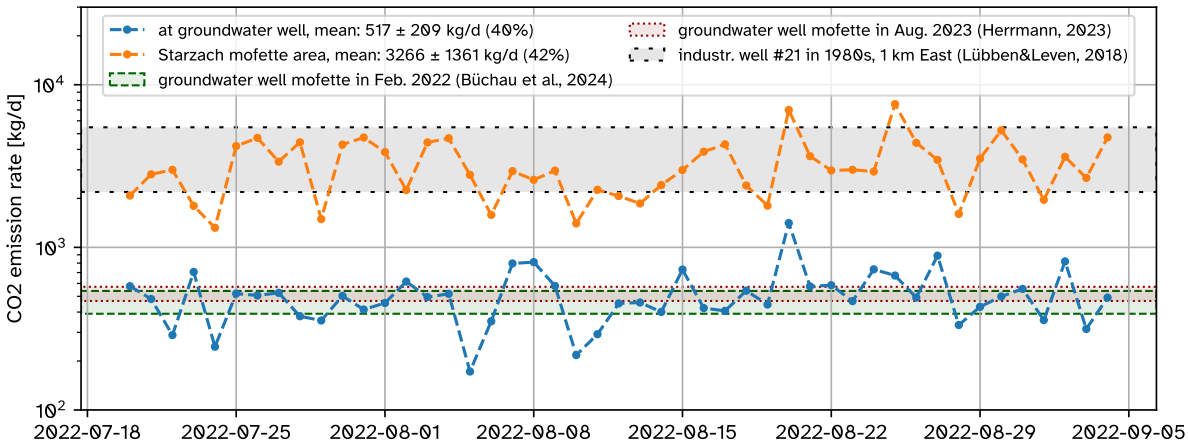

Figure 15: *Total CO_2 rate derived with Equation 10 from cross-correlations between CO_2 point measurement time series (Figure 13) in summer 2022, for the core Starzach mofette area (Figure 14) and downstream of the mofette examined in subsection 3.2. Figure reproduced from Büchau and Bange (2025, Appendix D, page 117, licensed under CC-BY-4.0)*

the lowermost values of $\dot{m}_{CO2}$ in Figure 15 are above $1000\,\mathrm{kg\,d^{-1}}$. As Equation 10 includes a lot more spatial and temporal information than the other estimates, its outputs can be considered more reliable. An interpretation of this is that diffuse degassing, i.e. not originating from visibly active mofettes (Figure 2a), is more important than previously thought, and the use of measurement techniques such as accumulation chambers (e.g. Carapezza et al., 2009; Lewicki et al., 2009) for their targeted quantification is advisable. Roughly extrapolating this result to include the other abandoned wells in the area (Lübben and Leven, 2018, and Figure 1) could give an order of magnitude of $\sim 10\,\mathrm{t\,d^{-1}}$ (Büchau and Bange, 2025).

4 Conclusion

From the above investigations of mofette CO_2 emissions at the Starzach site, the following conclusions for the research questions posed in subsection 2.2 can be drawn:

Research Question 1. The atmospheric CO_2 concentration in 50 cm height above ground at the Starzach site is generally elevated at daytime ($\sim$1000 ppm versus typical concentrations above 400 ppm, and highly increased (up to 40 000 ppm, 4 vol%, the used sensor's upper output limit) at night (Büchau et al., 2022). Due to surface accumulation of CO_2, concentrations decrease drastically with height, even at night the concentrations in 1 m height only reach $\sim$2000 ppm (Figure 11). This causes strong vertical gradients to develop at night, when wind-driven atmospheric mixing, and with it the vertical turbulent gas transport, comes to a halt (subsection 3.3). The spatial distribution of atmospheric CO_2 near the surface is highly heterogeneous, as are its sources, and variable with time, as evident from CO_2 time series featuring over 1000 daily peaks. Adjacent measurements that are a few meters apart can be highly correlated (Büchau and Bange, 2025).

Research Question 2. Which mofette is the most active has changed over the last decade. A previous study from 2015 measured the most visibly active mofette (Figure 2b) to emit 53–99 kg d^{-1} (Lübben and Leven, 2022). Independently, in 2014, a groundwater monitoring well was installed at the site. A few months later, this well started degassing CO_2 as the site's most active mofette, presumably because it presents a less resistive path for uprising CO_2, which was quantified in winter 2022 to emit 465 kg d^{-1} $\pm$16 % of CO_2 gas (Büchau et al., 2024a).

Research Question 3. The groundwater well mofette degassings have periodicities on several time scales (Büchau et al., 2024a). On the short term, there is a clear eruption cycle every 3–5 s, because the uprising gas needs to pass through a water column. There is no diurnal cycle or influence by meteorological parameters, most notably no 'atmospheric pumping' effect could be observed. Instead, separated by a few days, two flow rate anomalies were measured, that abruptly increased the flow rate by around 25 % (Figure 8), and a subsequent slow decrease back to baseline over the next day. This behaviour was already seen in 2015 for a different mofette, and is explained here with dampened cold-water geyser mechanics. A correlation with known seismic events in the broader region could not be confirmed (Figure 8), however precise on-site seismic measurements (e.g. with geophones) might prove otherwise, and further the understanding of the subsurface processes at the Starzach site. Furthermore, a possible seasonal cycle due to varying groundwater levels is suspected, based on an increased exhaust rate measured in summer compared to winter a year prior (Herrmann, 2023), although this needs further investigation.

Research Question 4. Three independent approaches for quantification of the total CO_2 emission rate at the core Starzach mofette area (20 m × 20 m, Figure 1) were performed: extrapolation of the degassing of an individual mofette ($\sim$1500 kg d^{-1}, subsection 3.2), near-surface eddy covariance and flux-gradient approach ($\sim$900 kg d^{-1}, subsection 3.3), and a custom method that applies Gauss's divergence theorem to CO_2 advection vectors derived from cross-correlations between time series of a CO_2 sensor network (3266 kg d^{-1} $\pm$42 %, subsection 3.4), the latter being the most reliable due to its areal coverage. Together with the other mofettes and abandoned CO_2 wells in the area in roughly 100 m distance (Figure 1), this rate might extrapolate to an order of magnitude of 10 t d^{-1}. These values are comparable to other measurements of non-volcanic CO_2 emissions in Italy (Giammanco et al., 2007) and in the Czech Republic (Kämpf et al., 2019). To put it into perspective: In one day, the Starzach site emits roughly as much CO_2-equivalent GHG as an average European person causes in one year (yearly average per-capita CO_2-equivalent GHG emissions in Europe in 2024: 7 tCO2eq/a, Crippa et al., 2025). Or conversely: Around 400 average Europeans emit as much CO_2-equivalent GHG per day as the Starzach site does. All three applied methods can be transferred to comparable gas-emitting sites, but might require slight adjustments, such as spatial and temporal coverage or sensor selection, depending on the target location. Real-time applicability is possible for all presented methods.

Research Question 5. Low-cost equipment was capable of quantifying atmospheric CO_2 concentrations with a conservative accuracy of $\pm$100 ppm $\pm$10 %, which was determined by comparison with a LI-COR 840A closed-path gas analyser in a calibration chamber, and by in-field comparison with an IRGASON eddy covariance station above a mofette. The CO_2 outflow of an individual mofette could be measured to a precision of 16 %, based on a maximum error estimation of Equation 1. The best estimate of the total degassing rate of the core Starzach mofette area was calculated with a divergence-theorem-based approach including eleven near-surface CO_2 sensor stations, and has an average spread of $\pm$42 % between days in late summer 2022.

5 Outlook

From the discussions in section 3, several strategies to improve the results for the total CO_2 degassing rate at the Starzach site become evident. Most importantly, for all above methods, an increased spatial and temporal measurement coverage of the Starzach site is expected to reduce the respective error margins. Aligned with the objectives of the overarching German Research Foundation (DFG) project that funded it (BA 1988-19-1), this dissertation prioritised the rigorous development and evaluation of CO_2 quantification methods and measurement systems over spatial and temporal measurement coverage. The latter is planned for the project's second phase, for which a proposal is in progress.

The outgassing of each visible mofette on the site, wet or dry, should be quantified with a funnel system as described in subsection 3.2 and Büchau et al. (2024a, Appendix B), ideally in parallel and over a continuous and long period of time, to investigate the suspected seasonal degassing periodicity and the observed flow rate anomalies in Figure 8. This requires building additional funnel systems, potentially with customized design elements such as a modified diameter of the 3D-printed funnel to fit different mofettes and degassing rates.

Complementing the funnel systems with measurements of accumulation chambers is advisable to punctually quantify the diffuse degassing at the site (Figure 1). A low-cost design for a floating accumulation chamber is described by Martinsen et al. (2018) and could be adapted for application at the Starzach site, for example by incorporating one or more Sensirion SCD30 CO_2 sensors, which have been shown to be suitable around mofettes (Büchau et al., 2022). One important feature of an accumulation chamber is the mechanism that regularly replaces the air in the sample volume. This is typically achieved by opening the chamber or by ventilation with a pump. Both of these methods rely on mechanical components that might eventually fail under field conditions. In subsection 3.3 it was concluded that there is practically no vertical turbulent CO_2 transport at night due to atmospheric stability, resulting in accumulation of CO_2 at ground level. This nightly lack of vertical transport could make it possible to instead use a passive, open-top chamber without moving parts (e.g. Messerli et al., 2015), where the diurnal cycle in atmospheric mixing provides the air replacement mechanism. Gergely et al. (2025) recently presented a similar approach at a mofette in Romania.

There is a possible synergy for the flux-gradient approach (subsection 3.3), which has been shown to be only applicable at daytime when there is sufficient atmospheric mixing, and the divergence-theorem-based sensor network approach (subsection 3.4), which covers the temporal counterpart, the night, when vertical fluxes can be neglected. If each sensor station is equipped with two or more vertically arranged sensors, the vertical CO_2 gradient can be used to parametrise vertical turbulent fluxes at daytime during neutral atmospheric stability, while the horizontal CO_2 distribution yields the divergence-derived CO_2 emission rate at night. With sufficient spatial sensor density, this could also

solve the small-footprint problem of near-surface turbulent fluxes. An increased number of stations can generally be expected to improve the divergence-derived estimate of the emission rate $\dot{m}_{\mathrm{CO2}}$ for the covered area (Equation 10), because CO_2 movement patterns can be detected more reliably with less distance between the stations. In Figure 14, each of the eleven CO_2 near-surface sensor stations had a closest neighbour in 1–6 m distance. Reducing these distances (e.g. to 0.5–3 m), especially around mofettes, is therefore advisable.

Ultimately, a high-resolution microscale model such as the Microscale Transport and Stream Model (MITRAS) (Grawe et al., 2013) should be used to simulate the wind field and the intricate movements of near-surface CO_2 at the Starzach site, thereby allowing for the further confirmation of the present assumptions and results. The in-situ measurements from the sensor network could furthermore be used to validate certain model processes and parametrisations.

6 References

[1] Büchau, Y. *CO2 Time Series Data of Eleven Sensor Stations in Summer 2022 at the Starzach Site in South-Western Germany*. dataset. Zenodo, 4th Sept. 2025. DOI: 10.5281/zenodo.17055782.

[2] Büchau, Y. G. and Bange, J. 'Quantification of Natural CO2 Emissions from Mofettes Using a Low-Cost Sensor Network at the Starzach Site in South-West Germany'. In: *PLOS Climate* 4.11 (25th Nov. 2025), e0000741. ISSN: 2767-3200. DOI: 10.1371/journal.pclm.0000741.

[3] Cannon, A. J. 'Twelve Months at 1.5 °C Signals Earlier than Expected Breach of Paris Agreement Threshold'. In: *Nature Climate Change* 15.3 (Mar. 2025), 266–269. ISSN: 1758-6798. DOI: 10.1038/s41558-025-02247-8.

[4] Crippa, M., Guizzardi, D., Pagani, F., Banja, M., Muntean, M., Schaaf, E., Quadrelli, R., Risquez Martin, A., Taghavi-Moharamli, P., Köykkä, J. et al. *GHG Emissions of All World Countries - 2025 Report*. JRC143227. Luxembourg: Publications Office of the European Union, 2025. 293 pp. ISBN: 978-92-68-31401-2. DOI: 10.2760/5917997.

[5] Gergely, A., Szakács, A., Gál, Á. and Néda, Z. 'CO2 Dynamics in a Mofette: Measurement and Modeling'. In: *Geosciences* 15.9 (17th Sept. 2025), 368. ISSN: 2076-3263. DOI: 10.3390/geosciences15090368.

[6] Krauthausen, B. *Anfrage Geysir Andernach*. E-mail. Zur Physik des Kaltwassergeysirs von Andernach/Namedy. Krauthausen, B. und Henne, P., HYDROSOND-Akten (2006). unpublished. 23rd Oct. 2025.

[7] Lefstad, L. and Rivadeneira, N. R. 'From the Rainforest to the Fjords: Examining Equity in Carbon Capture and Storage Climate Policy'. In: *Climate Policy* 0.0 (14th Jan. 2025), 1–15. ISSN: 1469-3062. DOI: 10.1080/14693062.2025.2451644.

[8] Liu, F., Liu, W., Nesar Rather, K., Panda, H. S., Mahalik, M. K. and Gozgor, G. 'Do Digital Technology and Political Risk Reduce CO2 Emissions Inequality in OECD Economies? Panel Evidence'. In: *Journal of Environmental Management* 392 (1st Sept. 2025), 126742. ISSN: 0301-4797. DOI: 10.1016/j.jenvman.2025.126742.

[9] Büchau, Y. G., Leven, C. and Bange, J. 'A Portable Low-Cost Device to Quantify Advective Gas Fluxes from Mofettes into the Lower Atmosphere: First Application to Starzach Mofettes (Germany)'. In: *Environmental Monitoring and Assessment* 196 (11th Jan. 2024), 138. ISSN: 1573-2959. DOI: 10.1007/s10661-023-12114-8.

[10] Büchau, Y. G., Mashni, H., Bramati, M., Savvakis, V., Schäfer, I., Jung, S., Miranda-Garcia, G., Hardt, D. and Bange, J. 'PARMESAN: Meteorological Timeseries and Turbulence Analysis Backed by Symbolic Mathematics'. In: *Journal of Open Source Software* 9.94 (9th Feb. 2024), 6127. DOI: 10.21105/joss.06127.

[11] Feng, L., Liu, Y., Wang, Y., Zhou, H., Lu, Z. and Li, T. 'Ultra-Compact Dual-Channel Integrated CO2 Infrared Gas Sensor'. In: *Microsystems & Nanoengineering* 10.1 (21st Oct. 2024), 151. ISSN: 2055-7434. DOI: 10.1038/s41378-024-00782-6.

[12] Schaper, J. L., Cirpka, O. A., Lewandowski, J. and Zarfl, C. 'Electrical Conductivity Fluctuations as a Tracer to Determine Time-Dependent Transport Characteristics in Hyporheic Sediments'. In: *Journal of Hydrology* 643 (1st Nov. 2024), 131914. ISSN: 0022-1694. DOI: 10.1016/j.jhydrol.2024.131914.

[13] Upton, S., Reichstein, M., Gans, F., Peters, W., Kraft, B. and Bastos, A. 'Constraining Biospheric Carbon Dioxide Fluxes by Combined Top-down and Bottom-up Approaches'. In: *Atmospheric Chemistry and Physics* 24.4 (28th Feb. 2024), 2555–2582. ISSN: 1680-7324. DOI: 10.5194/acp-24-2555-2024.

[14] Van Ramshorst, J. G. V., Knohl, A., Callejas-Rodelas, J. Á., Clement, R., Hill, T. C., Siebicke, L. and Markwitz, C. 'Lower-Cost Eddy Covariance for CO_2 and H_2 O Fluxes over Grassland and Agroforestry'. In: *Atmospheric Measurement Techniques* 17.20 (17th Oct. 2024), 6047–6071. ISSN: 1867-8548. DOI: 10.5194/amt-17-6047-2024.

[15] Bell, C., Ilonze, C., Duggan, A. and Zimmerle, D. 'Performance of Continuous Emission Monitoring Solutions under a Single-Blind Controlled Testing Protocol'. In: *Environmental Science & Technology* 57.14 (11th Apr. 2023), 5794–5805. ISSN: 0013-936X. DOI: 10.1021/acs.est.2c09235.

[16] Büchau, Y., Dörner, L. and Bange, J. *Short-Term Comprehensive CO2 Degassing Dataset from a Mofette at the Starzach Site in Winter 2022 Obtained with a Custom Flow Meter, Including Atmospheric Variables*. dataset bundled publication. PANGAEA, 2023. DOI: 10.1594/PANGAEA.963786.

[17] Calvin, K., Dasgupta, D., Krinner, G., Mukherji, A., Thorne, P. W., Trisos, C., Romero, J., Aldunce, P., Barrett, K., Blanco, G. et al. *IPCC, 2023: Climate Change 2023: Synthesis Report. Contribution of Working Groups I, II and III to the Sixth Assessment Report of the Intergovernmental Panel on Climate Change [Core Writing Team, H. Lee and J. Romero (Eds.)]. IPCC, Geneva, Switzerland.* Intergovernmental Panel on Climate Change (IPCC), 25th July 2023. DOI: 10.59327/IPCC/AR6-9789291691647.

[18] Czubaszek, R. and Wysocka-Czubaszek, A. 'Temporal Dynamics of CO2 Fluxes Measured with Eddy Covariance System in Maize, Winter Oilseed Rape and Winter Wheat Fields'. In: *Atmosphere* 14.2 (Feb. 2023), 372. ISSN: 2073-4433. DOI: 10.3390/atmos14020372.

[19] Dabla-Norris, E., Khalid, S., Magistretti, G. and Sollaci, A. 'Public Support for Climate Change Mitigation Policies: A Cross Country Survey'. In: *IMF Working Papers* 2023.223 (27th Oct. 2023). DOI: 10.5089/9798400258138.001.A001.

[20] Friedlingstein, P., O'Sullivan, M., Jones, M. W., Andrew, R. M., Bakker, D. C. E., Hauck, J., Landschützer, P., Le Quéré, C., Luijkx, I. T., Peters, G. P. et al. 'Global Carbon Budget 2023'. In: *Earth System Science Data* 15.12 (5th Dec. 2023), 5301–5369. ISSN: 1866-3516. DOI: 10.5194/essd-15-5301-2023.

[21] Herrmann, K. *Design Reiteration of a Chimney Gas Flowmeter for Natural CO2 Emissions from Mofettes: Differential Pressure Measurement Increases Resolution and Accuracy*. Bachelor's Thesis. Tübingen: Universität Tübingen, 2023. DOI: 10.15496/PUBLIKATION-89337.

[22] Hounshell, A. G., D'Acunha, B. M., Breef-Pilz, A., Johnson, M. S., Thomas, R. Q. and Carey, C. C. 'Eddy Covariance Data Reveal That a Small Freshwater Reservoir Emits a Substantial Amount of Carbon Dioxide and Methane'. In: *Journal of Geophysical Research: Biogeosciences* 128.3 (Mar. 2023), e2022JG007091. ISSN: 2169-8953, 2169-8961. DOI: 10.1029/2022JG007091.

[23] Krause, K., Wittrock, F., Richter, A., Busch, D., Bergen, A., Burrows, J. P., Freitag, S. and Halbherr, O. 'Determination of NO_x Emission Rates of Inland Ships from Onshore Measurements'. In: *Atmospheric Measurement Techniques* 16.7 (3rd Apr. 2023), 1767–1787. ISSN: 1867-1381. DOI: 10.5194/amt-16-1767-2023.

[24] Tejada, G., Gatti, L. V., Basso, L. S., Cassol, H. L. G., Silva-Junior, C. H. L., Mataveli, G., Marani, L., Arai, E., Gloor, M., Miller, J. B., Cunha, C. L., Domingues, L. G., Ipia, A., Correia, C. S. C., Crispim, S. P., Neves, R. A. L. and Von Randow, C. 'CO2 Emissions in the Amazon: Are Bottom-up Estimates from Land Use and Cover Datasets Consistent with Top-down Estimates Based on Atmospheric Measurements?' In: *Frontiers in Forests and Global Change* 6 (23rd Aug. 2023). ISSN: 2624-893X. DOI: 10.3389/ffgc.2023.1107580.

[25] Wüsteney, S. *Bodenwassergehalts-Messung in tonigen Böden des Starzacher Mofetten-Gebiets mittels SMT100 Sensoren: Korrektur der Topp-Gleichung*. Bachelorarbeit. Tübingen: Universität Tübingen, 2023. DOI: 10.15496/publikation-89327.

[26] Büchau, Y. G., van Kesteren, B., Platis, A. and Bange, J. 'An Autarkic Wireless Sensor Network to Monitor Atmospheric CO2 Concentrations'. In: *Meteorologische Zeitschrift* 31.4 (13th Oct. 2022), 331–345. DOI: 10.1127/metz/2022/1125.

[27] Lübben, A. and Leven, C. 'A Gas-Flow Funnel System to Quantify Advective Gas Emission Rates from the Subsurface'. In: *Environmental Earth Sciences* 81.15 (29th July 2022), 399. ISSN: 1866-6299. DOI: 10.1007/s12665-022-10512-8.

[28] Mar, K. A., Unger, C., Walderdorff, L. and Butler, T. 'Beyond CO2 Equivalence: The Impacts of Methane on Climate, Ecosystems, and Health'. In: *Environmental Science & Policy* 134 (1st Aug. 2022), 127–136. ISSN: 1462-9011. DOI: 10.1016/j.envsci.2022.03.027.

[29] Badeke, R., Matthias, V. and Grawe, D. 'Parameterizing the Vertical Downward Dispersion of Ship Exhaust Gas in the near Field'. In: *Atmospheric Chemistry and Physics* 21.8 (20th Apr. 2021), 5935–5951. ISSN: 1680-7316. DOI: 10.5194/acp-21-5935-2021.

[30] Esters, L., Rutgersson, A., Nilsson, E. and Sahlée, E. 'Non-Local Impacts on Eddy-Covariance Air–Lake CO_2 Fluxes'. In: *Boundary-Layer Meteorology* 178.2 (1st Feb. 2021), 283–300. ISSN: 1573-1472. DOI: 10.1007/s10546-020-00565-2.

[31] Foken, T., Hellmuth, O., Huwe, B. and Sonntag, D. 'Physical Quantities'. In: *Springer Handbook of Atmospheric Measurements*. Ed. by Foken, T. Cham: Springer International Publishing, 2021, 107–151. ISBN: 978-3-030-52171-4. DOI: 10.1007/978-3-030-52171-4_5.

[32] Grimmond, S. and Ward, H. C. 'Urban Measurements and Their Interpretation'. In: *Springer Handbook of Atmospheric Measurements*. Ed. by Foken, T. Cham: Springer International Publishing, 2021, 1391–1423. ISBN: 978-3-030-52171-4. DOI: 10.1007/978-3-030-52171-4_52.

[33] Heard, D., Whalley, L. K. and Brown, S. S. 'Gas Analysers and Laser Techniques'. In: *Springer Handbook of Atmospheric Measurements*. Ed. by Foken, T. Cham: Springer International Publishing, 2021, 475–508. ISBN: 978-3-030-52171-4. DOI: 10.1007/978-3-030-52171-4_16.

[34] Lee, T. R., Buban, M. and Meyers, T. P. 'Application of Bulk Richardson Parameterizations of Surface Fluxes to Heterogeneous Land Surfaces'. In: *Monthly Weather Review* 149.10 (15th Sept. 2021), 3243–3264. ISSN: 1520-0493, 0027-0644. DOI: 10.1175/MWR-D-21-0047.1.

[35] Mauder, M., Foken, T., Aubinet, M. and Ibrom, A. 'Eddy-Covariance Measurements'. In: *Springer Handbook of Atmospheric Measurements*. Ed. by Foken, T. Cham: Springer International Publishing, 2021, 1473–1504. ISBN: 978-3-030-52171-4. DOI: 10.1007/978-3-030-52171-4_55.

[36] Pan, G., Xu, Y. and Ma, J. 'The Potential of CO2 Satellite Monitoring for Climate Governance: A Review'. In: *Journal of Environmental Management* 277 (1st Jan. 2021), 111423. ISSN: 0301-4797. DOI: 10.1016/j.jenvman.2020.111423.

[37] Wichura, B. and Foken, T. 'Atmospheric Measurements for Different Purposes'. In: *Springer Handbook of Atmospheric Measurements*. Ed. by Foken, T. Cham: Springer International Publishing, 2021, 1187–1197. ISBN: 978-3-030-52171-4. DOI: 10.1007/978-3-030-52171-4_43.

[38] Franco, A. and Leccese, F. 'Measurement of CO2 Concentration for Occupancy Estimation in Educational Buildings with Energy Efficiency Purposes'. In: *Journal of Building Engineering* 32 (Nov. 2020), 101714. ISSN: 2352-7102. DOI: 10.1016/j.jobe.2020.101714.

[39] Kim, S.-M., Choi, Y. and Suh, J. 'Applications of the Open-Source Hardware Arduino Platform in the Mining Industry: A Review'. In: *Applied Sciences* 10.14 (Jan. 2020), 5018. ISSN: 2076-3417. DOI: 10.3390/app10145018.

[40] Lee, T. R. and Buban, M. 'Evaluation of Monin–Obukhov and Bulk Richardson Parameterizations for Surface–Atmosphere Exchange'. In: *Journal of Applied Meteorology and Climatology* 59.6 (15th June 2020), 1091–1107. ISSN: 1558-8424, 1558-8432. DOI: 10.1175/JAMC-D-19-0057.1.

[41] Maronga, B., Banzhaf, S., Burmeister, C., Esch, T., Forkel, R., Fröhlich, D., Fuka, V., Gehrke, K. F., Geletič, J., Giersch, S. et al. 'Overview of the PALM Model System 6.0'. In: *Geoscientific Model Development* 13.3 (20th Mar. 2020), 1335–1372. ISSN: 1991-959X. DOI: 10.5194/gmd-13-1335-2020.

[42] Müller, M., Graf, P., Meyer, J., Pentina, A., Brunner, D., Perez-Cruz, F., Hüglin, C. and Emmenegger, L. 'Integration and Calibration of Non-Dispersive Infrared (NDIR) CO_2 Low-Cost Sensors and Their Operation in a Sensor Network Covering Switzerland'. In: *Atmospheric Measurement Techniques* 13.7 (15th July 2020), 3815–3834. ISSN: 1867-1381. DOI: 10.5194/amt-13-3815-2020.

[43] Myers, M., White, C., Pejcic, B., Feitz, A., Roberts, J., Oh, Y.-Y., Xu, L., Ricard, L., Michael, K., Avijegon, A., Rachakonda, P. K., Woltering, M., Larcher, A., Stalker, L. and Hortle, A. 'CSIRO In-Situ Lab: A Multi-Pronged Approach to Surface Gas and Groundwater Monitoring at Geological CO2 Storage Sites'. In: *Chemical Geology* 545 (July 2020), 119642. ISSN: 00092541. DOI: 10.1016/j.chemgeo.2020.119642.

[44] Camarda, M., De Gregorio, S., Capasso, G., Di Martino, R. M. R., Gurrieri, S. and Prano, V. 'The Monitoring of Natural Soil CO2 Emissions: Issues and Perspectives'. In: *Earth-Science Reviews* 198 (1st Nov. 2019), 102928. ISSN: 0012-8252. DOI: 10.1016/j.earscirev.2019.102928.

[45] Forde, O. N., Cahill, A. G., Beckie, R. D. and Mayer, K. U. 'Barometric-Pumping Controls Fugitive Gas Emissions from a Vadose Zone Natural Gas Release'. In: *Scientific Reports* 9.1 (1st Oct. 2019), 14080. ISSN: 2045-2322. DOI: 10.1038/s41598-019-50426-3.

[46] Kämpf, H., Broge, A. S., Marzban, P., Allahbakhshi, M. and Nickschick, T. 'Nonvolcanic Carbon Dioxide Emission at Continental Rifts: The Bublak Mofette Area, Western Eger Rift, Czech Republic'. In: *Geofluids* 2019.1 (2019), 4852706. ISSN: 1468-8123. DOI: 10.1155/2019/4852706.

[47] Orcutt, B. N., Daniel, I. and Dasgupta, R., eds. *Deep Carbon: Past to Present*. 1st ed. Cambridge University Press, 17th Oct. 2019. ISBN: 978-1-108-67795-0 978-1-108-47749-9 978-1-108-73360-1. DOI: 10.1017/9781108677950.

[48] Pisso, I., Sollum, E., Grythe, H., Kristiansen, N. I., Cassiani, M., Eckhardt, S., Arnold, D., Morton, D., Thompson, R. L., Groot Zwaaftink, C. D. et al. 'The Lagrangian Particle Dispersion Model FLEXPART Version 10.4'. In: *Geoscientific Model Development* 12.12 (2nd Dec. 2019), 4955–4997. ISSN: 1991-959X. DOI: 10.5194/gmd-12-4955-2019.

[49] Ryoo, J.-M., Iraci, L. T., Tanaka, T., Marrero, J. E., Yates, E. L., Fung, I., Michalak, A. M., Tadić, J., Gore, W., Bui, T. P., Dean-Day, J. M. and Chang, C. S. 'Quantification of CO_2 and CH_4 Emissions over Sacramento, California, Based on Divergence Theorem Using Aircraft Measurements'. In: *Atmospheric Measurement Techniques* 12.5 (29th May 2019), 2949–2966. ISSN: 1867-8548. DOI: 10.5194/amt-12-2949-2019.

[50] Wong, K., Mason, E., Brune, S., East, M., Edmonds, M. and Zahirovic, S. 'Deep Carbon Cycling Over the Past 200 Million Years: A Review of Fluxes in Different Tectonic Settings'. In: *Frontiers in Earth Science* 7 (11th Oct. 2019), 263. ISSN: 2296-6463. DOI: 10.3389/feart.2019.00263.

[51] Zhao, J., Zhang, M., Xiao, W., Wang, W., Zhang, Z., Yu, Z., Xiao, Q., Cao, Z., Xu, J., Zhang, X., Liu, S. and Lee, X. 'An Evaluation of the Flux-Gradient and the Eddy Covariance Method to Measure CH4, CO2, and H2O Fluxes from Small Ponds'. In: *Agricultural and Forest Meteorology* 275 (15th Sept. 2019), 255–264. ISSN: 0168-1923. DOI: 10.1016/j.agrformet.2019.05.032.

[52] Bui, M., S. Adjiman, C., Bardow, A., J. Anthony, E., Boston, A., Brown, S., S. Fennell, P., Fuss, S., Galindo, A., A. Hackett, L. et al. 'Carbon Capture and Storage (CCS): The Way Forward'. In: *Energy & Environmental Science* 11.5 (2018), 1062–1176. DOI: 10.1039/C7EE02342A.

[53] Feitz, A., Schroder, I., Phillips, F., Coates, T., Negandhi, K., Day, S., Luhar, A., Bhatia, S., Edwards, G., Hrabar, S. et al. 'The Ginninderra CH4 and CO2 Release Experiment: An Evaluation of Gas Detection and Quantification Techniques'. In: *International Journal of Greenhouse Gas Control* 70 (1st Mar. 2018), 202–224. ISSN: 1750-5836. DOI: 10.1016/j.ijggc.2017.11.018.

[54] Lübben, A. and Leven, C. 'The Starzach Site in Southern Germany: A Site with Naturally Occurring CO2 Emissions Recovering from Century-Long Gas Mining as a Natural Analog for a Leaking CCS Reservoir'. In: *Environmental Earth Sciences* 77.8 (20th Apr. 2018), 316. ISSN: 1866-6299. DOI: 10.1007/s12665-018-7499-y.

[55] Martinsen, K. T., Kragh, T. and Sand-Jensen, K. 'Technical Note: A Simple and Cost-Efficient Automated Floating Chamber for Continuous Measurements of Carbon Dioxide Gas Flux on Lakes'. In: *Biogeosciences* 15.18 (19th Sept. 2018), 5565–5573. ISSN: 1726-4170. DOI: 10.5194/bg-15-5565-2018.

[56] Platt, U., Bobrowski, N. and Butz, A. 'Ground-Based Remote Sensing and Imaging of Volcanic Gases and Quantitative Determination of Multi-Species Emission Fluxes'. In: *Geosciences* 8.2 (Feb. 2018), 44. ISSN: 2076-3263. DOI: 10.3390/geosciences8020044.

[57] Braun, C. 'Not in My Backyard: CCS Sites and Public Perception of CCS'. In: *Risk Analysis* 37.12 (2017), 2264–2275. ISSN: 1539-6924. DOI: 10.1111/risa.12793.

[58] Chor, T. L., Dias, N. L., Araújo, A., Wolff, S., Zahn, E., Manzi, A., Trebs, I., Sá, M. O., Teixeira, P. R. and Sörgel, M. 'Flux-Variance and Flux-Gradient Relationships in the Roughness Sublayer over the Amazon Forest'. In: *Agricultural and Forest Meteorology* 239 (28th May 2017), 213–222. ISSN: 0168-1923. DOI: 10.1016/j.agrformet.2017.03.009.

[59] Krüger, T. 'Conflicts over Carbon Capture and Storage in International Climate Governance'. In: *Energy Policy* 100 (1st Jan. 2017), 58–67. ISSN: 0301-4215. DOI: 10.1016/j.enpol.2016.09.059.

[60] Martin, C. R., Zeng, N., Karion, A., Dickerson, R. R., Ren, X., Turpie, B. N. and Weber, K. J. 'Evaluation and Environmental Correction of Ambient CO_2 Measurements from a Low-Cost NDIR Sensor'. In: *Atmospheric Measurement Techniques* 10.7 (3rd July 2017), 2383–2395. ISSN: 1867-1381. DOI: 10.5194/amt-10-2383-2017.

[61] Acemoglu, D., Akcigit, U., Hanley, D. and Kerr, W. 'Transition to Clean Technology'. In: *Journal of Political Economy* 124.1 (Feb. 2016), 52–104. ISSN: 0022-3808, 1537-534X. DOI: 10.1086/684511.

[62] Cook, J., Oreskes, N., Doran, P. T., Anderegg, W. R. L., Verheggen, B., Maibach, E. W., Carlton, J. S., Lewandowsky, S., Skuce, A. G., Green, S. A., Nuccitelli, D., Jacobs, P., Richardson, M., Winkler, B., Painting, R. and Rice, K. 'Consensus on Consensus: A Synthesis of Consensus Estimates on Human-Caused Global Warming'. In: *Environmental Research Letters* 11.4 (Apr. 2016), 048002. ISSN: 1748-9326. DOI: 10.1088/1748-9326/11/4/048002.

[63] Etminan, M., Myhre, G., Highwood, E. J. and Shine, K. P. 'Radiative Forcing of Carbon Dioxide, Methane, and Nitrous Oxide: A Significant Revision of the Methane Radiative Forcing'. In: *Geophysical Research Letters* 43.24 (2016), 12, 614–12, 623. ISSN: 1944-8007. DOI: 10.1002/2016GL071930.

[64] Štefanica, J., Smutná, J., Kočí, V., Machač, P. and Pilař, L. 'Environmental Gains and Impacts of a CCS Technology – Case Study of Post-combustion CO2 Separation by Ammonia Absorption'. In: *Energy Procedia*. The 8th Trondheim Conference on CO2 Capture, Transport and Storage 86 (1st Jan. 2016), 215–218. ISSN: 1876-6102. DOI: 10.1016/j.egypro.2016.01.022.

[65] Eugster, W. and Merbold, L. 'Eddy Covariance for Quantifying Trace Gas Fluxes from Soils'. In: *SOIL* 1.1 (20th Feb. 2015), 187–205. ISSN: 2199-3971. DOI: 10.5194/soil-1-187-2015.

[66] Goepel, A., Lonschinski, M., Viereck, L., Büchel, G. and Kukowski, N. 'Volcano-Tectonic Structures and CO2-degassing Patterns in the Laacher See Basin, Germany'. In: *International Journal of Earth Sciences* 104.5 (1st July 2015), 1483–1495. ISSN: 1437-3262. DOI: 10.1007/s00531-014-1133-3.

[67] Kljun, N., Calanca, P., Rotach, M. W. and Schmid, H. P. 'A Simple Two-Dimensional Parameterisation for Flux Footprint Prediction (FFP)'. In: *Geoscientific Model Development* 8.11 (17th Nov. 2015), 3695–3713. ISSN: 1991-959X. DOI: 10.5194/gmd-8-3695-2015.

[68] Messerli, J., Bertrand, A., Bourassa, J., Bélanger, G., Castonguay, Y., Tremblay, G., Baron, V. and Seguin, P. 'Performance of Low-Cost Open-Top Chambers to Study Long-Term Effects of Carbon Dioxide and Climate under Field Conditions'. In: *Agronomy Journal* 107.3 (2015), 916–920. ISSN: 1435-0645. DOI: 10.2134/agronj14.0571.

[69] Shao, C., Chen, J., Stepien, C. A., Chu, H., Ouyang, Z., Bridgeman, T. B., Czajkowski, K. P., Becker, R. H. and John, R. 'Diurnal to Annual Changes in Latent, Sensible Heat, and CO2 Fluxes over a Laurentian Great Lake: A Case Study in Western Lake Erie'. In: *Journal of Geophysical Research: Biogeosciences* 120.8 (2015), 1587–1604. ISSN: 2169-8961. DOI: 10.1002/2015JG003025.

[70] Stephens, J. C. 'Carbon Capture and Storage: A Controversial Climate Mitigation Approach'. In: *The International Spectator* 50.1 (2nd Jan. 2015), 74–84. ISSN: 0393-2729. DOI: 10.1080/03932729.2015.994336.

[71] UNFCCC. *The Paris Agreement*. United Nations Framework Convention on Climate Change, 2015. URL: https://unfccc.int/process-and-meetings/the-paris-agreement (visited on: 17.05.2025).

[72] Zängl, G., Reinert, D., Rípodas, P. and Baldauf, M. 'The ICON (ICOsahedral Non-hydrostatic) Modelling Framework of DWD and MPI-M: Description of the Non-Hydrostatic Dynamical Core'. In: *Quarterly Journal of the Royal Meteorological Society* 141.687 (2015), 563–579. ISSN: 1477-870X. DOI: 10.1002/qj.2378.

[73] Kondo, F., Ono, K., Mano, M., Miyata, A. and Tsukamoto, O. 'Experimental Evaluation of Water Vapour Cross-Sensitivity for Accurate Eddy Covariance Measurement of CO_2 Flux Using Open-Path CO_2/H_2O Gas Analysers'. In: *Tellus B: Chemical and Physical Meteorology* 66.1 (1st Jan. 2014), 23803. ISSN: 1600-0889, 0280-6509. DOI: 10.3402/tellusb.v66.23803.

[74] Leclerc, M. Y. *Footprints in Micrometeorology and Ecology*. 1st ed. Berlin, Heidelberg: Springer Berlin / Heidelberg, 2014. 239 pp. ISBN: 978-3-642-54544-3.

[75] Leclerc, M. Y. and Foken, T. 'Surface-Layer Properties and Parameterizations'. In: *Footprints in Micrometeorology and Ecology*. Ed. by Leclerc, M. Y. and Foken, T. Berlin, Heidelberg: Springer, 2014, 21–70. ISBN: 978-3-642-54545-0. DOI: 10.1007/978-3-642-54545-0_2.

[76] Meredith, L. K., Commane, R., Munger, J. W., Dunn, A., Tang, J., Wofsy, S. C. and Prinn, R. G. 'Ecosystem Fluxes of Hydrogen: A Comparison of Flux-Gradient Methods'. In: *Atmospheric Measurement Techniques* 7.9 (3rd Sept. 2014), 2787–2805. ISSN: 1867-8548. DOI: 10.5194/amt-7-2787-2014.

[77] Monson, R. K. and Baldocchi, D. 'Observations of Turbulent Fluxes'. In: *Terrestrial Biosphere-Atmosphere Fluxes*. Cambridge (GB): Cambridge university press, 2014, 327–351. ISBN: 978-1-107-04065-6.

[78] Xiao, W., Liu, S., Li, H., Xiao, Q., Wang, W., Hu, Z., Hu, C., Gao, Y., Shen, J., Zhao, X., Zhang, M. and Lee, X. 'A Flux-Gradient System for Simultaneous Measurement of the CH_4 , CO_2 , and H_2 O Fluxes at a Lake–Air Interface'. In: *Environmental Science & Technology* 48.24 (16th Dec. 2014), 14490–14498. ISSN: 0013-936X, 1520-5851. DOI: 10.1021/es5033713.

[79] Burton, M. R., Sawyer, G. M. and Granieri, D. 'Deep Carbon Emissions from Volcanoes'. In: *Reviews in Mineralogy and Geochemistry* 75.1 (1st Jan. 2013), 323–354. ISSN: 1529-6466. DOI: 10.2138/rmg.2013.75.11.

[80] Dasgupta, R. 'Ingassing, Storage, and Outgassing of Terrestrial Carbon through Geologic Time'. In: *Reviews in Mineralogy and Geochemistry* 75.1 (1st Jan. 2013), 183–229. ISSN: 1529-6466. DOI: 10.2138/rmg.2013.75.7.

[81] Grawe, D., Schlünzen, K. H. and Pascheke, F. 'Comparison of Results of an Obstacle Resolving Microscale Model with Wind Tunnel Data'. In: *Atmospheric Environment* 79 (1st Nov. 2013), 495–509. ISSN: 1352-2310. DOI: 10.1016/j.atmosenv.2013.06.039.

[82] Han, W. S., Lu, M., McPherson, B. J., Keating, E. H., Moore, J., Park, E., Watson, Z. T. and Jung, N.-H. 'Characteristics of CO2-driven Cold-Water Geyser, Crystal Geyser in Utah: Experimental Observation and Mechanism Analyses'. In: *Geofluids* 13.3 (2013), 283–297. ISSN: 1468-8123. DOI: 10.1111/gfl.12018.

[83] Karion, A., Sweeney, C., Pétron, G., Frost, G., Michael Hardesty, R., Kofler, J., Miller, B. R., Newberger, T., Wolter, S., Banta, R., Brewer, A., Dlugokencky, E., Lang, P., Montzka, S. A., Schnell, R., Tans, P., Trainer, M., Zamora, R. and Conley, S. 'Methane Emissions Estimate from Airborne Measurements over a Western United States Natural Gas Field'. In: *Geophysical Research Letters* 40.16 (2013), 4393–4397. ISSN: 1944-8007. DOI: 10.1002/grl.50811.

[84] Sauer, U., Schütze, C., Leven, C., Schlömer, S. and Dietrich, P. 'An Integrative Hierarchical Monitoring Approach for Detecting and Characterizing CO2 Releases'. In: *Energy Procedia*. GHGT-11 Proceedings of the 11th International Conference on Greenhouse Gas Control Technologies, 18-22 November 2012, Kyoto, Japan 37 (1st Jan. 2013), 4257–4267. ISSN: 1876-6102. DOI: 10.1016/j.egypro.2013.06.328.

[85] Streets, D. G., Canty, T., Carmichael, G. R., de Foy, B., Dickerson, R. R., Duncan, B. N., Edwards, D. P., Haynes, J. A., Henze, D. K., Houyoux, M. R., Jacob, D. J., Krotkov, N. A., Lamsal, L. N., Liu, Y., Lu, Z., Martin, R. V., Pfister, G. G., Pinder, R. W., Salawitch, R. J. and Wecht, K. J. 'Emissions Estimation from Satellite Retrievals: A Review of Current Capability'. In: *Atmospheric Environment* 77 (1st Oct. 2013), 1011–1042. ISSN: 1352-2310. DOI: 10.1016/j.atmosenv.2013.05.051.

[86] Van Kesteren, B., Hartogensis, O. K., van Dinther, D., Moene, A. F. and De Bruin, H. A. R. 'Measuring H2O and CO2 Fluxes at Field Scales with Scintillometry: Part I – Introduction and Validation of Four Methods'. In: *Agricultural and Forest Meteorology*. Special Issue:Drought Inner Asia 178–179 (15th Sept. 2013), 75–87. ISSN: 0168-1923. DOI: 10.1016/j.agrformet.2012.09.013.

[87] Burba, G., Schmidt, A., Scott, R. L., Nakai, T., Kathilankal, J., Fratini, G., Hanson, C., Law, B., McDermitt, D. K., Eckles, R., Furtaw, M. and Velgersdyk, M. 'Calculating CO2 and H2O Eddy Covariance Fluxes from an Enclosed Gas Analyzer Using an Instantaneous Mixing Ratio'. In: *Global Change Biology* 18.1 (2012), 385–399. ISSN: 1365-2486. DOI: 10.1111/j.1365-2486.2011.02536.x.

[88] Gu, L., Massman, W. J., Leuning, R., Pallardy, S. G., Meyers, T., Hanson, P. J., Riggs, J. S., Hosman, K. P. and Yang, B. 'The Fundamental Equation of Eddy Covariance and Its Application in Flux Measurements'. In: *Agricultural and Forest Meteorology* 152 (15th Jan. 2012), 135–148. ISSN: 0168-1923. DOI: 10.1016/j.agrformet.2011.09.014.

[89] Pindado, S., Sanz, A. and Wery, A. 'Deviation of Cup and Propeller Anemometer Calibration Results with Air Density'. In: *Energies* 5.3 (9th Mar. 2012), 683–701. ISSN: 1996-1073. DOI: 10.3390/en5030683.

[90] Stremme, W., Krueger, A., Harig, R. and Grutter, M. 'Volcanic SO_2 and SiF_4 Visualization Using 2-D Thermal Emission Spectroscopy – Part 1: Slant-columns and Their Ratios'. In: *Atmospheric Measurement Techniques* 5.2 (2nd Feb. 2012), 275–288. ISSN: 1867-1381. DOI: 10.5194/amt-5-275-2012.

[91] Szulczewski, M. L., MacMinn, C. W., Herzog, H. J. and Juanes, R. 'Lifetime of Carbon Capture and Storage as a Climate-Change Mitigation Technology'. In: *Proceedings of the National Academy of Sciences* 109.14 (3rd Apr. 2012), 5185–5189. ISSN: 0027-8424, 1091-6490. DOI: 10.1073/pnas.1115347109.

[92] Gal, F., Michel, B., Gilles, B., Frédéric, J. and Karine, M. 'CO2 Escapes in the Laacher See Region, East Eifel, Germany: Application of Natural Analogue Onshore and Offshore Geochemical Monitoring'. In: *International Journal of Greenhouse Gas Control* 5.4 (1st July 2011), 1099–1118. ISSN: 1750-5836. DOI: 10.1016/j.ijggc.2011.04.004.

[93] Leven, C., Weiß, H., Vienken, T. and Dietrich, P. 'Direct-Push-Technologien – Effiziente Untersuchungsmethoden für die Untergrunderkundung'. In: *Grundwasser* 16.4 (1st Dec. 2011), 221–234. ISSN: 1432-1165. DOI: 10.1007/s00767-011-0175-8.

[94] Patel, N. R., Dadhwal, V. K. and Saha, S. K. 'Measurement and Scaling of Carbon Dioxide (CO2) Exchanges in Wheat Using Flux-Tower and Remote Sensing'. In: *Journal of the Indian Society of Remote Sensing* 39.3 (1st Sept. 2011), 383–391. ISSN: 0974-3006. DOI: 10.1007/s12524-011-0107-1.

[95] Stockie, J. M. 'The Mathematics of Atmospheric Dispersion Modeling'. In: *SIAM Review* 53.2 (Jan. 2011), 349–372. ISSN: 0036-1445. DOI: 10.1137/10080991X.

[96] Mayrwöger, J., Reichl, W., Krutzer, C. and Jakoby, B. 'Gas Monitoring with a Fabry–Perot Based Bolometer: Cross-sensitivity to Water Vapor'. In: *Procedia Engineering*. Eurosensor XXIV Conference 5 (1st Jan. 2010), 1220–1223. ISSN: 1877-7058. DOI: 10.1016/j.proeng.2010.09.332.

[97] Nisbet, E. and Weiss, R. 'Top-Down Versus Bottom-Up'. In: *Science* 328.5983 (4th June 2010), 1241–1243. DOI: 10.1126/science.1189936.

[98] Schrier-Uijl, A. P., Kroon, P. S., Hensen, A., Leffelaar, P. A., Berendse, F. and Veenendaal, E. M. 'Comparison of Chamber and Eddy Covariance-Based CO2 and CH4 Emission Estimates in a Heterogeneous Grass Ecosystem on Peat'. In: *Agricultural and Forest Meteorology*. Special Issue on Eddy Covariance (EC)Flux Measurements of CH4 and N2O 150.6 (15th June 2010), 825–831. ISSN: 0168-1923. DOI: 10.1016/j.agrformet.2009.11.007.

[99] Alfieri, J. G., Blanken, P. D., Smith, D. and Morgan, J. 'Concerning the Measurement and Magnitude of Heat, Water Vapor, and Carbon Dioxide Exchange from a Semiarid Grassland'. In: *Journal of Applied Meteorology and Climatology* 48.5 (1st May 2009), 982–996. ISSN: 1558-8432, 1558-8424. DOI: 10.1175/2008JAMC1873.1.

[100] Carapezza, M. L., Ricci, T., Ranaldi, M. and Tarchini, L. 'Active Degassing Structures of Stromboli and Variations in Diffuse CO2 Output Related to the Volcanic Activity'. In: *Journal of Volcanology and Geothermal Research*. The 2007 Eruption of Stromboli 182.3 (10th May 2009), 231–245. ISSN: 0377-0273. DOI: 10.1016/j.jvolgeores.2008.08.006.

[101] Lewicki, J. L., Hilley, G. E., Fischer, M. L., Pana, L., Oldenburg, C. M., Dobeck, L. and Spangler, L. 'Detection of CO2 Leakage by Eddy Covariance during the ZERT Project's CO2 Release Experiments'. In: *Energy Procedia*. Greenhouse Gas Control Technologies 9 1.1 (1st Feb. 2009), 2301–2306. ISSN: 1876-6102. DOI: 10.1016/j.egypro.2009.01.299.

[102] Grachev, A. A., Andreas, E. L., Fairall, C. W., Guest, P. S. and Persson, P. O. G. 'Turbulent Measurements in the Stable Atmospheric Boundary Layer during SHEBA: Ten Years After'. In: *Acta Geophysica* 56.1 (1st Mar. 2008), 142–166. ISSN: 1895-7455. DOI: 10.2478/s11600-007-0048-9.

[103] Kulmala, L., Launiainen, S., Pumpanen, J., Lankreijer, H., Lindroth, A., Hari, P. and Vesala, T. 'H_2O and CO_2 Fluxes at the Floor of a Boreal Pine Forest'. In: *Tellus B: Chemical and Physical Meteorology* 60.2 (1st Jan. 2008), 167. ISSN: 1600-0889, 0280-6509. DOI: 10.1111/j.1600-0889.2007.00327.x.

[104] Vesala, T., Kljun, N., Rannik, Ü., Rinne, J., Sogachev, A., Markkanen, T., Sabelfeld, K., Foken, Th. and Leclerc, M. Y. 'Flux and Concentration Footprint Modelling: State of the Art'. In: *Environmental Pollution* 152.3 (1st Apr. 2008), 653–666. ISSN: 0269-7491. DOI: 10.1016/j.envpol.2007.06.070.

[105] Williams-Jones, G., Stix, J. and Hickson, C. *The COSPEC Cookbook: Making SO2 Measurements at Active Volcanoes*. IAVCEI, 2008. DOI: 10.13140/RG.2.2.13728.99845.

[106] Giammanco, S., Parello, F., Gambardella, B., Schifano, R., Pizzullo, S. and Galante, G. 'Focused and Diffuse Effluxes of CO2 from Mud Volcanoes and Mofettes South of Mt. Etna (Italy)'. In: *Journal of Volcanology and Geothermal Research* 165.1–2 (Aug. 2007), 46–63. ISSN: 03770273. DOI: 10.1016/j.jvolgeores.2007.04.010.

[107] Foken, T. '50 Years of the Monin–Obukhov Similarity Theory'. In: *Boundary-Layer Meteorology* 119.3 (1st June 2006), 431–447. ISSN: 1573-1472. DOI: 10.1007/s10546-006-9048-6.

[108] Horton, K. A., Williams-Jones, G., Garbeil, H., Elias, T., Sutton, A. J., Mouginis-Mark, P., Porter, J. N. and Clegg, S. 'Real-Time Measurement of Volcanic SO2 Emissions: Validation of a New UV Correlation Spectrometer (FLYSPEC)'. In: *Bulletin of Volcanology* 68.4 (1st Feb. 2006), 323–327. ISSN: 1432-0819. DOI: 10.1007/s00445-005-0014-9.

[109] Wallace, J. M. and Hobbs, P. V. *Atmospheric Science: An Introductory Survey*. 2nd ed. International Geophysics Series v. 92. OCLC: ocm62421169. Amsterdam ; Boston: Elsevier Academic Press, 2006. 483 pp. ISBN: 978-0-12-732951-2.

[110] Glennon, J. A. and Pfaff, R. M. 'The Operation and Geography of Carbon Dioxide-Driven, Cold-Water "Geysers"'. In: *The GOSA Transactions* 9 (2005), 184–192. URL: https://www.researchgate.net/profile/Alan-Glennon/publication/216876596_The_operation_and_geography_of_carbon-dioxide-driven_cold-water_geysers/links/5b444580458515f71cb8a698/The-operation-and-geography-of-carbon-dioxide-driven-cold-water-geysers.pdf (visited on: 22.10.2025).

[111] Kljun, N., Calanca, P., Rotach, M. W. and Schmid, H. P. 'A Simple Parameterisation for Flux Footprint Predictions'. In: *Boundary-Layer Meteorology* 112.3 (1st Sept. 2004), 503–523. ISSN: 1573-1472. DOI: 10.1023/B:BOUN.0000030653.71031.96.

[112] Galle, B., Oppenheimer, C., Geyer, A., McGonigle, A. J. S., Edmonds, M. and Horrocks, L. 'A Miniaturised Ultraviolet Spectrometer for Remote Sensing of SO2 Fluxes: A New Tool for Volcano Surveillance'. In: *Journal of Volcanology and Geothermal Research* 119.1 (1st Jan. 2003), 241–254. ISSN: 0377-0273. DOI: 10.1016/S0377-0273(02)00356-6.

[113] Lin, J. C., Gerbig, C., Wofsy, S. C., Andrews, A. E., Daube, B. C., Davis, K. J. and Grainger, C. A. 'A Near-Field Tool for Simulating the Upstream Influence of Atmospheric Observations: The Stochastic Time-Inverted Lagrangian Transport (STILT) Model'. In: *Journal of Geophysical Research: Atmospheres* 108.D16 (2003), 4493. ISSN: 2156-2202. DOI: 10.1029/2002JD003161.

[114] Mörner, N.-A. and Etiope, G. 'Carbon Degassing from the Lithosphere'. In: *Global and Planetary Change* 33.1–2 (June 2002), 185–203. ISSN: 09218181. DOI: 10.1016/S0921-8181(02)00070-X.

[115] Kormann, R. and Meixner, F. X. 'An Analytical Footprint Model For Non-Neutral Stratification'. In: *Boundary-Layer Meteorology* 99.2 (1st May 2001), 207–224. ISSN: 1573-1472. DOI: 10.1023/A:1018991015119.

[116] Lowenstern, J. B. 'Carbon Dioxide in Magmas and Implications for Hydrothermal Systems'. In: *Mineralium Deposita* 36.6 (1st Sept. 2001), 490–502. ISSN: 1432-1866. DOI: 10.1007/s001260100185.

[117] Hsieh, C.-I., Katul, G. and Chi, T.-w. 'An Approximate Analytical Model for Footprint Estimation of Scalar Fluxes in Thermally Stratified Atmospheric Flows'. In: *Advances in Water Resources* 23.7 (1st June 2000), 765–772. ISSN: 0309-1708. DOI: 10.1016/S0309-1708(99)00042-1.

[118] Pope, S. B. 'Gradient-Diffusion and Turbulent-Viscosity Hypotheses'. In: *Turbulent Flows*. Cambridge ; New York: Cambridge University Press, 2000, 92–95. ISBN: 978-0-521-59125-6.

[119] Rogie, J. D., Kerrick, D. M., Chiodini, G. and Frondini, F. 'Flux Measurements of Nonvolcanic CO2 Emission from Some Vents in Central Italy'. In: *Journal of Geophysical Research: Solid Earth* 105.B4 (10th Apr. 2000), 8435–8445. ISSN: 2169-9313. DOI: 10.1029/1999JB900430.

[120] Rosenfeld, A. H., Kaarsberg, T. M. and Romm, J. 'Technologies to Reduce Carbon Dioxide Emissions in the Next Decade'. In: *Physics Today* 53.11 (1st Nov. 2000), 29–34. ISSN: 0031-9228, 1945-0699. DOI: 10.1063/1.1333283.

[121] Draxler, R. R. and Hess, G. D. 'An Overview of the HYSPLIT_4 Modelling System for Trajectories'. In: *Australian meteorological magazine* 47.4 (1998), 295–308.

[122] Tsoukias, N. M., Tannous, Z., Wilson, A. F. and George, S. C. 'Single-Exhalation Profiles of NO and CO_2 in Humans: Effect of Dynamically Changing Flow Rate'. In: *Journal of Applied Physiology* 85.2 (1st Aug. 1998), 642–652. ISSN: 8750-7587, 1522-1601. DOI: 10.1152/jappl.1998.85.2.642.

[123] Simmonds, J. G. 'The Gradient, the Del Operator, Covariant Differentiation, and the Divergence Theorem'. In: *A Brief on Tensor Analysis*. Ed. by Simmonds, J. G. New York, NY: Springer, 1994, 71–105. ISBN: 978-1-4419-8522-4. DOI: 10.1007/978-1-4419-8522-4_4.

[124] Cellier, P. and Brunet, Y. 'Flux-Gradient Relationships above Tall Plant Canopies'. In: *Agricultural and Forest Meteorology* 58.1 (1st Mar. 1992), 93–117. ISSN: 0168-1923. DOI: 10.1016/0168-1923(92)90113-I.

[125] Nilson, R. H., Peterson, E. W., Lie, K. H., Burkhard, N. R. and Hearst, J. R. 'Atmospheric Pumping: A Mechanism Causing Vertical Transport of Contaminated Gases through Fractured Permeable Media'. In: *Journal of Geophysical Research: Solid Earth* 96.B13 (1991), 21933–21948. ISSN: 2156-2202. DOI: 10.1029/91JB01836.

[126] Gurrieri, S. and Valenza, M. 'Gas Transport in Natural Porous Mediums: A Method for Measuring CO2 Flows from the Ground in Volcanic and Geothermal Areas'. In: *Rendiconti della Societa Italiana di Mineralogia e Petrologia* 43 (1988), 1151–1158.

[127] Stull, R. B., ed. *An Introduction to Boundary Layer Meteorology*. Dordrecht: Springer Netherlands, 1988. ISBN: 978-90-277-2769-5. DOI: 10.1007/978-94-009-3027-8.

[128] Webb, E. K., Pearman, G. I. and Leuning, R. 'Correction of Flux Measurements for Density Effects Due to Heat and Water Vapour Transfer'. In: *Quarterly Journal of the Royal Meteorological Society* 106.447 (1980), 85–100. DOI: 10.1002/qj.49710644707.

[129] Louis, J.-F. 'A Parametric Model of Vertical Eddy Fluxes in the Atmosphere'. In: *Boundary-Layer Meteorology* 17.2 (1st Sept. 1979), 187–202. ISSN: 1573-1472. DOI: 10.1007/BF00117978.

[130] Busch, N. E., Chang, S. W. and Anthes, R. A. 'A Multi-Level Model of the Planetary Boundary Layer Suitable for Use with Mesoscale Dynamic Models'. In: *Journal of Applied Meteorology and Climatology* 15.9 (1st Sept. 1976), 909–919. ISSN: 1520-0450. DOI: 10.1175/1520-0450(1976)015<0909:AMLMOT>2.0.CO;2.

[131] Broecker, W. S. 'Climatic Change: Are We on the Brink of a Pronounced Global Warming?' In: *Science* 189.4201 (8th Aug. 1975), 460–463. DOI: 10.1126/science.189.4201.460.

[132] Dyer, A. J. 'A Review of Flux-Profile Relationships'. In: *Boundary-Layer Meteorology* 7.3 (1st Nov. 1974), 363–372. ISSN: 1573-1472. DOI: 10.1007/BF00240838.

[133] Rinehart, J. S. 'Fluctuations in Geyser Activity Caused by Variations in Earth Tidal Forces, Barometric Pressure, and Tectonic Stresses'. In: *Journal of Geophysical Research (1896-1977)* 77.2 (1972), 342–350. ISSN: 2156-2202. DOI: 10.1029/JB077i002p00342.

[134] Sawyer, J. S. 'Man-Made Carbon Dioxide and the "Greenhouse" Effect'. In: *Nature* 239.5366 (Sept. 1972), 23–26. ISSN: 1476-4687. DOI: 10.1038/239023a0.

[135] Businger, J. A., Wyngaard, J. C., Izumi, Y. and Bradley, E. F. 'Flux-Profile Relationships in the Atmospheric Surface Layer'. In: *Journal of the Atmospheric Sciences* 28.2 (1st Mar. 1971), 181–189. ISSN: 0022-4928, 1520-0469. DOI: 10.1175/1520-0469(1971)028<0181:FPRITA>2.0.CO;2.

[136] Delsol, F., Miyakoda, K. and Clarke, R. H. 'Parameterized Processes in the Surface Boundary Layer of an Atmospheric Circulation Model'. In: *Quarterly Journal of the Royal Meteorological Society* 97.412 (1971), 181–208. ISSN: 1477-870X. DOI: 10.1002/qj.49709741205.

[137] Dyer, A. J. and Hicks, B. B. 'Flux-Gradient Relationships in the Constant Flux Layer'. In: *Quarterly Journal of the Royal Meteorological Society* 96.410 (1970), 715–721. ISSN: 1477-870X. DOI: 10.1002/qj.49709641012.

[138] Businger, J. A., Miyake, M., Dyer, A. J. and Bradley, E. F. 'On the Direct Determination of the Turbulent Heat Flux Near the Ground'. In: *Journal of Applied Meteorology and Climatology* 6.6 (1st Dec. 1967), 1025–1032. ISSN: 1520-0450. DOI: 10.1175/1520-0450(1967)006<1025:OTDDOT>2.0.CO;2.

[139] Dyer, A. J. and Maher, F. J. 'Automatic Eddy-Flux Measurement with the Evapotron'. In: *Journal of Applied Meteorology and Climatology* 4.5 (1st Oct. 1965), 622–625. ISSN: 1520-0450. DOI: 10.1175/1520-0450(1965)004<0622:AEFMWT>2.0.CO;2.

[140] Keeling, C. D. 'The Concentration and Isotopic Abundances of Carbon Dioxide in the Atmosphere'. In: *Tellus* 12.2 (May 1960), 200–203. ISSN: 00402826, 21533490. DOI: 10.1111/j.2153-3490.1960.tb01300.x.

[141] Callendar, G. S. 'On the Amount of Carbon Dioxide in the Atmosphere'. In: *Tellus* 10.2 (1st Jan. 1958), 243–248. ISSN: 0040-2826. DOI: 10.3402/tellusa.v10i2.9231.

[142] Meyers, C. and Van Dusen, M. 'The Vapor Pressure of Liquid and Solid Carbon Dioxide'. In: *Bureau of Standards Journal of Research* 10.3 (Mar. 1933), 381. ISSN: 0091-1801. DOI: 10.6028/jres.010.029.

[143] Ekholm, N. 'On the Variations of the Climate of the Geological and Historical Past and Their Causes'. In: *Quarterly Journal of the Royal Meteorological Society* 27.117 (1901), 1–62. ISSN: 1477-870X. DOI: 10.1002/qj.49702711702.

[144] Arrhenius, S. 'XXXI. On the Influence of Carbonic Acid in the Air upon the Temperature of the Ground'. In: *The London, Edinburgh, and Dublin Philosophical Magazine and Journal of Science* 41.251 (1st Apr. 1896), 237–276. ISSN: 1941-5982. DOI: 10.1080/14786449608620846.

[145] Fourier, J. 'Remarques Générales Sur Les Températures Du Globe Terrestre et Des Espaces Planétaires'. In: *Annales de Chemie et de Physique*. Vol. 27. 1824, 136–167.

7 Appendix

The following appendix contains the publications listed in subsection 1.1 ‘First-Author Publications’.

A Büchau et al. (2022): Atmospheric CO_2 dynamics in Starzach

Büchau, Y. G., van Kesteren, B., Platis, A. and Bange, J. 'An Autarkic Wireless Sensor Network to Monitor Atmospheric CO2 Concentrations'. In: *Meteorologische Zeitschrift* 31.4 (13th Oct. 2022), 331–345. DOI: 10.1127/metz/2022/1125.

Meteorol. Z. (Contrib. Atm. Sci.), Vol. **31**, No. 4, 331–345 (published online June 24, 2022)

Measurement Techniques

An Autarkic Wireless Sensor Network to Monitor Atmospheric CO_2 Concentrations

Yann Georg Büchau*, Bram van Kesteren, Andreas Platis and Jens Bange

Center for Applied Geoscience, University of Tübingen, Germany

(Manuscript received December 31, 2021; in revised form February 28, 2022; accepted March 17, 2022)

Abstract

In this study an autarkic low-cost wireless network infrastructure suitable for areas spanning a couple of hectares is introduced. Open source hard- and software components make up the infrastructure's core, rendering it very scalable in terms of cost and deployment density. The network is designed to operate continuously throughout the year in a wide range of weather conditions.Four different embedded, low-cost Sensirion SCD30 non-dispersive infrared (NDIR) CO_2 sensors are evaluated under laboratory conditions and tested for cross-sensitivity on water vapour and linear characteristics, of which the Sensirion SCD30 sensor exhibits the best overall performance. An in-field comparison of eleven Sensirion sensors with an eddy-covariance station verifies its outdoor applicability. The network's suitability to monitor natural CO_2 emissions was tested at a site in the upper Neckar Valley in southwestern Germany. A station with a single Sensirion sensor observed a strong diurnal cycle of the near-surface CO_2 concentration over the course of several months. While only slightly elevated CO_2 levels above 400 ppm prevailed during the day, concentrations reached the sensor's output limit of 40 000 ppm during the night when wind speeds are low.

Keywords: sensor network, low-cost, NDIR CO_2 sensors, CO_2 degassing

1 Introduction

The significance of the atmospheric carbon dioxide (CO_2) concentration for the earth's greenhouse effect has been investigated extensively over the last decades (Sawyer, 1972; Hansen et al., 1981; Forster et al., 2007; Anderson et al., 2016) and researchers consent on the relevance of anthropogenic sources for global warming (Cook et al., 2016). Thus, quantification and understanding of both anthropogenic and natural CO_2 sources contributing to the atmospheric concentration is of great importance.

There exist numerous sites with significant natural CO_2 emissions originating from different geological sources across the globe (Rogie et al., 2000; Kerrick, 2001; Beaubien et al., 2003; Battani et al., 2010). Some of them are suited as natural analogs for leaking carbon capture and storage (CCS) sites (Lewicki et al., 2007; Burnside et al., 2013; Lübben and Leven, 2018). Advancing systems that are able to continuously monitor gas leakage at such locations is therefore vital.

Long-term observations of such gas fluxes over flatland or water can either be performed with micrometeorological equipment employing the eddy-covariance (EC) method (Baldocchi et al., 1988; Patel et al., 2019) or the accumulation chamber technique (Chiodini and Frondini, 2001; Elío et al., 2012). The EC method is best suited for flat and homogeneous terrain and stationary atmospheric conditions, rendering it difficult to apply at sites with complex orography or heavy vegetation (Baldocchi, 2003; Belcher et al., 2012; Scholz et al., 2021). While the accumulation chamber technique does not share these limitations, it is only applicable to measure gas microseepage with fluxes typically in the order of magnitude of 10 g m^{-2} d^{-1} (Klusman, 2011; Elío et al., 2012). Due to its design principle of collecting the gas of interest in a fixed volume, accumulation chambers are not usable to quantify strong advective fluxes which are often found at sites with natural CO_2 exhalations (Rogie et al., 2000; Lübben and Leven, 2018). Both of these systems are generally rather expensive and therefore usually only allow for very few simultaneous measurements at different locations. This is especially limiting at sites with significant naturally ocurring CO_2 emissions, which often feature highly localized and inhomogeneous gas exhalations (Rogie et al., 2000; Lübben and Leven, 2018). To quantify the horizontal and vertical distribution of the atmospheric gas concentration and its variability at these sites, a distributed collection of multiple sensors is necessary. Gas fluxes can then be deduced by approaches like the flux-gradient method (Zhao et al., 2019).

The Starzach site

Situated in the upper Neckar valley in southwestern Germany between the municipalities of Sulzau, Börstingen and Bierlingen, the Starzach site is a meadow of about two hectares in area which is known for its natural degassing of carbon dioxide. During the last century,

*Corresponding author: Yann Georg Büchau, Center for Applied Geoscience, University of Tübingen, Germany, e-mail: yann-georg.buechau@uni-tuebingen.de

DOI 10.1127/metz/2022/1125

Gebrüder Borntraeger Science Publishers, Stuttgart, www.borntraeger-cramer.com

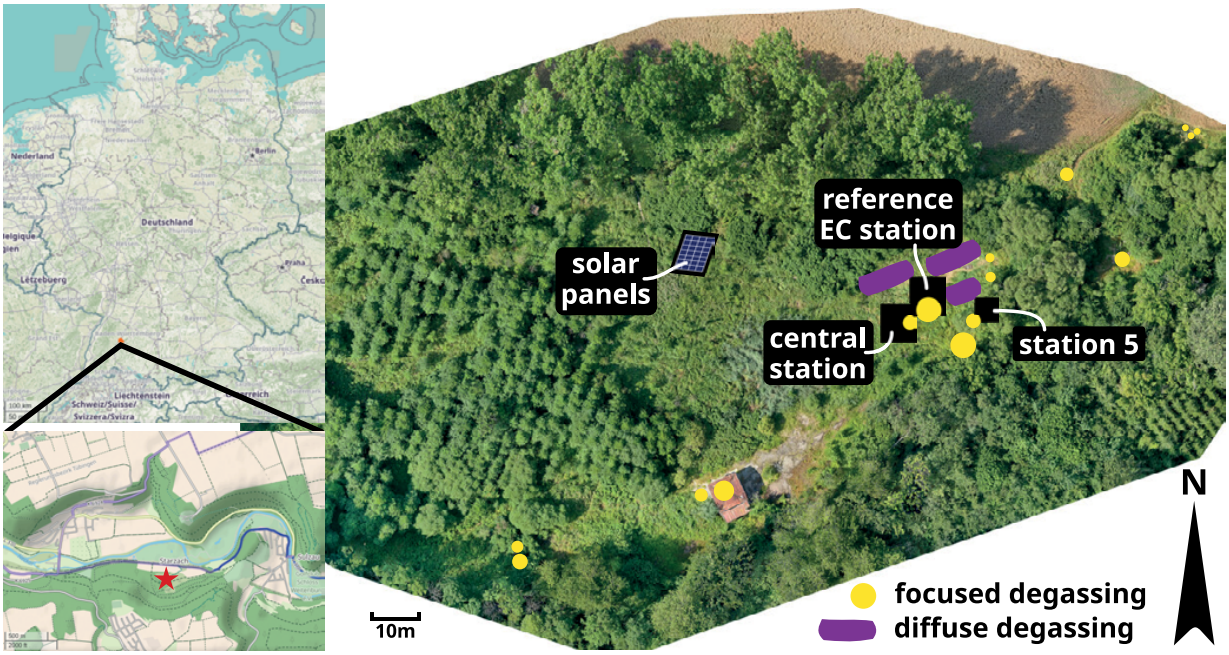

Figure 1: Aerial view of the Starzach site taken in summer 2019 by Martin Schön and map of Germany with part of the Neckar valley region as orientation. Visible focused CO_2 exhalation spots are marked as yellow dots, their size loosely indicating the apparent intensity. Fields of diffuse degassing are indicated as purple areas. Degassing spots appear in SW-NE direction across the site and are discussed by Lübben and Leven (2018) to be associated with a geological fault line. Map data © OpenStreetMap contributors (2021).

industrial CO_2 mining was performed in the broader region until yields eventually stagnated (Lübben and Leven, 2018). The site is bounded by the northern slope of the Neckar valley to the south and a row of tall trees to the north, separating it from cropland (Figure 1). Small trees, tall grass, shrub and reed are the most common types of vegetation on the meadow. Several relics of the industrial gas mining period including sheds, sealed CO_2 extraction wells and pipes can be found there. Interestingly, natural advective CO_2 exhalation spots, also commonly called *mofettes*, have continued to reappear at the site over the last years. Numerous mofettes of different sizes up to 30 cm in diameter are aligned in SW-NE direction across the site (Figure 1, Figure 2) and are discussed to be associated with a geological fault line (Lübben and Leven, 2018).

The site was intensively investigated recently (Schütze et al., 2015; Lübben and Leven, 2018) and small-diameter monitoring wells were run down some of these degassing locations to simplify access and measurements (Figure 2c). Lübben and Leven (2018) concluded that the predominant portion of the gas is probably of non-volcanic magmatic origin, rendering it a virtually inexhaustible source. They also estimated the CO_2 emission from one of the smaller mofettes on the site to 92 kg over the course of one day (Schütze et al., 2015) and introduced the Starzach site as a natural analog for leaking CCS sites. However, neither the total emission rate across the whole field nor the diurnal or seasonal variations of the CO_2 degassing on the site have been quantified yet.

The site's CO_2 gas exhalations can be categorized as either *diffuse* or *focused*. Except for irritation of the vegetation, *diffuse* exhalation is neither visible nor audible. Usually in spring, ongoing precipitation causes the site to be flooded for several weeks which uncovers the diffuse exhalations as streams of ascending gas bubbles (Figure 2a). Most *focused* degassing spots are covered permanently with water. The uprising gas thus has to overcome the hydrostatic pressure of the water column, resulting in repeated eruptions every few seconds (Figure 2c). Some focused degassing spots are dry however and generate a rather continuous audible hissing sound. Still, the gas is emitted at significant pressure, preventing the use of accumulation chambers. The site's heavy vegetation and orography also complicate the application of eddy-covariance method and footprint analysis.

Over the last years, cost-effective gas sensors are increasingly considered for scientific investigations. Research applications include assessments of their general suitability for scientific air quality measurements (Jiao et al., 2016; Martin et al., 2017; Spinelle et al., 2017), gas flux measurements in terrestrial or aquatic environments (Bastviken et al., 2015; Martinsen et al., 2018) and lately also the quantification of the indoor transmission risk for COVID-19 (Peng and Jimenez, 2021).

Building on this, we developed a low-cost wireless sensor network infrastructure for long-term monitoring

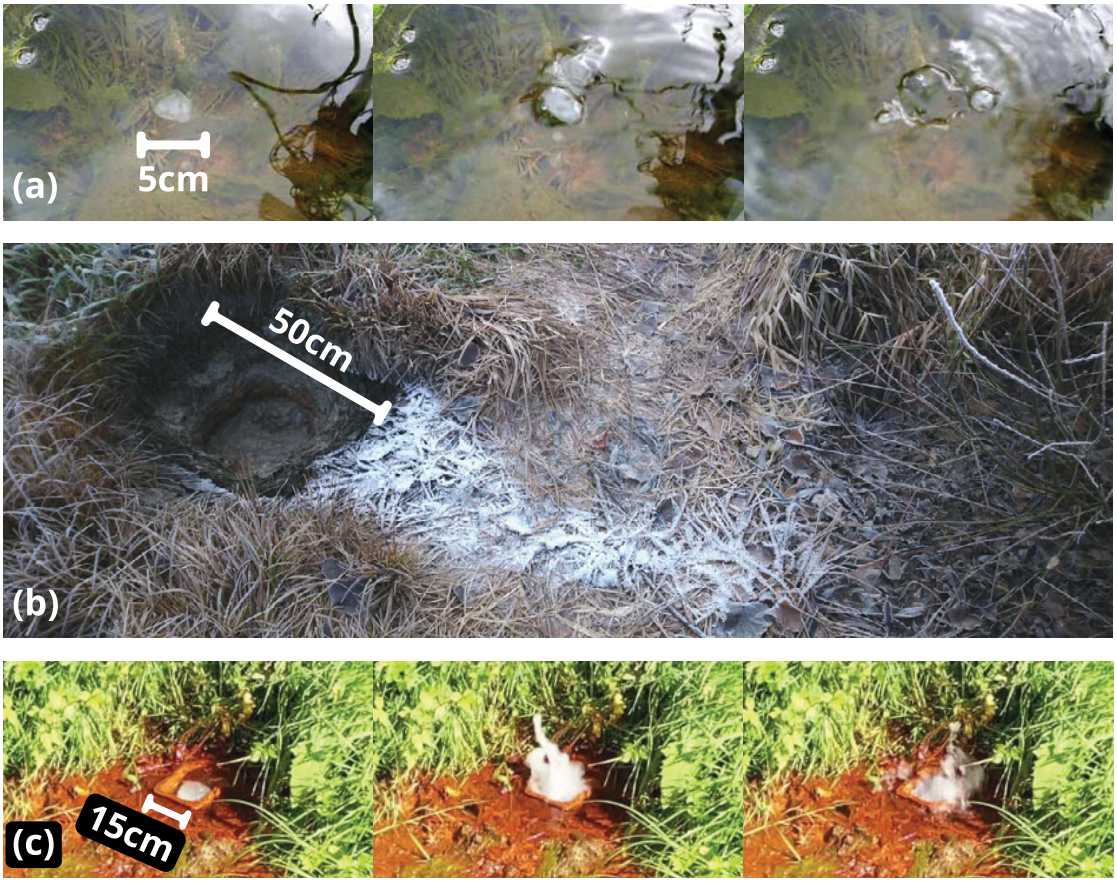

Figure 2: Selection of CO_2 exhalation spots at the Starzach site: (a) time-lapse of diffuse exhalation visible as a stream of ascending gas bubbles during spring 2020 when the site was flooded, (b) the site's largest mofette during winter 2019 with a line of icing indicating the exiting gas' path and (c) time-lapse of the focused degassing of the mofette with the largest pressure and exhalation velocity. This mofette developed several months after the installation of a ground-water monitoring well. Pictures in (c) taken in summer 2019 by Martin Schön.

of natural CO_2 emissions. The establishment of this network is part of an ongoing investigation to quantify the leakage of natural CO_2 at the Starzach site. This flexible infrastructure is based on open-source hard- and software components and capable of handling a wide variety of environmental sensors of both professional and cost-effective type. It operates self-sufficiently without a grid power-supply, can be maintained remotely and is able to withstand a wide range of weather conditions across all seasons. This versatility enables conducting various long-term atmospheric measurements related to gas emissions, of which we present the most vital one – continuously monitoring the atmospheric gas concentration – in the following.

2 Sensor network infrastructure

Besides self-sufficiency, our most important requirement for the sensor network infrastructure is having unrestricted *control over the data* aquisition, transport and storage. This enables implementing custom real-time calibrations, calculations and backups and most importantly a possibility for *live monitoring* of the measurements. Furthermore, *extension* by more or different sensors should be simple, while keeping the overall costs low. These specifications led to a design largely based on open source hard- and software components supplemented by own developments (Figure 3): A single-board computer acting as the central on-site entity establishes a wireless network for all network components to connect. Sensor stations consisting of a microcontroller and one or more sensors connect to this network to communicate wirelessly with each other and the central station. The central station is connected to the internet via the mobile phone network and maintains a permanent connection to an off-site server. This connection can be used in reverse to get remote maintenance access to the field equipment from off-site locations at any time. Relevant network traffic including data of the sensor stations is logged to a database on the central station and mirrored over the internet to the off-site server, where a redundant backup is made. Uploading a selection of low frequency data from the off-site server to the openSenseMap platform (Pfeil et al., 2015) then allows for live monitoring and presentation of the most vital measurements like CO_2 concentration and air temperature at the sensor stations as well as operational information like power sup-

Table 1: Summary of the sensor network infrastructure components.

Hardware	
sensor station microcontroller	Espressif Systems ESP8266
central station computer	Raspberry Pi 3 Model B+ single-board computer
off-site server computer	Raspberry Pi 4 Model B single-board computer
wireless transmission technique	2.4 GHz Wireless Local Area Network (WLAN)
sensor station local data storage	Secure Digital (SD) Memory Card
sensor station real-time clock (RTC)	Maxim Integrated DS3231
sensor station CO_2 sensor	Sensirion SCD30 non-dispersive infrared (NDIR) CO_2 sensor
sensor station temperature, humidity and pressure sensor	Bosch BME280
Software	
microcontroller software framework	Arduino Framework
network protocol	Message Queuing Telemetry Transport (MQTT)
MQTT broker implementation	mosquitto (Light, 2017)
tunneling between central station and server	Secure Shell (SSH)
sensor station time synchronzation	via RTC, network time protocol (NTP) or MQTT
database type	SQLite and compressed plain text

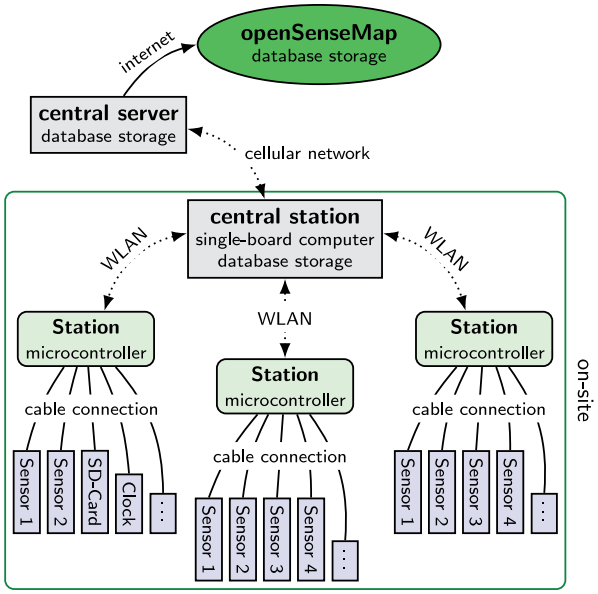

Figure 3: Network infrastructure schematic. An on-site single-board computer acts as a central station and establishes a Wireless Local Area Network (WLAN) to which all stations connect. Stations store their sensor data locally and transmit it wirelessly to the central station, where data is logged to a database. The central station maintains an internet connection to an off-site server to enable remote maintenance and live data monitoring. This server mirrors the on-site network traffic and relays a selection of the measurements to the openSenseMap platform for data display and live monitoring.

ply voltage. A summary of core hard- and software used in the network infrastructure is provided in Table 1.

2.1 Sensor stations

Each sensor station is controlled by a microcontroller in a waterproof enclosure which interfaces one or more sensors as well as other peripheral devices such as a real-time clock and a memory card. The real-time clock provides the time to the microcontroller in case the network connectivity is lost or the central station fails to provide the time. Measurement data of the sensor station is stored locally on the memory card. We designed and milled custom circuit boards to mount these peripherals and connect them to the microcontroller (Figure 4).

The atmospheric sensors used with the sensor stations (Table 1) rely on ventilation and ultimately on diffusion of ambient air into their sample chamber. Consequently, the sensors must be placed in free air. For protection from precipitation and solar irradiation, the outdoor sensors are mounted on a custom circuit board under a simple plastic shield which can be positioned independently from the microcontroller (Figure 4b and c). Additionally, to prevent corrosion from ambient humidity, sensitive electronics on the sensor boards were coated with MG Chemicals silicone modified conformal coating. The outdoor sensor circuit board is connected to the microcontroller via a patch cable with RJ45 connector as commonly used for Ethernet connections which we chose due to their extensive availability in different lengths, qualities and shapes.

The microcontrollers are programmed using the Arduino framework, which has proven to be useful in research and education (D'Ausilio, 2012; Kubínová and Šlégr, 2015). This greatly simplifies the quick inclusion of arbitrary new components and sensors into the network. We designed the firmware to allow for wireless updates. This implies that every station can be reprogrammed and -configured both with a direct cable connection to the microcontroller as well as remotely via the central station and by means of its permanent internet connection also from off-site locations.

2.2 CO_2 sensor

The two most common types of compact and low-cost CO_2 sensors are non-dispersive infrared (NDIR) sen-

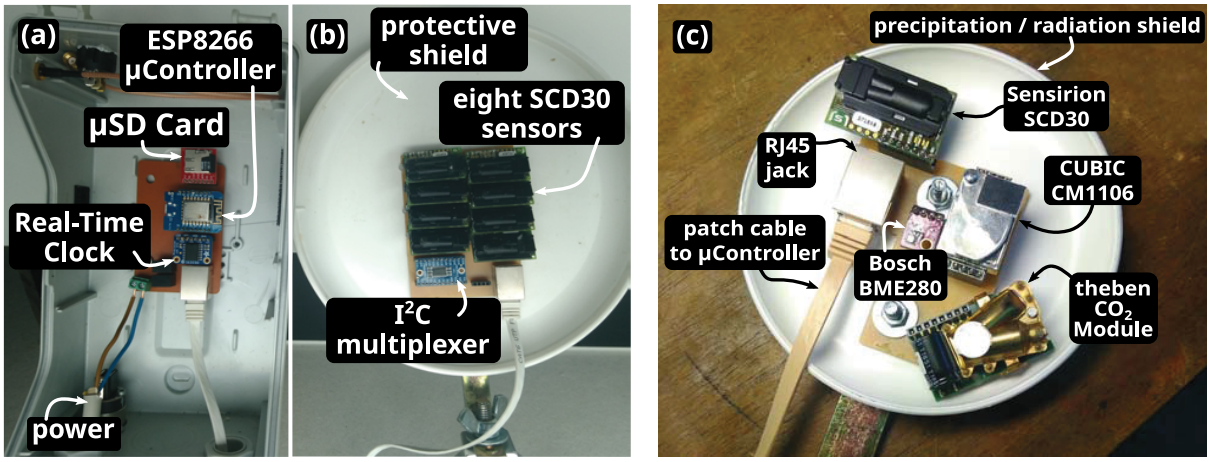

Figure 4: General design of a sensor station. (a) An ESP8266 microcontroller mounted on a custom circuit board in a weatherproof box is powered externally via a 12 V two-wire cable. (b) A custom circuit board capable of holding up to eight Sensirion SCD30 CO_2 sensors mounted below a simple radiation shield is connected to the microcontroller via a patch cable with RJ45 connector. (c) Radiation shield holding a custom multi-sensor circuit board with Sensirion SCD30 CO_2 sensor, Bosch BME280 environmental sensor (atmospheric pressure, temperature, relative humidity), CUBIC CM1106 CO_2 sensor and theben CO_2 Sensor Module.

sors and electrochemical sensors. Electrochemical sensors are available for a variety of gases and can reach parts-per-billion (ppb) precisions (Mead et al., 2013). Unfortunately, they typically suffer from strong dependence on environmental conditions (Mead et al., 2013), require a very high operating temperature and have response times in the magnitude of minutes (Struzik et al., 2018). Miniature NDIR sensors for CO_2 on the other hand have response times of seconds and parts-per-million (ppm) accuracy (Hodgkinson et al., 2013; Martin et al., 2017), which is still reasonable for our application.

We selected four different models of miniature, low-cost (i.e. price well below 100 € per unit) NDIR CO_2 sensors which have a rated accuracy within our requirement range of ±100 ppm ± 10 %: CUBIC CM1106, theben CO_2 sensor module, SenseAir LP8 and Sensirion SCD30 (Table 2). The sensors were evaluated in an EdgeTech RH CAL calibration chamber where various combinations of temperature, relative humidity and CO_2 concentration were generated. A LI-COR 840A closed-path infrared gas analyzer served as CO_2 reference which was previously zero and span calibrated using a gas mixing system at concentrations of 0 ppm, 400 ppm and 9800 ppm CO_2 in synthetic air. The results are discussed in Subsection 3.1.

2.3 Power

There is no usable power line within a reasonable radius of the Starzach site. To drive the equipment continuously with as little maintenance as possible, a self-sufficient powering approach is thus needed. An initial decentralized attempt with each individual sensor station having an own solar panel, charge controller and battery proved to be inefficient, expensive and too time-consuming to optimize and operate. This is a consequence of the site being located at a northern slope, which is suboptimal for a decentralized solar-powered approach due to low solar irradiation throughout the year, especially in winter. So for this specific site we compromised and opted for a centralized power supply instead: A collection of monocrystalline silicon solar panels (Figure 5) provides power to a solar charge controller charging a lead-acid deep-cycle 60 Ah 12 V battery to supply the entire field equipment, which requires 10 to 15 W of continuous baseline power. The bordering hillside to the south effectively blocks the site from direct sunlight for multiple hours during sunrise and sunset. This requires placing the solar panels as far to the north and away from the slope as possible, resulting in a supply power line of around 40 m length between battery and field equipment. This power line is the only physical connection between the field components, which communicate wirelessly with each other. During the winter months when the solar elevation is decreased dramatically and the battery capacity is reduced due to low temperatures, the energy yield of the photovoltaic panels is insufficient to power the field equipment continuously – despite their generous dimensioning. To overcome these difficulties, a methanol fuel cell is employed in addition, delivering uninterrupted power on demand in case the solar charge controller cannot charge the battery sufficiently. We expect that the fuel cell will not be necessary in other locations where there is less shading and therefore a usual amount of solar irradiation.

2.4 Central station

The central station is located near a hotspot of gas exhalations (Figure 1, Figure 6). It provides a Wireless

Table 2: Specifications of four miniature, low-cost NDIR CO_2 sensor models evaluated for application in our project.

	Sensirion SCD30	**SenseAir** LP8	**CUBIC** CM1106	**theben** CO2 Module
	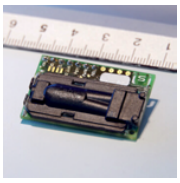	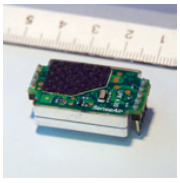	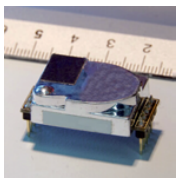	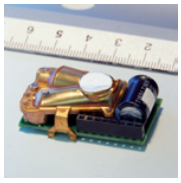
unit price at the time of writing		well below 100 €		
target CO_2 range [ppm]	400–10 000	0–10 000	0–2 000	0–5 000
output CO_2 range [ppm]	0–40 000	0–10 000	0–2 000	0–N.A.
accuracy (acc. to manufacturer)	±30 ppm ± 3 %, ±2.5 ppm/K	±50 ppm ± 3 %	±50 ppm ± 5 %	±50 ppm ± 3 %*
average power consumption	≈ 60 mW	≈ 1 mW	≈ 200 mW	≈ 30 mW
shortest output interval [s]	2 s	16 s	1 s	15 s
behaviour outside target CO_2 range	linear	–	–	non-linear
behaviour outside output CO_2 range	constant	constant	constant	non-linear
humidity cross-sensitivity	negligible	strong	negligible	negligible
temperature sensor	SHT31	onboard	onboard	onboard
humidity sensor	SHT31	–	–	–

* increases to up to ±100 ppm ± 5 % * for CO_2 concentrations above 2 000 ppm

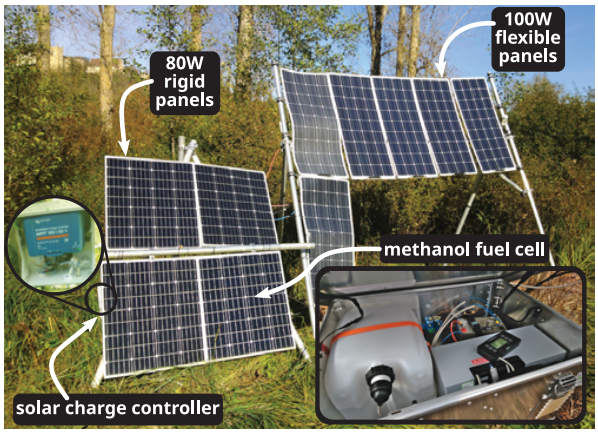

Figure 5: Setup providing power to the entire field equipment: A collection of monocrystalline solar panels mounted on a structure of aluminium rods charges a 60 Ah lead-acid battery via a solar charge controller. All field equipment is connected to this battery. If the battery voltage drops below a threshold, e.g. due to a lack of input from the solar charge controller, an EFOY Pro methanol fuel cell continues charging. An under-voltage switch protects the battery from discharging too deeply by electrically disconnecting all field equipment in case of total power failure.

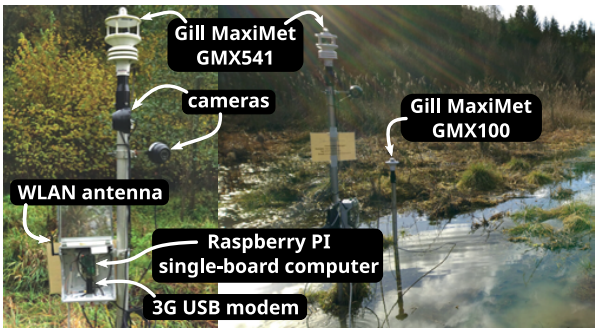

Figure 6: Close-up of the central station (left) and during spring 2020 when the site was flooded (right). A Raspberry Pi 3 Model B+ is equipped with a WLAN antenna and a 3G surfstick for networking, two outdoor cameras for site surveillance and a Gill MaxiMet GMX541 compact weather station with a GMX100 optical rain gauge.

Local Area Network (WLAN) for all sensor stations to connect. On-site tests yielded WLAN connectivity distances of well above 100 m across the field if at least one of the communicating devices is equipped with a 2.4 GHz antenna, which is the case for the central station. A customary modem and a SIM-card with a data flatrate plan connect the central station to the internet. A permanent internet connection to an off-site server is kept to facilitate remote maintenance of all field components as well as data retrieval from off-site locations.

The central station retrieves its clock time over the internet via the Network Time Protocol and regularly broadcasts it to the sensor stations via the network. As the central station is the main component of the network its availability is crucial. To make sure its internet connection is maintained continuously, the modem is connected via a software-switchable hub to enable power-cycling it in case of connection problems. A supercapacitor-based uninterruptible power supply buffers short power outages and provides enough time for a safe shutdown in case of complete power failure. Attached to the central station, a Gill MaxiMet GMX541 compact weather station together with periodic pictures of two surveillance cameras provide a continuous overview of the meterological situation.

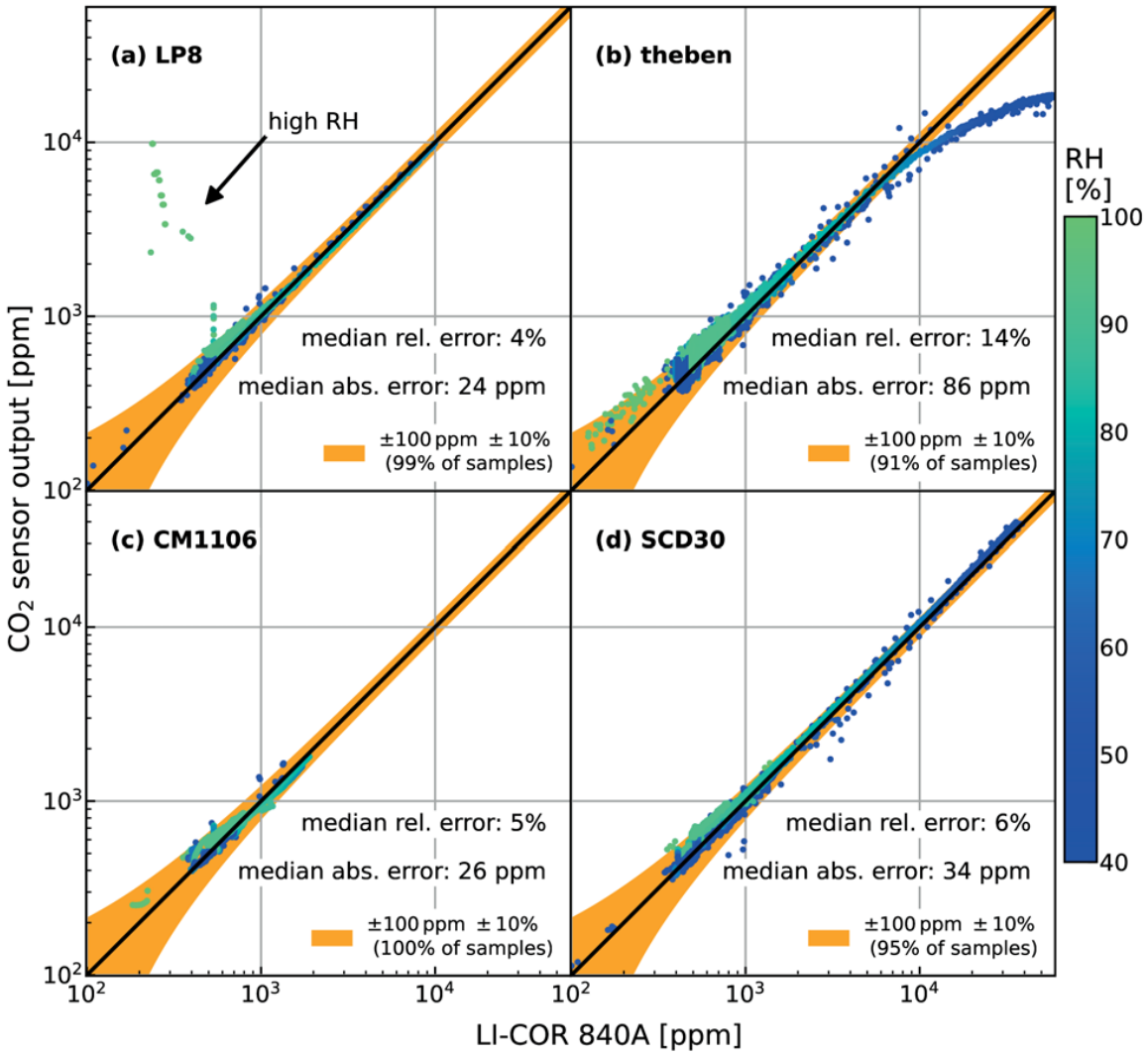

Figure 7: Comparison of four different low-cost miniature CO_2 sensor models considered for application in our project: (a) SenseAir LP8, (b) theben CO_2 Module, (c) Cubic CM1106 and (d) Sensirion SCD30 with median absolute and relative error compared to the LI-COR 840A closed-path gas analyzer reference according to Equation (3.1) and (3.1). The point colour indicates the relative humidity. Measurements were taken in an EdgeTech RH CAL calibration chamber where different combinations of temperature (10–43 °C) and relative humidity (8–100 %) were generated. Varying CO_2 concentrations were generated by manually injecting CO_2 from a gas bottle into the calibration chamber. Obvious outliers attributable to the experimental design have been removed.

3 Results and discussion

3.1 CO_2 sensor lab performance

The results of the comparison between the four tested CO_2 sensor models in the calibration chamber (Figure 7 and 8) reveal that all sensors exhibit a median absolute error (MAE) less than 100 ppm and a median relative error (MRE) mostly below 10 % to the LI-COR 840A gas analyzer across various temperature and relative humidity conditions. MAE and MRE are defined as:

$$\mathrm{MAE} = \mathrm{median}\left(|\mathrm{CO_2} - \mathrm{CO_{2\,ref}}|\right) \tag{3.1}$$

$$\mathrm{MRE} = \mathrm{median}\left(\left|\frac{\mathrm{CO_2} - \mathrm{CO_{2\,ref}}}{\mathrm{CO_{2\,ref}}}\right|\right) \tag{3.2}$$

The median is preferred over the arithmetic mean here to prevent individual outliers from distorting the average. These accuracies largely match our requirement range of ±100 ppm and ±10 %.

All sensor models have different characteristics: With a median absolute error of 24 ppm and a median relative error of 4 %, the SenseAir sensor exhibits the highest precision of the four. It also has by far the the lowest power consumption. But it has a rather low upper out-

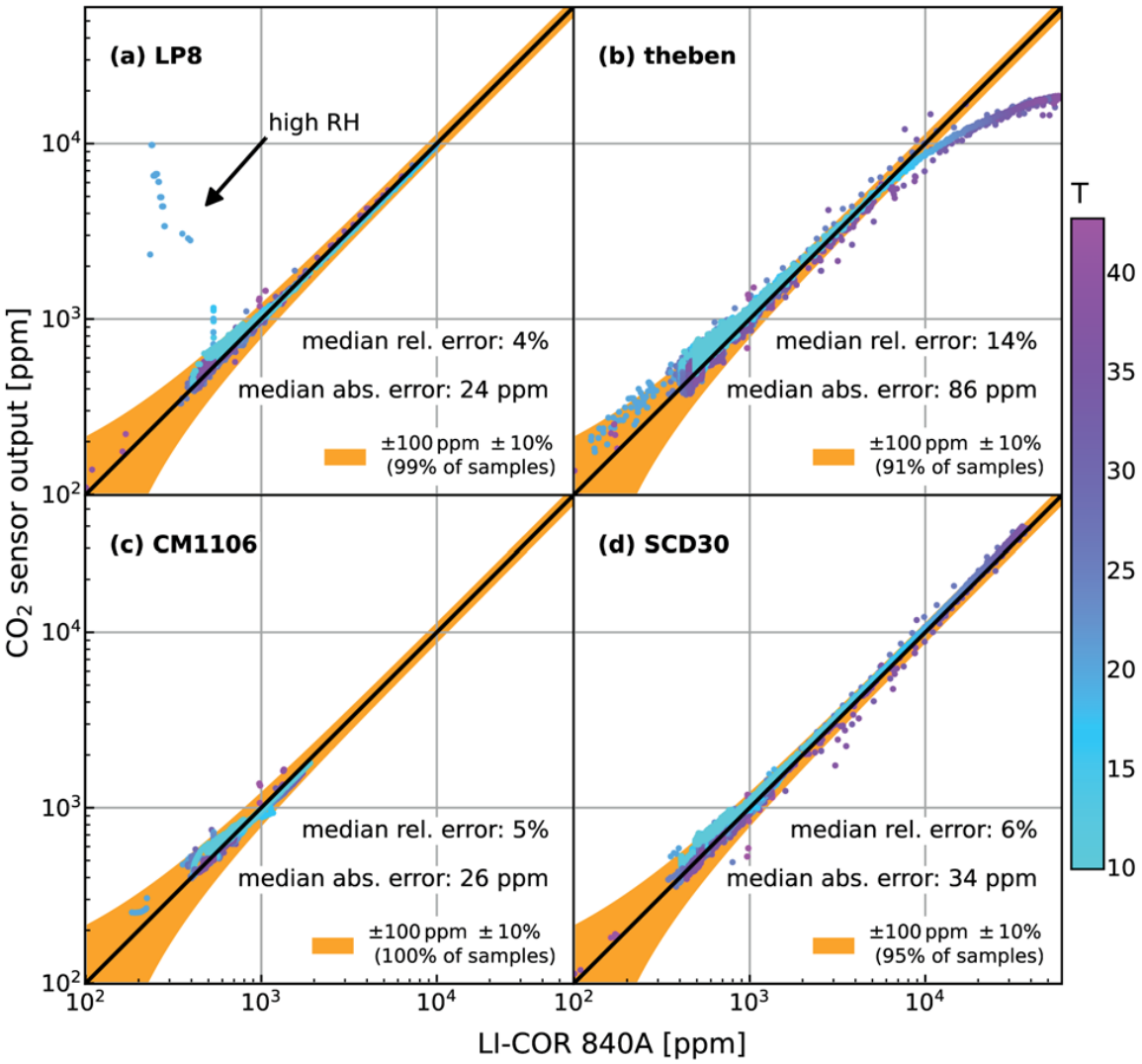

Figure 8: Comparison of four different low-cost miniature CO_2 sensor models considered for application in our project under the same conditions as in Figure 7 but with the point colour indicating the *temperature* instead of relative humdity.

put limit of 10 000 ppm and a strong cross-sensitivity on water vapour at elevated relative humidity levels. Since highly increased levels of relative humidity can be expected at outdoor sites and especially at night, this renders the SenseAir sensor inappropriate for our use case. The theben sensor module covers the largest range of CO_2 concentration of all four sensor models. But its response becomes nonlinear above CO_2 concentrations of around 10 000 ppm, requiring an empirical correction in post-processing. The CUBIC sensor is as accurate as the SenseAir sensor with a median absolute error below 30 ppm and a median relative error of only 5 %. It is the only sensor of which 100 % of samples lie within our required accuracy range of ±100 ppm and ±10 % and also the only sensor which is already coated for outdoor application. But its upper measurement limit of 2 000 ppm is very low. This renders it inappropriate for measurements close to the surface or in direct proximity to a strong source of CO_2 where atmospheric CO_2 concentrations can easily exceed this limit (Schütze et al., 2015; Lübben and Leven, 2018). The Sensirion sensor performs consistently well from 0 to 20 000 ppm, which is the specified measurement range of the reference LI-COR 840A according to the manufacturer. However, even beyond this threshold the Sensirion sensor agrees very well with the reference up to its own output limit of 40 000 ppm with 95 % of all samples falling within our requirement range of ±100 ppm and ±10 %. Since the Sensirion SCD30 sensor also has a built-in SHT31 temperature and humidity sensor we concluded that it meets our requirements best and continued using it in favor of the other sensors.

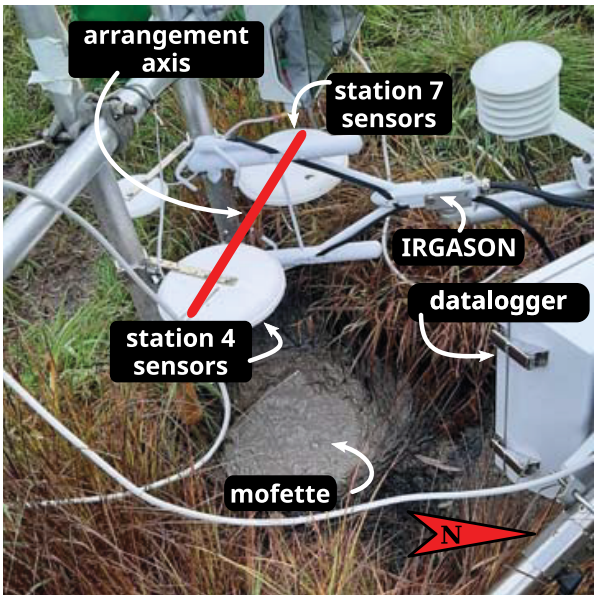

Figure 9: Reference eddy-covariance station (Campbell Scientific IRGASON, CR6 datalogger) with the sensors of station 4 and station 7 arranged alongside over the site's largest mofette. Background picture taken by Mosaab Sajidi.

3.2 CO_2 sensor field performance

Having determined the Sensirion SCD30 sensor as suitable CO_2 sensor under laboratory conditions as discussed above, we tested a collection of SCD30 sensors under field conditions at the Starzach site. Two sensor stations, hereafter called station 4 and station 7, were each equipped with eight SCD30 sensors on a circuit board as shown in Figure 4b. The sensor shields were arranged on either side of the measurement volume of an eddy-covariance station, 50 cm above the site's largest mofette (Figure 9). The eddy-covariance station is connected to the central station via WLAN, enabling live data monitoring and download similar to the sensor stations in the network. One month of data was obtained in this setup. Measurements of station 4 and 7 have a temporal resolution of 10 s, the eddy-covariance station data was logged with 10 Hz resolution.

Due to a connection problem on the circuit board, the data of three sensors of station 4 couldn't be recorded. Two further sensors yielded mostly unusable values, leaving station 4 with data of three sensors. As only sensors of station 4 are affected by this and all eight sensors of station 7 worked fine, we suspect issues with the circuit board of station 4 to be the cause, not the sensors themselves.

Positioning the sensors over a strong source of CO_2 is necessary to obtain measurements over a large range of CO_2 concentrations, but introduces inhomogeneous conditions across the sensors in case of advection along their horizontal arrangement axis (Figure 9). The upwards gas transport and thus which sensor picks up the majority of a particular burst of gas from the mofette depends heavily on the local wind field around the setup. To address this, only wind directions perpendicular to the arrangement axis are considered for the comparison of SCD30 sensor data and eddy-covariance station measurements.

The results show a good in-field agreement between SCD30 sensor measurements and the eddy-covariance station data in its calibrated range up to 3000 ppm when median-averaged to 10-minute intervals (Figure 10 and 11). Only considering wind directions perpendicular to the sensors' horizontal arrangement axis reduces the inhomogeneities across the sensors, but only to a degree. The mofette erupts gas at irregular intervals every few seconds, causing an inhomogeneous distribution of CO_2 in the atmosphere near the surface. The increased scattering of the SCD30 sensor measurements at elevated CO_2 concentrations is thus likely caused mostly by said inhomogeneities in the atmospheric CO_2 concentration above the mofette and not exclusively due to sensor imprecisions.

Considering the challenging outdoor conditions (very humid air at night, dew formation on the sensors, flooding as shown in Figure 6, dirty water droplets ejected from the mofette below, insects nesting, etc.), the field performance of the SCD30 sensor is well in line with the performance under laboratory conditions shown in Figure 7 and 8 and within our requirement range of ±100 ppm and ±10 %. The agreement of each *individual* SCD30 sensor with the eddy-covariance station deviates only marginally from the per-station average, indicating that single-sensor stations are viable (Figure 10 and 11). Based on this and the consistent behaviour of the SCD30 sensor in a controlled environment (Figure 7 and 8), we assume that it performs equally precise in its entire measurement range up to 40 000 ppm under field conditions as well.

3.3 Diurnal Cycle at the Starzach Site

From April to October 2020, one station, hereafter called station 5, was positioned roughly 50 cm above ground next to a dry mofette close to the central station (Figure 1, Figure 12). Station 5 was equipped with one SCD30 CO_2 sensor which had previously been offset-calibrated at fresh air using a LI-COR 840A closed-path infrared gas analyzer. Except for a ten-day period in July 2020 where no data is available, station 5 delivered uninterrupted data at 10 s intervals more than 90 % of the time. Reasons for data gaps were mostly power supply problems and maintenance interruptions of the network.

The CO_2 concentration at station 5 (Figure 13) shows a clear diurnal cycle with variations across the sensor's entire measurment range up to 40 000 ppm (4 vol.%). It can be assumed that the real maximum concentration exceeded this range as the gas emitted from the mofettes is almost 100 vol.% CO_2 (Schütze et al., 2015; Lübben and Leven, 2018). During the day, moderatly increased CO_2 concentrations up to 5000 ppm prevail, while at night the concentrations are highly elevated and hit the

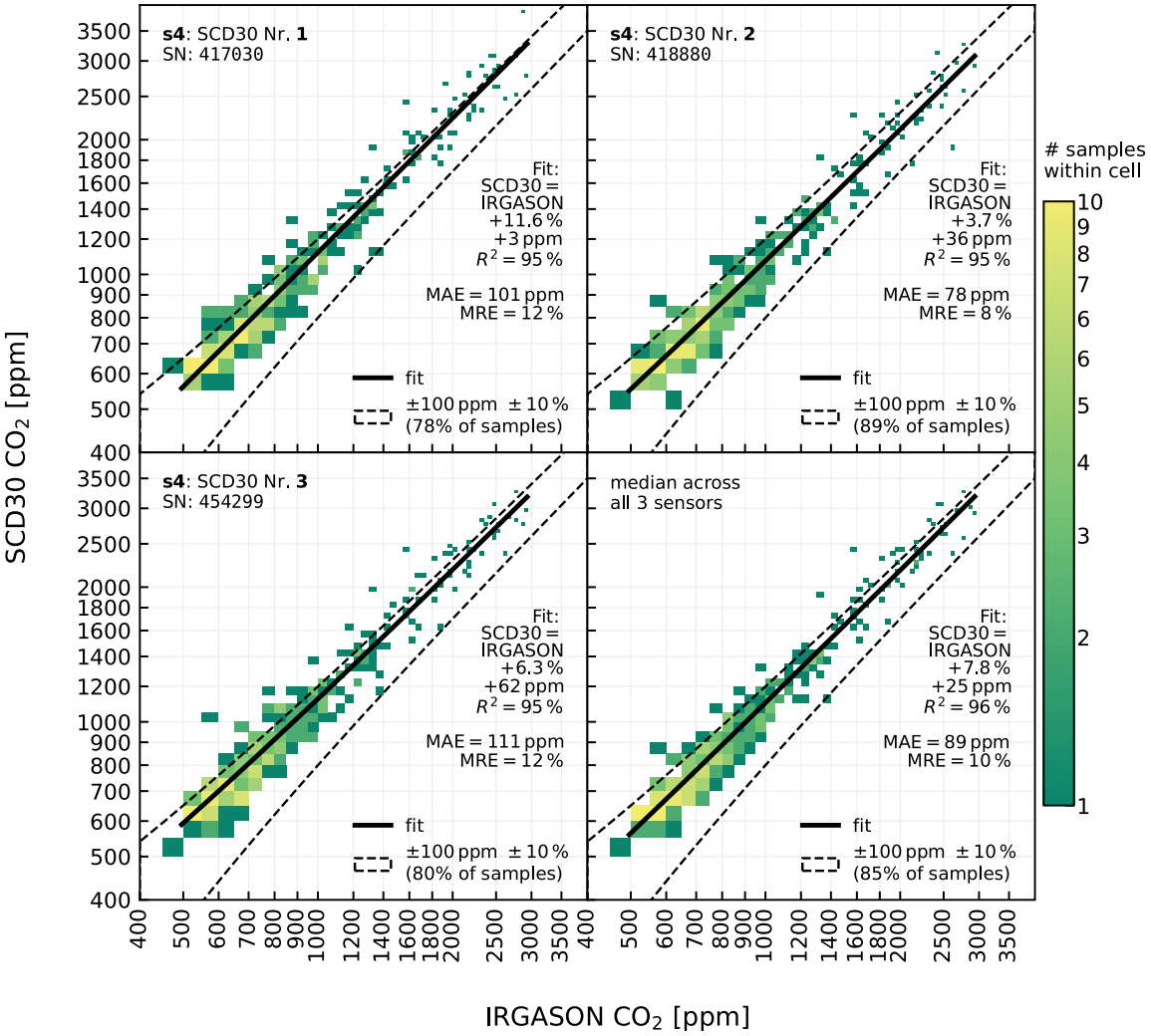

Figure 10: Comparison of CO_2 measurements from 15 September to 15 October 2020 of station 4 (s4) with the eddy-covariance station in the setup shown in Figure 9 over the site's largest mofette. For each individual sensor, the measurements were resampled into 10-minute averages, using the median for measurements of station 4 to account for temporal outliers and the arithmetic mean for the eddy-covariance station data. The data was filtered to only include situations with wind directions to and from 175° ±10°, i.e. perpendicular to the horizontal arrangement axis of the sensors to reduce the influence of sideways CO_2 advection from the mofette below. The median absolute error (MAE) and median relative error (MRE) indicate the average error between measurements of the sensor stations and the eddy-covariance station according to Equation (3.1) and (3.1).

Table 3: Correlation coefficient r of meteorological parameters with diurnal CO_2 concentration at station 5 (Figure 13).

	01 Jun–31 Aug 2020	15 Sep–15 Oct 2020
$r_{\overline{CO_2},\overline{v}}$	−0.79	−0.86
$r_{\overline{CO_2},\overline{T}}$	−0.69	−0.81
$r_{\overline{CO_2},\overline{R}}$	−0.74	−0.84

sensor's upper output limit of 40 000 ppm. Wind speed, temperature and global short-wave radiation exhibit a strong negative correlation r to the average CO_2 concentration (Table 3).

The deviation between night and daytime can be explained by the different atmospheric boundary layer regimes. At night energy is lost to the atmosphere. This results in cooling of the lower air masses and the development of a stable boundary layer that suppresses turbulence and prevents vertical mixing (Stull, 1988), impeding the upwards transport and removal of near-surface CO_2 emitted from the natural sources at the site. Wind speeds close to the surface are typically low, because the surface roughness generates friction and obstructs the flow, further favouring an accumulation of CO_2 near the ground which explains the highly elevated atmospheric CO_2 concentrations at night.

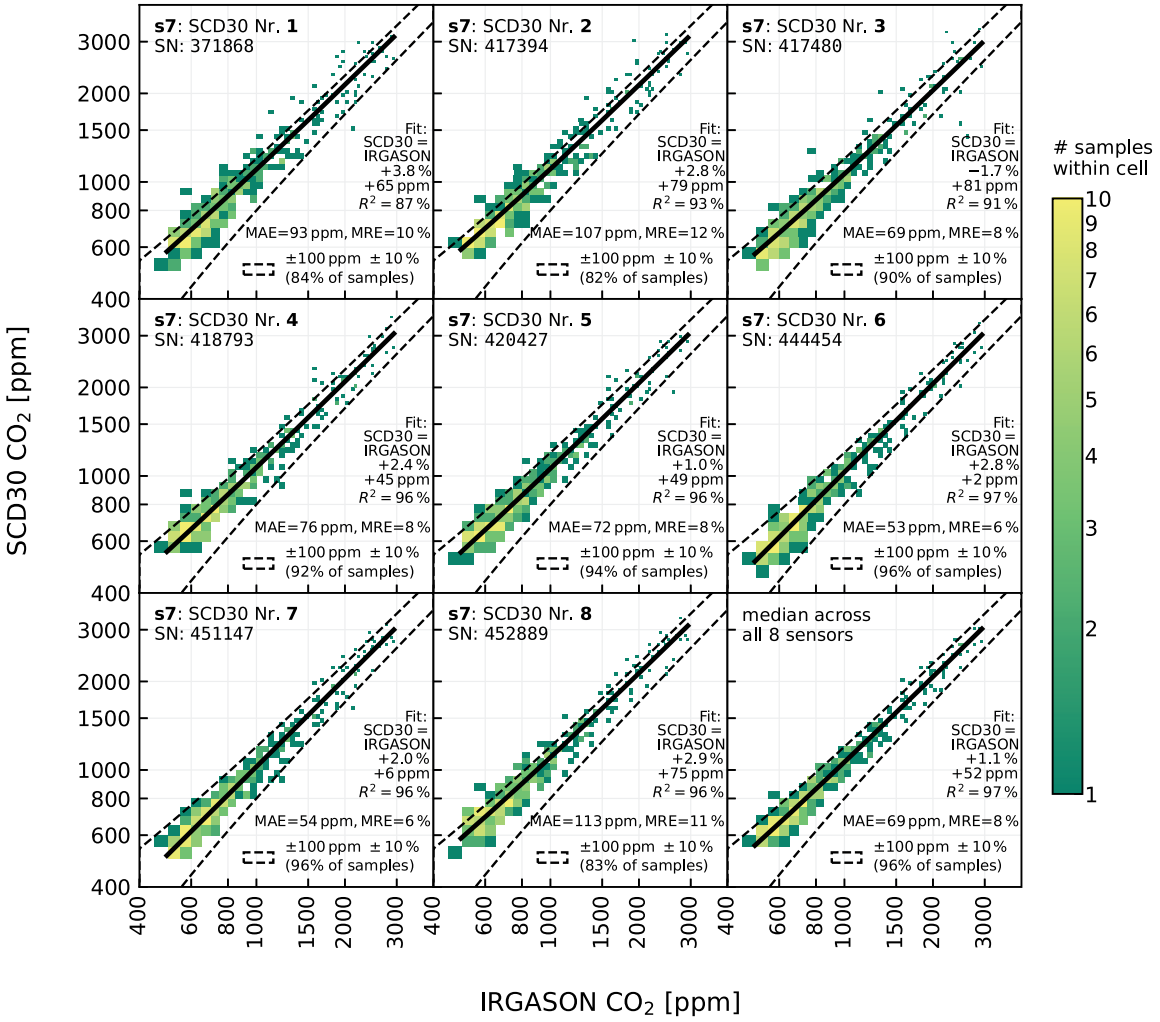

Figure 11: Comparison of CO_2 measurements of station 7 (s7) with the eddy-covariance station in the setup shown in Figure 9. Data was processed similarly to station 4 as described in Figure 10.

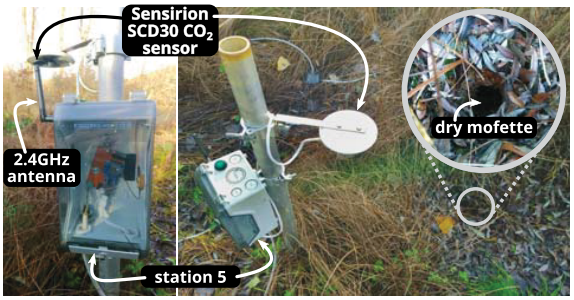

Figure 12: Station 5 equipped with one Sensirion SCD30 CO_2 sensor and located near a dry mofette. The on-site positioning is indicated in Figure 1. Measurements of station 5 are shown in Figure 13.

At dawn, the incoming solar irradiation increases rapidly so that an energy excess occurs at the surface. The air is heated again, resulting in a raising temperature and the onset of vertical mixing due to buoyancy. The wind speed increases, because air parcels with high momentum from aloft are mixed with air parcels with low momentum at the surface. Parallel with momentum and heat, CO_2 is transported rapidly upwards in the convective, unstable boundary layer and the accumulated CO_2 concentration diminishes. Additionally, sunlight allows the plant physiological process that is photosynthesis to become active, which typically depletes CO_2 at a rate in the order of magitude of 0.1–1 mg m^{-2} s^{-1} (Van Kesteren et al., 2013; Schrier-Uijl et al., 2010; Patel et al., 2011), contributing to the decrease in atmospheric CO_2 concentration. However, compared to the emission rate of a single mofette of around 1 g s^{-1} (Schütze et al., 2015) which is orders of magnitude

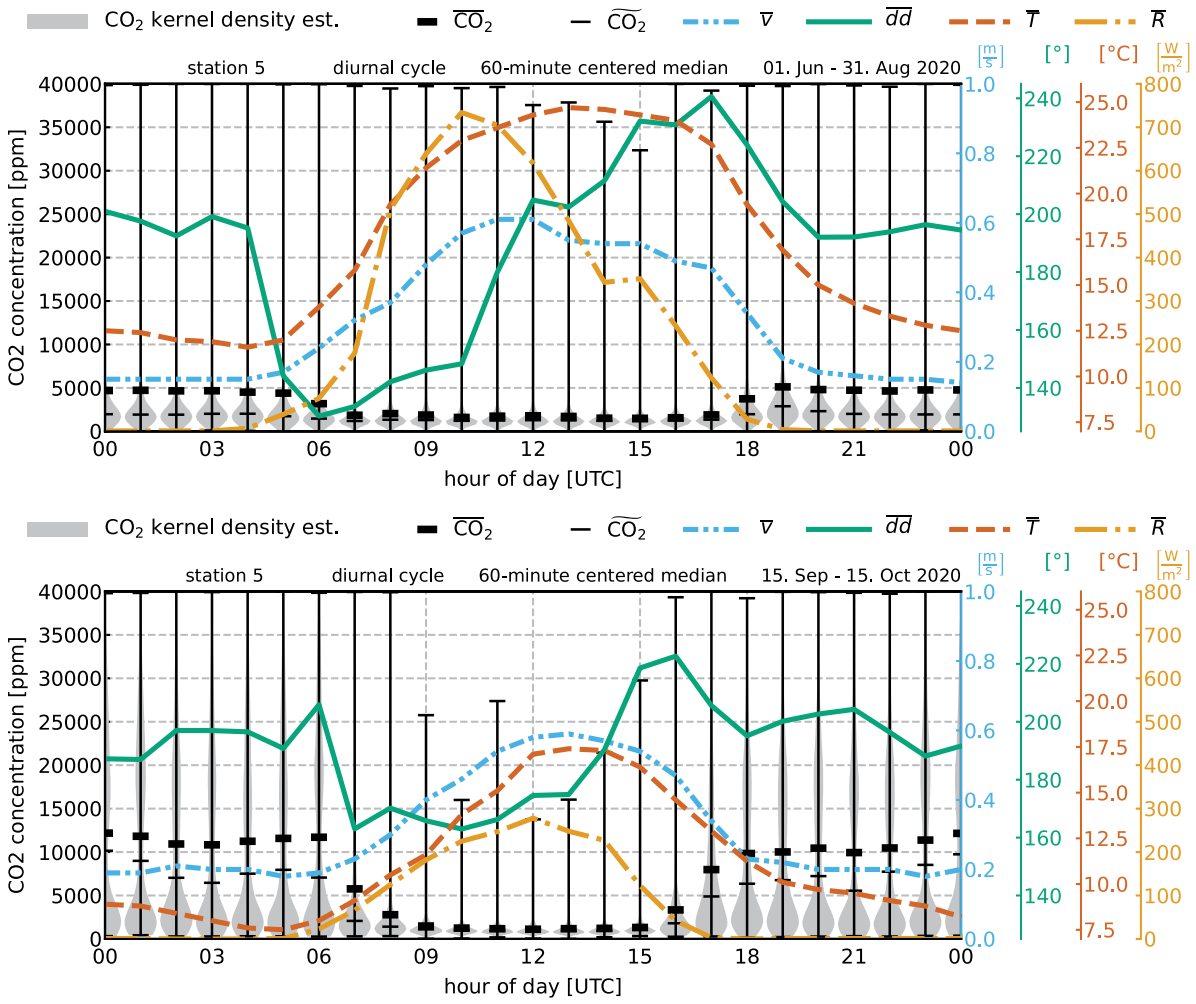

Figure 13: Average diurnal cycle at the Starzach site during summer from June to August 2020 (top) and during the comparison period (same as for Figure 10 and Figure 11) from mid of September to mid of October 2020 (bottom). In the background, a violin plot (Hintze and Nelson, 1998) of the diurnal CO_2 concentration at station 5 (Figure 12) is displayed with the grey areas representing the distribution, the thin black lines indicating the median and the bold line the arithmetic mean. The meteorological parameters wind speed $\overline{v}$, wind vector direction $\overline{dd}$, temperature $\overline{T}$ and global incoming short-wave radiation $\overline{R}$ were measured by a Gill MaxiMet GMX541 compact weather station at the central station in two meters height above ground (Figure 6). Obvious outliers were removed. Measurements were aggregated to 60-minute intervals of a day for averaging.

larger and considering station 5 is located in close proximity to a mofette, the CO_2 depletion by photosynthesis presumably plays a minor role in the atmospheric CO_2 budget at station 5. These processes continue until in the afternoon the global incoming radiation decreases and the available energy input at the surface becomes zero just after sunset. Now the processes of the stable boundary layer start over again.

Wind speeds at the Starzach site are generally low with a 30-minute median well below 1 m s^{-1} (Figure 13) and correlate with the air temperature and the incoming solar radiation as explained above. Still, the observations show a distinct diurnal pattern of the wind direction which could be caused by an orographically induced wind oscillation: At night, low southern winds prevail consistently as katabatic winds flow down the bordering slope to the south of the site (Stull, 1988). An overview of the site's complex terrain is provided in Figure 1. At dawn, the wind direction abruptly changes to south-south-east, gradually turning to south-south-west over the day. A possible explanation for this could be that the opposite southern slope of the Neckar valley is heated up by the sun which induces northwards air mass movement into that direction, following the upslope anabatic winds. Due to its jigsaw shape, different parts of the southern slope are heated over the course of the day.

This could explain why the direction of this air mass movement tracks the direction of the sun rays hitting the southern slope.

4 Conclusions and outlook

We developed and introduced an autarkic, flexible wireless sensor network infrastructure suitable for densely monitoring the atmospheric CO_2 concentration without grid power access. The network was tested at the Starzach site in southwestern Germany, a site with naturally occurring CO_2 emissions and proved to work reliably under challenging environmental conditions such as high relative humidity and limited solar radiation. Four different models of low-cost CO_2 sensors were evaluated under laboratory conditions for precision and cross-sensitivity on humidity and temperature, of which the Sensirion SCD30 sensor performed best. It was shown that the Sensirion SCD30 CO_2 sensor is capable of picturing the diurnal variations in atmospheric CO_2 concentration under outdoor conditions reliably to a reasonable accuracy. Under calm and stable conditions, e.g. at night, the near-surface atmospheric CO_2 concentration at the Starzach site increases drastically, especially around mofettes, up to 40 000 ppm – a concentration two orders of magnitude larger than usual in the lower atmosphere which averages at about 400 ppm. The wireless and autarkic sensor network design allows for easy application at various remote locations, including monitoring of carbon capture and storage (CCS) sites or could easily be adapted for other trace gas measurements such as nitrogen oxide or methane. This network lays the foundation for further research at the site in order to quantify the total emission of CO_2. Future research at the site will include horizontal and vertical profiles of atmospheric CO_2 concentration and meteorological parameters to quantify the accumulation of CO_2 in more detail in relation to atmospheric stability. Furthermore, vertical profiles of CO_2 in conjunction with the reference eddy-covariance station will facilitate the application of the flux-gradient method to deduce CO_2 fluxes.

Acknowledgments

This work was supported by the German Research Foundation (DFG) under grant number BA 1988/19-1. The equipment was largely financed by the Alfred-Teufel Foundation. We would like to thank Max-Richard Freiherr von Rassler for the field access and the good cooperation and Carsten Leven for his support with the site. We would also like to thank the workgroup of Prof. Weimar at the Institute of Physical and Theoretical Chemistry at the University of Tübingen and especially André Sackmann for providing us access to their gas sensor calibration equipment to calibrate our own reference devices. Further thanks to Martin Schön for taking the aerial pictures of the site and especially Björn Riebandt for assistance with field work and calibration experiments. We also thank the two anonymous reviewers for their suggestions to improve the manuscript. Finally, we acknowledge support by the Open Access Publishing Fund of the University of Tübingen.

References

Anderson, T.R., E. Hawkins, P.D. Jones, 2016: CO_2, the greenhouse effect and global warming: from the pioneering work of Arrhenius and Callendar to today's Earth System Models. – Endeavour **40**, 178–187, DOI: 10.1016/j.endeavour.2016.07.002.

Baldocchi, D., 2003: Assessing the eddy covariance technique for evaluating carbon dioxide exchange rates of ecosystems: past, present and future. – Glob. Change Biol. **9**, 479–492, DOI: 10.1046/j.1365-2486.2003.00629.x.

Baldocchi, D.D., B.B. Hincks, T.P. Meyers, 1988: Measuring biosphere-atmosphere exchanges of biologically related gases with micrometeorological methods. – Ecology **69**, 1331–1340, DOI: 10.2307/1941631.

Bastviken, D., I. Sundgren, S. Natchimuthu, H. Reyier, M. Gålfalk, 2015: Technical note: Cost-efficient approaches to measure carbon dioxide (CO_2) fluxes and concentrations in terrestrial and aquatic environments using mini loggers. – Biogeosci. **12**, 3849–3859, DOI: 10.5194/bg-12-3849-2015.

Battani, A., E. Deville, J.L. Faure, E. Jeandel, S. Noirez, E. Tocqué, Y. Benoît, J. Schmitz, D. Parlouar, P. Sarda, F. Gal, K. Le Pierres, M. Brach, G. Braibant, C. Beny, Z. Pokryszka, A. Charmoille, G. Bentivegna, J. Pironon, P. de Donato, C. Garnier, C. Cailteau, O. Barrès, G. Radilla, A. Bauer, 2010: Geochemical study of natural CO_2 emissions in the French Massif Central: How to predict origin, processes and evolution of CO_2 leakage. – Oil Gas Sci. Technol. **65**, 615–633, DOI: 10.2516/ogst/2009052.

Beaubien, S., G. Ciotoli, S. Lombardi, 2003: Carbon dioxide and radon gas hazard in the Alban Hills area (central Italy). – J. Volcanol. Geoth. Res. **123**, 63–80, DOI: 10.1016/S0377-0273(03)00028-3.

Belcher, S.E., I.N. Harman, J.J. Finnigan, 2012: The wind in the willows: Flows in forest canopies in complex terrain. – Annu. Rev. Fluid Mech. **44**, 479–504, DOI: 10.1146/annurev-fluid-120710-101036.

Burnside, N.M., Z.K. Shipton, B. Dockrill, R.M. Ellam, 2013: Man-made versus natural CO_2 leakage: A 400 k.y. history of an analogue for engineered geological storage of CO_2. – Geology **41**, 471–474, DOI: 10.1130/G33738.1.

Chiodini, G., F. Frondini, 2001: Carbon dioxide degassing from the Albani Hills volcanic region, Central Italy. – Chem. Geol. **177**, 67–83, DOI: 10.1016/S0009-2541(00)00382-X.

Cook, J., N. Oreskes, P.T. Doran, W.R.L. Anderegg, B. Verheggen, E.W. Maibach, J.S. Carlton, S. Lewandowsky, A.G. Skuce, S.A. Green, D. Nuccitelli, P. Jacobs, M. Richardson, B. Winkler, R. Painting, K. Rice, 2016: Consensus on consensus: a synthesis of consensus estimates on human-caused global warming. – Env. Res. Lett. **11**, DOI: 10.1088/1748-9326/11/4/048002.

D'Ausilio, A., 2012: Arduino: A low-cost multipurpose lab equipment. – Behav. Res. **44**, 305–313, DOI: 10.3758/s13428-011-0163-z.

Elío, J., M.F. Ortega, E. Chacón, L.F. Mazadiego, F. Grandia, 2012: Sampling strategies using the "accumulation chamber" for monitoring geological storage of CO_2. – Int. J. Greenh. Gas Con. **9**, 303–311, DOI: 10.1016/j.ijggc.2012.04.006.

Forster, P., V. Ramaswamy, P. Artaxo, T. Berntsen, R. Betts, D.W. Fahey, J. Haywood, J. Lean, D.C. Lowe, G. Myhre, J. Nganga, R. Prinn, G. Raga, M. Schulz, R. Van Dorland, 2007: Changes in atmospheric constituents and in radiative forcing. – In: S. Salomon, D. Qin, M. Manning, Z. Chen, M. Marquis, K.B. Averyt, M. Tignor, and H.L. Miller (Eds.), Climate Change 2007: The Physical Science Basis. Contribution of Working Group I to the Fourth Assessment Report of the Intergovernmental Panel on Climate Change, Cambridge University Press, chapter 2, 129–234.

Hansen, J., D. Johnson, A. Lacis, S. Lebedeff, P. Lee, D. Rind, G. Russell, 1981: Climate impact of increasing atmospheric carbon dioxide. – Science **213**, 957–966, DOI: 10.1126/science.213.4511.957.

Hintze, J., R. Nelson, 1998: Violin plots: A box plot-density trace synergism. – Am. Stat. **52**, 181–184, DOI: 10.2307/2685478.

Hodgkinson, J., R. Smith, W.O. Ho, J.R. Saffell, R.P. Tatam, 2013: Non-dispersive infra-red (NDIR) measurement of carbon dioxide at 4.2 μm in a compact and optically efficient sensor. – Sensor. Actuat. B: Chem. **186**, 580–588, DOI: 10.1016/j.snb.2013.06.006.

Jiao, W., G. Hagler, R. Williams, R. Sharpe, R. Brown, D. Garver, R. Judge, M. Caudill, J. Rickard, M. Davis, L. Weinstock, S. Zimmer-Dauphinee, K. Buckley, 2016: Community Air Sensor Network (CAIRSENSE) project: evaluation of low-cost sensor performance in a suburban environment in the Southeastern United States. – Atmos. Meas. Tech. **9**, 5281–5292, DOI: 10.5194/amt-9-5281-2016.

Kerrick, D.M., 2001: Present and past nonanthropogenic CO_2 degassing from the solid earth. – Rev. Geophys. **39**, 565–585, DOI: 10.1029/2001RG000105.

Klusman, R.W., 2011: Comparison of surface and near-surface geochemical methods for detection of gas microseepage from carbon dioxide sequestration. – Int. J. Greenh. Gas Con. **5**, 1369–1392, DOI: 10.1016/j.ijggc.2011.07.014.

Kubínová, Š., J. Šlégr, 2015: ChemDuino: Adapting Arduino for low-cost chemical measurements in lecture and laboratory. – J. Chem. Educ. **92**, 1751–1753, DOI: 10.1021/ed5008102.

Lewicki, J.L., J. Birkholzer, C.F. Tsang, 2007: Natural and industrial analogues for leakage of CO_2 from storage reservoirs: identification of features, events, and processes and lessons learned. – Env. Geol. **52**, 457–467, DOI: 10.1007/s00254-006-0479-7.

Light, R.A., 2017: Mosquitto: server and client implementation of the MQTT protocol. – J. Open Src. Soft. **2**, 265, DOI: 10.21105/joss.00265.

Lübben, A., C. Leven, 2018: The Starzach site in Southern Germany: a site with naturally occurring CO_2 emissions recovering from century-long gas mining as a natural analog for a leaking CCS reservoir. – Env. Earth Sci. **77**, DOI: 10.1007/s12665-018-7499-y.

Martin, C.R., N. Zeng, A. Karion, R.R. Dickerson, X. Ren, B.N. Turpie, K.J. Weber, 2017: Evaluation and environmental correction of ambient CO_2 measurements from a low-cost NDIR sensor. – Atmos. Meas. Tech. **10**, 2383–2395, DOI: 10.5194/amt-10-2383-2017.

Martinsen, K.T., T. Kragh, K. Sand-Jensen, 2018: Technical note: A simple and cost-efficient automated floating chamber for continuous measurements of carbon dioxide gas flux on lakes. – Biogeosci. **15**, 5565–5573, DOI: 10.5194/bg-15-5565-2018.

Mead, M.I., O.A.M. Popoola, G.B. Stewart, P. Landshoff, M. Calleja, M. Hayes, J.J. Baldovi, M.W. McLeod, T.F. Hodgson, J. Dicks, A. Lewis, J. Cohen, R. Baron, J.R. Saffell, R.L. Jones, 2013: The use of electrochemical sensors for monitoring urban air quality in low-cost, high-density networks. – Atmos. Env. **70**, 186–203, DOI: 10.1016/j.atmosenv.2012.11.060.

OpenStreetMap contributors, 2021: Planet dump retrieved from https://planet.osm.org. – https://www.openstreetmap.org.

Patel, N.R., V.K. Dadhwal, S.K. Saha, 2011: Measurement and scaling of carbon dioxide (CO_2) exchanges in wheat using flux-tower and remote sensing. – J. Indian Soc. Remote Sens. **39**, 383–391, DOI: 10.1007/s12524-011-0107-1.

Patel, N.R., H. Padalia, S.P.S. Kushwaha, S. Nandy, T. Watham, J. Ahongshangbam, R. Kumar, V.K. Dadhwal, A. Senthil Kumar, 2019: CO_2 flux tower and remote sensing: Tools for monitoring carbon exchange over ecosystem scale in Northwest Himalaya. – In: Navalgund, R.R., A.S. Kumar, S. Nandy (Eds.), Remote Sensing of Northwest Himalayan Ecosystems, Springer, Singapore, chapter 14, 313–327, DOI: 10.1007/978-981-13-2128-3_14.

Peng, Z., J.L. Jimenez, 2021: Exhaled CO_2 as a COVID-19 infection risk proxy for different indoor environments and activities. – Envir. Sci. Tech. Lett. **8**, 392–397, DOI: 10.1021/acs.estlett.1c00183.

Pfeil, M., T. Bartoschek, J.A. Wirwahn, 2015: OPENSENSEMAP – a citizen science platform for publishing and exploring sensor data as open data. – In: Free and Open Source Software for Geospatial (FOSS4G) Conference Proceedings, volume 15, 122–139. DOI: 10.7275/R56971SW.

Rogie, J.D., D.M. Kerrick, G. Chiodini, F. Frondini, 2000: Flux measurements of nonvolcanic CO_2 emission from some vents in Central Italy. – J. Geophys. Res. **105**, 8435–8445, DOI: 10.1029/1999JB900430.

Sawyer, J.S., 1972: Man-made carbon dioxide and the "greenhouse" effect. – Nature **239**, 23–26, DOI: 10.1038/239023a0.

Scholz, K., E. Ejarque, A. Hammerle, M. Kainz, J. Schelker, G. Wohlfahrt, 2021: Atmospheric CO_2 exchange of a small mountain lake: limitations of eddy covariance and boundary layer modeling methods in complex terrain. – J. Geophys. Res.-Biogeo. **126**, e2021JG006286, DOI: 10.1029/2021JG006286.

Schrier-Uijl, A.P., P.S. Kroon, A. Hensen, P.A. Leffelaar, F. Berendse, E.M. Veenendaal, 2010: Comparison of chamber and eddy covariance-based CO_2 and CH_4 emission estimates in a heterogeneous grass ecosystem on peat. – Agr. Forest Meteorol. **150**, 825–831, DOI: 10.1016/j.agrformet.2009.11.007.

Schütze, C., K. Bräuer, P. Dietrich, V. Engnath, M. Gisi, G. Horak, C. Leven, A. Lübben, I. Möller, M. Nierychlo, S. Schlömer, A. Schuck, U. Sefling, A. Simon, T. Streil, U. Sauer, 2015: MONACO - monitoring approach for geological CO_2 storage sites using a hierarchical observation concept. – In: A. Liebscher and U. Münch (Eds.), Geological Storage of CO_2 – Long Term Security Aspects, Advanced Technologies in Earth Sciences, Springer, chapter 2, 33–57, DOI: 10.1007/978-3-319-13930-2_2.

Spinelle, L., M. Gerboles, M.G. Villani, M. Aleixandre, F. Bonavitacola, 2017: Field calibration of a cluster of low-cost commercially available sensors for air quality monitoring. Part B: NO, CO and CO_2. – Sensor. Actuat. B: Chem. **238**, 706–715, DOI: 10.1016/j.snb.2016.07.036.

Struzik, M., I. Garbayo, R. Pfenninger, J.L.M. Rupp, 2018: A simple and fast electrochemical CO_2 sensor based on $Li_7La_3Zr_2O_{12}$ for environmental monitoring. – Advan. Materials **30**, 1804098, DOI: 10.1002/adma.201804098.

Stull, R.B., 1988: An Introduction to Boundary Layer Meteorology. Atmospheric Sciences Library. – Kluwer Academic Publishers.

Van Kesteren, B., O. Hartogensis, D. Van Dinther, A.F. Moene, H.A.R. De Bruin, 2013: Measuring H_2O and CO_2 fluxes at field scales with scintillometry: Part I – introduction and validation of four methods. – Agr. Forest Meteorol. **178-179**, 75–87, DOI: 10.1016/j.agrformet.2012.09.013.

Zhao, J., M. Zhang, W. Xiao, W. Wang, Z. Zhang, Z. Yu, Q. Xiao, Z. Cao, J. Xu, X. Zhang, S. Liu, X. Lee, 2019: An evaluation of the flux-gradient and the eddy covariance method to measure CH_4, CO_2, and H_2O fluxes from small ponds. – Agr. Forest Meteorol. **275**, 255–264, DOI: 10.1016/j.agrformet.2019.05.032.

B Büchau et al. (2024a): CO_2 Exhaust of a Single Starzach Mofette

Büchau, Y. G., Leven, C. and Bange, J. 'A Portable Low-Cost Device to Quantify Advective Gas Fluxes from Mofettes into the Lower Atmosphere: First Application to Starzach Mofettes (Germany)'. In: *Environmental Monitoring and Assessment* 196 (11th Jan. 2024), 138. ISSN: 1573-2959. DOI: 10.1007/s10661-023-12114-8.

Environ Monit Assess (2024) 196:138
https://doi.org/10.1007/s10661-023-12114-8

RESEARCH

A portable low-cost device to quantify advective gas fluxes from mofettes into the lower atmosphere: First application to Starzach mofettes (Germany)

Yann Georg Büchau · **Carsten Leven** · **Jens Bange**

Received: 28 June 2023 / Accepted: 7 November 2023 / Published online: 11 January 2024

Abstract In this study, we introduce a portable low-cost device for in situ gas emission measurement from focused point sources of CO_2, such as mofettes. We assess the individual sensors' precision with calibration experiments and perform an independent verification of the system's ability to measure gas flow rates in the range of liters per second. The results from one week of continuous CO_2 flow observation from a wet mofette at the Starzach site is presented and correlated with the ambient meteorological dynamics. In the observed period, the gas flow rate of the examined mofette exhibits a dominant cycle of around four seconds that is linked to the gas rising upwards through a water column. We find the examined mofette to have a daily emission of 465 kg ±16 %. Furthermore, two events were observed that increased the flow rate abruptly by around 25 % within only a few minutes and a decaying period of 24 hours. These types of events were previously observed by others at the same site but dismissed as measurement errors. We discuss these events as a hydrogeological phenomenon similar to cold-water geyser eruptions. For meteorological events like the passages of high pressure fronts with steep changes in atmospheric pressure, we do not see a significant correlation between atmospheric parameters and the rate of gas exhalation in our one-week time frame, suggesting that on short timescales the atmospheric pumping effect plays a minor role for wet mofettes at the Starzach site.

Keywords CO_2 · Degassing · Earth mantle · Low-cost · Monitoring

Y. G. Büchau ( ) · C. Leven · J. Bange
Center for Applied Geoscience, University of Tübingen, Schnarrenbergstr. 94-96, Tübingen 72076, Baden-Württemberg, Germany
e-mail: yann-georg.buechau@uni-tuebingen.de

C. Leven
e-mail: carsten.leven-pfister@uni-tuebingen.de

J. Bange
e-mail: jens.bange@uni-tuebingen.de

1 Introduction

Due to its increasing atmospheric concentration, carbon dioxide (CO_2) currently has the largest bulk impact on total effective radiative forcing and is therefore the most relevant greenhouse gas (GHG) today (Forster et al., 2021), followed by methane (CH_4) and nitrous oxide (N_2O), which are more potent but less abundant greenhouse gases (Wallace & Hobbs, 2006). Under the globally adopted Paris Agreement (UNFCCC, 2015), countries are obliged to report annually on up-to-date GHG emission inventories to accepted standards (IPCC, 2006). The establishment of these inventories requires an array of methods, techniques and instruments to quantify gas fluxes over a variety of spatial scales. These range from in-situ point source estimation (Carapezza & Granieri, 2004, Chiodini et al., 1998, Lübben & Leven, 2022) to satellite remote sensing (Chevallier et al., 2005, Pan et al., 2021)

and (global) inverse gas transport modelling for emission source back-tracing and budgeting (Gaubert et al., 2019, Pickett-Heaps et al., 2011). Ongoing GHG emissions and their consequences make it increasingly clear that negative emissions, e.g. in form of Carbon Capture and Sequestration (CCS), are needed to counter global warming (Gasser et al., 2015). Monitoring of CCS sites is important to ensure the security of CO_2 storage (Flohr et al., 2021, Holloway, Pearce, Hards, Ohsumi, and Gale, 2007), and surface monitoring techniques should be as mobile as possible (Jones et al., 2014). In general, uncertainty quantification is also desired and necessary for GHG emission estimations (Jonas et al., 2019).

In addition to anthropogenic causes, the earth mantle is another and permanent source of CO_2 due to its degassing of the magma during crystallization (Lowenstern, 2001). The solubility of CO_2 in the magmatic fluid decreases during crystallization (Dasgupta, 2013), resulting in magmatic CO_2 exsolution which is then eventually capable of rising to the surface. CO_2 may enter the lower atmosphere e.g., through active or dormant subaerial volcanos, fumaroles, mofettes, at mid-ocean ridges, geothermal systems and geysers (Glennon & Pfaff, 2005; Kerrick, 2001; Werner & Cardellini, 2006; Werner et al., 2019). Although these non-anthropogenic CO_2 emissions are estimated to be two orders of magnitude smaller than anthropogenic emissions (Burton et al., 2013), they remain an integral baseline of the earth's GHG budget. Past research has shown repeatedly that estimates for the total volcanic CO_2 emissions vary greatly and better quantification is needed (Burton et al., 2013, Chiodini et al., 2004, Kerrick, 2001). Furthermore, such degassing can impact crop or forest growth (Farrar et al., 1995) and be hazardous to lifestock or humans (Beaubien et al., 2003). Temporal degassing anomalies around volcanos also show promising potential as precursors of volcanic eruptions (Inguaggiato, Vita, Cangemi, and Calderone, 2020, Pérez et al., 2022), and could improve the still insufficient early-warning systems (Winson et al., 2014). Therefore, the advancement of quantification methods for natural degassing from the solid earth remains an important task.

There exist several in-situ and remote sensing methods to quantify degassing from the solid earth, each suitable for one specific use case. While approaches to estimate gas *flux* (amount per area and time) vary, the vast majority of methods use spectrometry to quantify the gas *concentration*.

Satellite data provides coarse global gas concentration data (Chevallier et al., 2005, Pan et al., 2021). One-dimensional column measurements of sulfur dioxide (SO_2) on scales up to several kilometers are performed with remote sensing spectrometry that use the solar spectrum as a reference, such as correlation spectroscopy (COSPEC) (Williams-Jones et al., 2008) and its more compact iterations FlySPEC (Horton et al., 2006) and mini-DOAS (Galle et al., 2003, McGonigle et al., 2002), which give comparable results (Elias et al., 2006). Given further assumptions and boundary conditions such as the wind speed, these measurements can be translated into a gas flux or be used as proxy for other gases such as CO_2 if not directly measured (Williams-Jones et al., 2008). However, the equipment for these techniques is rather expensive and requires careful operation and frequent calibration. Furthermore, a direct line of sight to sunlight is required, preventing its use during the night or in constrained locations. This also makes it less suitable for small, focused degassing point sources or weak diffuse degassing. There exist also similar laser or Fourier-Transform Infrared Spectroscopy (FTIR)-based approaches (Feitz et al., 2018) and local modelling techniques to merge and unify data from different sources (Feitz et al., 2022).

For diffuse degassing from soil or cropland, in-situ measurements are typically employed. A versatile technique suitable for homogeneous, flat terrain with a horizontal footprint up to hundreds of meters is the eddy-covariance method for directly measuring the turbulent vertical gas exchange (Mauder et al., 2021). While the eddy-covariance method can deliver high-frequency flux data (up to 20 Hz), it is unsuitable for complex terrain or very heterogeneous surface emissions (Baldocchi, 2003, Scholz et al., 2021). To a degree, the high-frequency data availability can be traded for lower cost by employing the flux-gradient approach, where the vertical gradient of slower gas concentration measurements is parameterised to yield an average flux, though losing precision. However, this method requires knowledge, calibration or approximation of the eddy diffusivity K and its dependence on atmospheric conditions (Zhao et al., 2019).

Another in-situ method for diffuse soil gas flux quantification is the dynamic concentration method (Camarda et al., 2019, Gurrieri & Valenza, 1988). Here,

gas is pumped from the soil with increasing intensity until a constant gas concentration is sampled, signaling an equilibrium between pump flow and soil gas flux. While comparably simple to execute, this method is prone to overestimation and very dependant on soil permeability according to Carapezza and Granieri (2004). Instead, the accumulation chamber technique has proven to be a powerful alternative (Chiodini et al., 1998, Haro et al., 2019) by deriving a flux from the rate of concentration increase in a closed volume above the soil of interest.

However, the above-mentioned methods have been developed to investigate mainly diffuse degassing and so none of them is capable of directly quantifying advective gas fluxes of intense gas exhalations such as fumaroles or mofettes as the flow rates are either too high or the exhalations too focused. For strong advective degassing from vents, a robust method is to channel the exhaled gas and measure its velocity and concentration to determine the mass flow (Lübben & Leven, 2022, Rogie et al., 2000). However, to our knowledge, no such design has been published that focuses on continuous, unattended operation, high temporal resolution, low-cost components and adaptability to different magnitudes of degassing. In this study, we present a system with such potential. We assess the suitability of each individual component and demonstrate it by short-term application to a mofette at the Starzach site in Germany (Lübben & Leven, 2018). The degassing behaviour of the investigated mofette is discussed and a first, preliminary look is taken at the effects of meteorological parameters such as atmospheric pumping (Forde et al., 2019, Nilson et al., 1991).

2 Geological setting of the test site

The Starzach site (Fig. 1) is located in Southwest Germany in the Upper Neckar valley, approximately 30 km southwest of Tübingen. In this region, the River Neckar cuts deep into the competent limestone of the Middle Triassic ("Muschelkalk") forming a valley with relatively steep hillslopes formed by hillside depris covering the rock faces of the Middle Triassic. The site itself is located at the bottom of the Neckar valley, and is known for its natural CO_2 degassing from mofettes and springs. In the region, CO_2 was mined industrially over the last century until yields eventually declined, and stricter environmental regulations rendered the mining uneconomical. After a recovery period, degassing activity has increased again in the last decades, motivating current research activities in the area, for which Lübben and Leven (2018) introduced the Starzach site as a natural analog for leaking CCS sites. Their investigations show that the active gas exhalations are most likely linked to a fault zone following the major tectonic Swabian-Franconian direction, and that the emitted gas is most likely of non-volcanic magmatic origin consisting of a mixture of CO_2 (>98 %), nitrogen (∼1 %), oxygen (∼0.2 %) and smaller amounts of helium, argon and methane. A detailed description of the site and its geological setting is given in Lübben and Leven (2018).

A groundwater well was installed in May 2014 at a location without natural CO_2 degassing for access to groundwater (Figs. 1c and 2a). The 2"-well (DN50) targets the transition of the Quaternary aquifer to the Triassic bedrock unit ("Middle Muschelkalk", Middle Triassic, Upper Anisium) and reaches a depth of 9.4 m, while the lowermost 3 m of the well are screened to access the groundwater. The undisturbed water level in the well after its completion was approx. 1.7 m below ground surface. At the time of installation, the well did not emit any noticeable amount of gas, but turned into a mofette approximately six months after, and the gas exhalation increased over the years through the well. Simultaneously, an adjacent smaller mofette in a distance of approx. 2 m disappeared over the years, and likewise the exhalation activity declined visibly at the larger mofette "R" (Lübben & Leven, 2018). This indicates a small-scale shift in the underground gas flow, a change contributing to the temporal and spatial heterogeneity of atmospheric CO_2 concentration at the site. Lübben and Leven (2022) presented a custom funnel flow meter with which they determined flow rate magnitudes in the order of a few liters per second from specific mofettes such as mofette "R" at the site in 2015.

Recently, Büchau et al. (2022) deployed a wireless sensor network at the site to monitor atmospheric CO_2 concentration and meteorological parameters and to provide infrastructure for further measurements. A strong diurnal cycle in atmospheric CO_2 concentration was observed with typical, low baseline concentrations of range 400 ppm to 500 ppm during the day and strongly elevated concentrations up to 40 000 ppm during the night, caused by a lack of wind.

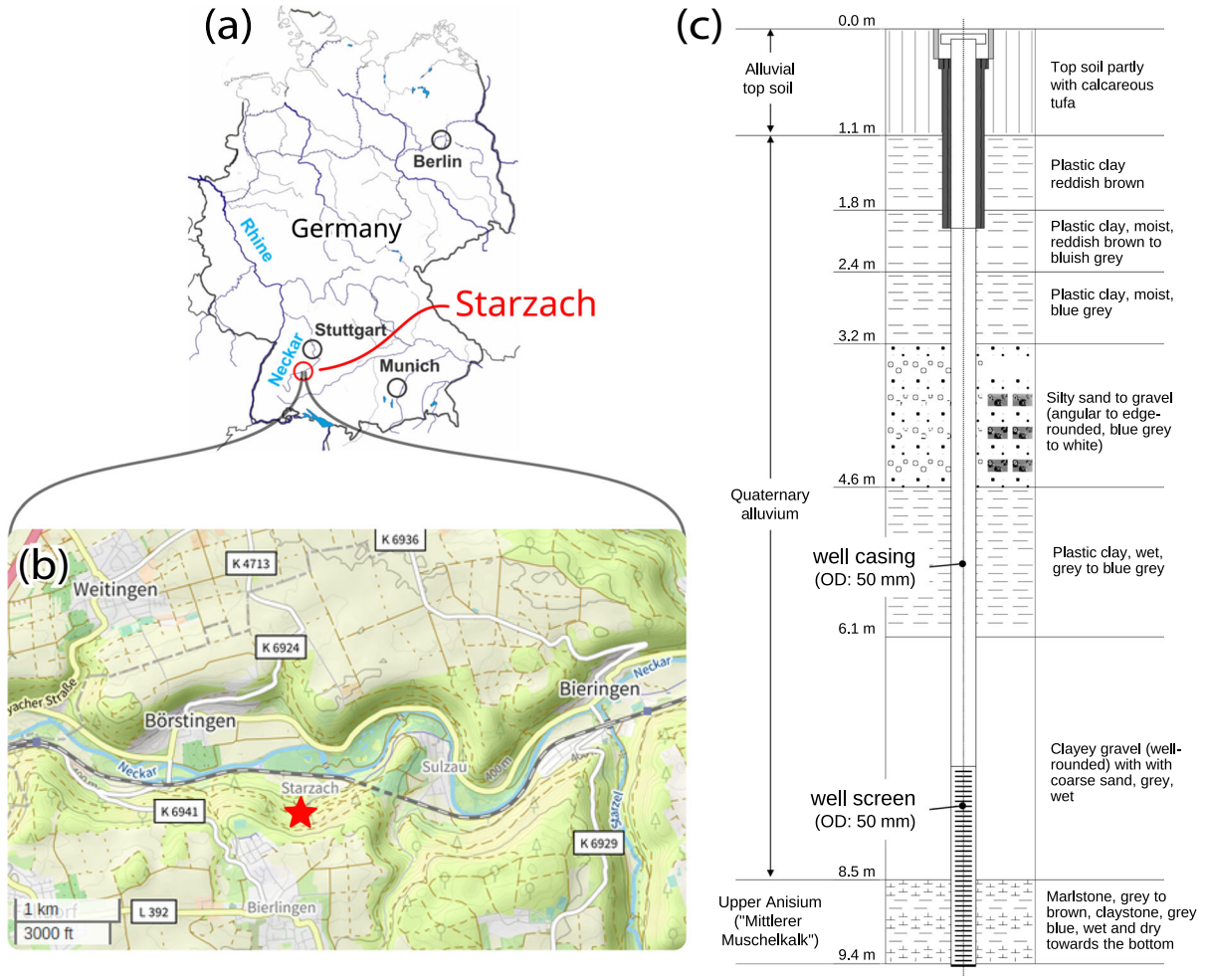

Fig. 1 Overview of the Starzach site. (**a**) geographic location in Germany. (**b**) local map of the Neckar valley (OpenStreetMap contributors, 2023). (**c**) well log of a groundwater monitoring well at the Starzach site (Fig. 2a) with lithological description. The first ~6.4 m of the well pipe are unscreened, while the lower ~3 m are screened to access the groundwater

3 Methods

3.1 Chimney design

Chimney-based designs to measure advective gas fluxes from mofettes were already introduced by Rogie et al. (2000) and Lübben and Leven (2022). However, those setups are not suitable for prolonged continuous monitoring. Both applied a hot-wire anemometer to measure flow velocity and expensive infrared gas analysers for the gas concentration. Lübben and Leven (2022) found that the exact placement of their hot-wire anemometer inside the chimney had a strong impact on the estimated gas flux. Furthermore it was susceptible to measurement errors due to water deposition on the weakly heated element.

The design we present here addresses these problems: We focus on reduced cost, continuous operation, low power consumption and the ability to record data with high temporal resolution ($\Delta t < 1$ s) to study the flow dynamics of the gas source.

With a chimney-based funnel design, given the volumetric gas flow rate $\dot{V}$ $[\mathrm{m^3\,s^{-1}}]$, the volumetric concentration of the gas of interest X_{gas} [ratio] (in

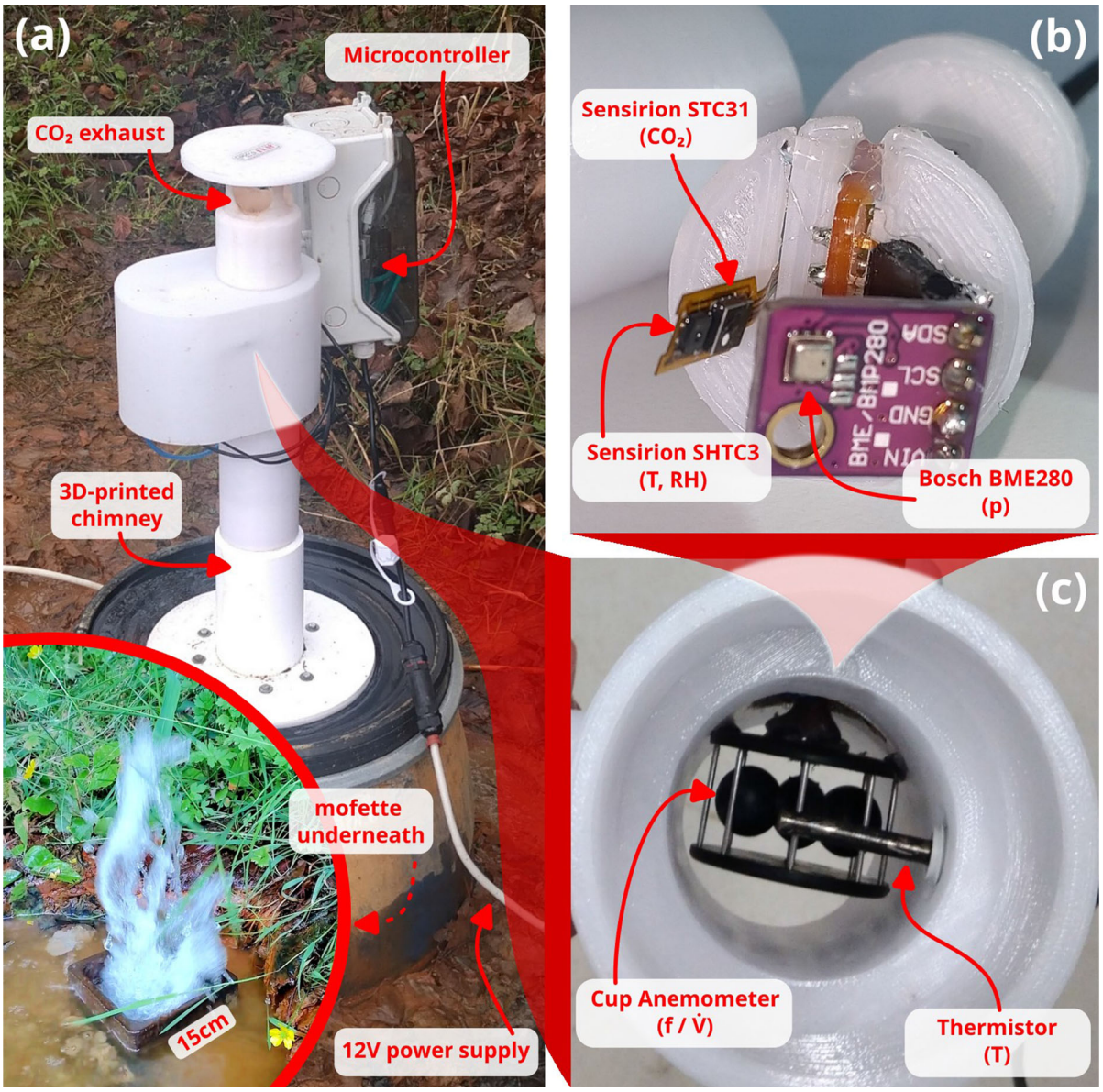

Fig. 2 The chimney-based design to measure advective CO_2 fluxes from mofettes. **(a)** Assembled hood deployed at the Starzach site over an erupting mofette as shown in the small inset and in Figure 2c of Büchau et al. (2022). Note: This is a different mofette than the one examined by Lübben and Leven (2022). **(b)** Gas sensor unit mounted laterally in the chimney consisting of Sensirion STC31 CO_2 sensor, Sensirion SHTC3 temperature and humidity sensor and Bosch BME280 absolute atmospheric pressure sensor. **(c)** View from below through the chimney with the fitted cup anemometer and thermistor visible

this case for CO_2: X_{CO_2} [ratio]), the temperature T [K] and pressure p [Pa] in the chimney, the mass flux $\dot{m}_{CO_2}$ $\left[\mathrm{kg\,s^{-1}}\right]$ can be calculated with

$$\dot{m}_{CO_2} = X_{CO_2} \cdot \dot{V} \cdot \frac{p \cdot M_{CO_2}}{R^* \cdot T} \quad (1)$$

where $R^* \approx 8.314\,\mathrm{JK^{-1}\,mol^{-1}}$ denotes the universal gas constant and $M_{CO_2} \approx 0.044\,\mathrm{kg\,mol^{-1}}$ the molar mass of CO_2.

To quantify the CO_2 mass flux $\dot{m}_{CO_2}$, the volumetric flow rate $\dot{V}$, the volumetric CO_2 concentration X_{CO2}, gas pressure p and temperature T need to be measured.

In the following we detail the respective sensors we employ and the calibration procedures we performed to validate those.

3.2 Flow rate $\dot{V}$ measurement

Anemometry techniques to measure air flow velocity have evolved to a variety of choices for different applications and environments, from simpler working principles like pitot tubes, vane and cup anemometers, to sophisticated techniques such as hot-wire, ultrasonic or laser-Doppler anemometry (Camuffo, 2019, Foken, 2021). For our application of measuring the gas flow velocity of advective gas emissions, a small anemometer fitting into a tube with a diameter of a couple of centimeters is desirable. Anemometers that measure the flow velocity independently of the medium's composition are especially favorable for the case of gas mixtures. In addition, robustness against water droplets, dew and elevated water vapour concentration in general is necessary to withstand the extremely humid conditions in the gas exhaled from a wet mofette. This rules out hot-wire anemometers as they are delicate devices mostly suitable for lab environments. Differential pressure sensors needed for Pitot tubes or other pressure-based flow rate measurement approaches are often designed for dry conditions only. Pitot tubes and vane anemometers must be calibrated or corrected for density (Foken, 2021). While ultrasonic and laser-Doppler anemometers are fundamentally independent of the medium by their physical design principles (Foken, 2021), commercially available devices are expensive and often large. A good balance between cost and medium-independence is the cup anemometer: In the simplified model of a two-cup anemometer, as it reaches a constant rotation frequency f in a stationary flow of velocity v, the opposing drag forces F_{cx} and F_{cv} acting on the convex and concave cup side, respectively, are at an equilibrium:

$$F_{cx} = F_{cv}$$
$$\frac{1}{2} A \rho c_{w,cx} (2\pi f r + v)^2 = \frac{1}{2} A \rho c_{w,cv} (2\pi f r - v)^2 \quad (2)$$

where the medium density ρ and the cups' cross-sectional area A cancel out. This leaves the rotation frequency f a sole function of the flow velocity v and the design parameters (the cup sides' drag coefficents $c_{w,cx}$ and $c_{w,cv}$ and the cup centers' distance r from the rotation axis). The intrinsic difference in drag between the shells, however, causes faster acceleration than deceleration and thus a hysteresis in rotation frequency in unsteady flows due to inertia, often referred to as overspeeding (Busch and Kristensen, 1976, Papadopoulos et al., 2001). Still, a cup anemometer can be a cost-effective way of measuring the gas flow rate inside a pipe independently of the gas composition as the influence of the overspeeding effect can be controlled for by comparison with reference measurements.

Small-sized cup anemometers are less common and mostly available as handheld devices which are unsuitable for automated continuous data logging. So we detached the protective cage containing the rotating cups from a commercially available handheld device. As is common for miniature cup anemometers, our model (Fig. 2c) has an axle with pointed ends sitting in metal sockets. This minimizes the amount of moving parts and friction contacts in comparison with e.g. a needle bearing, thus reducing the chance of failure under condensing conditions. We added an infrared light-emitting diode (LED) and a photodiode to act as light barrier for detecting the rotation frequency of the cups. The inverse of the pulse time divided by the amount of cups (four in this case) is then the cup anemometer's rotation frequency. A microcontroller finds the pulse edges and records the time in between. As a consequence, the data rate for the cup anemometer's rotation frequency is not constant as it depends on the rotation frequency itself.

Instead of parameterising the flow rate $\dot{V}$ as the product of cross-sectional area A and flow velocity v ($\dot{V} = A \cdot v$, cf. Lübben and Leven (2022); Rogie et al. (2000)), we calibrated our system as a whole to translate the rotational frequency f of the cup anemometer directly to the flow rate $\dot{V}$. This avoids that the effective cross-sectional area might be unknown due to the geometry of the chimney and flow obstructions such as the anemometer itself. Furthermore, friction causes the flow velocity to diminish near the walls of the chimney, resulting in a lateral velocity profile instead of a constant value across the cross-section, which is an implicit assumption for the parametrisation $\dot{V} = A \cdot v$. This effect is increased with smaller Reynolds numbers as the velocity peak in the center of the chimney becomes more prominent (Etling, 2008, Štigler, 2012). The

Reynolds number for a setup like ours (55 mm inner chimney diameter, CO_2, 1 m s^{-1} velocity) ranges from 4500 to 10 000, taking into account variations in temperature, pressure (Foken, 2021, Schäfer et al., 2015), flow velocity and dimensional uncertainties. Considering that the flow through the chimney is obstructed by sensors and a protective water shield at the inlet and outlet (Fig. 2), it is reasonable to assume the chimney flow will not be laminar but weakly turbulent, unifying the velocity throughout the cross-section.

We carried out two experiments to ensure our flow rate measurement is valid. First, to determine the relationship between f and $\dot{V}$ we connected our chimney to an LTG 227VM-05 volumetric flow sensor that is part of our research facility's building ventilation system and recorded the cup anemometer's rotational frequency f while varying the flow rate by gradually closing the shutt-off valve of the ventilation. Second, in the field we repeatedly took the time it takes to fill up plastic bags of known volume with gas from a mofette and compared this to the estimate derived from the lab results. These results are discussed in Section 4.1.

3.3 CO_2 measurement X_{CO_2}

A CO_2 sensor for measuring advective CO_2 fluxes from mofettes needs to fulfil several criteria: First, it needs to be able to measure high CO_2 concentrations close to 100 % (Büchau et al., 2022, Lübben & Leven, 2018, 2022). It also has to be small enough for fitting into a chimney next to the other sensors. A reasonably high measuring frequency ($\geq$ 1Hz) is necessary if dynamics of flow rate and gas concentration are to be analysed. Finally, extremely humid environments should neither harm the sensor nor influence the measurement too strongly. This combination of requirements is rather unusual and the market offer of the gas sensor industry is quite limited in this regard. Many embedded non-dispersive infrared (NDIR) CO_2 sensors suffer from the cross-sensitivity on water vapour, have slow response times and can only measure low CO_2 levels (Büchau et al., 2022, Müller et al., 2020). Initial tests with a GSS ExplorIR-M NDIR CO_2 sensor which can measure up to 100 % CO_2 were unsuccessful under very humid conditions.

Another approach to measure gas concentrations is using a proxy quantity that is strongly influenced by the gas mixture (e.g. sonic speed or heat conductivity) and deducing a concentration given assumptions and further information about the gas composition. The Sensirion STC31 CO_2 sensor is such a model which derives a CO_2 concentration from the heat conductivity. Compared to other embedded CO_2 sensors such as those evaluated in Büchau et al. (2022), the STC31 sensor is an order of magnitude smaller with a size of only 3 mm × 3.5 mm × 1 mm (Fig. 2b). Furthermore, the STC31 sensor covers the entire CO_2 concentration range from 0 % to 100 % – a capability most comparable NDIR-based CO_2 sensors lack (Büchau et al., 2022).

The STC31 sensor needs to have the temperature, pressure and relative humidity communicated to it before it performs a measurement, then internally calculates and reports a CO_2 concentration. We employ an evaluation kit where a Sensirion SHTC3 temperature and humidity sensor is mounted directly next to the STC31 CO_2 sensor (Fig. 2b). Readings of the former sensor are communicated to the STC31 CO_2 sensor. The pressure measurement is performed by a Bosch BME280 environmental sensor, a common miniature low-cost absolute atmospheric pressure sensor with a rated absolute accuracy of around $\pm$1.5 hPa (Fig. 2b). During operation we disable the STC31 sensor's automatic self-calibration to prevent it from wrongly interpreting the high CO_2 concentration as an implicit baseline.

To assess the STC31 sensor's suitability we exposed it to various combinations of temperature, relative humidity and CO_2 concentration inside an EdgeTech RH CAL relative humidity calibration chamber together with the intake of a LI-COR 840A closed-path infrared gas analyser. An automated gas injection system flooded the calibration chamber periodically with CO_2 about every 30minutes after each successful transition to the next temperature/relative humidity level. The LI-COR sensor's calibration range only reaches up to 20 000 ppm (2 vol%). However, its maximum data output limit is as high as 200 000 ppm (20 vol%). So for comparison with the LI-COR sensor, we capped the CO_2 concentration during flooding of the calibration chamber at this level to reduce the idle time where no overlapping data within its calibration range is available. LI-COR measurements beyond 2 vol% are expected to have a larger error, but are nevertheless included here for reference.

To account for high CO_2 concentrations, the same temperature and relative humidity profile was repeated

but with periodic CO_2 injections without an upper concentration limit. Furthermore, a separate setup with the STC31 sensor in the gas volume at the top of a bottle with carbonated water was performed to simulate saturated humidity and CO_2 conditions similar to the situation in the field. The results are discussed in Section 4.2.

3.4 Temperature T and humidity RH measurement

Two temperature measurements are installed in the chimney device; one measurement close to the CO_2 sensor laterally in the chimney (small SHTC3 temperature and humidity sensor as described above, Fig. 2b) and one measurement right in the center of the chimney to record the actual temperature of the emitted gas without outside influence. For the latter measurement we use a positive temperature coefficient (PTC) thermistor in a metal housing for durability. Both sensors were calibrated in our RH CAL calibration chamber. The results are discussed in Section 4.3.

3.5 Field measurements

Having calibrated the individual sensors, field tests were carried out at the Starzach site (Section 2). The mofette that developed from a groundwater monitoring well (Fig. 1c) was chosen for the measurements described here (Fig. 2a, same mofette as Figure 2c in Büchau et al. 2022).

A wireless sensor network is presently deployed at the Starzach site (Büchau et al., 2022). Sensor stations send data via a Wireless Local Area Network (WLAN) established by a central single-board computer with cellular internet access. Data is stored on µSD-cards on each sensor station as well as the central station and an off-site server where data is relayed to. Currently, all devices are powered from one 12 V lead-acid battery charged by a series of solar panels and a methanol fuel cell for backup, but every station could be powered independently to increase mobility. The chimney device itself has an average power consumption of around 0.5 W and was integrated into this network as a sensor station for one week of continuous operation. Data of a Gill MaxiMet GMX541 compact weather station located at the central station is available as meteorological reference. The obtained measurements are discussed in Section 4.4.

4 Results and discussion

As a measure of similarity between two quantities x and y we employ the Mean Absolute Error (MAE):

$$\mathrm{MAE}\,(x,\,y) = \mathrm{mean}\,(|\mathrm{x} - \mathrm{y}|) \tag{3}$$

For conservative sensitivity analysis, the maximum absolute error $\Delta y_{\max}$ and maximum relative error $\Delta y_{\max,\mathrm{rel}}$ [%] of a quantity y derived from input quantities $x_1, \ldots, x_\mathrm{n}$ can be calculated via

$$\begin{aligned} \Delta y_{\max}(x_1, \ldots, x_\mathrm{n}) &= \sum_{i=1}^{n} \left|\frac{\partial y}{\partial x_\mathrm{i}}\right| \cdot \Delta x_{\mathrm{i}_{\max}} \\ \Delta y_{\max,\mathrm{rel}} &= \frac{\Delta y_{\max}}{\overline{y}} \end{aligned} \tag{4}$$

where $\Delta x_{\mathrm{i}_{\max}}$ is the maximum expected absolute error of quantity x_i and $\overline{y}$ the mean of y.

4.1 Flow rate $\dot{V}$ calibration

Comparing the rotational frequency of the cup anemometer installed in the chimney (Fig. 2c) to the volumetric flow rate obtained from an LTG 227VM-05 volumetric flow sensor under laboratory conditions, we find a linear relationship (coefficient of determination $R^2 = 99.4\,\%$) with an average error of $0.34\,\mathrm{Ls}^{-1}$ (Fig. 3). As expected of cup anemometers due to the initial friction in the mechanical bearing (Alfonso-Corcuera et al., 2021), flow rates below $3\,\mathrm{Ls}^{-1}$ are slightly underestimated in our setup.

With this relationship determined, we took the device to the field and installed it on a mofette (Fig. 2a). We removed the top chimney roof segment and repeatedly attached plastic bags with nominal volumes of 60 L, 120 L and 240 L to the exhaust of the chimney to fill them up with gas exiting from the mofette. The measured time Δt it takes to fill up a bag of volume V was

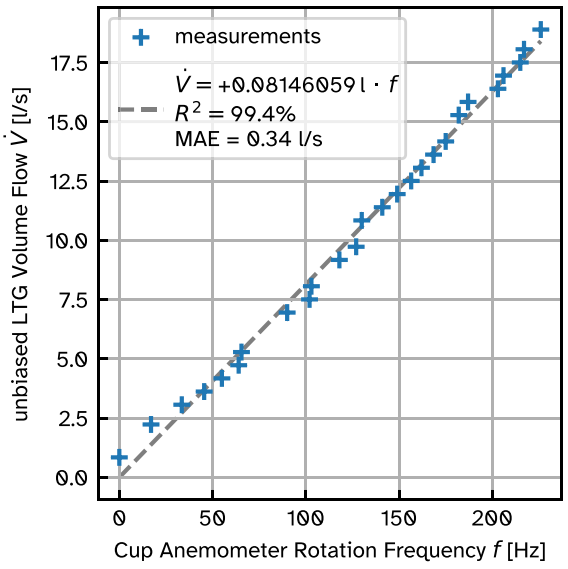

Fig. 3 Calibration of cup anemometer rotational frequency inside chimney against flow rate of LTG 227VM-05 volumetric flow sensor

then used to calculate the average flow rate during the filling time period:

$$\dot{V} = \frac{V}{\Delta t} \tag{5}$$

When inflated, the plastic bags had non-trivial shapes, so we estimated their volume very conservatively from dimensional measurements assuming a cylindrical shape as approximation. Applying Eq. 4 to Eq. 5 then also yields a propagated error estimation for the average flow rate. Data of the individual bag fills is listed in Table 1.

During the bag fills we recorded flow rate data deduced from the cup anemometer's rotational frequency at an average data rate of 3 Hz. This time series together with the flow rate estimation from the bag fills is plotted in Fig. 4. The observed flow rate varies between 1 Ls^{-1} and 6 Ls^{-1} with an average slightly below 3 Ls^{-1}.

When bags are attached to the chimney, the flow rate initially plummets and is then slowly restored during inflation. The drop in flow rate is especially prominent for the smaller bags 1 and 2. On initial contact between bag and chimney, the introduced orifice at the interface is limiting the flow. Furthermore, during inflation the bag foil needs to straighten from its wrinkled state, providing resistance for incoming gas. Both effects decrease in intensity the more the bag is inflated, allowing the flow rate to recover.

Due to the shorter filling times and uneven shapes of the smaller bags 1, 2 and 7, their flow rate uncertainties are the largest. Still, the flow rate deduced from the cup anemometer generally lies within the flow rate range estimated from the respective bag fill. This indicates that our lab calibration is correct and also applicable under field conditions.

A dominant cycle is present in the flow rate signal with a period of 4 seconds, responsible for more than half (57 %) of the total signal variance (Fig. 4, bottom). This 4 s-cycle corresponds to the observable bubbling that is characteristic for wet mofettes at the site and is visible in Fig. 2a and in c of Büchau et al. (2022). Our understanding of this 4 s-cycle is that it is caused by a periodically shifting pressure equilibrium within the well pipe shown in Fig. 1c. The gas ascends up to the point where the pipe perforation ends in 6.4 m depth. At this point, the water column maintains a hydrostatic pressure of ~63 kPa when the well pipe is filled to the top. As more gas accumu-

Table 1 Bag calibration data visualised in Fig. 4

Nr	Bag volume V [L]	duration Δt [s]	Flow rate $\dot{V}$ [Ls^{-1}]
1	50 ± 20	27.6 ± 1.0	1.4 ± 0.8
2	100 ± 30	26.7 ± 1.0	4.1 ± 1.3
3	240 ± 50	78.3 ± 1.0	3.1 ± 0.7
4	240 ± 50	81.8 ± 1.0	2.9 ± 0.6
5	240 ± 50	75.0 ± 1.0	3.2 ± 0.7
6	240 ± 50	75.1 ± 1.0	3.2 ± 0.7
7	60 ± 20	22.2 ± 1.0	2.7 ± 1.0

The uncertainties of bag volume and duration were estimated very conservatively from on-site dimensional and timing measurements and video footage of the experiments using Eq. 4, then translated into the flow rate uncertainty by applying Eqs. 4 to 5

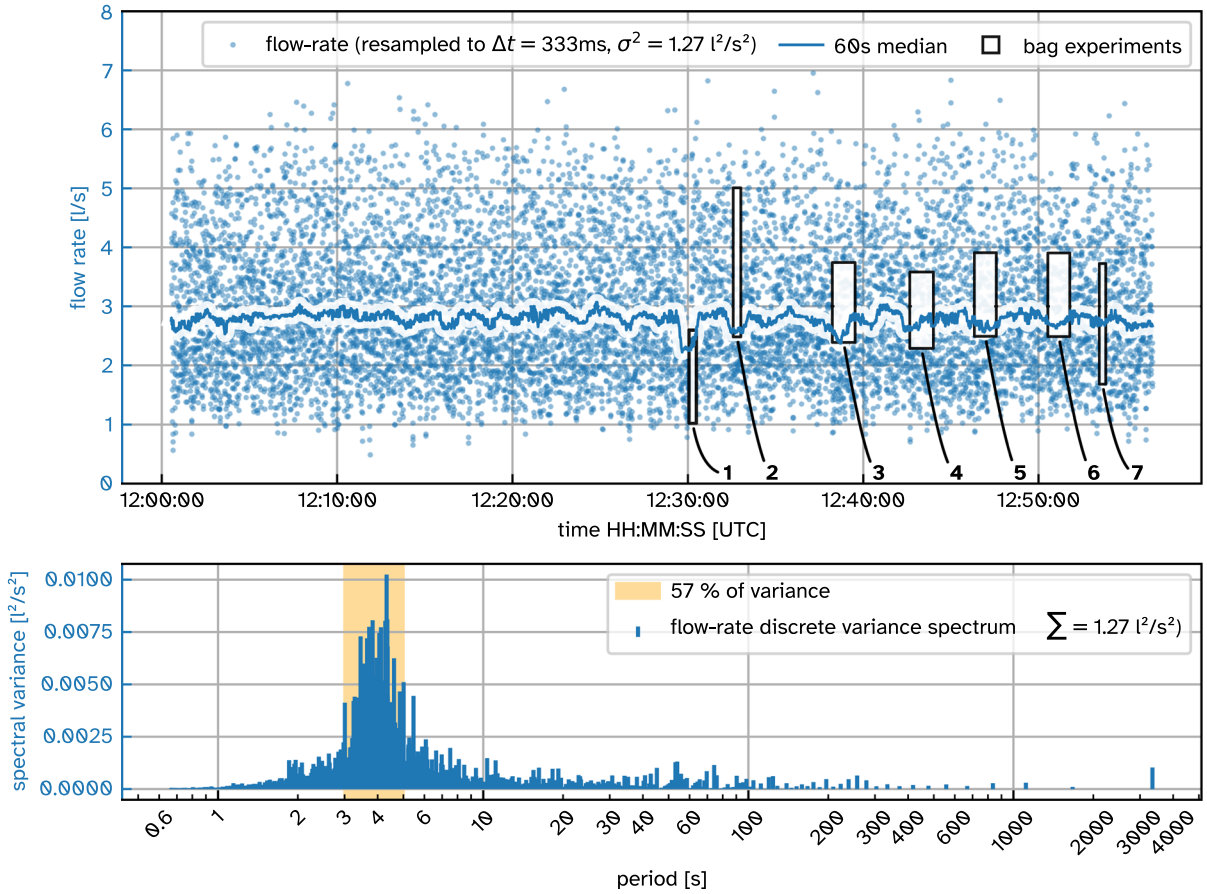

Fig. 4 Time series of measured volumetric flow rate from the examined mofette (Fig. 2a) with a temporal resolution resampled to 3 Hz. Each outlined box indicates a bag fill detailed in Table 1. *Bottom*: Variance spectrum of the volumetric flow rate time series

lates from below, this pressure is eventually overcome so that an eruption happens, releasing the built-up gas pressure. Measurements with a closed chimney exhaust showed maximum differences to atmospheric pressure of ~100 kPa (1bar), which supports this explanation. Surrounding ground water constantly enters the well pipe through the perforation, refilling the water column. This cycle apparently repeats with a period of 4 s.

4.2 CO_2 Measurement X_{CO_2} Verification

In the calibration chamber setup detailed in Section 3.3, the temperature ranged from 11 °C to 40 °C. Due to the periodically injected dry CO_2 gas, the calibration chamber struggled generating very humid conditions, resulting in a range of generated relative humidity from 6 % to 74 %. Under these conditions, both CO_2 sensors (STC31 and LI-COR 840A) agree very well over the entire LI-COR output range up to 20 vol% with a mean absolute error of 0.3 vol%, even beyond the LI-COR sensor's calibrated range where the relationship becomes non-linear (Fig. 5). The non-linear relationship above 2 vol% can not be explained with a mismatch in response times of the two sensors - filtering either sensor with an optimized exponentially-weighted moving average (EMWA) did not result in any significant linearization. Still, the deviation between both sensors lies within the STC31 sensor's specifications and is only weakly correlated with chamber temperature (21 %) and relative humidity (-18 %). These two sensors have fundamentally different measuring principles (LI-COR: infrared absorption vs. STC31: heat conductivity) and it is unlikely that both are biased identically. As a consequence, the good aggreement between the two indicates that the LI-COR sensor's

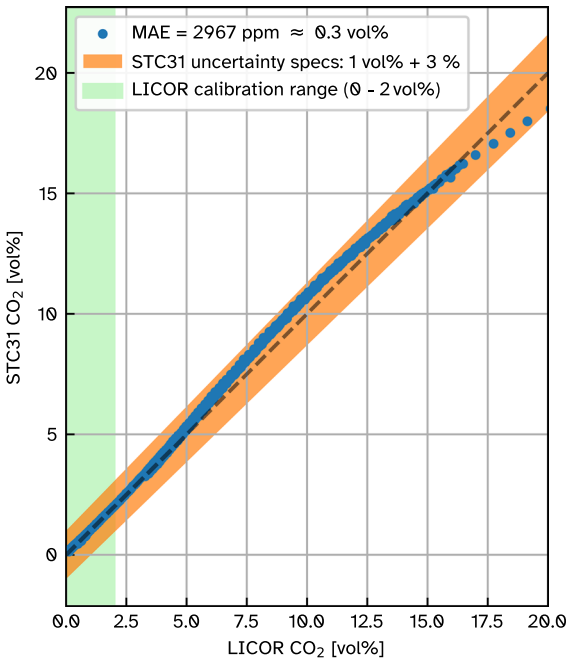

Fig. 5 Comparison of LI-COR840A closed-path infrared gas analyser and STC31 heat conductivity CO_2 sensor measurements in an EdgeTech RHCAL calibration chamber for various combinations of relative humidity and temperature

measurements can still be relied upon beyond its calibrated range, though with a larger margin of error.

During the 23 periodic full CO_2 floodings of the calibration chamber the CO_2 concentration peaks measured by the STC31 sensor had an average magnitude of 97.6 vol% and a maximum of 99 vol%. A slightly lower result than full CO_2 saturation is expected as the calibration chamber constantly feeds outside air into the volume for purposes of mixing the humid air, thus diluting the introduced CO_2. This result proves that the STC31 sensor can reliably measure high CO_2 levels under dry conditions.

A matching measurement of 99.4 vol% was obtained in the gaseous volume of the carbonated water bottle. We allowed the gas phase to reach an equilibrium for three hours, approaching full saturation of the mixture of water vapour and CO_2; similar conditions to what we expect to find in the field. From SHTC3 and BME280 measurements ($T = 20\,°C$, $RH = 83\,\%$, $p = 978\,hPa$) it can be estimated that water vapour should take up ~2 vol% of the mixture, leaving ~98 vol% for CO_2. For simplicity of this estimation, we ignore the quite complex effects of dissolved CO_2 on saturation water vapour pressure (Privat & Jaubert, 2014) here. The obtained CO_2 concentration of 99.4 vol% still lies within the STC31 sensor's uncertainty of ±1 vol% ±3 %. Thus, in contrast to infrared CO_2 sensors which can have a strong cross-sensitivity on water vapour (Büchau et al., 2022), the STC31 sensor is also suitable for humid conditions.

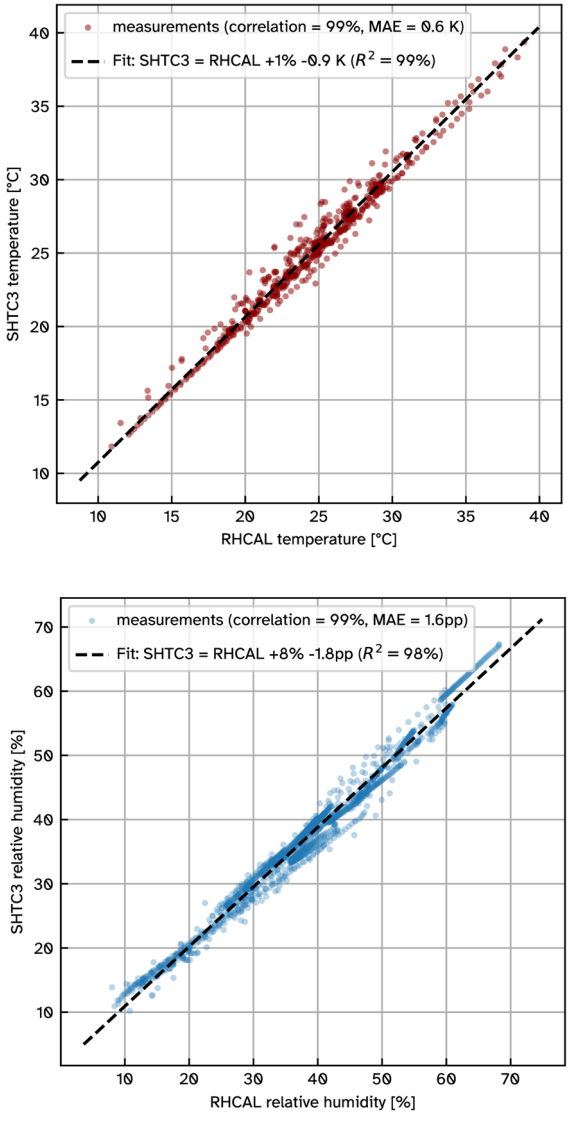

Fig. 6 Verification measurements of SHTC3 sensor inside RHCAL calibration chamber for temperature (top) and humidity (bottom). The data was obtained in the same setup as in Fig. 5

4.3 Temperature T and humidity RH calibration

During the same calibration experiment as described above, the SHTC3 temperature and humidity sensor (Fig. 2b) was present to feed its data to the STC31 CO_2 sensor. Comparing its data to the calibration chamber measurements (Fig. 6), an average accuracy of 0.6 K for temperature and 1.6 pp (percent points) for relative humidity is asserted across the entire experiment time series including the CO_2 floodings.

In another independent setup, the thermistor (Fig. 2c) was calibrated in the calibration chamber. In addition to a temperature profile from the calibration chamber, one data point in ice water was added to increase the reference range. A polynomial fit of third degree describes the thermistor's temperature dependency to an accuracy of 0.1 K (Fig. 7).

4.4 Field measurements discussion

An under-sampling analysis in the post-processing of the flow rate validation discussed in Section 4.1 showed that a 10 s sampling interval for the cup anemometer frequency measurement introduces an error of just ±1 % for the average flow rate compared to a sampling rate of 3 Hz. To keep network traffic low, we thus chose a data interval of 10 s for the continuous measurements. One week of data was recorded with the device mounted on the mofette shown in Fig. 2a. This data together with meteorological measurements from a Gill MaxiMet GMX541 compact weather station is shown in Fig. 8. Except for an 8 h data gap due to intermittent transmission problems in the night of the 05.02.2022, the instrument delivered data continuously.

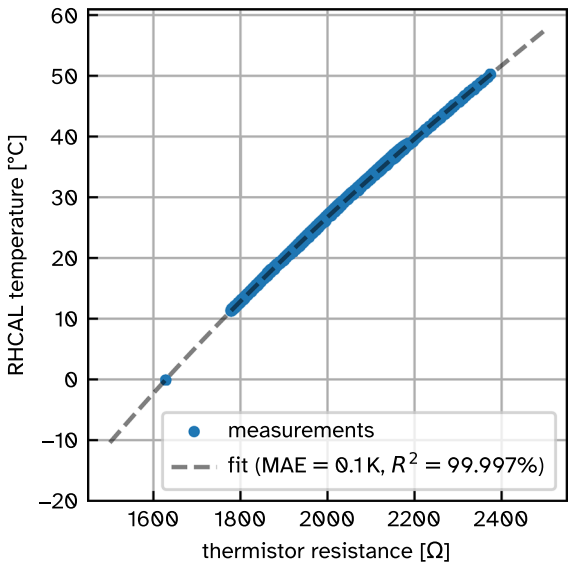

Fig. 7 Thermistor calibration in reference to RH CAL calibration chamber with a polynomial fit of 3rd degree

Meteorological situation

The observation period took place in the late winter of 2022, from February 3rd to 10th. Temperatures at 2 m height above ground regularly dropped below 0 °C during night time and reached up to 11 °C during the day. As the site is being situated at a northern slope of the river valley, incoming solar radiation is further reduced in the morning and evening (Büchau et al., 2022). Consequently, relative humidity was constantly elevated with a minimum of 60 %. Two cold air front passages with precipitation events were observed within the monitoring period, a weaker first front right before midnight between 04. and 05.02.2022 and a very distinct second front at midnight between 06. and 07.02.2022. Both fronts caused a significant temperature drop (∼3 K within 30 min), an intermittent increase in wind speed and a sudden increase in atmospheric pressure. The air mass trailing the second front raised the atmospheric pressure by nearly 30 hPa over the next day.

Measurement artifacts

There is a clear and opposite relationship between STC31 CO_2 readings and all temperature measurements. The strongest correlation is -86 % with the thermistor temperature. Such a significant temperature dependence was not observed under laboratory conditions (Section 4.2, Fig. 5). An explanation for a *positive* correlation could have been that each eruption brings a new volume of CO_2-rich gas which is also warmer than the atmosphere surrounding the chimney. The observed behaviour, by contrast, rather indicates an inadequacy of the thermal model implemented in the STC31 CO_2 sensor for the gas mixture emitted by the mofette. The STC31 sensor must be configured to assume the remaining non-CO_2 gas as either nitrogen (N_2) or air (our setting). Other than CO_2, the

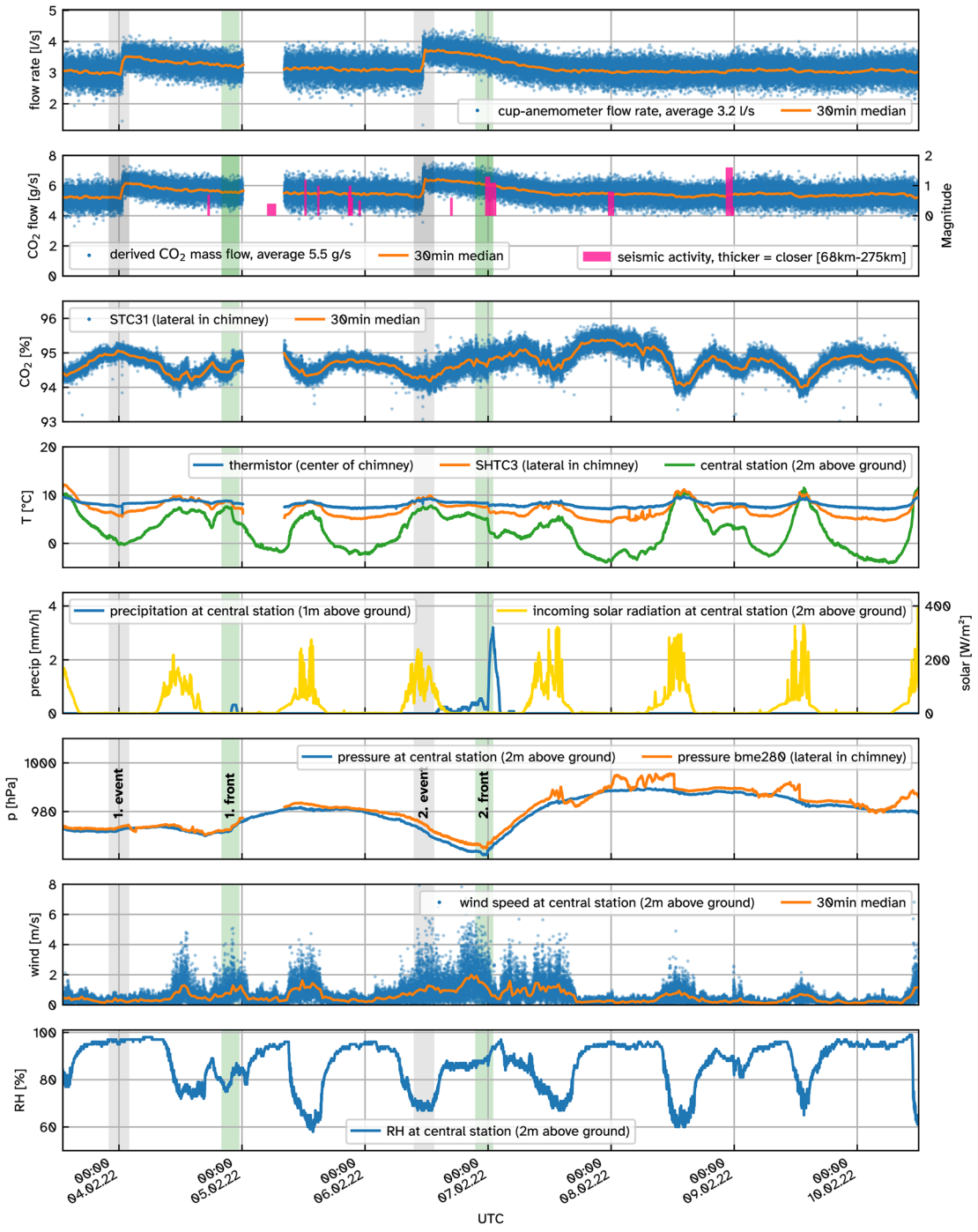

Fig. 8 One week of continuous measurements of the chimney device mounted on a mofette (Fig. 2a) at the Starzach site at 10 s resolution. Meteorological data is provided by a Gill MaxiMet GMX541 compact weather station ("central station" in Büchau et al. 2022). Two front passages are marked as green vertical lines. Gray vertical lines indicate the times of the two flow rate events. In the first hours of the 05.02.2022 there was a data gap due to intermittent transmission problems. Seismic activity data was obtained from https://erdbeben.led-bw.de (Landeserdbebendienst, Landesamt für Geologie, Rohstoffe und Bergbau, Regierungspräsidium Freiburg, Baden-Württemberg, Germany) on 29.09.2023

gas mixture emitted from the Starzach mofettes consists of nitrogen (∼1 %), oxygen (∼0.2 %) and smaller amounts of helium, argon and methane (Lübben & Leven, 2018). Furthermore, ∼1 % of water vapour is reasonable to assume with full saturation at 10°C, similar to our estimation for the carbonated water bottle experiment in Section 4.2. In total, these remaining gases sum up to ∼2 vol%, leaving ∼98 vol% for CO_2. Even with the fluctuations introduced by the apparent temperature dependency, the CO_2 readings remain within the sensor's rated accuracy of 1 vol% ±3 %.

Readings of the BME280 atmospheric pressure sensor mounted laterally in the chimney (Fig. 2b) exhibit some artifacts starting at noon on 07.02.2022. We assume these to be caused by condensation on the sensor as it is not rated for extremely humid conditions. Other models such as the BMP384 or BMP585 could be promising alternatives with a protective layer of gel.

CO_2 exhaust

Over the course of the observation period, our instrument measured an average baseline CO_2 exhaust from the single mofette of 5.4 gs^{-1} which extrapolates to 465 $kg\,d^{-1}$ (excluding the anomalies discussed below). Applying Eq. 4 to Eq. 1 yields that the maximum relative error of the mass flux $\Delta\dot{m}_{max,rel}$ can be estimated as the sum of relative errors of its independent variables:

$$\Delta\dot{m}_{max,rel} = \Delta T_{max,rel} + \Delta\dot{V}_{max,rel} + \Delta X_{CO_2,max,rel} + \Delta p_{max,rel} \quad (6)$$

Inserting values determined above, this maximum relative error sums up to $\Delta\dot{m}_{max,rel} \approx \pm 16\,\%$, to which our mass flow estimates are accurate with high confidence. At their examined mofette (the visually most prominent one at that time in 2015), Lübben & Leven (2022) determined average mass flow rates of around 75 $kg\,d^{-1}$, which is significantly smaller. Still, our notably larger estimate for the visually most striking mofette today could signify a general increase in degassing activity at the site – a trend that has been going on since industrial mining of the gas has stopped (Lübben & Leven, 2018).

Flow rate $\dot{V}$ anomalies

As highlighted in Fig. 8, two events were observed where the flow rate rapidly increased by ∼25 % within a few minutes and then gradually declined over ∼24 h to settle back to baseline. The first event happened around midnight between 04. and 05.02.2022 and a second one 60 h later at noon on the 06.02.2022. Excluding these events from averaging results in a 3 % underestimation of exhaled mass, motivating a continuous monitoring solution for wet mofettes with comparable dynamics. Similar anomalies were observed by Lübben & Leven (2022) at a different mofette "R" at the site (Lübben & Leven, 2018), but dismissed as measurement error, as the event was only monitored once in their time-series. The reproducibility of these measurements with a completely different system as ours suggests there is an underlying process causing these events. Timing and magnitude of seismic activity in the wider region appear to be largely unrelated to the occurrence of flow anomalies during the period observed. Though no record of groundwater levels is present for the site, the flow anomalies can be assumed to be unrelated to groundwater levels of the Quaternary aquifer, as they are mainly controlled by the water level changes in the adjacent River Neckar, and there are no other disturbances of the aquifer in the closer vicinity, such as water supply wells. Besides the leap in flow rate, several other anomalies were measured during such an event: Most prominently, both events coincided with a very short (<1 min) but significant temperature drop of nearly 2 K measured by the thermistor mounted in the center of the chimney (Fig. 2c). Furthermore, right at the beginning of each event, one single measurement of a greatly reduced flow rate was recorded. A very brief and dramatic reduction in CO_2 concentration to around 50 % (not visible in Fig. 8) is also noticeable at this time. A drop this large is unlikely to be a consequence of the sensor's temperature dependence discussed above.

These observations suggest that the advective CO_2 degassing at the Starzach site obeys cold-water geyser mechanics (Han et al., 2013), albeit less effectively. Only a few cold-water geysers are known globally, with the world's most prominent CO_2-driven cold-water geyser being located in Andernach, Germany (Glennon & Pfaff, 2005). The periodic eruptions of a cold water geyser originate from the saturation of a water-filled cavity, which is constantly being supplied with gas from below. Oversaturation of the dissolved gas eventually leads to exsolution and uprising of gas bubbles. This reduces the pressure exerted by the overlying water column and initiates a positive feedback as the reduced pressure favours even more exsolution, resulting in an

eruption (Glennon & Pfaff, 2005, Han et al., 2013). Eruption intervals and durations of known cold-water geysers vary between minutes and hours (Glennon & Pfaff, 2005). Jung et al. (2015) found eruption intervals and durations to be roughly proportional for the Crystal Geyser (Utah, USA) while the factor changes over time. The flow rate anomalies we observed would accordingly correspond to eruptions with an interval of several days and a duration of one day. Han et al. (2013) found steep temperature drops during eruptions of the Crystal Geyser and explain those with Joule-Thomson cooling and endothermic CO_2 exsolution. However, the temperature drops we saw here are intermittent. This, together with the brief dips in flow rate, suggest a different cause. The cup anemometer we utilize for flow measurement is inherently independent of flow direction (Section 3.2). However, both a complete temporary flow stop as well as a flow change to the opposite direction will cause its rotation to decrease – albeit briefly. The latter seems to be the case here: As the mofette changes from exhaling to inhaling, cold surrounding air is transported inside the chimney to the thermistor, explaining both its measured temperature drop and the decrease in CO_2 concentration. Apparently, this flow direction change happens over a short time period of 5 s to 15 s, as for both events only exactly one of the 10 s-spaced measurements captures it.

Lübben & Leven (2018) present a conceptual geologic model in which the claystone of the *Röt Formation* at the top of the *Upper Buntsandstein* in approx. 50 m depth acts as an impermeable barrier and therefore as a capstone for the uprising gas. Below, CO_2 ascends through the water-saturated sandstones of the *Middle and Lower Buntsandstein*, which presents a potential reservoir for gas accumulation. Tectonic faults through the *Röt Formation* and the *Lower Muschelkalk* act as relatively undisturbed pathways to the surface and eventually to our examined well (Fig. 1c). We assume the oversaturation of water with CO_2 happens initially below the *Röt Formation* in the reservoir. However, longer time series and further research is needed to further quantify this process.

Influence of meteorological parameters

The data obtained during our observation week does not suggest any significant connection between meteorological parameters and the degassing behaviour. The two flow rate anomalies described above do not coicide with any change in temperature, atmospheric pressure, precipitation or other atmospheric variables we recorded. In general, pressure inside the chimney closely follows atmospheric pressure measured at the central station. This is expected for a chimney diameter this large as no significant pressure is built up. Atmospheric pressure is known to influence diffuse degassing via the "atmospheric pumping" effect (Forde et al., 2019, Nilson et al., 1991) or change geyser eruption activity (Rinehart, 1972). Nevertheless, neither of the two cold air front passages resulted in an immediately noticeable variation in exhaled gas amount. However, when comparing the settling times it took to return to baseline flow after an event, a slightly faster decline can be observed after the second event, immediately after the second front has passed. This is a plausible connection given that the final 30 hPa pressure increase the second front introduced should correspond to an additional virtual ∼30 cm water column the ascending gas needs to overcome for an eruption, effectively reducing the flow rate. But the short time series we recorded here is insufficient to quantify this. Longer measurement periods spanning multiple seasons are needed to further investigate this effect.

5 Conclusion and outlook

Chimney-based designs are well suited to continuously monitor degassing from vents. We introduced a low-cost, portable chimney device for continuously monitoring advective degassing from a mofette. An examined mofette was found to exhale 465 kg ±16 % of CO_2 per day, a result that is in line with previous measurements at the site (Lübben & Leven, 2022). During a short observation period of one week, meteorological parameters such as atmospheric pressure were found to have no immediate effect on the degassing behaviour, even during significant events as cold-front passages with steep atmospheric pressure changes.

Contrary to existing designs, our volumetric flow rate measurement is density-independent and can thus be used for a variety of other gases and gas mixtures. Being developed for continuous operation, this instru-

ment is suitable to monitor long-term changes such as the observed shift of degassing intensity from one mofette to another or geyser-like eruptions happening on different time scales. Finding a correlation to earthquake activity is another reasonable application (Han et al., 2013, Rinehart, 1972, Woith et al., 2023). This could be especially interesting for the Starzach site where small-magnitude earthquakes happen occasionally in the region.

For degassing of greatly different output magnitudes, the 3D-printed chimney can be easily reprinted with an appropriate diameter, followed by a recalibration of the flow rate according to the procedure we described here. The adapter from chimney to vent (a 50 cm-diameter cut-open plastic barrel in Fig. 2a) can also be chosen freely, for example by 3D-printing a custom cup or even employing flexible material such as used by Rogie et al. (2000).

An improvement of the temporal resolution could be achieved by introducing a pinhole disk in the chimney and deriving the flow rate from the difference in pressure before and after the constriction (Bentley, 2005). The density-dependence of this approach needs to be accounted for, though. Another possibility is to integrate a custom 1D-ultrasonic anemometer into the chimney, which can measure the flow velocity independently of the gas by design. In general, utilization of waterproof pressure sensors such as the Bosch BMP384 or BMP585 is preferrable. Furthermore, local on-device storage of the data on a memory card can be implemented if offline operation is desired. For future flow rate calibrations using a similar bag-filling technique as demonstrated in this paper, we suggest using foil-balloons of a more quantifiable geometric shape (e.g. a sphere) with a large diameter (e.g. >50 cm) to decrease the volumetric uncertainty.

Acknowledgements We would like to thank Max-Richard Freiherr von Rassler for the field access and the good cooperation. Thanks to Kevin Hörmle, Verena Mühlberger, Lukas Dörner and Björn Riebandt for support with field work and parts of the design. We furthermore appreciate the comments of two anonymous reviewers, which helped to improve the manuscript.

Author contributions Yann Büchau designed the instrument, performed the measurements and analyses, and prepared the manuscript. Carsten Leven supported the preparation of the manuscript with the site-related descriptions and proofreading. Jens Bange provided guidance and proofreading.

Funding Open Access funding enabled and organized by Projekt DEAL. This work was supported by the German Research Foundation (DFG) under grant number BA 1988/19-1. The equipment was largely financed by the Alfred-Teufel Foundation.

Availability of data and materials Field data is available from PANGAEA Büchau et al. (2023).

Code availability Code is available at https://gitlab.com/tue-umphy/co2mofetten.

Declarations

All authors have read, understood, and have complied as applicable with the statement on "Ethical responsibilities of Authors" as found in the Instructions for Authors.

Conflict of interest/Conflict of interest The authors have no relevant financial or non-financial interests to disclose.

Ethics approval Not applicable

Consent to participate Not applicable

Consent for publication Not applicable

References

Alfonso-Corcuera, D., Pindado, S., Ogueta-Gutiérrez, M., & Sanz-Andrés, A. (2021). Bearing friction effect on cup anemometer performance modelling. *Journal of Physics: Conference Series* (vol. 2090, p.012101). https://doi.org/10.1088/1742-6596/2090/1/012101

Baldocchi, D. (2003). Assessing the eddy covariance technique for evaluating carbon dioxide exchange rates of ecosystems: past, present and future. *Global Change Biology, 9*(4), 479–492. https://doi.org/10.1046/j.1365-2486.2003.00629.x

Beaubien, S., Ciotoli, G., & Lombardi, S. (2003). Carbon dioxide and radon gas hazard in the Alban Hills area (central Italy).

Journal of Volcanology and Geothermal Research, 123(1–2), 63–80. https://doi.org/10.1016/S0377-0273(03)00028-3. Retrieved from https://www.sciencedirect.com/science/article/pii/S0377027303000283

Bentley, J. P. (2005). *Principles of measurement systems* (4th ed.). Pearson Education.

Büchau, Y.G., van Kesteren, B., Platis, A., Bange, J. (2022). An Autarkic Wireless Sensor Network to Monitor Atmospheric CO2 Concentrations. *Meteorologische Zeitschrift (Contrib. Atm. Sci.)*, https://doi.org/10.1127/metz/2022/1125

Büchau, Y., Dörner, L., Bange, J. (2023). Short-term Comprehensive CO2 Degassing Dataset from a Mofette at the Starzach Site in Winter 2022 Obtained with a Custom Flow Meter, Including Atmospheric Variables [data set]. https://doi.org/10.1594/PANGAEA.963786. PANGAEA. Retrieved from https://doi.pangaea.de/10.1594/PANGAEA.963786 (https://doi.pangaea.de/10.1594/PANGAEA.963786).

Burton, M. R., Sawyer, G. M., & Granieri, D. (2013). Deep Carbon Emissions from Volcanoes. *Reviews in Mineralogy and Geochemistry, 75*(1), 323–354. https://doi.org/10.2138/rmg.2013.75.11. https://pubs.geoscienceworld.org/msa/rimg/article-pdf/75/1/323/2954430/323_REV075C11.pdf

Busch, N. E., & Kristensen, L. (1976). Cup anemometer overspeeding. *J. Appl. Meteorol., 15*(12), 1328–1332.

Camarda, M., De Gregorio, S., Capasso, G., Di Martino, R. M., Gurrieri, S., & Prano, V. (2019). The monitoring of natural soil CO2 emissions: Issues and perspectives. *Earth-Science Reviews, 198*, 102928. https://doi.org/10.1016/j.earscirev.2019.102928 Retrieved from https://www.sciencedirect.com/science/article/pii/S0012825219301151

Camuffo, D. (2019). Measuring wind and indoor air motions. *Microclimate for cultural heritage* (pp. 483–511). Elsevier.

Carapezza, M. L., & Granieri, D. (2004). CO2 soil flux at Vulcano (Italy): Comparison between active and passive methods. *Applied Geochemistry, 19*(1), 73–88. https://doi.org/10.1016/S0883-2927(03)00111-2 Retrieved from https://www.sciencedirect.com/science/article/pii/S0883292703001112

Chevallier, F., Fisher, M., Peylin, P., Serrar, S., Bousquet, P., Bréon, F.-M, ..., Ciais, P. (2005). Inferring CO2 sources and sinks from satellite observations: Method and application to TOVS data. *Journal of Geophysical Research: Atmospheres*, *110*(D24), https://doi.org/10.1029/2005JD006390

Chiodini, G., Cardellini, C., Amato, A., Boschi, E., Caliro, S., Frondini, F., Ventura, G. (2004). Carbon dioxide Earth degassing and seismogenesis in central and southern Italy. *Geophysical Research Letters*, *31*(7), https://doi.org/10.1029/2004gl019480

Chiodini, G., Cioni, R., Guidi, M., Raco, B., & Marini, L. (1998). Soil CO2 flux measurements in volcanic and geothermal areas. *Applied Geochemistry, 13*(5), 543–552. https://doi.org/10.1016/S0883-2927(97)00076-0 Retrieved from https://www.sciencedirect.com/science/article/pii/S0883292797000760

Dasgupta, R. (2013). Ingassing, Storage, and Outgassing of Terrestrial Carbon through Geologic Time. *Reviews in Mineralogy and Geochemistry., 75*(1), 183–229. https://doi.org/10.2138/rmg.2013.75.7 https://pubs.geoscienceworld.org/msa/rimg/article-pdf/75/1/183/2952840/183_REV075C07.pdf

Elias, T., Sutton, A. J., Oppenheimer, C., Horton, K. A., Garbeil, H., Tsanev, V., ..., & Williams-Jones, G. (2006). Comparison of COSPEC and two miniature ultraviolet spectrometer systems for SO2 measurements using scattered sunlight. *Bulletin of Volcanology, 68*(4), 313–322. https://doi.org/10.1007/s00445-005-0026-5

Etling, D. (2008). *Theoretische Meteorologie: Eine Einführung*. Springer-Verlag.

Farrar, C. D., Sorey, M. L., Evans, W. C., Howle, J. F., Kerr, B. D., Kennedy, B. M., ..., & Southon, J. R. (1995). Forest-killing diffuse CO2 emission at Mammoth Mountain as a sign of magmatic unrest. *Nature, 376*(6542), 675–678. https://doi.org/10.1038/376675a0

Feitz, A., Radke, B., Ricard, L., Glubokovskikh, S., Kalinowski, A., Wang, L., ..., & Credoz, A. (2022). The CO2CRC Otway shallow CO2 controlled release experiment: Fault characterization and geophysical monitoring design. *Int. J. Greenh. Gas Con., 118*, 103667. https://doi.org/10.1016/j.ijggc.2022.103667

Feitz, A., Schroder, I., Phillips, F., Coates, T., Negandhi, K., Day, S., ..., & Griffith, D. (2018). The Ginninderra CH4 and CO2 release experiment: An evaluation of gas detection and quantification techniques. *International Journal of Greenhouse Gas Control, 70*, 202–224. https://doi.org/10.1016/j.ijggc.2017.11.018

Flohr, A., Schaap, A., Achterberg, E. P., Alendal, G., Arundell, M., Berndt, C., ..., & Connelly, D. (2021). Towards improved monitoring of offshore carbon storage: A real-world field experiment detecting a controlled sub-seafloor CO2 release. *International Journal of Greenhouse Gas Control, 106*, 103237. https://doi.org/10.1016/j.ijggc.2020.103237 Retrieved from https://www.sciencedirect.com/science/article/pii/S1750583620306629

Foken, T. (2021). *Springer Handbook of Atmospheric Measurements*. Springer International Publishing. https://doi.org/10.1007/978-3-030-52171-4

Forde, O. N., Cahill, A. G., Beckie, R. D., & Mayer, K. U. (2019). Barometric-pumping controls fugitive gas emissions from a vadose zone natural gas release. *Scientific Reports, 9*(1), 1–9. https://doi.org/10.1038/s41598-019-50426-3

Forster, P., Storelvmo, T., Armour, K., Collins, W., Dufresne, J.-L., Frame, D., . . . Zhang, H. (2021). The Earth's Energy Budget, Climate Feedbacks, and Climate Sensitivity [Book Section]. In V. Masson-Delmotte et al. (Eds.), Climate change 021: The physical science basis. contribution of working group i to the sixth assessment report of the intergovernmental panel on climate change (pp. 923–1054). Cambridge, United Kingdom and New York, USA: Cambridge University Press. https://doi.org/10.1017/9781009157896.009

Galle, B., Oppenheimer, C., Geyer, A., McGonigle, A. J., Edmonds, M., & Horrocks, L. (2003). A miniaturised ultraviolet spectrometer for remote sensing of SO2 fluxes: A new tool for volcano surveillance. *Journal of Volcanology and Geothermal Research, 119*(1), 241–254. https://doi.org/10.1016/S0377-0273(02)00356-6 Retrieved from https://www.sciencedirect.com/science/article/pii/S0377027302003566

Gasser, T., Guivarch, C., Tachiiri, K., Jones, C. D., & Ciais, P. (2015). Negative emissions physically needed to keep global

warming below 2°C. *Nature Communications, 6*(1), 7958. https://doi.org/10.1038/ncomms8958

Gaubert, B., Stephens, B. B., Basu, S., Chevallier, F., Deng, F., & Kort, E.A.,..., Yin, Y. (2019). Global atmospheric CO2 inverse models converging on neutral tropical land exchange, but disagreeing on fossil fuel and atmospheric growth rate. *Biogeosciences (Online), 16*, 117–134. https://doi.org/10.5194/bg-16-117-2019 Retrieved from https://api.semanticscholar.org/CorpusID:56227065

Glennon, J. A., & Pfaff, R.M. (2005). The operation and geography of carbon dioxide-driven, cold-water "geysers". *The GOSA Transactions*, *9*, 184–192, Retrieved from https://www.researchgate.net//profile/Alan-Glennon/publication/216876596_The_operation_and_geography_of_carbon-dioxide-driven_cold-water_geysers/links/5b444580458515f71cb8a698/The-operation-and-geography-of-carbon-dioxide-driven-cold-water-geysers.pdf

Gurrieri, S., & Valenza, M. (1988). Gas transport in natural porous mediums: A method for measuring CO2 flows from the ground in volcanic and geothermal areas. *Rend. Soc. Ital. Mineral. Petrol., 43*, 1151–1158.

Han, W. S., Lu, M., McPherson, B. J., Keating, E. H., Moore, J., Park, E., ..., Jung, N.-H. (2013). Characteristics of CO2-driven cold-water geyser, Crystal Geyser in Utah: Experimental observation and mechanism analyses. *Geofluids, 13*(3), 283–297. https://doi.org/10.1111/gfl.12018

Haro, K., Ouarma, I., Nana, B., Bere, A., Tubreoumya, G. C., Kam, S. Z., ..., Koulidiati, J. (2019). Assessment of CH4 and CO2 surface emissions from Polesgo's landfill (Ouagadougou, Burkina Faso) based on static chamber method. *Adv. Clim. Change Res., 10*(3), 181–191. https://doi.org/10.1016/j.accre.2019.09.002 Retrieved from https://doi.org/www.sciencedirect.com/science/article/pii/S1674927819300929

Holloway, S., Pearce, J., Hards, V., Ohsumi, T., & Gale, J. (2007). Natural emissions of CO2 from the geosphere and their bearing on the geological storage of carbon dioxide. *Energy, 32*(7), 1194–1201. https://doi.org/10.1016/j.energy.2006.09.001

Horton, K. A., Williams-Jones, G., Garbeil, H., Elias, T., Sutton, A. J., Mouginis-Mark, P., ..., Clegg, S. (2006). Real-time measurement of volcanic SO2 emissions: Validation of a new UV correlation spectrometer (FLYSPEC). *B. Volcanol., 68*(4), 323–327. https://doi.org/10.1007/s00445-005-0014-9

Inguaggiato, S., Vita, F., Cangemi, M., Calderone, L. (2020). Changes in CO2 soil degassing style as a possible precursor to volcanic activity: The 2019 case of stromboli paroxysmal eruptions. *Applied Sciences, 10*(14), https://doi.org/10.3390/app10144757 Retrieved from https://www.mdpi.com/2076-3417/10/14/4757

IPCC. (2006). Guidelines for National Greenhouse Gas Inventories (H. Eggleston, L. Buendia, K. Miwa, T. Ngara, & K. Tanabe, Eds.). Inst. Glob. Environ. Strat. Retrieved from https://www.ipcc-nggip.iges.or.jp/public/2006gl/index.html (Prepared by the National Greenhouse Gas Inventories Programme)

Jonas, M., Bun, R., Nahorski, Z., Marland, G., Gusti, M., & Danylo, O. (2019). Quantifying greenhouse gas emissions. *Mitigation and Adaptation Strategies for Global Change, 24*(6), 839–852. https://doi.org/10.1007/s11027-019-09867-4

Jones, D., Barkwith, A., Hannis, S., Lister, T., Gal, F., Graziani, S., ..., Widory, D. (2014). Monitoring of near surface gas seepage from a shallow injection experiment at the CO2 Field Lab. *Norway. Int. J. Greenh. Gas Con., 28*, 300–317. https://doi.org/10.1016/j.ijggc.2014.06.021

Jung, N.-H., Han, W. S., Han, K., & Park, E. (2015). Regional-scale advective, diffusive, and eruptive dynamics of CO2 and brine leakage through faults and wellbores. *Journal of Geophysical Research: Solid Earth, 120*(5), 3003–3025. https://doi.org/10.1002/2014jb011722

Kerrick, D. M. (2001). Present and past nonanthropogenic CO2 degassing from the solid earth. *Reviews of Geophysics, 39*(4), 565–585. https://doi.org/10.1029/2001RG000105

Lowenstern, J. B. (2001). Carbon Dioxide in Magmas and Implications for Hydrothermal Systems. *Mineralium Deposita, 36*(6), 490–502. https://doi.org/10.1007/s001260100185

Lübben, A., & Leven, C. (2018). The Starzach site in Southern Germany: a site with naturally occurring CO2 emissions recovering from century-long gas mining as a natural analog for a leaking CCS reservoir. *Environ. Earth Sci., 77*(316), https://doi.org/10.1007/s12665-018-7499-y

Lübben, A., & Leven, C. (2022). A gas-flow funnel system to quantify advective gas emission rates from the subsurface. *Environmental Earth Sciences, 81*(15), 1–11. https://doi.org/10.1007/s12665-022-10512-8

Mauder, M., Foken, T., Aubinet, M., & Ibrom, A. (2021). Eddy-Covariance Measurements. In T. Foken (Ed.), *Springer handbook of atmospheric measurements* (pp. 1485–1515). Cham: Springer International Publishing. https://doi.org/10.1007/978-3-030-52171-4_55

McGonigle, A. J. S., Oppenheimer, C., Galle, B., Mather, T. A., & Pyle, D.M. (2002). Walking traverse and scanning DOAS measurements of volcanic gas emission rates. *Geophysical Research Letters*, *29*(20), 46–1–46–4, https://doi.org/10.1029/2002GL015827

Müller, M., Graf, P., Meyer, J., Pentina, A., Brunner, D., Perez-Cruz, F., & Emmenegger, L. (2020). Integration and calibration of non-dispersive infrared (NDIR) CO2 low-cost sensors and their operation in a sensor network covering Switzerland. *Atmospheric Measurement Techniques, 13*(7), 3815–3834. https://doi.org/10.5194/amt-13-3815-2020 Retrieved from https://amt.copernicus.org/articles/13/3815/2020

Nilson, R. H., Peterson, E. W., Lie, K. H., Burkhard, N. R., & Hearst, J. R. (1991). Atmospheric pumping: A mechanism causing vertical transport of contaminated gases through fractured permeable media. *J. Geophys. Res. - Sol. Ea., 96*(B13), 21933–21948. https://doi.org/10.1029/91JB01836

OpenStreetMap contributors (2023). *Planet dump retrieved from* https://planet.osm.org. https://www.openstreetmap.org.

Pan, G., Xu, Y., & Ma, J. (2021). The potential of CO2 satellite monitoring for climate governance: A review. *Journal of Environmental Management, 277*, 111423. https://doi.org/10.1016/j.jenvman.2020.111423 Retrieved from https://www.sciencedirect.com/science/article/pii/S0301479720313487

Papadopoulos, K. H., Stefantos, N. C., Paulsen, U. S., & Morfiadakis, E. (2001). Effects of turbulence and flow inclina-

tion on the performance of cup anemometers in the field. *Boundary-Layer Meteorology, 101*(1), 77–107. https://doi.org/10.1023/A:1019254020039

Pérez, N. M., Melián, G. V., Hernández, P. A., Padrón, E., Padilla, G. D., Baldago, M. C., ..., Lagmay, A. M. (2022). Diffuse CO2 degassing precursors of the January 2020 eruption of Taal volcano. *Philippines. Sci. Rep., 12*(1), 19091. https://doi.org/10.1038/s41598-022-22066-7

Pickett-Heaps, C. A., Rayner, P. J., Law, R. M., Ciais, P., Patra, P. K., Bousquet, P., ..., Sweeney, C. (2011). Atmospheric CO2 inversion validation using vertical profile measurements: Analysis of four independent inversion models. *Journal of Geophysical Research: Atmospheres, 116*(D12), D12305. https://doi.org/10.1029/2010JD014887

Privat, R., & Jaubert, J.-N. (2014). Predicting the Phase Equilibria of Carbon Dioxide Containing Mixtures Involved in CCS Processes Using the PPR78 Model. C.R.V. do Morgado and V.P.P. Esteves (Eds.), *CO2 Sequestration and Valorization* (chap. 15). Rijeka: IntechOpen. https://doi.org/10.5772/57058

Rinehart, J. S. (1972). Fluctuations in geyser activity caused by variations in Earth tidal forces, barometric pressure, and tectonic stresses. *Journal of Geophysical Research, 77*(2), 342–350. https://doi.org/10.1029/JB077i002p00342

Rogie, J. D., Kerrick, D. M., Chiodini, G., & Frondini, F. (2000). Flux measurements of nonvolcanic CO2 emission from some vents in Central Italy. *J. Geophys. Res., 105*(B4), 8435–8445. https://doi.org/10.1029/1999JB900430

Schäfer, M., Richter, M., & Span, R. (2015). Measurements of the viscosity of carbon dioxide at temperatures from (253.15 to 473.15)K with pressures up to 1.2MPa. *J. Chem. Thermodyn., 89*, 7–15. https://doi.org/10.1016/j.jct.2015.04.015 Retrieved from https://www.sciencedirect.com/science/article/pii/S002196141500107X

Scholz, K., Ejarque, E., Hammerle, A., Kainz, M., Schelker, J., Wohlfahrt, G. (2021). Atmospheric CO2 exchange of a small mountain lake: limitations of eddy covariance and boundary layer modeling methods in complex terrain. *J. Geophys. Res. – Biogeo.*, *126*, e2021JG006286, https://doi.org/10.1029/2021JG006286

Štigler, J. (2012). Analytical Velocity Profile in Tube for Laminar and Turbulent Flow. Retrieved from Retrieved from https://dx.doi.org/10.13140/2.1.3153.5046

UNFCCC. (2015). Adoption of the Paris Agreement. https://unfccc.int/process-and-meetings/the-paris-agreement. Retrieved from https://unfccc.int/process-and-meetings/the-paris-agreement; https://unfccc.int/resource/docs/2015/cop21/eng/l09r01.pdf (United Nations Framework Convention on Climate Change)

Wallace, J.M., & Hobbs, P.V. (2006). Atmospheric Science: An Introductory Survey (2nd ed., vol. 92). Elsevier. ISBN 9780127329512

Werner, C., & Cardellini, C. (2006). Comparison of carbon dioxide emissions with fluid upflow, chemistry, and geologic structures at the Rotorua geothermal system. *New Zealand. Geothermics, 35*(3), 221–238. https://doi.org/10.1016/j.geothermics.2006.02.006 Retrieved from https://www.sciencedirect.com/science/article/pii/S0375650506000186

Werner, C., Fischer, T.P., Aiuppa, A., Edmonds, M., Cardellini, C., Carn, S., ..., et al. (2019). Carbon Dioxide Emissions from Subaerial Volcanic Regions: Two Decades in Review. In B.N. Orcutt, I. Daniel, & R. Dasgupta (Eds.), Deep carbon: Past to present (pp. 188–236). Cambridge University Press. Retrieved from https://www.cambridge.org/core/books/deepcarbon/carbon-dioxide-emissions-from-subaerial-volcanicregions/F8B4EFAE0DAF5306A8D397C23BF3F0D7

Williams-Jones, G., Stix, J., Hickson, C. (2008). *The COSPEC Cookbook: Making SO2 Measurements at Active Volcanoes*. IAVCEI, Methods in Volcanology. https://doi.org/10.13140/RG.2.2.13728.99845

Winson, A. E. G., Costa, F., Newhall, C. G., & Woo, G. (2014). An Analysis of the Issuance of Volcanic Alert Levels During Volcanic Crises. *Journal of Applied Volcanology, 3*(1), 14. https://doi.org/10.1186/s13617-014-0014-6

Woith, H., Vlček, J., Vylita, T., Dahm, T., Fischer, T., Daskalopoulou, K, ..., Lanzendörfer, M. (2023). Effect of Pressure Perturbations on CO2 Degassing in a Mofette System: The Case of Hartoušov, Czech Republic. *Geosciences*, *13*(1), https://doi.org/10.3390/geosciences13010002 Retrieved from https://www.mdpi.com/2076-3263/13/1/2

Zhao, J., Zhang, M., Xiao, W., Wang, W., Zhang, Z., Yu, Z., ..., Lee, X. (2019). An evaluation of the flux-gradient and the eddy covariance method to measure CH4, CO2, and H2O fluxes from small ponds. *Agricultural and Forest Meteorology, 275*, 255–264. https://doi.org/10.1016/j.agrformet.2019.05.032

C Büchau et al. (2024b): PARMESAN Meteorological Analysis Software

Büchau, Y. G., Mashni, H., Bramati, M., Savvakis, V., Schäfer, I., Jung, S., Miranda-Garcia, G., Hardt, D. and Bange, J. 'PARMESAN: Meteorological Timeseries and Turbulence Analysis Backed by Symbolic Mathematics'. In: *Journal of Open Source Software* 9.94 (9th Feb. 2024), 6127. DOI: 10.21105/joss.06127.

The Journal of Open Source Software

PARMESAN: Meteorological Timeseries and Turbulence Analysis Backed by Symbolic Mathematics

Yann Georg Büchau [1¶], **Hasan Mashni**[1], **Matteo Bramati**[1], **Vasileios Savvakis** [1], **Ines Schäfer**[1], **Saskia Jung**[1], **Gabriela Miranda-Garcia** [1], **Daniel Hardt** [2], **and Jens Bange** [1]

1 Eberhard Karls Universität Tübingen, Germany **2** Akaflieg Braunschweig e.V., Braunschweig, Germany
¶ Corresponding author

DOI: 10.21105/joss.06127

Software

- Review
- Repository
- Archive

Editor: Martin Fleischmann

Reviewers:

- @kgoebber
- @arbennett

Submitted: 17 September 2023
Published: 09 February 2024

Summary

PARMESAN (the **P**ython **A**tmospheric **R**esearch Package for **ME**teorological Time**S**eries and Turbulence **AN**alysis) is a Python package providing common functionality for atmospheric scientists doing time series or turbulence analysis. Several meteorological quantities such as potential temperature, various humidity measures, gas concentrations, wind speed and direction, turbulence and stability parameters can be calculated. Furthermore, signal processing functionality such as properly normed variance spectra for frequency analysis is available. In contrast to existing packages with similar goals, its routines for physical quantities are derived from symbolic mathematical expressions, enabling inspection, automatic rearrangement, reuse and recombination of the underlying equations. Building on this, PARMESAN's functions as well as their comprehensive parameter documentation are mostly auto-generated, minimizing human error and effort. In addition, sensitivity/error propagation analysis is possible as mathematical operations like derivations can be applied to the underlying equations. Physical consistency in terms of units and value domains are transparently ensured for PARMESAN functions. PARMESAN's approach can be reused to simplify implementation of robust routines in other fields of physics.

Statement of need

The need to assert properly balanced physical units right from within running programs and models has been recognised for a long time now (Chizeck et al., 2009; Cooper & McKeever, 2008). Unit conversion errors in science and engineering have caused costly system failures such as the NASA Mars Climate Orbiter crash in 1999 (NASA, 1999).

Nowadays, the Python ecosystem comprises many packages that ease specific tasks when performing physical calculations: `numpy` (Harris et al., 2020) and `scipy` (Virtanen et al., 2020) provide efficient numerical routines, `pandas` (The pandas development team, 2023) and `xarray` (Hoyer & Hamman, 2017) provide structures to read, write and aggregate data, `pint` (Grecco & Chéron, 2023) handles physical units and the `uncertainties` package (Lebigot, 2023) simplifies linear error propagation. Partly based on those, collections of routines for atmospheric science exist such as `metpy` (May et al., 2022), `iris` (Met Office, 2010 - 2023) and `aoslib`/PyAOS (PyAOS, 2023). However these focus more on gridded, spatial data which is common in modelling and remote sensing and have little functionality for turbulence analysis. Turbulence plays an important role in atmospheric exchange processes, especially in the planetary boundary layer (Stull, 1988). It is a statistical process and thus mostly quantified through high-resolution in-situ measurement techniques (Foken, 2021). `metpy` and `iris` can both handle units and require the user to explicitly specify them. Their physical quantities are

The Journal of Open Source Software

calculated using hard-coded expressions. In contrast, the `atmos` package (McGibbon, 2023) has implemented an equation solving system for more flexible reusability and less hard-coding of relationships between quantities. Its development seems to have stalled since 2020, though. None of the above packages have a mechanism for transparently checking that input and output values are within reasonable physical bounds.

PARMESAN addresses the aforementioned gaps by providing functions for meteorological quantities that are backed by symbolic mathematical expressions employing SymPy (Meurer et al., 2017), a powerful computer algebra system written purely in Python. Inputs and outputs are checked for and potentially converted to correct units while asserting that the physical domains are not exceeded. It can rearrange its equations and thus flexibly increase the number of available functions. PARMESAN has already been used successfully in Büchau et al. (2022), Büchau et al. (2023), Wüsteney (2023) and Herrmann (2023) for data analysis of meteorological measurements.

Structure

Functions for physical quantities in PARMESAN are based on symbolic mathematical equations created using SymPy (Meurer et al., 2017). PARMESAN defines a descriptive list of symbols (i.e. variables and constants, Figure 1) and relates them to form the common laws of thermodynamics, parametrisations and definitions used in atmospheric science.

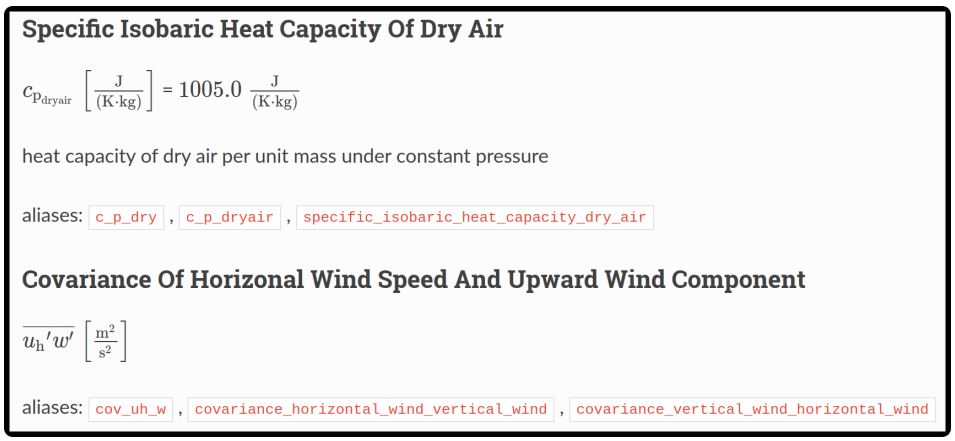

Figure 1: Excerpt of auto-generated symbol list in `parmesan.symbols`. Symbols have metadata such as descriptions, units and default values attached. For readability, they can be referred to with different variable names, which are also available as parameter aliases when calling functions in PARMESAN.

This approach has many advantages over the traditional method of hard-coding mathematical operations between function inputs using language-specific constructs. First of all, information about the mathematical relationship between quantities is not lost, but can instead be queried and reused. SymPy equations can be rearranged and recombined to generate new expressions, enabling the generation of many specific functions from a set of base equations. Additionally, SymPy expressions are translatable into code for numerous programming languages. PARMESAN uses this mechanism to turn its equations into executable Python functions that use the efficient `numpy` package internally (Harris et al., 2020), so no runtime overhead is introduced and array inputs and outputs are supported. Symbolic expressions are automatically simplified and terms cancelled accordingly, revealing the set of input parameters an equation really depends on. This information is then used to automatically generate extensive documentation for each individual function (Figure 2) - a great benefit for consistency and minimisation of human effort and oversight in the documentation.

JOSS
The Journal of Open Source Software

Creating new functions in or from PARMESAN thus often requires only very few lines of code. Here is a compacted version of PARMESAN's function for potential temperature specifically for dry air:

```
from parmesan.symbols import *   # Import all of PARMESAN's symbols
@from_sympy() # decorator turning SymPy expression into code and documentation
def potential_temperature(): # no arguments necessary, added automatically
    return T * (p_ref / p) ** (R_dryair / c_p_dryair)
    # SymPy expression - practically equal to typical Python code
```

In this case, the resulting quantity is derived from the function's name, documentation is generated (Figure 2) and the equation is immediately checked for units consistency employing the `pint` package (Grecco & Chéron, 2023). Each symbol has metadata attached, such as a physical unit and a domain (Figure 1). These are available to the resulting function for assertion, so a PARMESAN function will check and auto-convert input and output units and issue a warning when unphysical values arise such as negative absolute temperatures:

```
# Implicit Units
potential_temperature(T=300, p=100000) # K and Pa assumed
# 300.0 K

# Explicit Units
from parmesan.units import units # PARMESAN's predefined units
potential_temperature(T=units.Quantity(20,"°C"), p=950 * units.hPa)
# 297.477188635086 K

# Parameter/Symbol Aliases
potential_temperature(temperature=300, pressure=100000)
# 300.0 K

# Arrays
import numpy as np
potential_temperature(T=300, p=np.array([950,980,1010]) * units.hPa)
# Magnitude: [304.42830151978785 301.7364178157801 299.14844787358106]
#     Units: K

# Bounds check
potential_temperature(T=-10, p=1010*units.hPa) # temperature out of bounds
# OutOfBoundsWarning: 1 of 1 input values to potential_temperature for
# argument 'T' are out of bounds defined by 'positive': [-10] at indices [0]
# -9.971614929119369 K

# Units check
potential_temperature(T=300, p=1010*units.degrees) # wrong unit -> error
# DimensionalityError: potential_temperature():
#    p=<Quantity(1010, 'degree')> could not be converted to pascal:
#    Cannot convert from 'degree' (dimensionless) to 'pascal'
#    ([mass] / [length] / [time] ** 2)
```

The Journal of Open Source Software

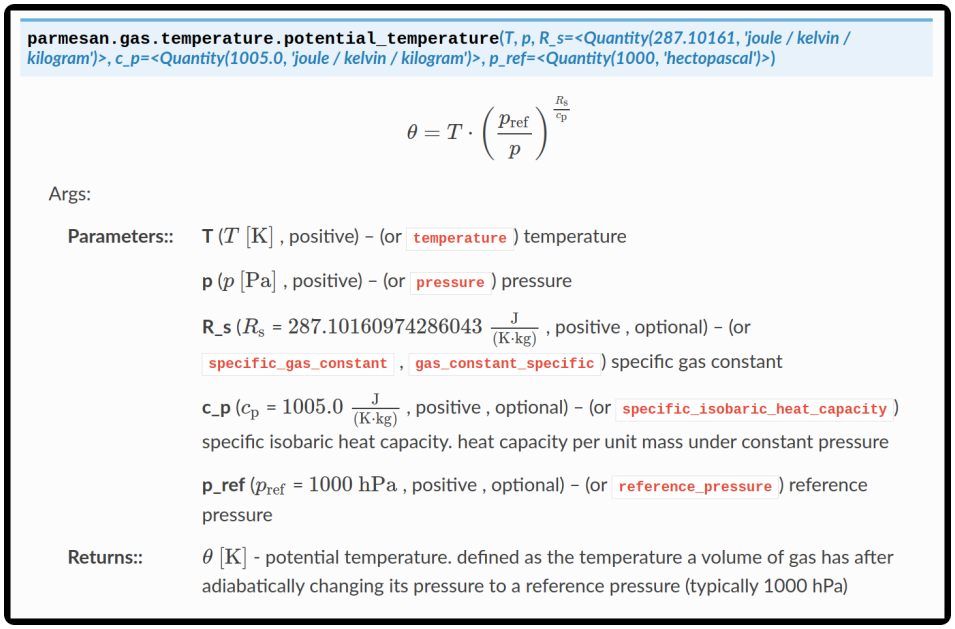

parmesan.gas.temperature.potential_temperature(*T, p, R_s=<Quantity(287.10161, 'joule / kelvin / kilogram')>, c_p=<Quantity(1005.0, 'joule / kelvin / kilogram')>, p_ref=<Quantity(1000, 'hectopascal')>*)

$$\theta = T \cdot \left(\frac{p_{\mathrm{ref}}}{p} \right)^{\frac{R_s}{c_p}}$$

Args:

Parameters:: **T** (T [K] , positive) – (or `temperature`) temperature

p (p [Pa] , positive) – (or `pressure`) pressure

R_s (R_s = 287.10160974286043 $\frac{\mathrm{J}}{(\mathrm{K \cdot kg})}$, positive , optional) – (or `specific_gas_constant` , `gas_constant_specific`) specific gas constant

c_p (c_p = 1005.0 $\frac{\mathrm{J}}{(\mathrm{K \cdot kg})}$, positive , optional) – (or `specific_isobaric_heat_capacity`) specific isobaric heat capacity. heat capacity per unit mass under constant pressure

p_ref (p_{ref} = 1000 hPa , positive , optional) – (or `reference_pressure`) reference pressure

Returns:: θ [K] - potential temperature. defined as the temperature a volume of gas has after adiabatically changing its pressure to a reference pressure (typically 1000 hPa)

Figure 2: Auto-generated comprehensive parameter documentation and LaTeX-formatted equation for PARMESAN's `potential_temperature()` function to calculate potential temperature from atmospheric pressure and temperature. Parameter aliases, units, defaults and bounds are taken from PARMESAN's symbol library (Figure 1) and used coherently across functions in PARMESAN.

Another benefit of having the underlying symbolic expression for an equation available is the possibility to do sensitivity analysis. PARMESAN can derive the maximum relative error $\Delta y_{\mathrm{max,rel}}$ (Equation 1) for its symbolic functions (Figure 3):

$$\begin{aligned} \Delta y_{\mathrm{max}}(x_1, \ldots, x_n) &= \sum_{i=1}^{n} \left| \frac{\partial y}{\partial x_i} \right| \cdot \Delta x_{i_{\mathrm{max}}} \\ \Delta y_{\mathrm{max,rel}} &= \frac{\Delta y_{\mathrm{max}}}{\overline{y}} \end{aligned} \tag{1}$$

The maximum relative error is a conservative estimation method for the propagation of errors of input quantities x_i to effective error in the output quantity y, assuming the most severe combination of input quantity deviations $\Delta x_{i_{\mathrm{max}}}$. Custom sensitivity analyses can also be implemented based on PARMESAN's equations.

JOSS The Journal of Open Source Software

▾ Click here to show maximum error estimation equation

Generated with `maximum_error_equation` (`relative=True`)

You can access this equation via `potential_temperature.maximum_error.equation` and the executable Python function via `potential_temperature.maximum_error`.

$$\Delta\theta_{\max_{\text{rel}}} = \Delta T_{\max_{\text{rel}}} + \Delta p_{\max_{\text{rel}}} \cdot \frac{R_\text{s}}{c_\text{p}}$$

Figure 3: Auto-generated maximum relative error equation (Equation 1) for PARMESAN's `potential_temperature()` function (Figure 2). Symbolic PARMESAN functions automatically have a sensitivity analysis attached to quantify how a change in input parameters affects the output. In this case, the maximum expected relative error of potential temperature [%] is the sum of the maximum relative errors of temperature and pressure [%], with the pressure term scaled by a factor.

PARMESAN can also rearrange its existing equations (Figure 4) for a quantity of interest by its provided `get_function()` function:

```
from parmesan.symbols import *
# get (or rearrange) functions that calculate mixing ratio
mixing_ratio_functions = list(get_function(result=mixing_ratio)
# get (or rearrange) functions that calculate mixing ratio
# from at least temperature and pressure
mixing_ratio_functions = list(get_function(result=mixing_ratio, inputs=(T, p))
```

The functions found can be called as usual or their underlying equations can be examined by accessing their `.equation` attribute. In a Jupyter notebook (Kluyver et al., 2016) the equations appear as formatted markup similar to what is depicted in Figure 4.

`absolute_humidity_from_water_vapour_pressure` $\rightarrow \rho_\text{w} = \frac{e_\text{w}}{R_\text{h2o} \cdot T}$

`mixing_ratio_via_densities` $\rightarrow r = \frac{\rho_\text{w}}{\rho - \rho_\text{w}}$

`mixing_ratio_via_masses` $\rightarrow r = \frac{m_\text{w}}{m_\text{tot} - m_\text{w}}$

`mixing_ratio_via_pressures` $\rightarrow r = \frac{M_\text{h2o} \cdot e_\text{w}}{M_\text{dry} \cdot (-e_\text{w} + p)}$

`relative_humidity_via_dewpoint` $\rightarrow \text{RH} = \frac{T \cdot e^{-\frac{B_{\text{magnus}_\text{w}} \cdot (T - T_\text{c0})}{C_{\text{magnus}_\text{w}} + T - 2 \cdot T_\text{c0}}} \cdot e^{\frac{B_{\text{magnus}_\text{w}} \cdot (-T_\text{c0} + T_\text{d})}{C_{\text{magnus}_\text{w}} - 2 \cdot T_\text{c0} + T_\text{d}}}}{T_\text{d}}$

Figure 4: Excerpt of auto-generated humidity equation list in PARMESAN's `humidity` module. As the underlying equations in PARMESAN's functions are available as symbolic expressions, it can provide overviews of all related equations.

Besides physical equations, PARMESAN provides tools often needed when analysing timeseries such as calculating second-order moments, variance spectrum (Figure 5), autocorrelation, structure function (variogram) and running covariance, e.g. for calculating eddy fluxes (Foken, 2021), backed by the `scipy` package (Virtanen et al., 2020) for efficient numerics and `matplotlib` (Hunter, 2007) for visualisation. PARMESAN integrates with the common pandas

The Journal of Open Source Software

data analysis framework (The pandas development team, 2023) by adding a `.parmesan` accessor to `DataFrame` and `Series` objects to apply PARMESAN functions such as a variance spectrum or autocorrelation directly to them.

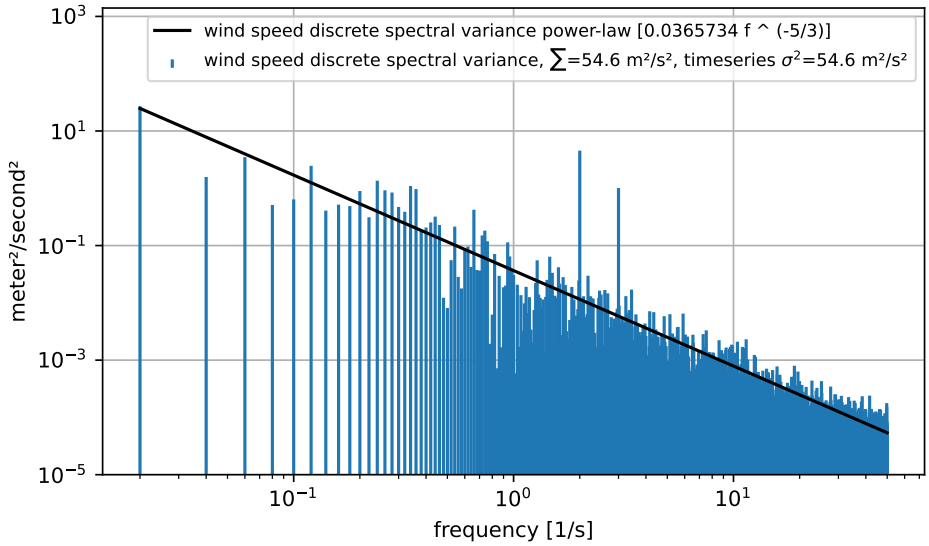

Figure 5: PARMESAN discrete `variance_spectrum()` of an artificial wind timeseries (random walk overlayed with 2Hz and 3Hz sine waves). Note how Parseval's Theorem (Stull, 1988) is correctly fulfilled as the timeseries variance equals the sum of discrete spectral variances. A Kolmogorov power-law fit (Ortiz-Suslow & Wang, 2019) was optionally added by PARMESAN.

Acknowledgements

This software originated in a project funded by the German Research Foundation (DFG) under grant number BA 1988/19-1.

References

Büchau, Y. G., Leven, C., & Bange, J. (2023). *A Portable low-cost Device to Quantify Advective Gas Fluxes from Mofettes into the Lower Atmosphere: First Application to Starzach Mofettes (Germany)*. https://doi.org/10.31223/X5ZX0D

Büchau, Y. G., van Kesteren, B., Platis, A., & Bange, J. (2022). An Autarkic Wireless Sensor Network to Monitor Atmospheric CO2 Concentrations. *Meteorol. Z. (Contrib. Atm. Sci.)*. https://doi.org/10.1127/metz/2022/1125

Chizeck, H. J., Butterworth, E., & Bassingthwaighte, J. B. (2009). Error detection and unit conversion. *IEEE Engineering in Medicine and Biology Magazine*, *28*(3), 50–58. https://doi.org/10.1109/MEMB.2009.932477

Cooper, J., & McKeever, S. (2008). A model-driven approach to automatic conversion of physical units. *Software: Practice and Experience*, *38*(4), 337–359. https://doi.org/10.1002/spe.828

Foken, T. (2021). *Springer Handbook of Atmospheric Measurements*. Springer International Publishing. https://doi.org/10.1007/978-3-030-52171-4

Grecco, H., & Chéron, J. (2023). pint: Operate and Manipulate Physical Quantities in Python. In *GitHub repository*. GitHub. https://github.com/hgrecco/pint

Harris, C. R., Millman, K. J., Walt, S. J. van der, Gommers, R., Virtanen, P., Cournapeau, D., Wieser, E., Taylor, J., Berg, S., Smith, N. J., Kern, R., Picus, M., Hoyer, S., Kerkwijk, M. H. van, Brett, M., Haldane, A., Río, J. F. del, Wiebe, M., Peterson, P., … Oliphant, T. E. (2020). Array programming with NumPy. *Nature*, *585*(7825), 357–362. https://doi.org/10.1038/s41586-020-2649-2

Herrmann, K. (2023). *Design Reiteration of a Chimney Gas Flowmeter for Natural CO2 Emissions from Mofettes: Differential Pressure Measurement Increases Resolution and Accuracy* [Bachelor's thesis]. University of Tübingen, Dept. of Geosciences. https://doi.org/10.15496/publikation-89337

Hoyer, S., & Hamman, J. (2017). xarray: N-D labeled arrays and datasets in Python. *Journal of Open Research Software*, *5*(1). https://doi.org/10.5334/jors.148

Hunter, J. D. (2007). Matplotlib: A 2D graphics environment. *Computing in Science & Engineering*, *9*(3), 90–95. https://doi.org/10.1109/MCSE.2007.55

Kluyver, T., Ragan-Kelley, B., Pérez, F., Granger, B., Bussonnier, M., Frederic, J., Kelley, K., Hamrick, J., Grout, J., Corlay, S., Ivanov, P., Avila, D., Abdalla, S., Willing, C., & team, J. development. (2016). Jupyter Notebooks – a publishing format for reproducible computational workflows. In F. Loizides & B. Scmidt (Eds.), *Positioning and Power in Academic Publishing: Players, Agents and Agendas* (pp. 87–90). IOS Press. https://doi.org/10.3233/978-1-61499-649-1-87

Lebigot, E. O. (2023). Uncertainties: a Python package for calculations with uncertainties. In *GitHub repository*. GitHub. https://github.com/lebigot/uncertainties/

May, R. M., Goebbert, K. H., Thielen, J. E., Leeman, J. R., Camron, M. D., Bruick, Z., Bruning, E. C., Manser, R. P., Arms, S. C., & Marsh, P. T. (2022). MetPy: A Meteorological Python Library for Data Analysis and Visualization. *Bulletin of the American Meteorological Society*, *103*(10), E2273–E2284. https://doi.org/10.1175/BAMS-D-21-0125.1

McGibbon, J. (2023). aoslib: An atmospheric sciences library for Python. In *GitHub repository*. GitHub. https://github.com/atmos-python/atmos

Met Office. (2010 - 2023). *Iris: A powerful, format-agnostic, and community-driven Python package for analysing and visualising Earth science data* (v3.6 ed.). https://doi.org/10.5281/zenodo.7948293

Meurer, A., Smith, C. P., Paprocki, M., Čertík, O., Kirpichev, S. B., Rocklin, M., Kumar, A., Ivanov, S., Moore, J. K., Singh, S., Rathnayake, T., Vig, S., Granger, B. E., Muller, R. P., Bonazzi, F., Gupta, H., Vats, S., Johansson, F., Pedregosa, F., … Scopatz, A. (2017). SymPy: symbolic computing in Python. *PeerJ Computer Science*, *3*, e103. https://doi.org/10.7717/peerj-cs.103

NASA. (1999). *Mars Climate Orbiter Mishap Investigation Board Phase I Report* (Mars Climate Orbiter Mishap Investigation Board, Ed.). National Aeronautics and Space Administration (NASA). https://llis.nasa.gov/llis_lib/pdf/1009464main1_0641-mr.pdf

Ortiz-Suslow, D. G., & Wang, Q. (2019). An Evaluation of Kolmogorov's -5/3 Power Law Observed Within the Turbulent Airflow Above the Ocean. *Geophysical Research Letters*, *46*(24), 14901–14911. https://doi.org/10.1029/2019GL085083

PyAOS. (2023). aoslib: A collection of standard atmospheric and oceanic sciences routines. In *GitHub repository*. GitHub. https://github.com/PyAOS/aoslib

Stull, R. B. (1988). *An Introduction to Boundary Layer Meteorology*. Kluwer Academic Publishers. https://doi.org/10.1007/978-94-009-3027-8

The pandas development team. (2023). *pandas-dev/pandas: Pandas* (Version v2.1.0rc0). Zenodo. https://doi.org/10.5281/zenodo.8239932

Virtanen, P., Gommers, R., Oliphant, T. E., Haberland, M., Reddy, T., Cournapeau, D., Burovski, E., Peterson, P., Weckesser, W., Bright, J., van der Walt, S. J., Brett, M., Wilson, J., Millman, K. J., Mayorov, N., Nelson, A. R. J., Jones, E., Kern, R., Larson, E., … SciPy 1.0 Contributors. (2020). SciPy 1.0: Fundamental Algorithms for Scientific Computing in Python. *Nature Methods*, *17*, 261–272. https://doi.org/10.1038/s41592-019-0686-2

Wüsteney, S. (2023). *Bodenwassergehalts-Messung in tonigen Böden des Starzacher Mofetten-Gebiets mittels SMT100 Sensoren: Korrektur der Topp-Gleichung* [Bachelor's thesis]. University of Tübingen, Dept. of Geosciences. https://doi.org/10.15496/publikation-89327

D Büchau and Bange (2025): Starzach CO_2 Emission Quantification with Sensor Network

Büchau, Y. G. and Bange, J. 'Quantification of Natural CO2 Emissions from Mofettes Using a Low-Cost Sensor Network at the Starzach Site in South-West Germany'. In: *PLOS Climate* 4.11 (25th Nov. 2025), e0000741. ISSN: 2767-3200. DOI: 10.1371/journal.pclm.0000741.

PLOS Climate

RESEARCH ARTICLE

Quantification of natural CO_2 emissions from mofettes using a low-cost sensor network at the Starzach site in South-West Germany

Yann Georg Büchau*, Jens Bange

Department of Geoscience, University of Tübingen, Tübingen, Baden-Württemberg, Germany

* yann-georg.buechau@uni-tuebingen.de

Abstract

We present a top-down method to derive CO_2 emissions from mofettes, using only point measurement time series at irregular locations. Notably, no wind vector information is needed, as gas transport is derived from cross-correlations between sensor stations and subsequently integrated using Gauss' divergence theorem. The method is applied to an existing low-cost sensor network at the Starzach site near the Black Forest in Germany, for which no comprehensive estimate of the total emissions exists yet. For validation, we use previous bottom-up measurements of individual mofette degassing and a Gaussian puff approach. Over a period of one and a half months around August 2022, we determine an average CO_2 emission rate of 3266 kg d^{-1} ±42% over a 400 m^2 area. This result is larger than expected and suggests that diffuse degassing plays a more important role at site than previously assumed. The method could also be applied for real-time monitoring of leaky CCS sites, for which the Starzach site is a natural analog.

OPEN ACCESS

Citation: Büchau YG, Bange J (2025) Quantification of natural CO_2 emissions from mofettes using a low-cost sensor network at the Starzach site in South-West Germany. PLOS Clim 4(11): e0000741. https://doi.org/10.1371/journal.pclm.0000741

Editor: Zhihua Zhang, Shandong University, CHINA

Received: September 4, 2025

Accepted: October 17, 2025

Published: November 25, 2025

Data availability statement: Analysed data is available at https://doi.org/10.5281/zenodo.17055782.

Funding: This work was supported by the DFG under grant number BA 1988/19-1.

Introduction

The greenhouse gases (GHGs) CO_2, methane (CH_4) and nitrous oxide (N_2O) are major drivers of global warming [1,2], with CO_2 having the strongest effect due to its increasingly high concentration in the Earth's atmosphere. Location and quantification of GHG emission sources is thus a vital step in identifying hotspots and verification of reduction methods. Both are tasks the countries under the Paris Agreement [3] have committed to, by keeping up-to-date emission inventories. In Germany for example, the Integrated Greenhouse Gas Monitoring System for Germany (ITMS) is a project working towards these tasks [4–6].

There is no single best method for such GHG emission quantification, as every approach fits a certain spatial and temporal scale of interest and requires specific data to exist, mostly atmospheric GHG concentrations and the wind field. While bottom-up approaches sum or extrapolate direct or indirect emission measurements at known sources, top-down methods use amospheric measurements to estimate the total emitted amount over an area [7,8]. Bottom-up and top-down estimates can differ

PLOS Climate

The equipment was largely financed by the Alfred-Teufel Foundation. The funders had no role in study design, data collection and analysis, decision to publish, or preparation of the manuscript.

Competing interests: The authors have declared that no competing interests exist.

significantly, with bottom-up being known for yielding lower total emissions because not all sources are known or their emissions being underreported [9,10]. If however the sources are known precisely, bottom-up estimates directly at their locations are more accurate, although their temporal resolution and long-term consistency are often lacking [11].

There exist several top-down trace gas emission quantification methods. As the transport of a trace gas in the atmosphere is governed by the equation of continuity, Fick's laws of diffusion, and ultimately the Navier-Stokes equations, common approaches for GHG emission quantification and source location are based on these physical laws, combinations or simplifications of them. Solving these equations numerically is done with Eularian atmospheric models such as ICON [12], PALM [13], MITRAS [14,15] and many others depending on the scale and complexity of interest. Provided initial and boundary conditions, preparatory work and significant computational resources, these eventually yield continuous fields of wind vector and potentially also trace gas concentrations for the simulated domain. This presents a versatile base for a variety of emission quantification schemes, most prominently inverse modelling by either solving a linear relationship between sources in the model and observations [16] or by simulating backwards transport of (an ensemble of) particles from observation points back to the sources. Examples of the latter are the inverse Lagrangian transport models HYSPLIT [17], STILT [18] and FLEXPART [19], which differ for example in their stochastic representation of turbulence.

In case no continuous Eularian model output is available, relying exclusively on measurements is possible for example by solving the Advection-Diffusion Equation (ADE) [20]. If numerical solving is unviable, common simplified analytical solutions of the ADE are the Gaussian plume or puff equation [20], which allow for quick simulation of concentration profiles or time series given meteorological conditions such as wind and atmospheric stability. Fitting a Gaussian plume or puff to concentration measurements with large, distinct peaks from emission events then give an estimate on the emitted mass of gas.

An even more rudimentary approach (often referred to as "mass balance approach") is based on the divergence theorem, where fluxes through a boundary around an emission hotspot are parametrised through wind and concentration measurements and then integrated to estimate the mass flow at the hotspot [21], potentially in combination with a Gaussian puff model [22]. A particular in-situ measurement type that provides both wind, concentrations, and gas flux data is the eddy covariance (EC) method, where fast measurements of the wind vector are correlated with fast trace gas concentration fluctuations to measure the turbulent transport by eddies directly [23]. While the quality of EC measurements is high, equipment is expensive, and the theory is difficult to apply in complex terrain or for inhomogeneous emissions [24] as the footprint of this single-point measurement depends heavily on the atmospheric conditions, raising representativeness concerns [25]. Furthermore, the standard EC method aims to quantify *vertical turbulent* gas transport resulting from the interplay of concentration and wind fluctuations and specifically neglects *horizontal* or *advective* fluxes with the mean wind, which might be very relevant depending on the site.

PLOS Climate

All of the above methods require knowledge of the wind vector, either by simulation, measurements, or assumptions. Furthermore, it is implicitly assumed that the trace gas of interest is transported directly with this wind vector. If for a GHG emitting site the prerequisites for the none above methods are satisfyingly fulfilled, custom solutions need to be developed. This can be the case for emission sites well in the meteorological microscale (spatial scale below 1 km) with heterogeneous emissions, and/or in complex terrain with intricate slope flows, heavy vegetation or small-scale features that reduce representativeness of wind measurements. The Starzach site, a site near the eastern slope of the Black Forest with natural, non-volcanic, magmatic CO_2 emissions from mofettes [26], falls into this category.

In the following, we present a top-down method for quantifying the CO_2 emissions at the Starzach site, based solely on CO_2 point measurement time series at irregular locations with no wind vector required. We cross-correlate sensor time series to reconstruct the near-surface CO_2 movement vector field, then apply the divergence theorem during situations of low vertical mixing to integrate the total emitted CO_2 flux over the area. The results are compared to previous bottom-up estimates and a Gaussian puff model approach.

Materials and methods

The Starzach site

The upper Neckar river valley east of the Black Forest in southern Germany is known for its natural CO_2 emissions of non-volcanic, magmatic origin [26]. During the 20th century, CO_2 gas was mined industrially in the area until yields eventually declined drastically, so that after around 100 years, practically no CO_2 exhaust was observable anymore [26]. In the 1980s, at the peak of active industrial extraction, individual wells in the Neckar valley, for which data exists, typically extracted 1000–4000 $t\,yr^{-1}$ (2800–11,000 $kg\,d^{-1}$) of CO_2, mostly by actively lowering the groundwater level with pumps to ease gas uprise [26]. The Starzach site is one of these extraction sites, located at a northern slope in the Neckar valley, with orographic structures, vegetation and trees far smaller than the resolution of common global circulation models (GCMs) or reanalyses datasets. To the authors' knowledge, no tailored wind field simulations exist for this region. Focused points of CO_2 exhalation (mofettes) with diameters up to 30 cm are scattered across the site, primarily along a north-westerly line, where a geological fault is suspected [26,27]. The main mofette area of interest in this analysis (Fig 1) has an extent of 20 m × 20 m. Over the 20 years after the termination of CO_2 mining, mofette activity gradually returned. In 2015, the mofette that was most prominent at the time was measured to emit around 75 $kg\,d^{-1}$ [29]. A three meter deep groundwater well that was added in 2014 has since transformed into the site's most active mofette, for which direct measurements yielded average emission rates of 465 $kg\,d^{-1}$ in winter 2022 [28], and roughly 520 $kg\,d^{-1}$ in summer 2023 [30]. All these post-mining bottom-up measurements were performed by direct quantification of CO_2 exhaust with gas funneling systems, but different equipment. They suggest an overall trend of increasing CO_2 emissions at the site over the years and a possible seasonal cycle due to variable groundwater levels. Judging from the previous measurements, the amount and visual activity of the mofettes in the core Starzach mofette area (Fig 1), a rough estimate of 1500 $kg\,d^{-1}$ of total emissions exclusively from individually identified mofettes can be made.

As CO_2 gas is nearly twice as dense as air under standard atmospheric conditions, it tends to flow or settle at the ground. This is visually evident for example in *Plate 4* of [31] from a smoke bomb plume following the terrain together with CO_2 from a gas vent in Italy, and an ice trail emerging from a Starzach mofette during winter in *Fig 2b* of [27]. Consequently, quantification efforts of the CO_2 emissions in Starzach must take this low-level horizontal gas flow into account by measuring close to the ground. Notably, the typical meteorological wind measurements in 2 m height above ground can not be used as a reliable proxy for near-surface CO_2 movements. Furthermore, classic eddy covariance measurements of the *vertical turbulent* CO_2 flux would be expected to dramatically underestimate the total emissions.

Starting in 2018, a low-cost near-surface CO_2 sensor network (Sensirion SCD30) and other meteorological equipment has been gradually deployed there for testing of different configurations and sensors [27], revealing a distinct diurnal pattern of wind direction due to the valley orography and very low wind speeds at night. This inhibits mixing and removal

PLOS Climate

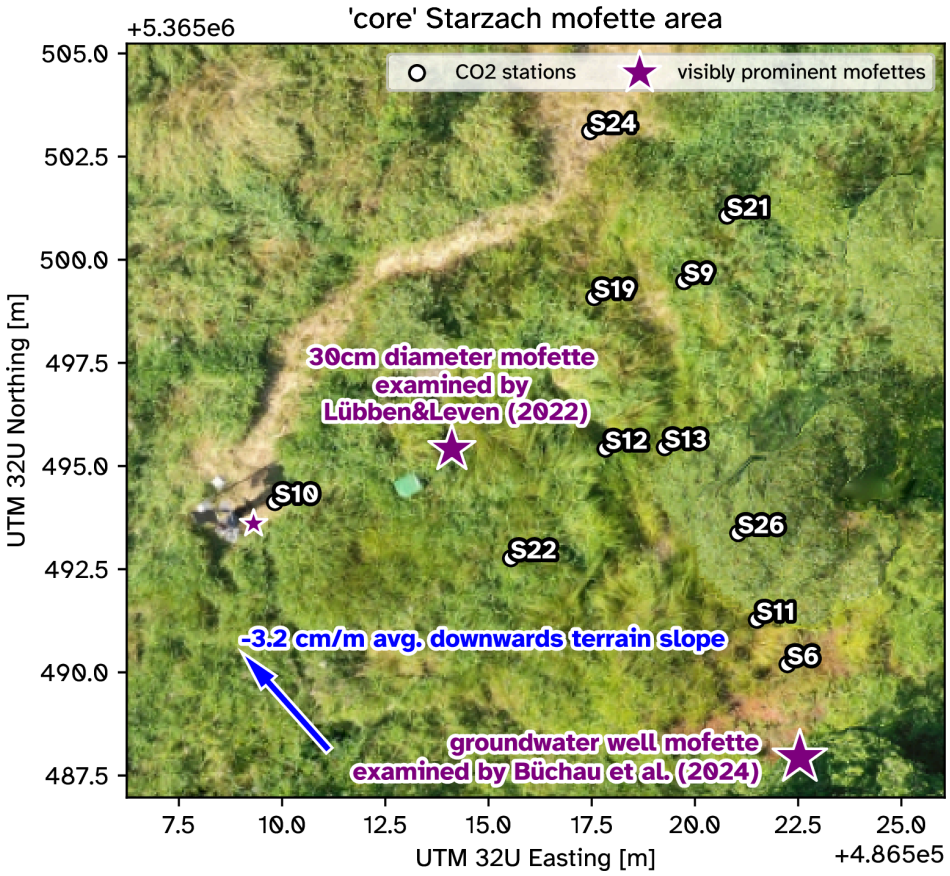

Fig 1. The Starzach site's main mofette area. Axes are in Universal Transverse Mercator (UTM) coordinates, offset from a value indicated at the upper end of each axis to keep numbers concise. Background picture taken by Martin Schön through aerial imaging in 2019. Purple stars indicate the visibly most active mofettes. Smaller mofettes and diffuse degassing area are not shown. The labels S6 through S26 indicate the positions of individual CO_2 monitoring stations. For a broader overview of the site and measurement system we refer to our previous publications [27,28].

https://doi.org/10.1371/journal.pclm.0000741.g001

of CO_2 and thus causes a significant diurnal cycle of near-surface atmospheric CO_2 concentrations up to 40,000 ppm (4 vol%, a 100-fold increase over the average atmospheric concentration) at night [27]. Fig 2 shows a typical diurnal near-surface CO_2 time series at 30 cm above ground with peak analysis. Stations are equipped with Sensirion SCD30 CO_2 sensors queried with the fastest measurement interval of two seconds. The stations usually observe around 1000 CO_2 concentration peaks (i.e. local maxima) per day, recurring in intervals of ten seconds up to a few minutes, and shorter peak durations of a few seconds up to a few minutes. During the day, peaks are slightly more frequent and shorter than during nighttime, while peak magnitude is mostly independent of time. Previous studies have shown, that the CO_2 degassing of an individual Starzach mofette does not exhibit any diurnal pattern [28,29], so this temporal difference can be explained with increased atmospheric mixing at daytime. Peak duration and intervals have a similar magnitude, which often causes significant overlap between peak flanks. Together with the high number of individual peaks, this complicates their isolation for fitting of Gaussian puffs or solving the ADE directly. Other gas emission quantification studies, like detection of industrial methane leaks or ship emissions with comparable release rates as the Starzach site at

PLOS Climate

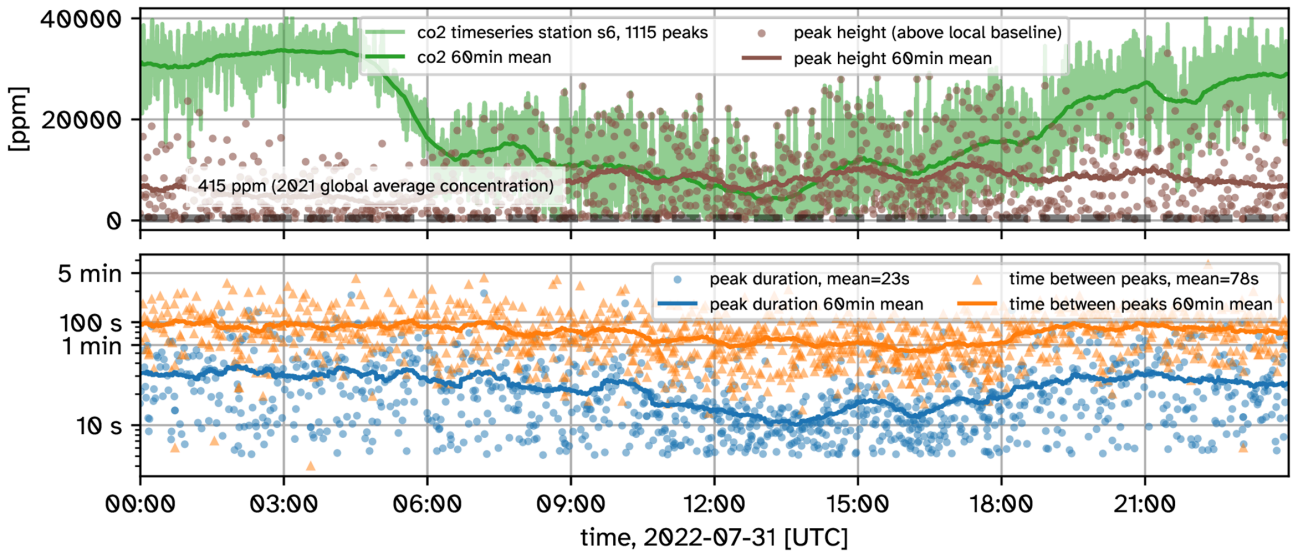

Fig 2. Typical 24 hour time series of a near-surface CO_2 station 6 at the Starzach site's main mofette area with global average CO_2 concentration reference of 415 ppm [2] (top), and peak duration and time between peaks (bottom).

https://doi.org/10.1371/journal.pclm.0000741.g002

an order of magnitude of 1000 kg d^{-1} ≈ 40 kg h^{-1}, typically fit Gaussian puffs or plumes to time series with 1–100 daily peaks (or "events") [32–34]. This is a lot less than in the present Starzach data (Fig 2) and consequently results in much reduced or no peak overlap – often a requirement for peak detection above a certain baseline and subsequent fitting. In fact, Gaussian puffs are generally used to quantify individual and separate release events, not a mostly continuous stream of gas emissions with only intermittent interruptions as found at the Starzach site.

CO_2 movement tracking

With no representative near-surface wind vector field available to parametrise CO_2 movement, we opted for a statistical approach as a proxy. The CO_2 concentration time series exhibit a large amount of local maxima (Fig 2), of which distinct patterns are often recognisable between neighbouring stations A and B at positions $\vec{p}_A$[m] and $\vec{p}_B$[m] respectively. The time shift Δt_{AB}[s] between these matching peak patterns is a function of time t[s] and a proxy for the duration it takes a packet of CO_2 to move from station A to station B. With the distance vector $\vec{d}_{AB}[m] = \vec{p}_B - \vec{p}_A$ pointing from station A to station B, an estimate for the CO_2 movement speed vector $\vec{u}_{AB}$[m s^{-1}] can be derived:

$$\vec{u}_{AB}(t) = \frac{\vec{d}_{AB}}{\Delta t_{AB}(t)} \tag{1}$$

To calculate Δt_{AB}, we apply a 10 min-rolling window to each station combination pair. In this window, we determine the best-matching time shift from the maximum of the cross-correlation function of the two stations' CO_2 concentration time series. Each station in the sensor network delivers CO_2 concentration data roughly every two seconds, which is the sensor's fastest measurement rate. We resampled and interpolated all individual station data to one-second intervals for a common time resolution, so this rolling cross-correlation yields best-matching time shifts Δt_{AB} and the respective correlation values R_{AB}[1] at a rate of 1 Hz, which are shown in Figs 3 and 4 for an exemplary day (31.07.2022) and station

PLOS Climate

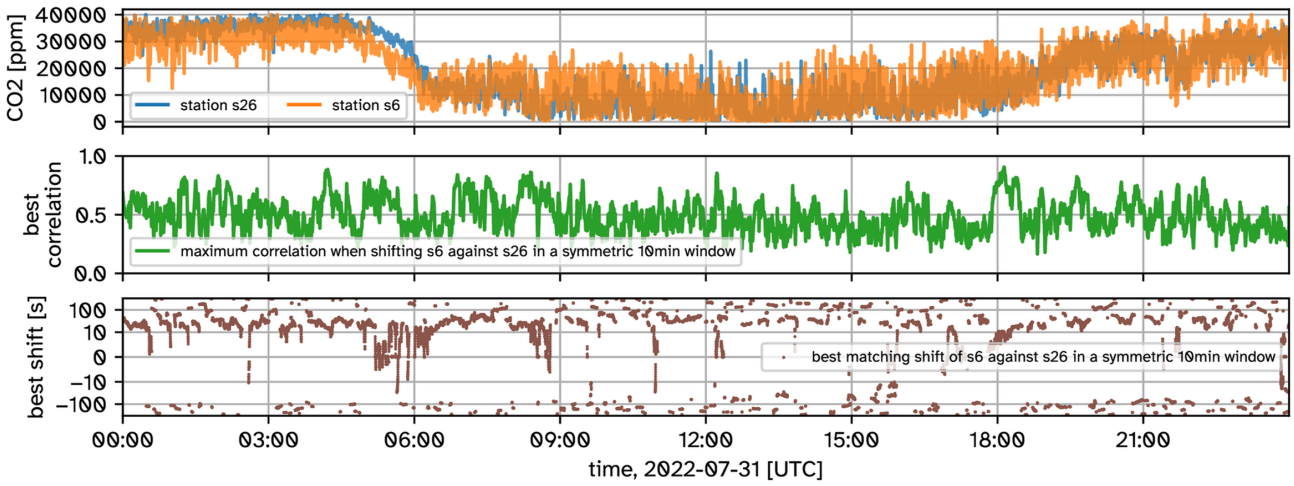

Fig 3. Time series of CO_2 concentration, best cross-correlation and shift of two stations at the Starzach site. Time series of station 6 and station 26 (top) are cross-correlated in a 10 min rolling window to determine the shift between them (bottom) from the highest cross-correlation value (center). In the lowest panel, the y-axis has a symmetric logarithmic scale, but the region −10 to 10 s is scaled linearly. See Fig 4 for a zoomed view.

https://doi.org/10.1371/journal.pclm.0000741.g003

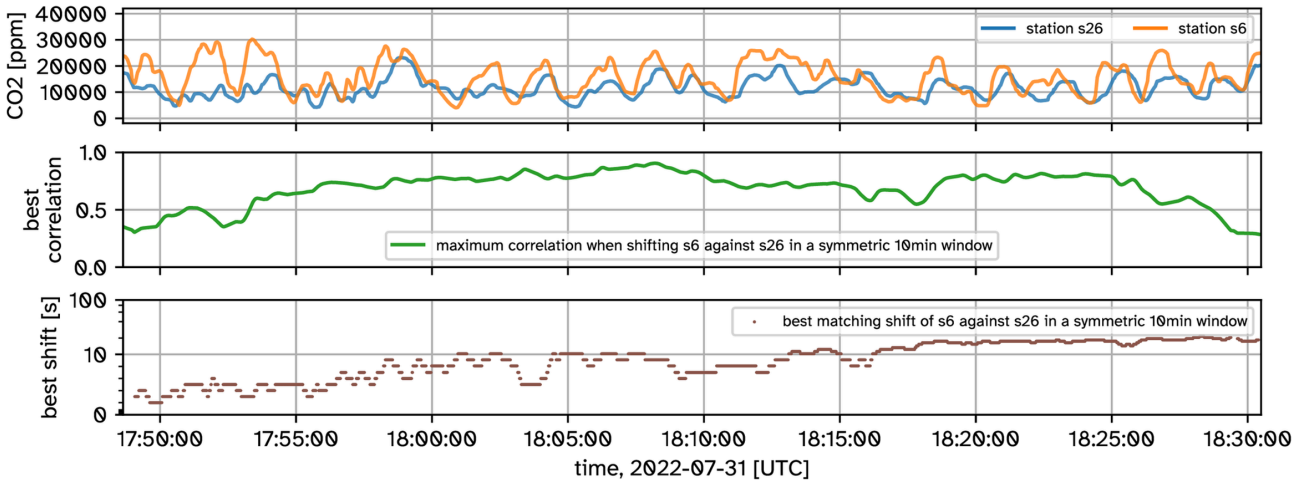

Fig 4. Zoomed view of Fig 3. A *positive* shift in the lowest panel means that the time series of of station **s6** needs to be moved *forward in time* (into the future) to match the time series of station **s26**.

https://doi.org/10.1371/journal.pclm.0000741.g004

pair (stations 6 and 26). The window size of 10 min was chosen, so enough surrounding peaks provide context for the cross-correlation to be meaningful. In other setups, this window size might need adjustment.

The magnitude of correlation between two stations varies significantly and covers the entire range from 0–100% (Figs 2 and 5). For this examined day, the stations closest to the central mofette have the highest correlations with each other, while stations from opposites sides of the area expectedly correlate poorly. The raw values of Δt_{AB} can jump erratically when there is a change in peak patterns that causes the cross-correlation to be numerically larger for a shift of opposite

PLOS Climate

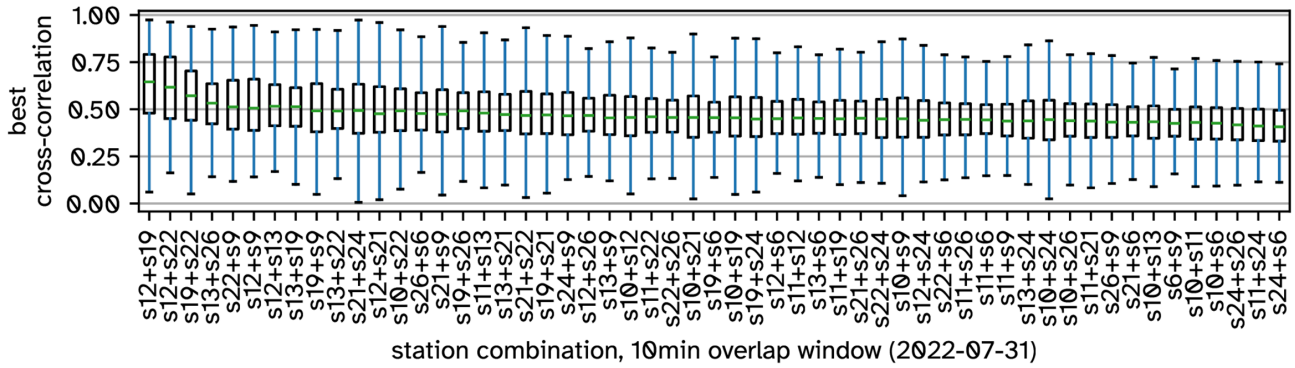

Fig 5. Boxplots of the best cross-correlation R_{AB} between CO_2 time series during one day (31.07.2022).

https://doi.org/10.1371/journal.pclm.0000741.g005

sign (Fig 3). When the overall level of correlation is high, this happens less or not at all (Fig 4). To extract a more robust estimate of time shift Δt_{AB} between stations, another 10 min rolling average was applied, weighted with the best cross-correlation R_{AB} raised to a power of six to filter out low correlation values.

Applying Eq (1), this rolling cross-correlation now contains CO_2 movement speed information on any line connecting a pair of stations. To map this irregularly distributed $\vec{u}_{AB}$ data onto a regular grid, we perform a weighted average, so the final CO_2 movement speed estimate $\vec{u}_{CO_2}$[m s^{-1}] in a grid cell center at location $\vec{p}$[m] is an average of all available $\vec{u}_{AB}$ estimates:

$$\underbrace{\vec{u}_{CO_2}(t,\vec{p})}_{CO_2\text{ speed estimate}} = \underbrace{\frac{\sum_{AB} w_{AB}(t,\vec{p}) \cdot \vec{u}_{AB}(t)}{\sum_{AB} w_{AB}(t,\vec{p})}}_{\text{weighted average of all speed estimates}} \tag{2}$$

with the following weight w_{AB} [1]:

$$\underbrace{w_{AB}(t,\vec{p})}_{CO_2\text{ speed weight}} = \underbrace{(R_{AB}(t))^3}_{\text{best correlation}} \cdot \underbrace{\exp\left(-\frac{\text{sdf}_{AB}(\vec{p})}{5\,\text{m}}\right)}_{\text{distance to both stations}} \cdot \underbrace{\exp\left(-\frac{|\vec{d}_{AB}|}{1\,\text{m}}\right)}_{\text{distance between stations}} \tag{3}$$

where $\text{sdf}_{AB}(\vec{p})$[m] is the closest distance of point $\vec{p}$ to the line segment connecting station A and B, also known as the *signed distance function* [35]. The weight w_{AB} ensures that *highly-correlated*, *close* neighbours, in the *near vicinity* are prioritised. The arbitrary normalisations of the individual factors of Eq (3) were chosen in accordance with the extents of its input variables and might need adjustments in a different setup. The product of CO_2 movement speed and mass concentration C_{CO_2}[kg m^{-3}] then yields the CO_2 mass transport or flux $\vec{F}_{CO_2}$[kg m^{-2}s^{-1}]:

$$\vec{F}_{CO_2}(t,\vec{p}) = \vec{u}_{CO_2}(t,\vec{p}) \cdot C_{CO_2}(t,\vec{p}) \tag{4}$$

Similar to $\vec{u}_{CO_2}$, for C_{CO_2} we average all concentration measurements weighted with the exponentially decaying distance to the respective station and a decay length of 1 m to inter- or extrapolate it to any location $\vec{p}$.

This presented cross-correlation method of estimating gas transports is inherently independent of spatial dimensionality, so it can be applied in one, two or three dimensions. In our case, we only have CO_2 data available in 30 cm height above ground, so we use a two-dimensional grid. In theory, $\vec{F}_{CO_2}$ can now be integrated over an arbitrarily-chosen

PLOS Climate

boundary of interest ("mass balance approach") to determine the total flow of CO_2 $\dot{m}_{CO_2}$[kg s^{-1}] out of the region. However, unless this boundary is placed *between* stations, which dramatically restricts the total possible area and is thus wasteful, the representativeness of $\vec{F}_{CO_2}$ at the exact boundary can be doubted. Furthermore, all other arguably more representative data *inside* the volume of interest is ignored. So instead, we employ Gauss' divergence theorem [36], which allows to substitute the surface-integral over the boundary S[m^2] with a volume-integral over the divergence:

$$\underbrace{\dot{m}_{CO_2}}_{\text{emission rate}} = \underbrace{\int_S \vec{F}_{CO_2}(t,\vec{p})dS}_{\text{mass flow through boundary}} = \underbrace{\int_V \nabla\cdot\vec{F}_{CO_2}(t,\vec{p})dV}_{\text{mass emergence within boundary}} \tag{5}$$

This emission rate $\dot{m}_{CO_2}$ can then be integrated over a time frame of interest, such as one day, to calculate the total emitted mass of CO_2.

Verification with Gaussian Puff model

To verify the CO_2 emission rate $\dot{m}_{CO_2}$ derived with Eq (5), we use the well-established Gaussian puff method to simulate CO_2 transport from a mofette to a sensor station. This requires selecting one of the many available Gaussian puff equations and parametrisations, which is physically sensible and appropriate for fitting to observed Starzach CO_2 time series. We start with the Gaussian puff equation for the concentration C[kg m^{-3}] with reflection at the ground and no wind shear [20,37]:

$$C(t,x,y,z) = \frac{\sqrt{2}m}{4\pi^{\frac{3}{2}}\sigma_x\sigma_y\sigma_z}\left(e^{-\frac{(z+z_0)^2}{2\sigma_z^2}} + e^{-\frac{(z-z_0)^2}{2\sigma_z^2}}\right)e^{-\frac{y^2}{2\sigma_y^2}-\frac{(-tu+x)^2}{2\sigma_x^2}} \tag{6}$$

where m[kg] is the instantaneously emitted mass, t[s] the time since the emission event, x[m] the downwind distance, y[m] the crosswind distance, z[m] the height above flat ground, z_0[m] the height of the emission source and $\sigma_x, \sigma_y, \sigma_z$[m] the puff spreads in the respective spatial directions. In this form, with constant puff spreads σ_i, an emitted packet of CO_2 moves with invariable speed and shape. While this Eq (6) is a physical solution of the advection-diffusion equation, constant puff spreads σ_i are unrealistic - a puff's extent *does* change gradually after its release [38]. It is thus common to parametrise the spreads σ_i with monotonic functions such as a power-law or a function that can be approximated by a power-law, either in terms of time t [38–41]:

$$\sigma_i(t) = a_i t^{b_i} \quad (\text{units: } [\sigma_i]=\text{m},\ [t]=\text{s},\ [a_i]=\text{ms}^{-b_i},\ [b_i]=1) \tag{7}$$

or in terms of downwind distance x [34,42–44]:

$$\sigma_i(x) = a_i x^{b_i} \quad (\text{units: } [\sigma_i]=\text{m},\ [a_i]=\text{m},\ [x]=\text{m},\ [b_i]=1) \tag{8}$$

Despite the original parametrisation being in terms of time t when the Gaussian puff model was introduced nearly a century ago [45], parametrisation in terms of downwind distance x have been more widely established - presumably because x is easier to quantify than travel time t. Therefore, several empirical tabular and graphical charts for parametrisations of puff spreads in terms of downwind distance x exist [46,47]. Due to the occurrences of the σ_i in Eq (6), these two parametrisations result in drastic differences in the simulated puff shape in space and time, and for the fulfillment of mass conservation. These differences are summarised in Table 1.

Mass conservation: Integrating the concentration over the entire spatial domain of a Gaussian puff yields the total distributed mass m_{tot}[kg], which should amount to the initially emitted mass m if mass conservation is fulfilled. In the case of Eq (6), this reads:

PLOS Climate

Table 1. Qualitative comparison of Gaussian puff spread σ_i parametrisations in terms of time or distance, based on with realistic (i.e. physically sensible or for Starzach data well-matching) and unphysical properties marked with color.

Parametr. →	with time: $\sigma_i(t) = a_i t^{b_i}$	with distance: $\sigma_i(x) = a_i x^{b_i}$
mass conservation	fulfilled	fulfilled for $b_x \leq \frac{1}{2}$ initial overestimation* for $\frac{1}{2} < b_x < 1$ not fulfilled for $b_x \geq 1$
peak shape in distance x	symmetric, Gaussian	asymmetric, "backward-leaning" (steep increase, shallow decrease)
peak shape in time t	asymmetric, "backward-leaning" (quick increase, slow decrease)	symmetric, Gaussian
peak movement	with speed u, everywhere	variable speed and mostly $\neq \frac{x}{t}$, artifacts with backwards-moving peak when off-axis ($\lvert y\rvert > 0$) and $b_i > \frac{1}{2}$
peak arrival time	different everywhere and mostly $\neq \frac{x}{u}$, artifacts where peak can arrive earlier downstream than upstream when off-axis ($\lvert y\rvert > 0$) with $b_i > \frac{1}{2}$	with speed u, $t_{\text{peak}} = \frac{x}{u}$ i.e. peak arrives as "wall" everywhere

*only $x > 0$ can be considered in Eq (9) here, so there is an initial phase where $50\% \leq \frac{m_{\text{tot}}}{m} \leq 100\%$, because diffusion in the backwards direction causes matter to be present at $x < 0$, thus not contributing to m_{tot}.

https://doi.org/10.1371/journal.pclm.0000741.t001

$$m_{\text{tot}} = \int_0^{\infty} \int_{-\infty}^{\infty} \int_{-\infty}^{\infty} C(t,x,y,z)\, dx\, dy\, dz \overset{\text{mass conservation}}{\overset{!}{=}} m \tag{9}$$

For time-based σ_i parametrisation, the emitted puff mass is always conserved. Distance-based σ_i parametrisation on the other hand only eventually ($t \to \infty$) conserves mass for moderate mixing along the direction of flow ($b_x < 1$), but linear or superlinear longitudinal spreading ($b_x \geq 1$) violates mass conservation, as it is too far from the actual physical solution, which is $b_i = 0$ or $\sigma_i = \text{const}$.

Peak shape: Whether t or x is present in the demoninator of Eq (6) controls the peak shape in space and time. Eq (6) does not include wind shear, a process that influences mixing and thus puff shape. Taking wind shear into account results in a slightly "forward-leaning" concentration profile along the wind shear direction [48]. Due to an accumulation of the trace gas at the front of the puff, this can be considered more realistic than plain symmetric Gaussian or asymmetric "backwards-leaning" (steep increase, shallow decrease) peak shapes as predicted by the respective σ_i parametrisation of Eq (6). Wind speeds at the Starzach site are already very low (section The Starzach site) and we do not have vertical wind profile information, so we neglect the numerically probably small wind shear for simulating Gaussian puffs.

Peak movement: Where the two σ_i parametrisations differ significantly is peak movement speed and arrival time, two important quantities in our CO_2 movement tracking method described in section *CO_2 Movement Tracking*. The downwind peak position x_{peak}[m] can be determined from the concentration maximum in x of Eq (6) analytically, i.e. solving $\frac{\partial}{\partial x} C(t,x,y,z) = 0$ for x. Analogously, peak arrival time t_{peak}[s] is found by solving $\frac{\partial}{\partial t} C(t,x,y,z) = 0$ for t. Counterintuitively, due to the nature of the chosen empirical parametrisations, these do not exclusively turn out as simple functions of the wind speed u, especially in the early phase of emission: Having the puff spread $\sigma_i(x)$ depend on distance results in variable peak speed and introduces artifacts where off-axis peaks can even move *backwards* temporarily when $b_x > \frac{1}{2}$. In addition, peaks arrive after time $t_{\text{peak}} = \frac{x}{u}$ regardless of lateral position y, which is unrealistic. On the other hand, with $\sigma_i(t)$ parametrisation, the CO_2 peaks move at a constant speed u regardless of location and peak arrival time increases with lateral distance y. Still, similar artifacts exist when $b_x > \frac{1}{2}$. So in conclusion, to minimize unphysical puff behaviour and for simplicity, we continue with $\sigma_i(t)$ parametrisation, $b_i = \frac{1}{2}$, $y = 0$, and $z_0 = 0$, because the mofettes emit at ground level:

PLOS Climate

$$C_{\text{sqrt-simple}}(t,x,z) = \frac{\sqrt{2}m}{2\pi^{\frac{3}{2}} a_x a_y a_z t^{\frac{3}{2}}} e^{-\frac{z^2}{2a_z^2 t} - \frac{(-tu+x)^2}{2a_x^2 t}} \tag{10}$$

Puffs expanding proportionally to the square root of elapsed time is also supported by [38,39], especially in the early phase after emission, which we are interested in here. To estimate a CO_2 mass emission rate $\dot{m}_{CO_2}$ with Eq (10), we choose a station in a time frame where it is evidently in line with the general movement direction of CO_2 emerging from a specific mofette and fit a summed series of Gaussian puffs to the concentration time series. Setting $y = 0$ is thus reasonable, and without information about lateral diffusion, we furthermore assume it equals longitudinal diffusion: $a_x = a_y$. The total of the fitted Gaussian puff masses $\sum m$ divided by the time frame is then an estimate of $\dot{m}_{CO_2}$ and can be compared to the results from Eq (5).

Results

For consistency, most figures in this paper depict data from the 31.07.2022, which we use as a demonstration day for our methods. The data we used is available at [49]. Fig 6 shows a time snapshot of the CO_2 transport vector $\vec{F}_{CO_2}$

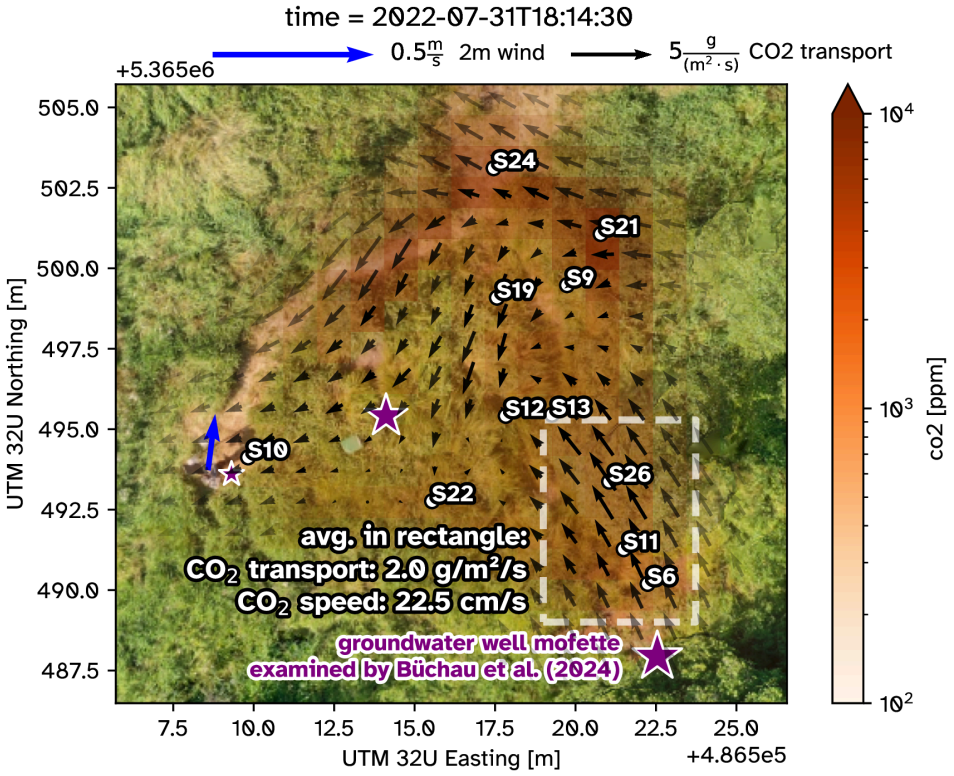

Fig 6. Snapshot of CO_2 transport vector field at the Starzach site in July 2022, derived from cross-correlations between concentration time series according to Eq (5) on a horizontal grid with 1 m resolution. To emphasize real data availability, the black CO_2 transport arrows' opacity is scaled with the smallest $\text{sdf}_{AB}(\vec{p})$, i.e. the closest distance to any station-connecting line segment. The purple stars indicate the visibly most prominent mofettes as in Fig 1. The white rectangle indicates the region used for the top graph in Fig 7 and as a reference in Fig 9.

https://doi.org/10.1371/journal.pclm.0000741.g006

PLOS Climate

calculated from Eq (4) in the early evening. At this time, sun is already blocked from reaching the site due to the hillslope in the south, leaving mostly very slow downslope northwards winds [27], in this case a practically negligible 2 m wind speed below 0.2 m s^{-1}. The emitted CO_2 is thus not advected with the wind, but can instead flow along the terrain due to its higher density [31]. This is particularly evident in the white marked rectangle in Fig 6, where $\vec{F}_{CO_2}$ resulting from CO_2 exhaust of the groundwater well clearly follows the general direction of the terrain gradient (Fig 1).

The lack of vertically resolved information requires an assumption of integration height in the volume integral of Eq (5), for which we choose one meter. The mofettes emit nearly 100 vol% CO_2 [26,28,29], which under calm conditions mostly accumulates near the surface. At 30 cm height, where our sensors are mounted, the highest recorded concentrations are around 4 vol%, so it should be safe to assume that the CO_2 concentration at 1 m height becomes negligible for Eq (5).

As can be seen from the black $\vec{F}_{CO_2}$ arrows in Fig 6, positive divergence (i.e. acceleration or radially pointing away from a specific location) is not exclusively the predominant pattern - negative divergence (i.e. convergence, deceleration or arrows pointing towards each other) does also occur. Positive divergence results from introduction of CO_2 from the site's sources into our chosen boundary, negative divergence from removal. The contribution of the vegetation through photosynthesis can be neglected, as it is three orders of magnitude smaller than the mofettes' exhaust [27]. Instead, we attribute the presence of negative divergence to the fact that we only have horizontal information in the plane 30 cm above ground, and CO_2 can escape out of this plane by moving vertically. The argument can be made that once a packet of CO_2 has moved downwards, it will most likely stay close to the ground due to its higher density. Conversely, if vertical mixing by eddies causes CO_2 to be moved upwards, this individual packet of CO_2 will probably not re-enter our horizontal measurement plane either as it is mixed away. So to handle this, we do not categorically ignore immediate negative divergence, but instead clip negative values of the integrated mass rate $\dot{m}_{CO_2}$ to zero, to filter out situations with significant vertical movements out of our horizontal plane, which we would falsely count negatively towards the emission rate.

Fig 7 shows a time series of the estimated CO_2 mass rate $\dot{m}_{CO_2}$ integrated from the CO_2 transport divergence in Eq (5) with all previously motivated assumptions. From the very low estimated rates at daytime (06:00–18:00 UTC) it is evident that the aforementioned vertical mixing (by convection and turbulence) is too significant in this time frame for our two-dimensional method to be reliable. However, at night (18:00–06:00 UTC) the average rate downstream of the groundwater well mofette matches its exhaust rate measured directly with a funnel system very well (414.7 kg d^{-1} vs. 465 kg d^{-1}) [28]. Another independent validation of this result comes from fitting a series of Gaussian puffs to the time series of station 6 (Fig 8), giving a result of 4.8 g s^{-1} that is equally well in line with the direct bottom-up measurement of 5.5 g s^{-1} [28]. The CO_2 flux in the white rectangle of Fig 6 averages to 2 g m^{-2} s^{-1}, which also comes close to this result when assuming a reference area sized 1 m (our integration height as argued above) by 2.5 m, roughly corresponding to the width of the rectangle. Expanding the temporal scale to one and a half months, a standard deviation of 40% (Fig 9) is introduced. But the average of 517 kg d^{-1} matches the most recently measured groundwater well CO_2 exhaust of roughly 520 kg d^{-1} in summer 2023 very well [30]. Applied to the entire core Starzach mofette area as defined by Fig 1, the average total CO_2 emission is estimated to be 3266 kg d^{-1}±42%. This range is comparable to available gas extraction data from a well one kilometer east of the Starzach site during industrial mining in the 1980s [26].

Discussion

The above results agree well with previous measurements and confirm that our design choices and assumptions are justified and sufficiently work around the method's limitations, which we discuss below. Interestingly, the result of 3266 kg d^{-1}±42% is twice as high as the rough estimate of mofette-only emissions with 1500 kg d^{-1} made in section *The Starzach site*. This suggests that non-mofette, invisible diffuse degassing plays a larger role than previously assumed.

Under calm conditions and on flat terrain, the ADE dictates that CO_2 emitted from a mofette diffuses radially outwards. Stations at comparable distances to a mofette such as station 12 and 22 thus experience similar fluctuations in their CO_2

PLOS Climate

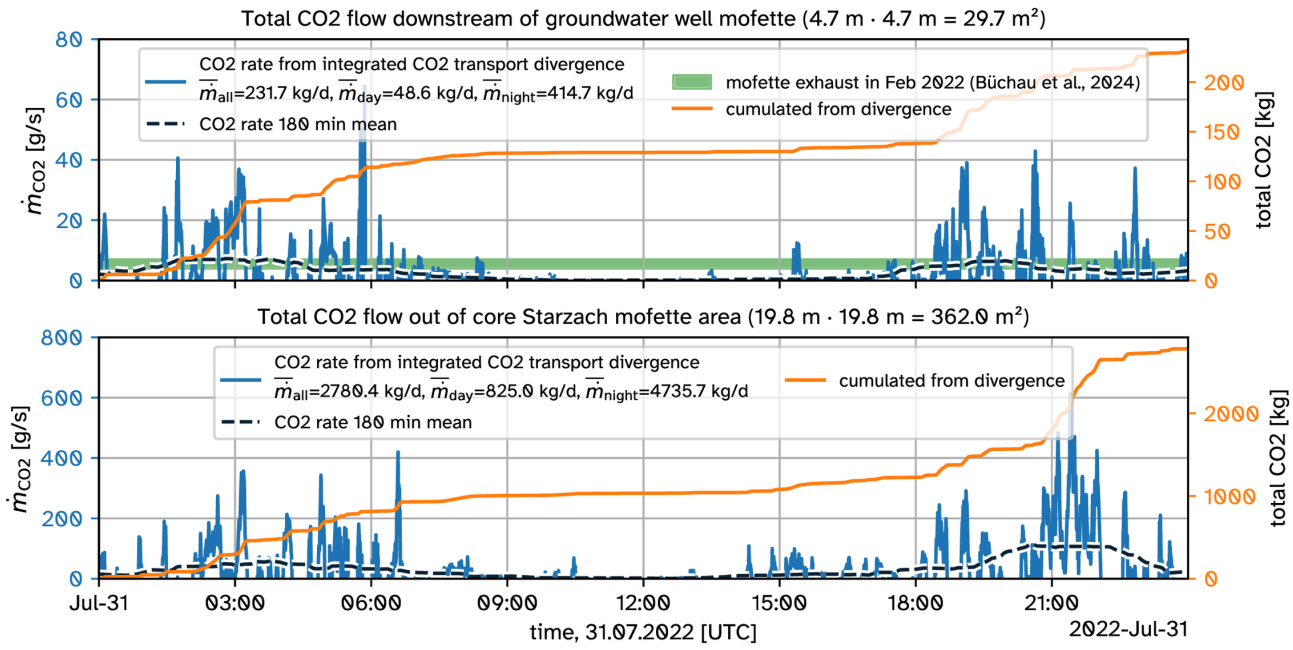

Fig 7. Time series of total CO_2 mass emission rate at the Starzach site, calculated from integrated CO_2 transport divergence according to Eq (5) for the white rectangle downstream fo the groundwater well mofette in Fig 6 (top) and the entire core Starzach mofette area (bottom). The mass rate averages $\bar{m}$ in the legends are calculated for **all** data, **day**time (06:00–18:00 UTC) and **night**time (18:00–06:00 UTC).

https://doi.org/10.1371/journal.pclm.0000741.g007

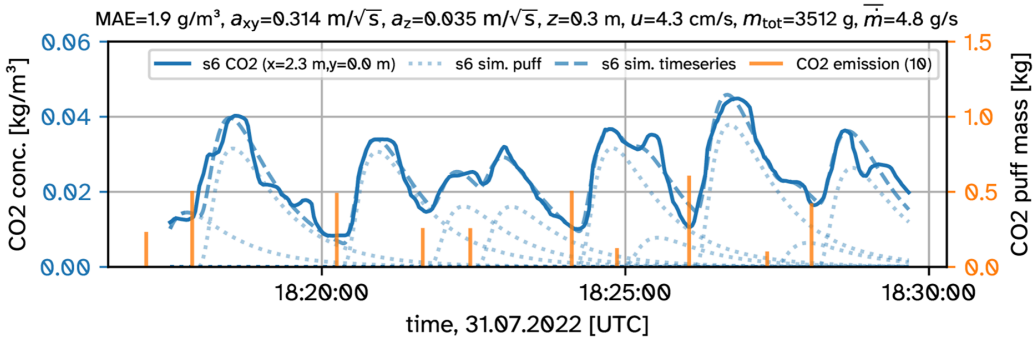

Fig 8. A series of Gaussian CO_2 puffs fitted to station 6 data based on Eq (10). Time and location match the white rectangle in Fig 6. Each individual simulated CO_2 puff of mass m (**orange** bars) contributes one peak (**blue** dotted lines) to the summed simulated time series (**blue** dashed line). Time shifts and masses for each puff and the parameters u, $a_x(=a_y)$ and a_z of Eq (10) were optimized iteratively with methods available in SciPy [50] to best match the measured CO_2 time series of station 6 (**blue** solid line).

https://doi.org/10.1371/journal.pclm.0000741.g008

concentration time series, resulting in a high cross-correlation at only a small time shift between them (Fig 5). Our cross-correlation method based on Eq (2) then falsely interprets this as a fast movement *between* these stations. While this artifact does occur, it is apparently canceled out to a large degree when averaging long enough (Fig 9). A mitigation strategy could be to place stations *around* mofettes in at least two outer ring formations, so the radial movements can be observed

PLOS Climate

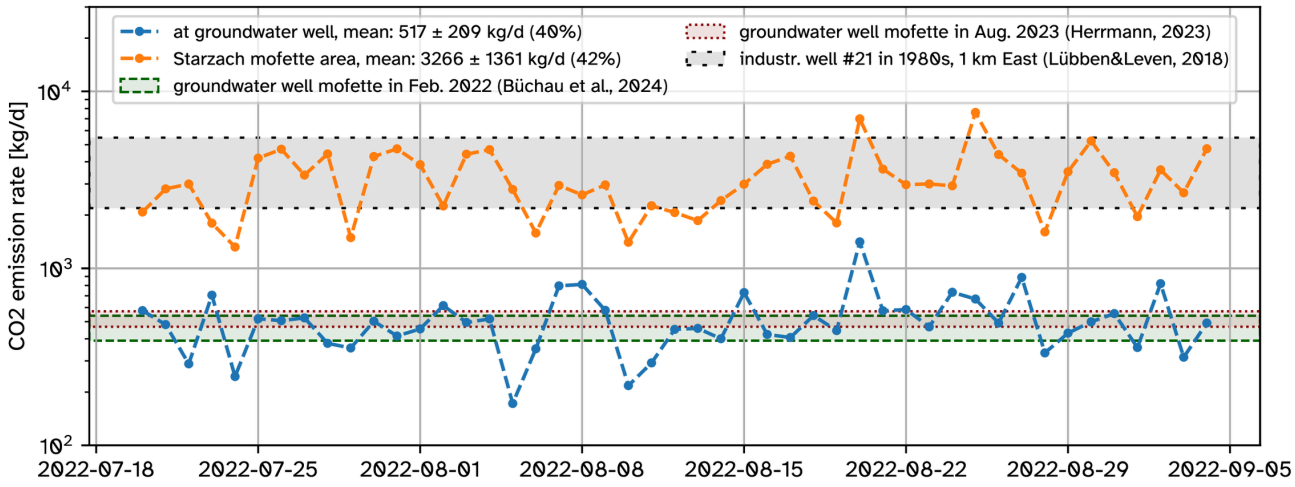

Fig 9. Average daily CO_2 emission rates at the Starzach site over 47 days. The **blue** and **orange** lines consist of the respective average CO_2 emission rates $\dot{m}_{CO_2}$ derived with Eq (5) in the night between 18:00 and 06:00 UTC as motivated by Fig 7.

https://doi.org/10.1371/journal.pclm.0000741.g009

properly. We thus attribute the rather high standard deviation of 40% for $\dot{m}_{CO_2}$ in Fig 9 mostly to a lack of spatial measurement density, and expect this spread to decrease when more sensor stations are used and especially the vertical distribution and movement of CO_2 is quantified.

An alternative gas movement tracking approach more robust against these artifacts would be to assume that an observed peak of CO_2 always originates from a radial movement away from a certain center point. A "dispersion circle" can then be fitted to three or more station's peak arrival times, directly yielding dispersion speed and origin. The ensemble of fitted circles would then also give a source location probability map to pinpoint emission hotspots. But this would introduce possibly non-deterministic iterative fitting as commonly done for Gaussian puff-based approaches [22,34], which our current method does not require.

Another noticeable observation is the discrepancy between mofette degassing periodicity (roughly every four seconds for the groundwater well [28]) and the significantly slower peak frequency (over one minute on average for station 6, Fig 2) in the sensor stations' CO_2 time series, and the simulated Gaussian puffs (Fig 8). While it is to be expected that downstream peak frequency reduces slightly with traveled distance due to mixing [51], an order of magnitude difference over such a short distance of a few meters can not be explained in this way. The time series patterns in Fig 4 might suggest a small-scale vertical atmospheric oscillation as the reason, periodically bringing CO_2-saturated air from below, then fresh air from above to the sensor. For a Brunt-Väisälä buoyancy frequency [52] ranging in the typical CO_2 peak recurrence time of 60–200 s (Fig 2), a very stable vertical potential temperature gradient of 0.03–0.3 K m^{-1} very close to the ground/directly at the surface is required. This is reasonable, considering that the emitted CO_2 has a temperature between 8–14 °C [28,30], which in this case is colder than the surrounding air, enhancing atmospheric stability. Another possibility is that emitted CO_2 first accumulates around the source, its movement initially inhibited by vegetation and small-scale terrain features, until a threshold is overcome and a larger idealised packet of CO_2 begins flowing at once. This theory could also explain the significantly less frequent time series peaks. It is furthermore supported by the good agreement of the peak shapes in time (Fig 8, quick increase, slower decrease) with the Gaussian puff solution (Eq (10), Table 1), suggesting the movement of a connected mass of CO_2. Interestingly, the fitted Gaussian puff speed u (4.3 cm s^{-1}, Fig 8) is much smaller than the more realistic correlation-based speed (22.5 cm s^{-1},

PLOS Climate

Fig 6). We ascribe this to our negligence of wind shear in Eq (10), causing the Gaussian puff to be transported with a constant speed even directly at the surface, resulting in a lower fitted virtual transport speed u to match model to reality. In any case, simulation of the wind field and CO_2 movements at the Starzach site with a Eularian model could clarify the interdependence of mofette degassing periodicity and the slower measured fluctuations in atmospheric CO_2 concentration.

Conclusion

A top-down method was presented to derive CO_2 mass emission rates over an area, based solely on arbitrarily-positioned atmospheric concentration time series. No wind vector information is required as it is derived from cross-correlations between sensors. The method only requires iteration in form of rolling operations, which are deterministic, predictable in runtime and can be reduced in resolution to adjust performance, rendering it real-time applicable. As it only requires a mostly unstructured array of spatial gas concentration measurements, it presents a viable monitoring strategy for environments such as CCS sites, for which the Starzach site in south-western Germany has been proposed as a natural analog [26]. The method was validated with a low-cost sensor network at the Starzach site, a location featuring naturally occurring CO_2 emissions from mofettes, with previous individual bottom-up measurements and a Gaussian puff approach. An average total CO_2 emission rate of 3266 kg d^{-1} ±42% was calculated over one and half months in late summer 2022 for the core Starzach mofette area, for which no such estimate has been available in the known literature until now. This result suggests that invisible, diffuse degassing at the site, which does not originate from visible mofettes, might be more significant than previously expected, and should be investigated further, for example with accumulation chambers. Furthermore, it demonstrates the viability of using low-cost sensors for gas emission quantification schemes: Data of only eleven commercially-available CO_2 sensors costing much less than 100 Euro each was used, together with an equally cost-effective infrastructure and automatic data collection strategy, which dramatically simplifies upscaling of spatial coverage. To reduce the result's uncertainty, the experiment should be repeated with a longer time frame and a higher special measurement density, notably with vertically resolved concentration measurements. Finally, the method should be compared to a Eularian model finely resolving the wind field and gas movements to confirm assumptions and results.

Acknowledgments

This work was supported by the German Research Foundation (DFG) under grant number BA 1988/19-1. The equipment was largely financed by the Alfred-Teufel Foundation. We thank Max-Richard Freiherr von Rassler for access to the field site and Björn Riebandt and Carsten Leven for their general support. We used PARMESAN for meteorological calculations [53], Sympy [54] for derivation, rearrangement and analysis of equations, SciPy [50] for fitting and other calculations and Matplotlib [55] for plotting.

Author contributions

Conceptualization: Yann Georg Büchau.

Data curation: Yann Georg Büchau.

Formal analysis: Yann Georg Büchau.

Funding acquisition: Jens Bange.

Investigation: Yann Georg Büchau.

Methodology: Yann Georg Büchau.

Project administration: Yann Georg Büchau.

Resources: Yann Georg Büchau.

Software: Yann Georg Büchau.

Supervision: Jens Bange.

Validation: Yann Georg Büchau.

Visualization: Yann Georg Büchau.

Writing – original draft: Yann Georg Büchau.

Writing – review & editing: Yann Georg Büchau, Jens Bange.

References

1. Filonchyk M, Peterson MP, Zhang L, Hurynovich V, He Y. Greenhouse gases emissions and global climate change: examining the influence of CO2, CH4, and N2O. Science of The Total Environment. 2024;935:173359. https://doi.org/10.1016/j.scitotenv.2024.173359
2. Calvin K, Dasgupta D, Krinner G, Mukherji A, Thorne PW, Trisos C, et al. Climate Change 2023: Synthesis Report. Geneva, Switzerland: Intergovernmental Panel on Climate Change (IPCC). 2023.
3. UNFCCC. The Paris Agreement. United Nations Framework Convention on Climate Change; 2015.
4. Gerbig C, Akinyede R, Custódio D, Gałkowski M, Ho D, Maier F. Steps towards improved inverse modelling of GHG fluxes: recent work within ITMS. In: Copernicus Meetings; 2025.
5. Harris SJ, Schwietzke S, France JL, Velandia Salinas N, Meixus Fernandez T, Randles C, et al. Methane emissions from the Nord Stream subsea pipeline leaks. Nature. 2025;637(8048):1124–30. https://doi.org/10.1038/s41586-024-08396-8
6. Munassar S, Rödenbeck C, Gałkowski M, Koch F-T, Totsche KU, Botía S, et al. To what extent does the CO2 diurnal cycle impact flux estimates derived from global and regional inversions?. Atmos Chem Phys. 2025;25(1):639–56. https://doi.org/10.5194/acp-25-639-2025
7. Nisbet E, Weiss R. Top-down versus bottom-up. Science. 2010;328(5983):1241–3. https://doi.org/10.1126/science.1189936
8. Janssens-Maenhout G, Petrescu AMR, Muntean M, Blujdea V. Verifying greenhouse gas emissions: methods to support international climate agreements. Greenhouse Gas Measurement and Management. 2011;1(2):132–3. https://doi.org/10.1080/20430779.2011.579358
9. Tejada G, Gatti LV, Basso LS, Cassol HLG, Silva-Junior CHL, Mataveli G, et al. CO2 emissions in the Amazon: are bottom-up estimates from land use and cover datasets consistent with top-down estimates based on atmospheric measurements?. Front For Glob Change. 2023;6. https://doi.org/10.3389/ffgc.2023.1107580
10. Sargent M, Barrera Y, Nehrkorn T, Hutyra LR, Gately CK, Jones T, et al. Anthropogenic and biogenic CO 2 fluxes in the Boston urban region. Proc Natl Acad Sci USA. 2018;115(29):7491–6. https://doi.org/10.1073/pnas.1803715115
11. Asefi-Najafabady S, Rayner PJ, Gurney KR, McRobert A, Song Y, Coltin K, et al. A multiyear, global gridded fossil fuel CO2 emission data product: Evaluation and analysis of results. JGR Atmospheres. 2014;119(17). https://doi.org/10.1002/2013jd021296
12. Zängl G, Reinert D, Rípodas P, Baldauf M. The ICON (ICOsahedral Non-hydrostatic) modelling framework of DWD and MPI-M: Description of the non-hydrostatic dynamical core. Quart J Royal Meteoro Soc. 2014;141(687):563–79. https://doi.org/10.1002/qj.2378
13. Maronga B, Banzhaf S, Burmeister C, Esch T, Forkel R, Fröhlich D, et al. Overview of the PALM model system 6.0. Geosci Model Dev. 2020;13(3):1335–72. https://doi.org/10.5194/gmd-13-1335-2020
14. Badeke R, Matthias V, Grawe D. Parameterizing the vertical downward dispersion of ship exhaust gas in the near field. Atmos Chem Phys. 2021;21(8):5935–51. https://doi.org/10.5194/acp-21-5935-2021
15. Grawe D, Schlünzen KH, Pascheke F. Comparison of results of an obstacle resolving microscale model with wind tunnel data. Atmospheric Environment. 2013;79:495–509. https://doi.org/10.1016/j.atmosenv.2013.06.039
16. Cho T, Chung J, Miller SM, Saibaba AK. Computationally efficient methods for large-scale atmospheric inverse modeling. Geosci Model Dev. 2022;15(14):5547–65. https://doi.org/10.5194/gmd-15-5547-2022
17. Draxler RR, Hess GD. An overview of the HYSPLIT_4 modelling system for trajectories. Australian Meteorological Magazine. 1998;47(4):295–308.
18. Lin JC, Gerbig C, Wofsy SC, Andrews AE, Daube BC, Davis KJ, et al. A near-field tool for simulating the upstream influence of atmospheric observations: The Stochastic Time-Inverted Lagrangian Transport (STILT) model. J Geophys Res. 2003;108(D16). https://doi.org/10.1029/2002jd003161
19. Pisso I, Sollum E, Grythe H, Kristiansen NI, Cassiani M, Eckhardt S, et al. The Lagrangian particle dispersion model FLEXPART version 10.4. Geosci Model Dev. 2019;12(12):4955–97. https://doi.org/10.5194/gmd-12-4955-2019
20. Stockie JM. The mathematics of atmospheric dispersion modeling. SIAM Rev. 2011;53(2):349–72. https://doi.org/10.1137/10080991x
21. Karion A, Sweeney C, Pétron G, Frost G, Michael Hardesty R, Kofler J, et al. Methane emissions estimate from airborne measurements over a western United States natural gas field. Geophysical Research Letters. 2013;40(16):4393–7. https://doi.org/10.1002/grl.50811

22. Daniels WS, Jia M, Hammerling DM. Detection, localization, and quantification of single-source methane emissions on oil and gas production sites using point-in-space continuous monitoring systems. Elem Sci Anth. 2024;12(1). https://doi.org/10.1525/elementa.2023.00110
23. Foken T. Springer handbook of atmospheric measurements. Cham: Springer; 2021.
24. Baldocchi DD. Assessing the eddy covariance technique for evaluating carbon dioxide exchange rates of ecosystems: past, present and future. Global Change Biology. 2003;9(4):479–92. https://doi.org/10.1046/j.1365-2486.2003.00629.x
25. Chu H, Luo X, Ouyang Z, Chan WS, Dengel S, Biraud SC, et al. Representativeness of Eddy-Covariance flux footprints for areas surrounding AmeriFlux sites. Agricultural and Forest Meteorology. 2021;301–302:108350. https://doi.org/10.1016/j.agrformet.2021.108350
26. Lübben A, Leven C. The Starzach site in Southern Germany: a site with naturally occurring CO2 emissions recovering from century-long gas mining as a natural analog for a leaking CCS reservoir. Environ Earth Sci. 2018;77(8). https://doi.org/10.1007/s12665-018-7499-y
27. Büchau YG, van Kesteren B, Platis A, Bange J. An Autarkic Wireless Sensor Network to Monitor Atmospheric CO2 Concentrations. metz. 2022;31(4):331–45. https://doi.org/10.1127/metz/2022/1125
28. Büchau YG, Leven C, Bange J. A portable low-cost device to quantify advective gas fluxes from mofettes into the lower atmosphere: first application to Starzach mofettes (Germany). Environ Monit Assess. 2024;196(2). https://doi.org/10.1007/s10661-023-12114-8
29. Lübben A, Leven C. A gas-flow funnel system to quantify advective gas emission rates from the subsurface. Environ Earth Sci. 2022;81(15). https://doi.org/10.1007/s12665-022-10512-8
30. Herrmann K. Design reiteration of a chimney gas flowmeter for natural CO2 emissions from mofettes: differential pressure measurement increases resolution and accuracy. 2023. https://doi.org/10.15496/PUBLIKATION-89337
31. Rogie JD, Kerrick DM, Chiodini G, Frondini F. Flux measurements of nonvolcanic CO2 emission from some vents in central Italy. J Geophys Res. 2000;105(B4):8435–45. https://doi.org/10.1029/1999jb900430
32. Bell C, Ilonze C, Duggan A, Zimmerle D. Performance of continuous emission monitoring solutions under a single-blind controlled testing protocol. Environ Sci Technol. 2023;57(14):5794–805. https://doi.org/10.1021/acs.est.2c09235
33. Krause K, Wittrock F, Richter A, Busch D, Bergen A, Burrows JP, et al. Determination of NOx emission rates of inland ships from onshore measurements. Atmos Meas Tech. 2023;16(7):1767–87. https://doi.org/10.5194/amt-16-1767-2023
34. Jia M, Fish R, Daniels WS, Sprinkle B, Hammerling D. A fast and lightweight implementation of the Gaussian puff model for near-field atmospheric transport of trace gasses. Sci Rep. 2025;15(1):18710. https://doi.org/10.1038/s41598-025-99491-x PMID: 40437081
35. Osher S, Fedkiw R. Signed distance functions. In: Osher S, Fedkiw R, editors. Level set methods and dynamic implicit surfaces. New York, NY: Springer. 2003. p. 17–22.
36. Simmonds JG. The gradient, the del operator, covariant differentiation, and the divergence theorem. In: Simmonds JG, editor. A brief on tensor analysis. New York, NY: Springer; 1994. p. 71–105.
37. Yamartino R. Gaussian puff modelling. Air quality modeling - theories, methodologies, computational techniques, and available databases and software. The EnviroComp Institute and the Air & Waste Management Association; 2008. p. 281–314.
38. Gifford FA. Tropospheric relative diffusion observations. J Appl Meteor. 1977;16(3):311–3. https://doi.org/10.1175/1520-0450(1977)016<0311:trdo>2.0.co;2
39. Edinger JG. A technique for measuring the detailed structure of atmospheric flow. In: International Symposium on Atmospheric Turbulence in the Boundary Layer. 1952. p. 241.
40. Measurement and analysis of puff dispersion above the atmospheric boundary layer using quantitative imagery. Journal of Applied Meteorology. 2002;41(10):1027–41. https://doi.org/10.1175/1520-0450(2002)041<1027:maaopd>2.0.co;2
41. Cao X, Roy G, Hurley WJ, Andrews WS. Dispersion coefficients for Gaussian Puff models. Boundary-Layer Meteorol. 2011;139(3):487–500. https://doi.org/10.1007/s10546-011-9595-3
42. Hanna SR, Briggs GA, Hosker J. Handbook on Atmospheric Diffusion. Oak Ridge, TN (USA): National Oceanic and Atmospheric Administration; 1982.
43. Griffiths RF. Errors in the use of the Briggs parameterization for atmospheric dispersion coefficients. Atmospheric Environment. 1994;28(17):2861–5. https://doi.org/10.1016/1352-2310(94)90086-8
44. Manheim DC, Newman S, Yeşiller N, Hanson JL, Guha A. Application of cavity ring-down spectroscopy and a novel near surface Gaussian plume estimation approach to inverse model landfill methane emissions. MethodsX. 2023;10:102048. https://doi.org/10.1016/j.mex.2023.102048
45. A theory of eddy diffusion in the atmosphere. Proc R Soc Lond A. 1932;135(826):143–65. https://doi.org/10.1098/rspa.1932.0025
46. Turner DB. Workbook of atmospheric dispersion estimates. Washington, D.C.: U.S. Government Printing Office/United States Environmental Protection Agency, Office of Air Programs; 1973.
47. EPA. Workbook for Plume Visual Impact Screening and Analysis (Revised). EPA-454/R-92-023. United States: Office of Air Quality Planning and Standards. 1992.
48. Walcek C. A Gaussian Dispersion/Plume Model Explicitly Accounting for Wind Shear. 13th Joint Conference on the Applications of Air Pollution Meteorology with the Air and Waste Management Association. 2004;.
49. Büchau Y. CO2 time series data of eleven sensor stations in summer 2022 at the Starzach site in south-western Germany. 2025. https://doi.org/10.5281/zenodo.17055782

50. Virtanen P, Gommers R, Oliphant TE, Haberland M, Reddy T, Cournapeau D, et al. SciPy 1.0: fundamental algorithms for scientific computing in Python. Nat Methods. 2020;17(3):261–72. https://doi.org/10.1038/s41592-019-0686-2

51. Huiru W, Zhanping Y, Fan M, Bin L, Peng H. Study on dispersion of carbon dioxide over the Shrubbery Region. Front Energy Res. 2021;9. https://doi.org/10.3389/fenrg.2021.695224

52. Stull RB. An introduction to boundary layer meteorology. Stull RB, editor. Dordrecht: Springer Netherlands. 1988.

53. Büchau YG, Mashni H, Bramati M, Savvakis V, Schäfer I, Jung S, et al. PARMESAN: meteorological timeseries and turbulence analysis backed by symbolic mathematics. JOSS. 2024;9(94):6127. https://doi.org/10.21105/joss.06127

54. Meurer A, Smith CP, Paprocki M, Čertík O, Kirpichev SB, Rocklin M, et al. SymPy: symbolic computing in Python. PeerJ Computer Science. 2017;3:e103. https://doi.org/10.7717/peerj-cs.103

55. Hunter JD. Matplotlib: a 2D graphics environment. Comput Sci Eng. 2007;9(3):90–5. https://doi.org/10.1109/mcse.2007.55